CHEMISTRY, PHOTOPHYSICS, AND BIOMEDICAL APPLICATIONS OF GOLD NANOTECHNOLOGIES

A Dissertation
Presented to
The Academic Faculty

by

Erik Christopher Dreaden

In Partial Fulfillment
of the Requirements for the Degree
Doctor of Philosophy in the
School of Chemistry and Biochemistry

Georgia Institute of Technology
May 2012

CHEMISTRY, PHOTOPHYSICS, AND BIOMEDICAL APPLICATIONS OF GOLD NANOTECHNOLOGIES

Approved by:

Dr. Mostafa A. El-Sayed, Advisor
School of Chemistry and Biochemistry
Georgia Institute of Technology

Dr. Bridgette A. Barry
School of Chemistry and Biochemistry
Georgia Institute of Technology

Dr. L. Andrew Lyon
School of Chemistry and Biochemistry
Georgia Institute of Technology

Dr. Adegboyega K. Oyelere
School of Chemistry and Biochemistry
Georgia Institute of Technology

Dr. Zhong Lin Wang
School of Materials Science and Engineering
Georgia Institute of Technology

Date Approved: February 29, 2012

To the two people I admire most – Mom and Dad. Thank you for all of your love and support.

ACKNOWLEDGEMENTS

Firstly, I wish to thank my thesis advisor, Mostafa El-Sayed, for sharing with me his limitless enthusiasm and dedication to scientific research. Without his encouragement, support, wisdom, and friendship, I would not be half the scientist I am today. I would also like to acknowledge Prof. Yomi K. Oyelere for his contributions to much of the work in this thesis. Thank you for all of your guidance and hard work – I look forward to following your research in the years to come. I would also like to express gratitude to my undergraduate research advisor, Prof. John L. Stickney, for sharing with me his passion for science and teaching, as well as my high school physics teacher, Dr. Russ Lee, for instilling in me a love for science. My thesis committee members – Profs. Barry, Wang, and Lyon – your support and encouragement are most certainly appreciated.

I would also like to acknowledge my friends and family for their unwavering love, support, and encouragement. Mom and Dad – you two are the most amazing people I have ever known; thank you for showing me the meaning of hard-work and sacrifice, for helping me to realize my potential, and for the amazing opportunities you've provided for myself and Tina. To my friends – Adam, Gaëlle, Chip, Jess, Helen, Ryan, Steven, Alexandra, Nick, Candace, Johnny, Veronique, Carley, Evan, and John – thanks for keeping my ego in check, giving me a reason to occasionally leave the lab, and encouraging my affinity for cheese plates. Linda – fika is the best part of my day; thank you for making the other 23.5 hours mildly tolerable. Tina – I have and will always look up to you. I don't know anyone as patient, caring, and as intelligent as you; thanks for putting up with me all these years and I look forward to watching you continue to succeed in the future.

I've had the opportunity to work with some tremendously talented and dedicated individuals over the past several years. (Prof.) Erin B. Dickerson – thank you for sharing with me your amazing

work ethic and for all of your continuing guidance and support; I hope to work with you again in the future. (Prof.) Xiaohua Huang – thank you for all of the knowledge and skills you shared with me early in my research career. (Prof.) Prashant Jain – thank you for entertaining my incessant questions and for sharing your passion and dedication to nanoscience. Profs. Ivan El-Sayed and Cathy Murphy – it's been a delight working with you in the past and I look forward to collaborating with you as an independent researcher in the not too distant future. Chris Tabor – thank you for letting me constantly bounce ideas off you. Berkley – I appreciate your sincerity and diligence; keep it up, I'm sure you'll do great things. Celinah – it was a pleasure collaborating with you; I wish you all the best moving forward. My coworkers – Steven, Lauren, Chun-Wan, Meg, Rachel, Paul, Mustafa, Brian, Justin, Bin, Guojun, Adam, Li-Kang, Ramazan, Wei, Susie, Qusai, Wei, Nageh, and Wenyu – thank you for helping to making LDL a dynamic (pun, most certainly intended), engaging, and enjoyable place to spend the last 5.75 years. I will very much miss you all. Thanks especially to Brian, Steven, Meg, Justin, and Lauren for assistance in editing this manuscript and to Lauren, Steven, Rachel, and Chun-Wan for their valuable collaborative efforts. Lastly, I'd like to thank Mike Riley, Mamie Gaskin, Shirley Tomes, Vincent and Brent Dreaden, D.F. Wallace, Cam Tyson, Seymour Levov, P. Mantis, V. Nabokov, Prof. M. Chomps, and Michele Yager. Without your help and support over the years, none of this would have been possible.

TABLE OF CONTENTS

LIST OF TABLES

LIST OF FIGURES

LIST OF SYMBOLS

ω	angular frequency
E	electric field
$\vec{\mu}$	electronic transition moment
k	field propagation vector (typically incicdent)
ε	spectroscopic cross section (typically M^{-1} cm^{-1})
γ	localized surface plasmon shape factor
ℓ	surface plasmon mode, order, symmetry, and/or angular momentum
W	watt
λ	wavelength (typically nm)
ζ	zeta potential

LIST OF ABBREVIATIONS

α-Bic	α-Bicalutamide ligand
ADT	androgen deprivation therapy
AFM	atomic force microscopy
AR	androgen receptor (or aspect ratio)
AuNP	gold nanoparticle
AuNR	gold nanorod
Azith	Azithromycin
β-Bic	β-Bicalutamide ligand
cAMP	cyclic adenosine monophosphate
Clarith	Clarithromycin
CPC	cetylpyridium chloride
CT	computed tomography
CTAB	cetyl trimethylammonium bromide
CTC	circulating tumor cell
CTAC	cetyl trimethylammonium chloride
DAPI	4',6-diamidino-2-phenylindole
DCA	dicarboxyacetone
DFSM	dark-field scattering microscopy
DHT	dihydrotestosterone
DPBS	Dulbecco's phosphate buffered saline
DPL	dip-pen lithography

E2	17b-estradiol
EBL	electron beam lithography
EGFR	epidermal growth factor receptor
EPR	enhanced permeability and retention
ER	estrogen receptor
HD	hydrodynamic diameter
IC_{50}	half maximal concentration
ID	initial dose (often g-1, per gram tissue)
iv	intravenous
LSCF	laser scanning confocal microscopy
LSPR	localized surface-plasmon resonance
mAR	membrane androgen receptor
MDR	multiple drug resistance
MPS	mononuclear phagocyte system
NIR	near-infrared
NSL	nanosphere lithography
OCT	optical coherence tomography
OD	spectroscopic optical density (extinction)
PBS	phosphate buffered saline
PEG	poly(ethylene glycol)
PEG-SH	thiol-polyethylene glycol
P-gp	MDR1 P-glycoprotein
PPTT	plasmonic photothermal therapy

PTT	photothermal therapy
PVP	poly(vinylpyrrolidone)
RES	reticuloendothelial system
SAM	self-assembled monolayer
SCC	squamous cell carcinoma
SD	standard deviation
SERS	surface enhanced Raman spectroscopy
siRNA	small interfering ribonucleic acid
SPR	surface plasmon resonance
STEPS	structural transformation by electrodeposition on patterned substrates
T	testosterone
TAM	tamoxifen or tumor-associated macrophage
TAM-PEG-SH	thiol-polyethylene glycol tamoxifen
TEM	transmission electron microscope/microscopy
TriKeto	Tricyclic Ketolide

SUMMARY

Gold nanoparticles exhibit a combination of physical, chemical, optical, and electronic properties unique from all other nanotechnologies. These structures can provide a highly multifunctional platform with which to diagnose and treat diseases and can dramatically enhance a variety of photonic and electronic processes and devices. The work herein highlights some newly emerging applications of these phenomena as they relate to the targeted diagnosis and treatment of cancer, improved charge carrier generation in photovoltaic device materials, and strategies for enhanced spectrochemical analysis and detection. Chapter 1 introduces the reader to the design, synthesis, and molecular functionalization of gold nanotechnologies, and provides a framework from which to discuss the unique photophysical properties and applications of these nanoscale materials and their physiological interactions in Chapter 2. Chapter 3 discusses ongoing preclinical research in our lab investigating the use of near-infrared absorbing gold nanorods as photothermal contrast agents for laser ablation therapy of solid tumors. In Chapter 4, we present recent work developing a novel strategy for the targeted treatment of hormone-dependent breast and prostate tumors using multivalent gold nanoparticles that function as highly selective and potent endocrine receptor antagonist chemotherapeutics. In Chapter 5, we discuss a newly-emerging tumor-targeting strategy for nanoscale drug carriers which relies on their selective delivery to immune cells that exhibit high accumulation and infiltration into breast and brain tumors. Using this platform, we further investigate the interactions of nanoscale drug carriers and imaging agents to a transmembrane protein considered to be the single most prevalent and single most important contributor to drug resistance and the failure of chemotherapy. Chapter 6 presents work from a series of studies exploring enhanced charge carrier generation and relaxation in a hybrid electronic system exhibiting resonant interactions

between photovoltaic device materials and plasmonic gold nanoparticles. Chapter 7 concludes by presenting studies investigating the contributions from so-called “dark” plasmon modes to the spectrochemical diagnostic method known as surface enhanced Raman scattering.

CHAPTER 1

INTRODUCTION TO GOLD NANOTECHNOLOGIES

1.1 Synthesis of Gold Nanoparticles: Bottom-Up Methods

While the first syntheses of colloidal gold pre-date much of the peer-reviewed literature, the first scientific report describing the production of gold nanoparticles came in 1857 when Michael Faraday found that the "fine particles" formed from the aqueous reduction of gold chloride by phosphorus could be stabilized by the addition of carbon disulfide, resulting in a "beautiful ruby fluid".[*1*] Today, most colloidal synthetic methods for obtaining gold nanoparticles (**Figure 1.1**) follow a similar strategy (**Table 1.1**), whereby solvated gold salt is reduced in the presence of surface capping ligands which prevent aggregation of the particles by electrostatic and/or physical repulsion. Particle size is adjusted by varying the gold ion:reducing agent and/or gold ion:stabilizer ratio, with larger (and typically less monodisperse) sizes obtained from larger ratios.

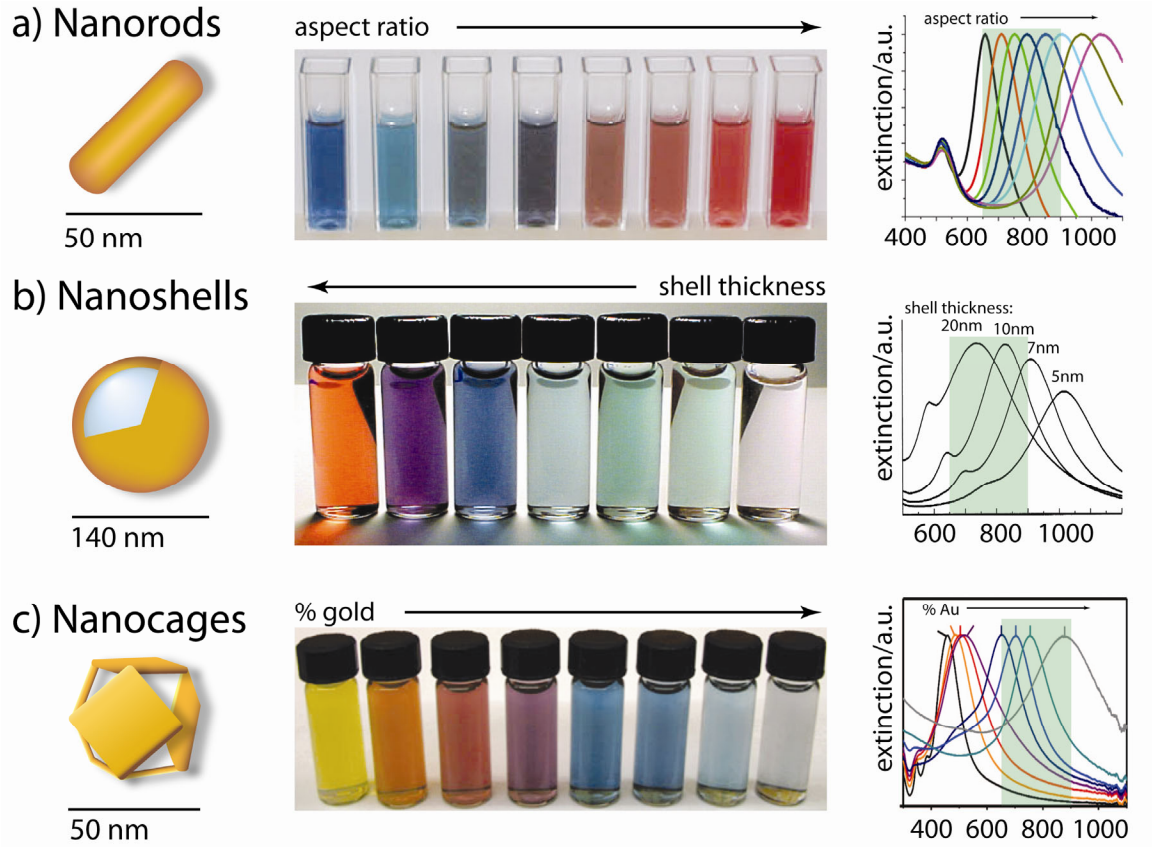

Figure 1.1. Gold nanoparticles commonly applied in biomedical applications. A) Gold nanorods, (B) silica-gold core-shell nanoparticles, and (C) gold nanocages. The intense colors of these nanoparticles (middle panel) arises from the collective excitation of their conduction electrons, or surface plasmon resonance (SPR) modes, which results in photon absorption/scattering (right panel) at wavelengths that vary with (A) aspect ratio, (B) shell thickness, and/or (C) galvanic displacement by gold. Adapted from Dreaden et al. [*2,3*].

Table 1.1. Summary of synthetic approaches to obtain various gold nanostructures.[a] Adapted from Dreaden et al. [*3*].

Au nanostructure	synthesis	primary literature
nanospheres	citrate-mediated reduction	J. Turkevich, P. C. Stevenson and J. Hillier, *Discuss. Faraday Soc.*, 1951, **11**, 55-75.
		G. Frens, *Nature*, 1973, **241**, 20-22.
nanoclusters	alkanethiol/phosphine-stabilized reduction	G. Schmid, R. Pfeil, R. Boese, F. Bandermann, S. Meyer, G. H. M. Calis and J. W. A. van der Velden, *Chem. Ber.*, 1981, **114**, 3634-3642.
		M. Brust, M. Walker, D. Bethell, D. J. Schiffrin and R. Whyman, *J. Chem. Soc. Chem. Commun.*, 1994, **7**, 801-802.
nanorods (colloidal)	seeded growth (CTAB)	N. R. Jana, L. Gearheart, C. J. Murphy, *Adv. Mater.*, 2001, **13**, 1389.
		B. Nikoobakht, M. A. El-Sayed, *Chem. Mater.*, 2003, **15**, 1957.
		Y. Y. Yu, S. S. Chang, C. L. Lee, C. R. C. Wang, *J. Phys. Chem. B*, 1997, **101**, 6661.
nanorods (electrochemical)	template-directed electrochemical deposition	H. Masuda, H. Tanaka and N. Baba, *Chem. Lett.*, 1990, **4**, 621-622.
		C. R. Martin, *Adv. Mater.*, 1991, **3**, 457-459.
striped nanorods (electrochemical)	sequential template-directed electrochemical deposition	S. R. Nicewarner-Peña, R. G. Freeman, B. D. Reiss, L. He, D. J. Peña, I. D. Walton, R. Cromer, C. D. Keating and M. J. Natan, *Science*, 2001, **294**, 137-141.
		L. Qin, S. Park, L. Huang and C. A. Mirkin, *Science*, 2005, **309**, 113-115.
nanoshells	overgrowth of core-bound particles	S. J. Oldenburg, R. D. Averitt, S. L. Westcott and N. J. Halas, *Chem. Phys. Lett.*, 1998, **288**, 243-247.
hollow nanospheres	overgrowth of core-bound particles, core removal; galvanic displacement	Z. Liang, A. Susha and F. Caruso, *Chem. Mater.*, 2003, **15**, 3176-3183.
		H.-P. Liang, L.-J. Wan, C.-L. Bai and L. Jiang, *J. Phys. Chem. B*, 2005, **109**, 7795-7800.
nanocages/frames	PVP-stabilized polyol, galvanic displacement	Y. Sun and Y. Xia, *Science*, 2002, **298**, 2176-2179.
		J. Chen, J. M. McLellan, A. Siekkinen, Y. Xiong, Z.-Y. Li and Y. Xia, *J. Am. Chem. Soc.*, 2006, **128**, 14776-14777.
nanocubes / octahedra	PVP-stabilized polyol; seeded growth (CPC); seeded growth (CTAC)	F. Kim, S. Connor, H. Song, T. Kuykendall and P. Yang, *Angew. Chem. Int. Ed.*, 2004, **43**, 3673-3677.
		W. Niu, S. Zheng, D. Wang, X. Liu, H. Li, S. Han, J. Chen, Z. Tang and G. Xu, *J. Am. Chem. Soc.*, 2008, **131**, 697-703.
		J. Zhang, M. R. Langille, M. L. Personick, K. Zhang, S. Li and C. A. Mirkin, *J. Am. Chem. Soc.*, 2010, **132**, 14012-14014.
icosahedra / tetrahedra	PVP-stabilized polyol; seeded growth (CTAC)	F. Kim, S. Connor, H. Song, T. Kuykendall and P. Yang, *Angew. Chem. Int. Ed.*, 2004, **43**, 3673-3677.
		J. Zhang, M. R. Langille, M. L. Personick, K. Zhang, S. Li and C. A. Mirkin, *J. Am. Chem. Soc.*, 2010, **132**, 14012-14014.
nanoprisms	biosynthesis; seeded growth (CTAB)	S. S. Shankar, A. Rai, B. Ankamwar, A. Singh, A. Ahmad and M. Sastry, *Nat. Mater.*, 2004, **3**, 482-488.
		J. E. Millstone, S. Park, K. L. Shuford, L. Qin, G. C. Schatz and C. A. Mirkin, *J. Am. Chem. Soc.*, 2005, **127**, 5312-5313.
tetrahexahedra / elongated tetrahexahedra	seeded growth (CTAB)	T. Ming, W. Feng, Q. Tang, F. Wang, L. Sun, J. Wang and C. Yan, *J. Am. Chem. Soc.*, 2009, **131**, 16350-16351.
obtuse triangluar bipyramids	seeded growth (CTAC)	M. L. Personick, M. R. Langille, J. Zhang, N. Harris, G. C. Schatz and C. A. Mirkin, *J. Am. Chem. Soc.*, 2011, **133**, 6170-6173.
rhombic dodecahedra / obtuse triangluar bipyramids	seeded growth (CPC); seeded growth (CTAC)	W. Niu, S. Zheng, D. Wang, X. Liu, H. Li, S. Han, J. Chen, Z. Tang and G. Xu, *J. Am. Chem. Soc.*, 2008, **131**, 697-703.
		M. L. Personick, M. R. Langille, J. Zhang, N. Harris, G. C. Schatz and C. A. Mirkin, *J. Am. Chem. Soc.*, 2011, **133**, 6170-6173.
trisoctahedra	ascorbate-mediated, CTAC-stabilized reduction	Y. Ma, Q. Kuang, Z. Jiang, Z. Xie, R. Huang and L. Zheng, *Angew. Chem. Int. Ed.*, 2008, **47**, 8901-8904.
nanosphere lithograph	nanosphere self-assembly, vapor-phase deposition, nanosphere removal	J. C. Hulteen and R. P. Van Duyne, *J. Vac. Sci. Technol. A*, 1995, **13**, 1553-1558.
dip-pen lithograph	vapor-phase deposition, AFM-patterned SAM, chemical etching	H. Zhang, Z. Li and C. A. Mirkin, *Adv. Mater.*, 2002, **14**, 1472-1474.
		H. Zhang and C. A. Mirkin, *Chem. Mater.*, 2004, **16**, 1480-1484.
nanoskived pattern	vapor-phase deposition on topologically-defined polymer, ultramicrotome, polymer removal	Q. Xu, R. M. Rioux and G. M. Whitesides, *ACS Nano*, 2007, **1**, 215-227.
		Q. Xu, R. M. Rioux, M. D. Dickey and G. M. Whitesides, *Acc. Chem. Res.*, 2008, **41**, 1566-1577.
STEPS pattern	directional vapor-phase deposition on topologically-defined polymer, electrochemical deposition of conducting polymer, secondary	P. Kim, A. K. Epstein, M. Khan, L. D. Zarzar, D. J. Lipomi, G. M. Whitesides and J. Aizenberg, *Nano Lett.*, 2011, ASAP.
nanocrescents	nanosphere template, shadow-mask vapor-phase deposition, template removal and dissolution	Y. Lu, G. L. Liu, J. Kim, Y. X. Mejia and L. P. Lee, *Nano Lett.*, 2005, **5**, 119-124.
nanopyramids	photoresist pattern on Si, Cr vapor-phase deposition/liftoff, Au vapor-phase deposition, Au film removal, Cr etch, Si etch	J. Lee, W. Hasan, C. L. Stender and T. W. Odom, *Acc. Chem. Res.*, 2008, **41**, 1762-1771.

[a] CTAB, cetyl trimethylammonium bromide; PVP, poly(vinylpyrrolidone); CPC, cetylpyridium chloride; CTAC, cetyl trimethylammonium chloride; AFM, atomic force microscopy; SAM, self-assembled monolayer; STEPS, structural transformation by electrodeposition on patterned substrates.

Using theoretical electrodynamics set forth by Maxwell in 1865,[*4*] Mie showed in 1908 that the intense colors from Faraday's gold sols arose from the absorption and scattering of light by spherical gold nanoparticles which they contained.[*5*] Following the advent of the electron microscope by Knoll and Ruska in 1932,[*6*] Turkevich provided the first structural studies of gold nanoparticles formed under varying synthetic conditions in 1951;[*7*] later in 1973, Frens performed systematic studies of Turkevich's citrate-mediated growth method, producing monodisperse spherical gold nanoparticles 16 – 150 nm in diameter (**Figure 1.2A**).[*8*] Mechanistically, citrate-mediated gold reduction occurs through a concerted redox reaction whereby citrate is both chemically oxidized by chloroauric acid and thermally oxidized by heating to form dicarboxyacetone (DCA; **Figure 1.3A**) and CO_2.[*9-11*] Electrons from DCA serve to reduce Au(III)Cl_3 to Au(I)Cl, which is believed to form a bidentate (COO^-) complex with DCA. Particle nuclei form via a disproportionation reaction, where (3) AuCl complexes combine to form (2) zero-valent Au atoms and (1) $AuCl_3$ complex. Particle size is generally adjusted by varying the Au salt:citrate ratio or reaction pH.[*9,12*] Until recently, the formation of these particles was presumed to proceed via spontaneous nucleation and isotropic growth (i.e. LaMer growth[*13*]). Recent studies by Pong et al. however, indicate that the small (ca. 5 nm diameter) nuclei formed from the citrate-mediated thermal reduction of chloroauric acid initially self-assemble into a network of interconnected chains that grow in diameter with increasing Au deposition.[*14*] Spherical particles are believed to break off from these structures forming the nanosphere product typically observed from the Turkevich method. This "necklace-breaking" mechanism is fundamentally distinct from other multiparticle mechanisms such as classic Ostwald ripening or oriented attachment (in which small crystalline particles fuse with one another along a crystalline face). In contrast, more recent studies by Polte et al., directly contradict these results, indicating that particle formation proceeds via four overlapping steps: i) nucleation, ii)

aggregation of nuclei, iii) slow isotropic growth via reduction and/or coalescence/Ostwald ripening [*15*], and iv) rapid consumption of the gold precursor.[*16*] Finer points of mechanistic detail notwithstanding, related approaches have been used to obtain monodisperse gold nanospheres as large as 430 nm (**Figure 1.2B**).[*17*]

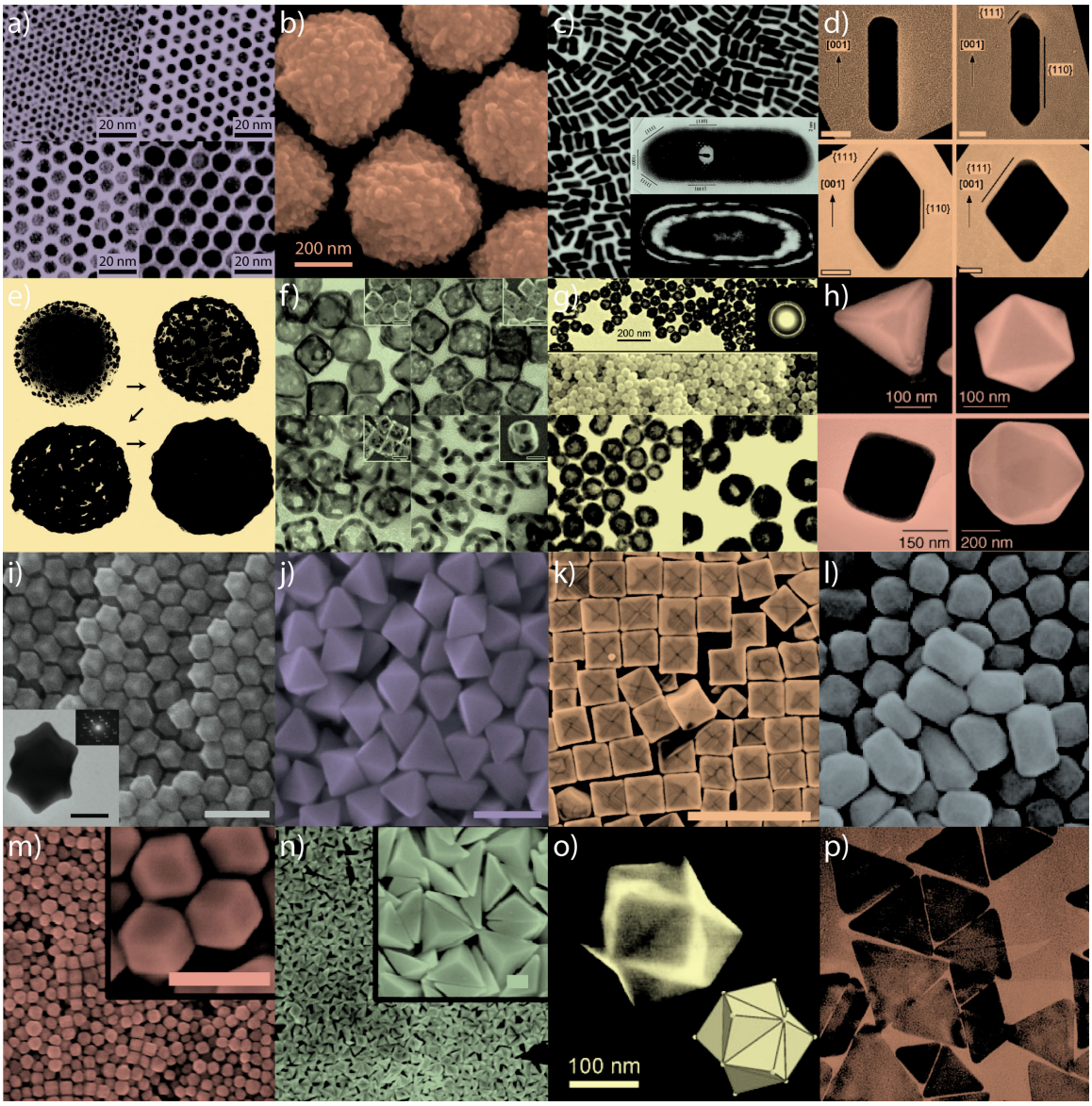

Figure 1.2. Gold nanoparticles of various size and shape with potential applications in biomedicine. A) Small and (B) large nanospheres, (C) nanorods, (D) sharpened nanorods, (E) nanoshells, (F) nanocages/frames, (G) hollow nanospheres, (H) tetrahedra/octahedra/cubes/icosahedra, (I) rhombic dodecahedra, (J) octahedra, (K) concave nanocubes, (L) tetrahexahedra, (M) rhombic dodecahedra, (N) obtuse triangular bipyramids, (O) trisoctahedra, and (P) nanoprisms. Adapted from Dreaden et al. [*3*].

In 1981, Schmid et al. showed that much smaller (1.4 ± 0.4 nm diameter) phosphine-stabilized gold particles could be produced from the reduction of PPh_3AuCl by diborane in benzene, yielding $Au_{55}(PPh_3)_{12}Cl_6$.[*18*] This cluster is a true molecule with a well-defined formula weight, unlike the colloidal gold solutions discussed in the previous paragraph. Hutchison later reported that gold clusters 1.4 – 10 nm in diameter could be obtained via ligand exchange and that these particles

could be similarly produced under ambient conditions and without the need for diborane gas.[*19*] In 1994, Brust and Schiffrin investigated the synthesis of thiol-stabilized gold clusters using a two-phase system in which gold chloride was solvated in toluene by way of a phase-transfer reagent (tetraoctylammouium bromide).[*20*] Here, dodecanethiol was used as a stabilizer for gold clusters formed in the organic phase as reducing sodium borohydride was added to the aqueous phase. These and similar clusters [*21*] have attracted much attention due to their molecule-like properties and facile conjugation, however due to their reported toxicity,[*22,23*] biomedical applications are somewhat limited, including uses in immunolabeling,[*24,25*] and as contrast agents for x-ray imaging [*26*] and radiation therapy.[*27*]

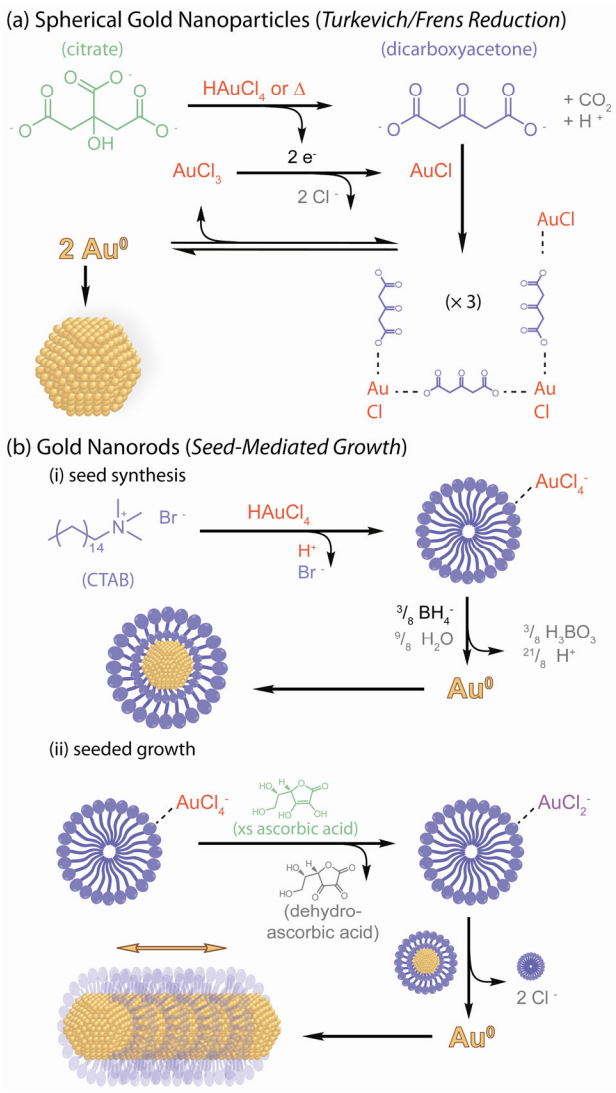

Figure 1.3. Turkevich/Frens Synthesis of Gold Nanoparticles and Seed-Mediated Growth of Gold Nanorods. A) Au(III) is reduced to Au(I) when citrate is oxidized to dicarboxyacetone (DCA) in the presence of chloroauric acid and/or heating. Au(I) chloride is believed to form a bidentate complex with DCA which undergoes a disproportionation reaction to form (2) zero-valent Au atoms and (1) Au(III) chloride. B.i) Au(III) chloride quantitatively displaces Br^- counterions in micelles of cetyltrimethylammonium bromide (CTAB) and subsequent borohydride reduction produces small (ca. 1.5 nm diameter) seed nanoparticles surface-stabilized by a CTAB-bilayer. B.ii) Au(III) bound to CTAB-micelles is reduced to Au(I) by ascorbic acid. Directional growth of Au nanorods occurs via crystallographically-preferential reduction of Au(I) onto the seed nanoparticles. For simplicity, note that (B) omits shape-directing contributions from adsorbed halide ions and/or Ag(I) ions. Adapted from Dreaden et al. [*28*].

Interest in the shape-controlled synthesis of gold nanostructures began to take hold in the early 1990's, when Masuda [*29*] and Martin [*30*] developed techniques to prepare gold nanorods by

electrochemical reduction into nanoporous aluminum oxide membranes. These methods produced relatively monodisperse structures, but due to the low yield and somewhat large diameter (>100 nm), the optical response from these nanorods was, at the time, difficult to discern and largely dominated by multipolar plasmon resonance modes due to phase retardation of the incident field, resulting in non-symmetric plasmon field density distribution.[*31,32*] Wang and coworkers later demonstrated the synthesis of much smaller gold nanorods (ca. 10 nm in diameter) by electrochemical oxidation of a gold plate electrode in the presence of cationic, quaternary ammonium surfactants (cetyltrimethylammonium bromide, or CTAB, and tetraoctylammonium bromide, or TOAB) and under ultrasonication.[*33*] The resulting nanorods solutions exhibited plasmon resonance modes for their short (transverse) and long (longitudinal) axis polarizations, verifying for the first time with gold nanorods the optical theory proposed by Gans 1912 for the scattering and absorption of spheroidal plasmonic nanoparticles.[*34*]

Murphy [*35*] and El-Sayed [*36*] later demonstrated a colloidal growth method to produce monodisperse gold nanorods in high yield based on seeded growth (**Figure 1.2C; Figure 1.3B**). In this method, small (ca. 1.5 nm diameter) single-crystal Au seed particles, produced from the reduction of chloroauric acid by borohydride in the presence of CTAB, are aliquoted into a growth solution containing additional surfactant and gold salt that has been mildly reduced by ascorbic acid, forming dehydroascorbic acid and resulting in an $AuCl_2^-$ surfactant complex.[*37*] Collisions between the Au(I) complex and the seed particles, together with contributions from surface-adsorbed halide ions, silver ions, and crystallographically-preferential surfactant adsorption, results in the anisotropic growth of gold nanorods ca. 10-20 nm in width and up to 300 nm in length, depending on the specific synthetic conditions employed.[*38*] Readers may wish to note that the bonding interaction between Au and CTAB is atypical of most all chemical conjugation schemes involving AuNPs. Br^-

anions are known to form atomic surface layers on gold and other metals/semiconductors (i.e. adlayers) and also form electrostatically coordinate CTA^+ cations and their micelles. The general consensus for AuNR-CTAB bonding involves the formation of a Br^- adlayer on the AuNR surface which coordinates N headgroups on CTA^+. The aliphatic tail of surface-bound CTA^+ then associates with another CTA^+ cation oriented with its N^+Br^- headgroup facing outwards [*39-41*]. Due to the relatively weak association between aliphatic CTA^+ tails, repeated centrifugal purification and or exposure to organic solvents can result in nanoparticle destabilization that can be mitigated by redispersion of the particles in aqueous CTAB (ca. 1 mM). Using this method, gold nanorods ca. 10 – 20 nm in diameter and up to 300 nm in length can be obtained in relatively high yield, allowing for their subsequent use in a number of biomedical applications (**See Chapter 2**).[*41*] Nanorod aspect ratio can be controlled by the seed/gold salt ratio or by the relative concentration of adsorbate ions. For some time, the precise mechanism and purported reproducibility of nanorod growth has remained a hotly debated topic, confounded by the fact that some nanorod preparations contained additive impurity ions such as silver while others did not.[*42*] Proposed contributions include underpotential deposition, halide adsorption, surface packing density, and alloy formation among others. Electron microscopy has indicated that the nanorods grow along the [001] direction with less stable crystalline facets along the sides of the rods and more stable crystalline facets at its tips,[*43*] although, a more recent re-analysis of these same gold nanorods suggest that the side faces are much higher-index facets than previously believed.[*44*] Pure gold nanorods made in the absence of silver ions show a pentatetrahedral twinned structure, again with the most stable bulk gold facets at the ends of the nanorods.[*45*] Recently, Mirkin and coworkers have shown that concentration of iodine contaminants present in various commercially-available CTAB stocks play a critical role in determining subsequent morphology and explain the apparent lack of reproducibility reported among

nanorod preparations employed by various research groups. The authors posited that preferential iodine adsorption on {111} facets at the nanorod tips prevent CTAB binding and thus promote longitudinal growth. Surprisingly, the roles of silver and halide ion adsorption in directing anisotropic growth remains a point of contention.[*38*] Zubarev and coworkers have further studied the CTAB / gold nanorod system and shown that the length and width of these nanorods can be amplified by addition excess Au(I) and that their lengths can be selectively etched by the addition of Au(III), allowing the size and optical properties of these structures to bet tailored via the disproportionation reaction of Au(I) to produce Au(III) and Au(0).[*46*] Liz-Marzán and coworkers also showed that spherically-capped colloidal gold nanorods could be reshaped to form single-crystal octahedra, using poly(vinylpyrrolidone) (PVP) functionalized gold nanorods as seeds for the ultrasound-induced reduction of chloroauric acid by N,N-dimethylformamide (DMF) in the presence of PVP.[*44*] The authors showed that by increasing the ratio of gold salt to nanorod seeds, that subsequent morphology varies from sharpened (octagonal) rods to tetragons to octahedra (**Figure 1.2D**). The authors attribute this transformation to differing Au growth rates on various crystallographic facets of the nanorods (i.e. {111}<{110}<{100}) and variations in surface energy due to the adsorption of ions and/capping agent(s).

Silica-gold core-shell nanoparticles, or gold nanoshells (**Figure 1.2E**), have recently attracted much attention due to their interesting optical properties and numerous biomedical applications. Kerker and coworkers predicted in 1951[*47*] that concentric spherical particle could exhibit tunable plasmon resonance which varies as a function of the ratio of shell thickness to core radius. Halas and coworkers showed in 1998 that near-infrared absorbing gold nanoshells could be prepared by electrostatically adsorbing small gold nanoparticles to the surfaces of silica nanoparticles and subsequently reducing additional gold onto the structures to form a conformal shell.[*48*] In a typical

synthesis, silica nanoparticle cores are synthesized by the base-catalyzed condensation of orthosilicate [*49*] (i.e. Stöber hydrolysis) and functionalized with an amine-terminal silane. Small, anionic gold nanoparticles synthesized from the aqueous reduction of chloroauric acid by tetrakis(hydroxymethyl)phosphonium chloride (THPC) are electrostatically adsorbed onto the surfaces of the silica cores and added to a solution of mildly reduced chloroauric acid. When formaldehyde is added to the solution, the adsorbed gold particles serve as nucleation sites for the further reduction of gold around the silica core, subsequently forming a conformal nanoshell. In later reports, reduction via carbon monoxide (rather than formaldehyde) was shown to produce thinner and more uniform nanoshells.[*50*] Other related structures with novel optical properties such as asymmetric "nanoeggs" and quadruply concentric "nanomatryushkas" have also been developed.[*51*]

Gold nanocages and nanoframes recently developed by Xia and coworkers (**Figure 1.2F**) also show promise in a variety of biomedical applications due to their desirable optical properties and potentially cargo-holding hollow structures.[*52,53*] The synthesis of these nanoparticles is based on a phenomena known as galvanic replacement, whereby more noble metal ions (e.g Au, Pt) spontaneously oxidize the surface atoms of a less noble metal (e.g. Ag, Cu) with concomitant reduction of the more noble metal.[*53*] In this case, gold nanocages/frames are produced by reacting Au(III) with silver nanocubes produced from the polyol reduction of silver nitrate. Because the reduction of one Au(III) ion requires surface oxidation to three Ag(I) ions, the density of the resulting structure is significantly decreased: in the case a single-crystal cube, initially forming hollow Au/Ag alloy "nanoboxes" which further react to form porous Au nanocages and eventually faceless Au "nanoframes".[*54*]

Near-infrared absorbing (spherical) hollow gold nanoparticles (**Figure 1.2G**) have also been recently developed for use in drug loading/delivery and photothermal therapy applications. Caruso

and coworkers obtained hollow gold nanospheres by calcination or dissolution of polystyrene–gold core–shell nanoparticles.[*55*] Here, polystyrene nanospheres were coated in polyelectrolyte multilayer films and small, 4-(dimethylamino)pyridine (DMAP) stabilized gold nanospheres (6 nm diameter) were electrostatically adsorbed to the polyelectrolyte surface. Hydroxylamine was then used to further reduce chloroauric acid onto the seed-coated polystyrene spheres, forming a nearly conformal gold shell. The polystyrene cores were then removed by dissolution in tetrahydrofuran (THF) or calcination at 310 °C to obtain hollow gold spheres ca. 650 nm in diameter. Liang et al. later showed that similar structures could be obtained by galvanic replacement with citrate-stabilized cobalt nanospheres synthesized from the reduction of $CoCl_2$ by borohydride under anaerobic conditions.[*56*] Subsequent addition of the cobalt nanospheres to chloroauric acid gave hollow gold nanoshells (ca. 60 nm diameter) in high yield. Wall thicknesses could be tuned by adjusting the ratio of gold salt to Co nanoparticles.

In 2004, Yang and coworkers showed that more geometrically complex gold nanostructures (100–300 nm in size) could be synthesized by a modified polyol process (**Figure 1.2H**).[*57*] Using ethylene glycol as a solvent/reducing agent and PVP as a particle stabilizer, tetrahedra, cubes, octahedra, and icosahedra were obtained in high yield with good monodispersity. The authors found that subsequent nanoparticle morphology was highly dependent on the concentration of gold present in the reaction solution, with tetrahedra formed at high concentrations and icosahedra (as well as a small number of octahedra) at lower concentrations. By adding a small quantity of silver nitrate during the reaction process, gold nanocubes were also obtained. Here, the authors suggested that crystallographically preferential adsorption of PVP resulted in enhanced [100] growth and suppressed [111] growth, yielding {111}-dominant tetrahedra and icosahedra. They also hypothesized that preferential adsorption of silver ions to {111} facets could lead to the formation of {100}-dominant

cubes. Murphy and Sau later demonstrated the high-yield synthesis of similarly complex gold nanostructures via seed-mediated growth methods closely related to that used to produce colloidal nanorods.[*58*] By varying the concentrations of Au(III), ascorbic acid, and silver nitrate present in the growth solution, as well as the quantity of added seeds, rectangular, hexagonal, cubic, triangular, and star-like nanoparticles were obtained. In 2006, Song and coworkers developed an analogous seed-less, modified polyol synthesis.[*59,60*] Briefly, chloroauric acid was reduced in/by 1,5-pentanediol in the presence of PVP stabilizer. As the concentration of $AgNO_3$ was increased during the reaction, subsequent morphology ranged from Au octahedra, truncated octahedra, cuboctahedra, cubes, to higher polygons. As previously hypothesized by Yang and coworkers, the authors attributed this control to the suppression of [100] growth and/or enhanced [111] growth. Niu et al. later showed that other complex gold nanostructures could be produced in high yield (>96%) by a related seeded growth method.[*61*] Here, CTAB-capped gold nanorods were amplified in a Au(III)/CTAB solution and functionalized with cetylpyridinium chloride (CPC) to serve a single-crystalline seeds (ca. 40 nm diameter) for the subsequent growth of rhombic dodecahedral, octahedral, and cubic gold nanocrystals from Au(I). Interestingly, the authors found that the CPC surfactant preferentially stabilized {100} > {110} > {111} facets, in contrast to their typically observed surface free energies (i.e. {110} > {100} > {111}). Rhombic dodecahedral morphology (**Figure 1.2I**) was observed when CPC-Au{100} (and to a lesser extent, -Au{110}) association was dominant and octahedral geometries (**Figure 1.2J**) were observed when CPC-Au{111} association was found to dominate. Cubic gold nanoparticles were found to form upon the addition of Br^- ions which the authors attributed to increasing stabilization of {100} facets by Br^- adsorption and subsequent electrostatic association of CP^+.

Recently, Mirkin and coworkers have also developed a method to produce monodisperse gold nanocubes in high yield (**Figure 1.2K**) by a seeded growth technique analogous to that used to produce nanorods, except in this case, using the chloride analog of CTAB: cetyltrimethylammonium chloride, CTAC.[*62*] The authors found that nanocube size could be adjusted by simply varying the amount of seeds added to the growth solution, obtaining cubes with edge lengths ranging from 38 ± 7 nm to 269 ± 18 nm with and as high as 95% yield. Due to the concavity of their faces, the nanocubes exhibited a surface plasmon resonance ca. 80 nm red-shifted from their {100}-faced counterparts and are expected to exhibit novel catalytic properties. The authors hypothesized that the formation of high-index {720} facets could be due to surface-bound Ag formed by underpotential deposition (UPD) and its increasing stabilization by a Cl^- adlayer. Ming et al. previously obtained structurally-related, near-infrared absorbing tetrahexahedral gold nanoparticles enclosed by 24 {037} facets using a similar synthetic approach involving CTAB (>95% yield) (**Figure 1.2L**).[*63*] Personick et al. showed that rhombic dodecahedra (**Figure 1.2M**) and obtuse triangluar bipyramids (**Figure 1.2N**) could be obtained by a seeded (7 nm diameter) growth involving CTAC and dilute Ag^+ concentrations, obtaining the only {110}-faceted bipyrimidal gold nanostructures reported to date (31 ± 5 nm and 270 ± 26 nm edge length, respectively).[*64*] Crystallographic analysis found that the rhombic dodecahedra contained 12 identical {110} facets while the near-infrared absorbing triangular bipyrimads contained 2 triangular prisms separated by bridging (111) planes. Further analysis indicated that these structural differences arose from the use of a mixture of seeds containing both single-crystals and twin-defected particles and that their product particles could be easily isolated by size-selective filtration. Interestingly, they also found that as the Au(III):seed ratio was increased that deposition increasingly favored growth on twinned bipyramidal particles, an effect they hypothesized resulted from the low(er) binding affinity of Cl^- for Au which allowed Ag UPD growth-directing

effects to dominate. Even more exotic structures such as gold trisoctahedra have been obtained in by a simple aqueous reduction of chloroauric acid (**Figure 1.2O**).[*65*] Zheng and coworkers showed that these nanostructures, 100-200 nm in diameter and enclosed by 24 {221} facets, are formed by the ascorbic acid reduction of chloroauric acid in the presence of CTAC (ca. 85% yield). While the precise mechanism for their formation is yet to be fully determined, the authors also found that CTA^+ and Cl^- were necessary for the formation of trisoctahedra and suggested that ascorbic acid or its oxidation products may stabilize high-energy concave faces.

Triangular, or prismatic, nanoparticles have been obtained by a number of methods including photoreduction, seed-mediated growth, plasmon-driven synthesis, and biosynthesis. Sastry and coworkers first obtained gold nanoprismatic structures in fair yield (ca. 200–500 nm in size, 45% yield) from the aqueous reduction of chloroauric acid by lemongrass extract.[*66*] The authors attributed this transformation to the reducing capacity of aldose sugars present in the plant extract, with shape-directing formation due to the crystographically preferential adsorption of aldehydes/ketones present in the extract. Schatz and Mirkin later showed that similar gold nanoprisms (144 ± 30 nm edge length) could be synthesized in high yield using a seeded growth method (**Figure 1.2P**).[*67*] In a typical synthesis, borohydride-reduced, citrate-capped spherical seeds (5.2 ± 0.6 nm diameter) are synthesized from chloroauric acid and sequentially amplified in a solutions of chloroauric acid, sodium hydroxide, ascorbic acid, and CTAB. The nanoprisms were isolated by filtration using a commercially-available aluminum oxide membrane (100 nm nominal pore size) and analyzed using optical spectroscopic and computational methods.

To the novice nano-synthetic chemist, all of the above methods sound alarmingly similar. Most include gold seed particles bearing ionic groups, the addition of metal ions with a reducing agent, and other additives which promote the formation of one shape or another. This similarity

highlights both the power and frustration of colloidal nanoparticle synthesis: that small changes in reaction conditions can lead to very different reaction products, suggesting overall that these nanoparticles are the result of kinetic, as opposed to thermodynamic, stabilization effects. Viable thermodynamic arguments can also be made, usually with the idea that the additives bind to particular facets of the gold and lower the surface energy of that facet; however, because the stability of hydrated, nanoscale metal crystalline facets is difficult to predict and control in the presence of ions, many groups have adopted the use a "hard template" approach to control nanoparticle shape.

Since its first demonstration in the early 1990s, template-based electrochemical deposition of gold nanostructures has found subsequent use in a variety of biomedical and bioanalytical applications. Keating and Natan have shown that multisegmented, template-deposited nanorod structures can be employed in a multiplexed bioanalytical detection scheme (i.e. nanobarcode, NBC, assay).[*68*] By electrodepositing metallic segments of varying length, surface chemistry, and composition (e.g. Au, Ag, Pt, Ni, Co, Cu), large nanorods (600 nm x ca. 10 microns or more) with striped features can be prepared. Subsequent chemistry to attach proteins and/or DNA to these multisegmented nanorods has led to detection of biomoecules with high sensitivity by fluorescence readout (e.g. sandwich-assay based configurations). Because the nanobarcodes and their segment patterns can be easily distinguished by optical microscopy, biomolecule detection schemes can be highly multiplexed: that is, the detection of the unique optical signature corresponding to each type of nanorod can indicate the presence of a specific biomolecule which it recognizes. Mirkin and coworkers later showed that by incorporating short segments of a selectively-etchable material (e.g. Ag, Ni) that discrete structures separated by sub-diffraction limited distances could be synthesized in high yield with good monodispersity (on-wire lithography, OWL).[*69*] In a typical synthesis, gold and silver segments are electrodeposited into the cylindrical pores of an aluminum oxide membrane

template by sequential addition and removal of metal salt solutions. The membrane template is then etched by hydroxide and the multisegmented nanorods are deposited onto a substrate. A thin layer of gold or glass is then deposited to cover one side of the nanorod, providing structural support across length of the multisegmented nanorod and allowing distances between gold segments to be maintained following removal and etching (e.g. nitric acid dissolution of Ag or Ni). The technique has been applied in a variety of applications including surface-enhanced Raman spectroscopic detection and molecular electronics.

Apart from colloidal nanostructures with well-defined geometry, branched gold nanostars [*70-73*] have also proven to be useful in a number of biomedical applications i) due to their intense scattering properties, amenable to microscopic labeling-based applications,[*71*] ii) their high spectral sensitivity to changes in the local dielectric environment, useful in bimolecular sensing applications,[*71,73*] and iii) their high near-infrared absorption which can be leveraged in laser photothermal therapy approaches or for electromagnetic enhancement of in vivo, in vitro,[*74*] and in situ [*75*] surface enhanced Raman spectroscopy (SERS).[*76,77*] Hafner and coworkers have obtained gold nanostars by replacing the small (1-2 nm diameter) gold seeds used in a typical gold nanorod synthesis with a commercially-available (10 nm diameter) gold nanospheres capped by citrate-mediated chloroauric acid reduction.[*71*] Liz-Marzán and coworkers have developed a method to produce gold nanostars with high yield and reproducibility using a method similar to that used to produce gold decahedra and octahedra (vide infra).[*78*] Briefly, an aqueous solution of chloroauric acid (Au^{3+}) is gently reduced (Au^{+}) by DMF in the presence of PVP (10 kDa), followed by further reduction by borohydride. The seeds are aged for 24 h and an aliquot is added to solution of chloroauric acid which has also been mildly reduced by DMF in the presence of PVP. Monodispersity was found to be improved upon pre-reduction of Au^{3+} to Au^{+} by DMF and

morphology/resonance wavelength was found to be controlled by the gold salt:seed ratio. Final nanostar dimensions were determined from the size of the seeds and increasingly sharp structures relevant to SERS- and sensing-based applications were formed at ambient temperatures. For a comprehensive survey of the synthesis, properties, and applications of gold nanostars, interested readers are directed to Ref. [*72*].

1.2 Synthesis of Gold Nanoparticles: Top-Down Methods

While biomedical applications of gold nanoparticles typically involve so-called "bottom-up" synthetic approaches, a number of diagnostic and bioanalytical applications can make use of the high uniformity and precise spatial arrangement(s) afforded by top-down fabrication methods. For example, in the late 1990's Van Duyne and coworkers developed a template-based synthesis in which gold nanoparticle arrays could be deposited using a shadow-mask approach (**Figure 1.4A**).[*79,80*] Here, two-dimensional close-packed arrays of polymer nanospheres were self-assembled onto flat substrates and gold was vapor deposited into the pyramidal voids formed at their intersections (termed nanosphere lithography, NSL). Following removal of the polymer spheres (e.g. in organic solvent), ordered arrays of plasmon resonant nanoparticles were obtained over large areas in high yield.[*80*] Moerner [*81*] and El-Sayed [*82*] have employed electron-beam lithographic methods to obtain arrays of gold nanostructures with precise control over structural morphology and interparticle spacing (**Figure 1.4Bb**). Whitesides and coworkers have shown that gold nanostructures (ca. ≥ 30 nm) can be fabricated by a so-called "nanoskiving" method whereby gold deposited onto flat or structured polymeric substrates (typically epoxy) are sectioned via ultramicrotome and released (e.g. by oxygen plasma etching) (**Figures 1.4C-E**).[*83*] Mirkin and coworkers have developed a lithographic method based on atomic force microscopy (AFM) in which chemical resists consisting of self-assembled monolayers are patterned onto gold thin films which are subsequently etched to reveal

precise, large-area patterned arrays of gold nanostructures (dip-pen lithography, DPL) (**Figures 1.4F-I**).[*84,85*] In a more recent report, Aizenberg and coworkers show that directional vapor deposition of gold and combined electrochemical deposition of conducting polymers onto PDMS-molded substrates can be used to fabricate gold nanostructured particle arrays with tapered, anisotropic, and overhanging features (structural transformation by electrodeposition on patterned substrates, STEPS) (**Figures 1.4J-L**).[*86*]

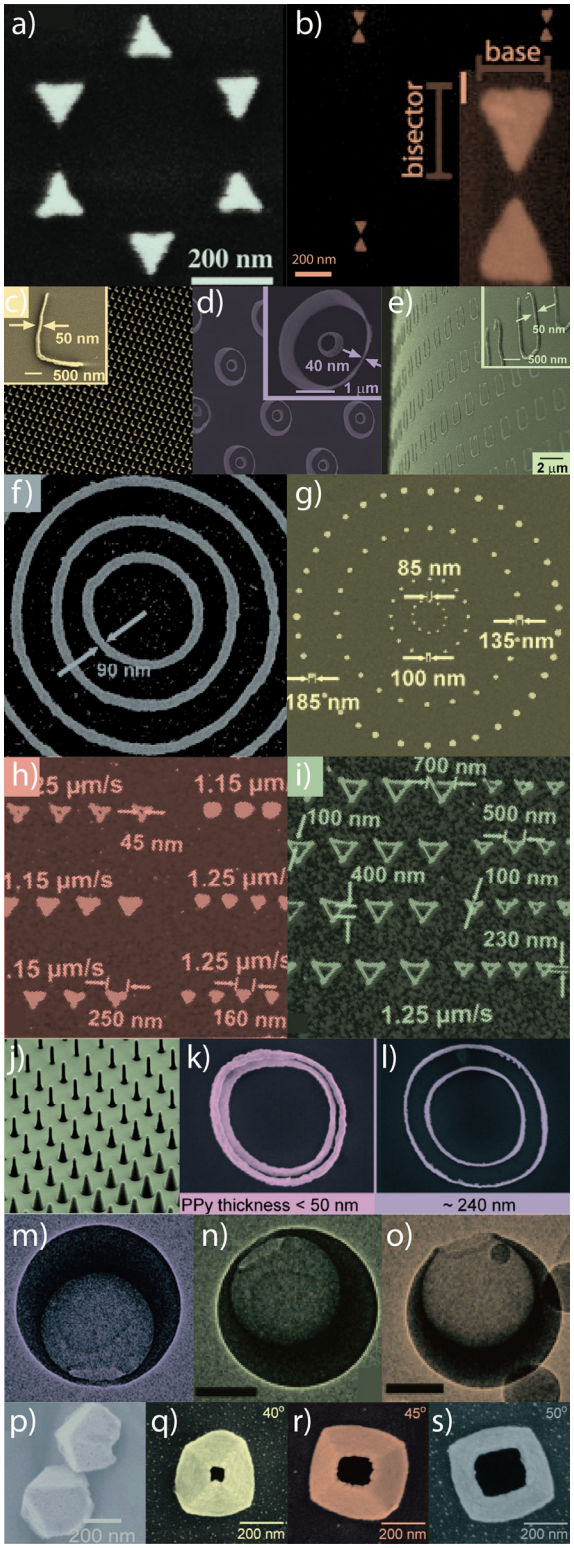

Figure 1.4. Exemplary gold nanostructures obtained by various "top-down" synthetic approaches. A) Nanosphere lithography (NSL), (B) electron-beam lithography (EBL), (C-E) nanoskiving, (F-I) dip-pen lithography (DPL) , (J-L) structural transformation by electrodeposition on patterned substrates (STEPS), (M-O) nanocrescent synthesis, and (P-S) nanopyramid synthesis. Adapted from Dreaden et al. [*3*].

Although many of the aforementioned "top-down" synthetic approaches often yield substrate-supported/bound gold nanostructures, these methods can also be used to produce free-standing gold nanoparticles amenable to colloidal dispersion and a variety of biomedical applications. Lee and coworkers have recently explored the use of three-dimensional, crescent-shaped hollow gold nanostructures (nanocrescent moons) obtained via shadow mask Au vapor deposition onto sacrificial template nanoparticles (**Figures 1.4M-O**).[*87,88*] In a typical synthesis, commercially-available polystyrene nanospheres are deposited onto a glass substrate coated with an acetone-soluble polymer (photoresist). The planar sample is then rotated as gold is directionally (i.e. electron-beam) deposited onto the polystyrene spheres, leaving a shadow-masked cavity at the sphere-substrate interface. Depending on the angle between the substrate and the incident flux of gold, as well as the size of the sacrificial templates, the geometry and thus, the optical properties of the nanocrescent structures can be easily tuned throughout the visible and near-infrared spectral regions. The template-bound nanocrescents are subsequently released from the substrate via acetone lift-off and the polystyrene templates are then removed via dissolution in toluene. The free nanocrescents can be functionalized with a variety of colloidal stabilizers and linker molecules for a range of biomedical diagnostic and therapeutic applications. Because of their sharp surface features and intraparticle plasmon coupling effects, these particles have proven to be highly useful as substrates for surface enhanced Raman scattering (SERS) [*87,88*] and can be synthesized in a hierarchical manner to incorporate other functional materials such as magnetic segments [*88*] which can facilitate ex vivo manipulation or enhanced contrast in magnetic resonance imaging (MRI).

Odom and coworkers have shown that free-standing, hollow, pyramidal gold nanostructures of varying geometry can be obtained in a related approach utilizing nanopatterned silicon and vapor-phase metal deposition (**Figures 1.4P-S**).[*89,90*] Here, the authors first fabricate an array of

cylindrical posts (ca. 250nm diameter) on a Si substrate via phase-shift photolithography using a positive-tone photoresist. A thin (ca. 20 nm) cladding film of Cr is next deposited onto the array and the photoresist is removed by lift-off in acetone. The exposed array of Si nanofeatures is then chemically etched by KOH/isopropyl alcohol (IPA) to yield an array of negative nanopyramidal pits. A thin (ca. 20-60 nm) film of gold (or another type/combination of metal/material) is then vapor deposited onto the array and the Cr template layer is removed using a commercial chemical etchant to reveal an array of substrate-bound, hollow gold nanopyramids. The nanopyramids are subsequently released via KOH/IPA Si etching and can be similarly functionalized with a variety of colloidal stabilizers or linker groups for the attachment of biomolecules. Like the hollow gold nanocrescents, because gold nanopyramids exhibit sharp surface features and intense intraparticle near-field coupling, these structures exhibit both near-infrared absorption for photothermal contrast and high electromagnetic SERS enhancement.[*91*] One particularly attractive feature of these structures is the ability to differentially functionalize the inner and outer surfaces of the nanopyramids by doing so before/after release from the Si support.[*92*] Tipless, or truncated, nanopyramidal structures can also be fabricated [*93*] by rotating the planar template array at some angle with respect to incident flux of collimated (electron-beam deposited) gold vapor, allowing for further SERS enhancement and an increase in multipolar plasmon contributions which can contribute to novel nonlinear optical phenomena such as Fano [*94,95*] resonance. Photothermal conversion from these structures in solution [*96*] ($\Delta T \leq 18$ °C) has been shown to be comparable to those obtainable with more conventional nanorod, nanoshell, nanocage, and hollow gold nanostcutures in vivo, well above those minimally required for therapeutic hyperthermia [*97*] (ΔT~3-6 °C).

1.3. Functionalization of Gold Nanoparticles

Chemical functionalization of the nanoparticle surface is necessary to impart biological compatibility and specificity to gold nanoparticles. The synthetic reagent CTAB, for example, which is so crucial in a number of preparations of gold nanorods and other shapes, is toxic to cells at micromolar concentrations on its own.[*98*] We do note, however, that in terms of delivery of nanoparticles to tumors, the "leaky vasculature" of tumor tissue itself favors (passive) nanoparticle localization there, without the need for (active) chemical functionalization.[*99-102*] We also note that the binding of a "toxic" agent such as CTAB to a nanoparticle surface makes it far less bioavailable than it would be if it were free in solution, and therefore the tolerable dose of a nanoparticle bearing a given molecule might be quite different than that of the molecule alone.[*98*]

Functionalization of gold nanoparticles for biomedical applications follows largely on work initially conducted by Nuzzo and Whitesides on the formation of self-assembled monolayers (SAMs) of molecules on planar gold [*103,104*] and later by Bard [*105,106*] and Murray [*107-109*] in studying the dynamics and conformations of these assemblies by electrochemical, scanning probe, and mass spectrometric methods. A rich variety of functional molecular linkers and passivating agents are currently employed in the conjugation of gold nanoparticles used in biomedical applications; however, the anchoring groups utilized for attachment of these molecules to the gold surface generally include: thiolate,[*20,110,111*] dithiolate, [*112*] dithiocarbamate,[*113*] amine,[*114*] carboxylate,[*114*] selenide,[*115*] isothiocyanate,[*110,114*] or phosphine[*18,111*] moieties. Recent evidence suggests that direct Au-C bond formation may be achieved by way of a trimethyl tin leaving group; however its use in biomedical- or nanoparticle- based applications has yet to be tested.[*116*] The choice of particular molecular anchor typically varies depending on the desired lability of the molecule for a specific application. Non-labile applications most often employ thiol-based anchoring groups while labile applications often make use of amine or carboxylate surface anchors (**Table 1.2**).

Burda and coworkers, for example have shown that therapeutic outcomes following gold nanoparticle-mediated delivery of photodynamic therapy agents drastically benefits from the use of more labile amino linkers versus stronger thiol groups due to vesicular sequestration of particle-bound drug molecules.[*117,118*]

Table 1.2. Useful Physiochemical Parameters for Gold Nanoparticles and Surfaces.

Physiochemical parameter	Value	Reference
Au-S bond	40 to 45 kcal mol^{-1}	[*119,120*]
Au-NH_2 bond	8 kcal mol^{-1}	[*121*]
Au-COO^- bond	2 kcal mol^{-1}	[*121*]
Maximum (111) Au surface density	1.5×10^{15} atoms cm^{-2}	[*105*]
Typical Au Adsorbate densities	10^{-10} to 10^{-9} mol cm^{-2}; 10 to 100 μC cm^{-2}	[*105*]
Au Fermi energy	-5.1 eV (v E_F^{VAC})	[*122*]
CTAB-AuNR longitudinal molar extinction cross section	$\lambda_{(nm)} * 12.3 \times 10^6 - 5.02 \times 10^9$	Interpolated from [*123*]
Citrate-AuNP molar extinction cross section	$\varepsilon_{(15)528nm} = 3.6 \times 10^8$ cm^{-1} M^{-1} $\varepsilon_{(30)530nm} = 3.0 \times 10^9$ cm^{-1} M^{-1} $\varepsilon_{(40)533nm} = 6.7 \times 10^9$ cm^{-1} M^{-1} $\varepsilon_{(50)535nm} = 1.5 \times 10^{10}$ cm^{-1} M^{-1} $\varepsilon_{(60)540nm} = 2.9 \times 10^{10}$ cm^{-1} M^{-1} $\varepsilon_{(80)550nm} = 6.9 \times 10^{10}$ cm^{-1} M^{-1}	[*124*]

In the case of common alkanethiols, room temperature surface adsorption is spontaneous, occurring over milliseconds to minutes.[*104*] Packing/reordering of the monolayer can occur over several hours, however in practice, overnight particle-ligand incubation with additional sonication or gentle heating is often sufficient to achieve optimal results. Murray place exchange [*107-109*] of the nanoparticle-bound SAMs can also be performed to functionalize gold nanoparticles with mixed or fully exchanged monolayers with coverages as high as 1.5×10^{15} molecules cm^{-2}, although, obtaining precise ratios of mixed self-assembled monolayers can be challenging if not performed simultaneously. Alkanethiol coverages are typically on the order of 1.5×10^{14} molecules cm^{-2}.[*105*]

While bond strength between anchoring groups and the gold surface play a critical role in determining subsequent functionality, packing density and surface energetics make equally important contributions. Although dithiolates are often viewed as preferable to their mono-thiolate counterparts due to multivalent binding avidity, these molecules are actually more prone to oxidative desorption due to inefficient packing.[*112*] In contrast, oxidative desorption of dithiolates from ZnS-passivated CdSe quantum dots has been shown to be significantly lower than that of mono-thiolates, due presumably to increasingly efficient surface packing/chemistry.[*125*] Cima and Langer have found that thiolates, most commonly employed for attachment to gold nanoparticles in non-labile biomedical applications, can remain stably adsorbed for up to 35 days under physiologic conditions.[*126*]

Common among most applications of gold nanoparticles in biomedicine is the need for adequate stabilization in biological environments containing high serum concentrations and high ionic strengths. Thiolated poly(ethylene glycol), PEG-SH, is by far the most commonly employed surface ligand used with biomedical gold nanoparticles. Its well-documented hydrophilicity permits the aqueous dispersion of gold nanoparticles conjugated with a wide range of lipophilic molecules [*127*] and increases circulatory half life [*128*] by blocking adsorption of serum proteins and opsonins which facilitate uptake and clearance by the mononuclear phagocyte system (MPS), less frequently referred to as the reticuloendothelial system (RES).[*129-132*] Recent studies by Dai and coworkers indicate that carbon nanotubes (far more hydrophobic than gold nanoparticles) functionalized with branched PEG ligands exhibit superior pharmacokinetics and minimal RES uptake compared with PEG ligands of the same molecular weight.[*133*] Circulating gold nanoparticles can be expected to benefit from similar functionalization strategies. Recent evidence from Jordan and coworkers also

suggest that polyoxazoline (POx) stabilizers may serve as suitable alternatives and/or superior ligands to PEG.[*134-136*]

Gold nanoparticles can be conjugated with a variety of biofunctional molecules by simple physical methods such as hydrophobic-hydrophobic interaction (**Figure 1.5A**) and charge-pairing (**Figure 1.5B**). Rotello and coworkers have shown that highly hydrophobic molecules (e.g. chemotherapeutics such as paclitaxel and doxorubicin) can be labily bound to biomedical gold nanoparticle conjugates via the use of amphiphilic ligands.[*137*] By creating a hydrophobic corona inside of a hydrophilic ligand shell, they were able to demonstrate the entrapment and efficient release of hydrophobic fluorescent molecules via "membrane-mediated diffusion".[*137*] Classical cross coupling reagents can also be employed for the non-labile conjugation of a wide range of biofunctional targeting, therapeutic, and imaging contrast agents (**Figure 1.5C**). Most applications involving amine-containing molecules/proteins employ classical carbodiimide cross coupling (carboxylate + amine → amide) with a number of commercial chemical manufacturers producing ready-made N-hydroxysuccinimide (NHS) -activated heterobifunctional polymers and ligands.[*138,139*] Linkage to sulfhydryl groups can be similarly achieved by way of maleimide-terminal ligands, also widely commercially available.[*140*] Huisgen cycloaddition (click, or azide-alkyne coupling) has been similarly employed in a number of gold nanoparticle conjugation strategies.[*139*]

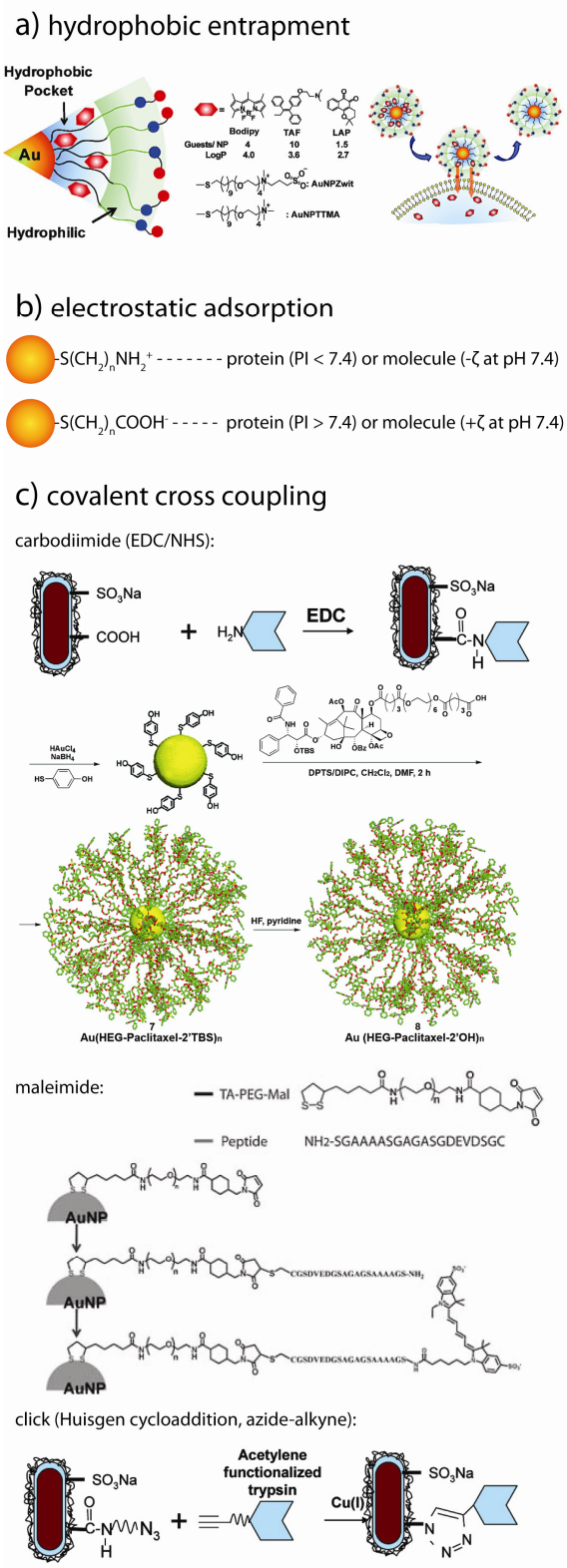

Figure 1.5. Schematics illustrating various methods by which gold nanoparticles can be conjugated with biofunctional molecules. A) hydrophobic entrapment, (B) electrostatic adsorption, and (C) covalent cross coupling by carbodiimide, maleimide, and click chemistry. Adapted from Dreaden et al. [*3*].

Functionalization of gold nanoparticles can be qualitatively verified by a number of means including vibrational spectroscopy (e.g. IR or Raman), plasmon resonance shift, thermogravimetric analysis (TGA),[*138*] and/or hydrodynamic diameter or zeta potential change (via dynamic light scattering, DLS). In practice however, quantitative measures such as absorption/fluorescence assay,[*127,141*] mass spectrometry (inductively-coupled plasma, ICP,[*123,142*] or matrix-assisted laser desorption ionization, MALDI[*143*]), x-ray photoelectron spectroscopy (XPS),[*144,145*] and/or cyclic voltammetry is often preferred.

Inorganic complexes such as cisplatin or its prodrug forms can also be datively bound to gold nanoparticle ligands by way of appropriate ligands (**Figure 1.6A**).[*146*] Lippard and coworkers have shown that a Pt(IV) prodrug form of cisplatin can be coordinated by carboxylate-terminal ligands on gold nanoparticles which facilitate intracellular transport and subsequent activation of the prodrug. Mirkin and coworkers have pioneered the use oligonucleotide-functionalized gold nanoparticles, employing thiolated ssDNA as surface linkers to which targeting ligand-, biomolecule-, and/or imaging contrast agent-tethered complementary ssDNA can be hybridized (**Figure 1.6B**).[*147,148*] Recently, Rotello and coworkers have demonstrated the synthesis, gold nanoparticle conjugation, and photo-triggered release of the cytotoxic thymidylate synthase inhibitor 5-fluorouracil (5-FU) by way of a photocleavable, o-nitrobenzyl PEG-SH linker, demonstrating significant toxicity following UV exposure and dramatically diminished cytotoxicity in its absence (**Figure 1.6C**).[*149*]

Other strategies for the functionalization of gold nanoparticle conjugates employ core-shell type geometries where the nanoparticle or other molecules are entrapped within a polymer or dielectric shell which can be further conjugated. Caruso and coworkers showed that gold nanospheres could be encapsulated via consecutive adsorption of charge-paired polyelectrolyte films, also known as layer-by-layer (LbL) assemblies.[*150*] Gold nanospheres were coated with alternating layers of

anionic sodium poly(styrenesulfonate) (PSS) (15.2 kDa) and cationic poly(diallyldimethylammonium chloride) (PDADMAC) (20 kDa) with the adsorption of each layer following centrifugal purification. The resulting nanoparticles exhibited tunable surface charge and allowed for the electrostatic adsorption of proteins (see **Figure 1.5B**) over a wide range of isoelectric points and solvent pH values. The same LbL concept works for coating gold nanorods, enabling switching of the effective surface charge from positive to negative, and overcoating the surfactant bilayer to present ammonium, sulfate, or other charged groups to the solvent.[*151,152*] Stable, hollow polymeric nanocapsules can be obtained by CN^- etching of both polymer-coated gold nanospheres[*150,153*] and nanorods.[*154*] Due to their hierarchical assembly and controllable interlayer diffusion, Hammond and coworkers have found LbL assemblies useful in a number of multidrug and gene delivery applications.[*155-159*]

In the mid 1990's, Liz-Marzán and Mulvaney[*160*] showed that gold nanoparticles could be fully encapsulated by silica (glass) shells [*161*] (**Figure 1.7A**) by vitreophobic surface conjugation and facile silane chemistry (**Figure 1.7B**).[*162*] This prospect is particularly attractive for use with gold nanorods, where compelling evidence showing complete removal/displacement of CTAB molecules from the sides of the rods has yet to be demonstrated. Natan[*163*] and Nie[*164*] have further explored this concept, fabricating gold-silica core-shell nanoconjugates containing entrapped Raman reporter molecules. Because the enhanced optical properties afforded by resonant excitation of the gold core's surface plasmon resonance (surface enhanced Raman scattering, SERS), highly multiplexed in vivo SERS has be demonstrated.[*165*]

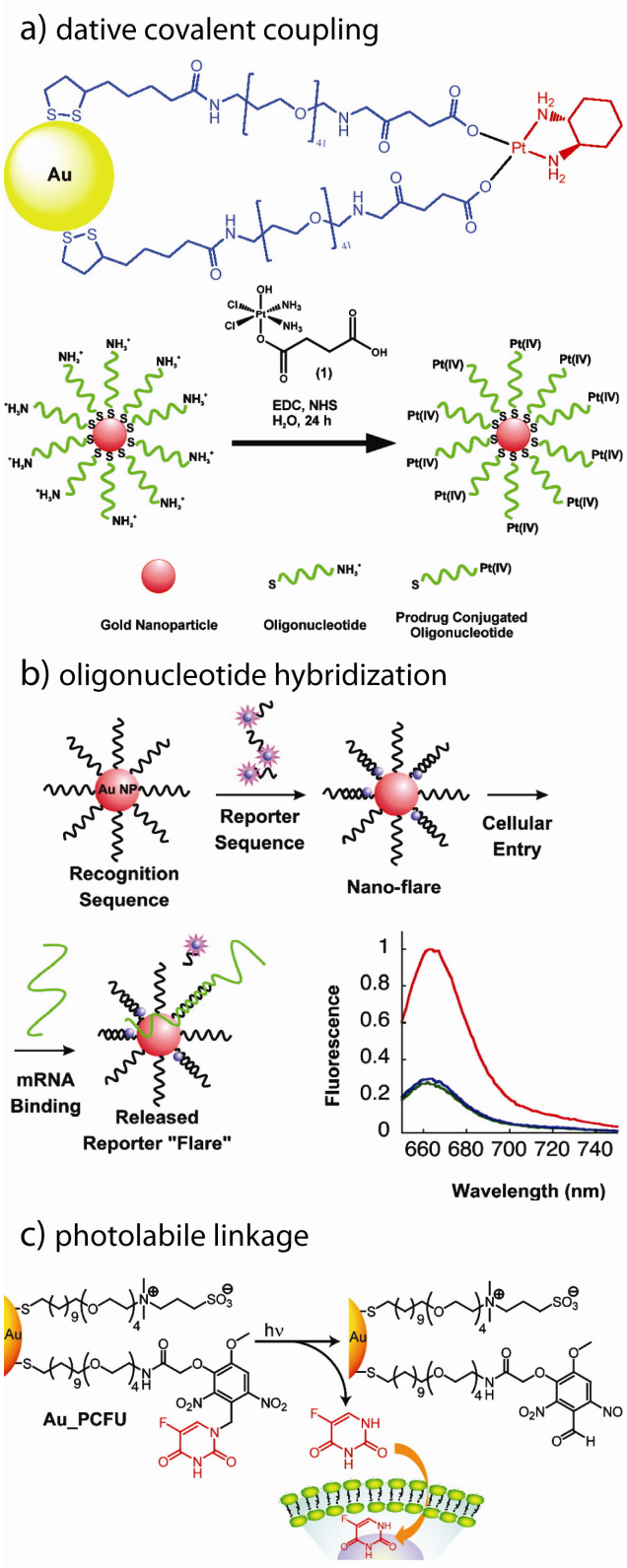

Figure 1.6. Schematics illustrating additional methods by which gold nanoparticles can be conjugated with biofunctional molecules. A) dative covalent bonding, (B) oligonucleotide hybridization, and (C) and photolabile linkage. Adapted from Dreaden et al. [*3*].

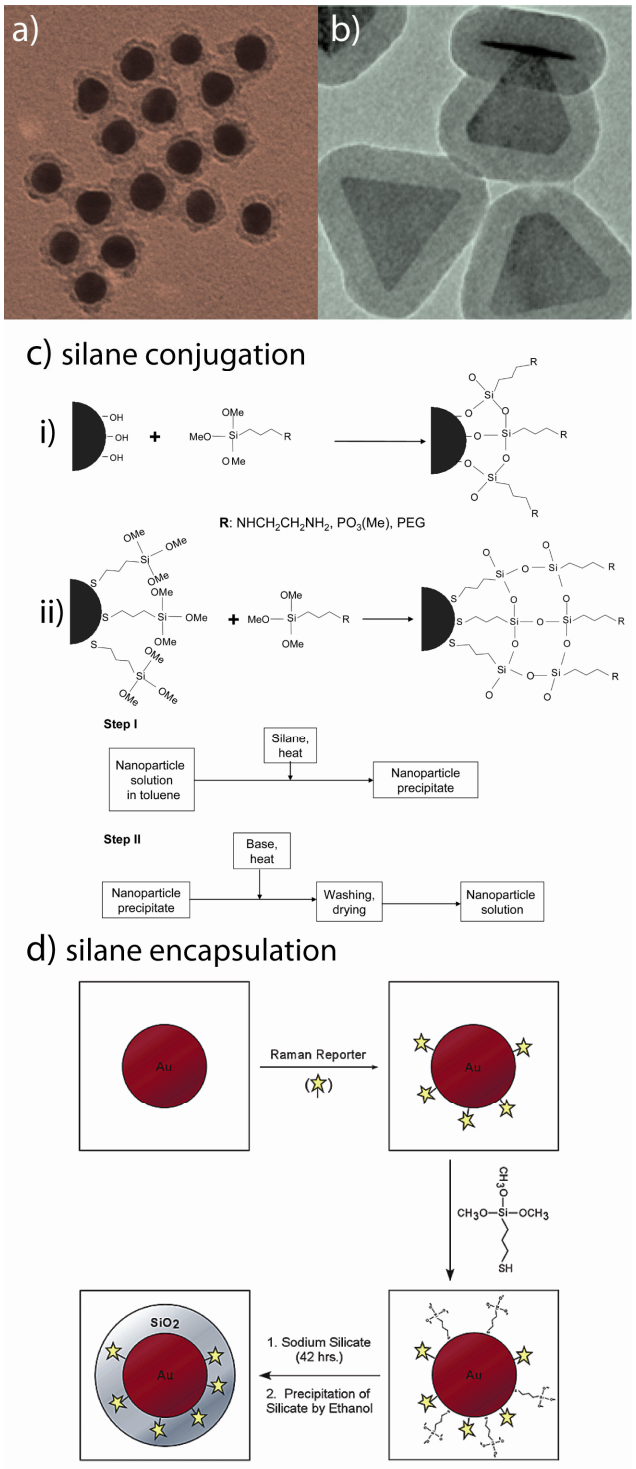

Figure 1.7. Silane conjugation chemistry for biomedical gold nanoparticle conjugates. Silica shell (Stöber) functionalized (A) gold nanospheres and (B) gold nanoprisms. C) Reaction schemes for conjugation to (i) hydroxyl- and (ii) silane-functionalized gold nanoparticles. D) Reaction scheme for the encapsulation of bioanalytically- and/or therapeutically-relevant molecules about gold nanoparticles. Adapted from Dreaden et al. [*3*].

1.4 Outlook and Conclusions

The aforementioned synthetic approaches can produce an incredibly diverse array of gold nanostructures with a cadre of varying chemical, photophysical, pharmacokinetic, and pharmacodynamic properties. The sections to follow will discuss novel biomolecular and photonic interactions of these functionalized nanomaterials and their applications in oncology, surface-enhanced spectroscopic detection, and photovoltaics.

1.5 References

1. Faraday, M. The Bakerian Lecture: Experimental Relations of Gold (and Other Metals) to Light. *Philos. Trans. R. Soc. London* **147**, 145-181 (1857).

2. Dreaden, E. C., Mackey, M. A., Huang, X., Kang, B., & El-Sayed, M. A. Beating cancer in multiple ways using nanogold. *Chem. Soc. Rev.* **40**, 3391-3404 (2011).

3. Dreaden, E. C., Alkilany, A. M., Huang, X., Murphy, C. J., & El-Sayed, M. A. The Golden Age: Gold Nanoparticles for Biomedicine. *Chem. Soc. Rev. (in press)* (2012).

4. Maxwell, J. C. A Dynamical Theory of the Electromagnetic Field. *Philos. Trans. R. Soc. London* **155**, 459-512 (1865).

5. Mie, G. Contributions to the Optics of Turbid Media, Especially Colloidal Metal Solutions. *Ann. Phys.* **25**, 377-445 (1908).

6. Knoll, M., & Ruska, E. Das Elektronenmikroskop. *Z. Phys.* **78**, 318-339 (1932).

7. Turkevich, J., Stevenson, P. C., & Hillier, J. A study of the nucleation and growth processes in the synthesis of colloidal gold. *Discuss. Faraday Soc.* **11**, 55-75 (1951).

8. Frens, G. Controlled Nucleation for the Regulation of the Particle Size in Monodisperse Gold Suspensions. *Nature* **241**, 20-22 (1973).

9. Ojea-Jiménez, I., Bastús, N. G., & Puntes, V. Influence of the Sequence of the Reagents Addition in the Citrate-Mediated Synthesis of Gold Nanoparticles. *J. Phys. Chem. C* **115**, 15752-15757 (2011).

10. Xia, H., Bai, S., Hartmann, J. r., & Wang, D. Synthesis of Monodisperse Quasi-Spherical Gold Nanoparticles in Water via Silver(I)-Assisted Citrate Reduction. *Langmuir* **26**, 3585-3589 (2009).

11. Rodríguez-González, B., Mulvaney, P., & Liz-Marzán, L. M. An Electrochemical Model for Gold Colloid Formation via Citrate Reduction. *Z. Phys. Chem.* **221**, 415-426 (2007).

12. Kimling, J., Maier, M., Okenve, B., Kotaidis, V., Ballot, H., & Plech, A. Turkevich Method for Gold Nanoparticle Synthesis Revisited. *J. Phys. Chem. B* **110**, 15700-15707 (2006).

13. LaMer, V. K., & Dinegar, R. H. Theory, Production and Mechanism of Formation of Monodispersed Hydrosols. *J. Am. Chem. Soc.* **72**, 4847-4854 (1950).

14. Pong, B.-K., Elim, H. I., Chong, J.-X., Ji, W., Trout, B. L., & Lee, J.-Y. New Insights on the Nanoparticle Growth Mechanism in the Citrate Reduction of Gold(III) Salt: Formation of the Au Nanowire Intermediate and Its Nonlinear Optical Properties. *J. Phys. Chem. C* **111**, 6281-6287 (2007).

15. Ostwald, W. *Lehrbuch der Allgemeinen Chemie*. Vol. 2 (Wilhelm Engelmann, 1896).

16. Polte, J. r., Ahner, T. T., Delissen, F., Sokolov, S., Emmerling, F., Thüemann, A. F., & Kraehnert, R. Mechanism of Gold Nanoparticle Formation in the Classical Citrate Synthesis Method Derived from Coupled In Situ XANES and SAXS Evaluation. *J. Am. Chem. Soc.* **132**, 1296-1301 (2010).

17. Wang, H., & Halas, N. J. Mesoscopic Au "Meatball" Particles. *Adv. Mater.* **20**, 820-825 (2008).

18. Schmid, G., Pfeil, R., Boese, R., Bandermann, F., Meyer, S., Calis, G. H. M., & van der Velden, J. W. A. Au55[P(C6H5)3]12CI6 — ein Goldcluster ungewöhnlicher Größe. *Chem. Ber.* **114**, 3634-3642 (1981).

19. Weare, W. W., Reed, S. M., Warner, M. G., & Hutchison, J. E. Improved Synthesis of Small (dCORE ≈ 1.5 nm) Phosphine-Stabilized Gold Nanoparticles. *J. Am. Chem. Soc.* **122**, 12890-12891 (2000).

20. Brust, M., Walker, M., Bethell, D., Schiffrin, D. J., & Whyman, R. Synthesis of thiol-derivatised gold nanoparticles in a two-phase Liquid-Liquid system. *Chem. Commun.*, 801-802 (1994).

21. Shimizu, T., Teranishi, T., Hasegawa, S., & Miyake, M. Size Evolution of Alkanethiol-Protected Gold Nanoparticles by Heat Treatment in the Solid State. *J. Phys. Chem. B* **107**, 2719-2724 (2003).

22. Pan, Y., Leifert, A., Ruau, D., Neuss, S., Bornemann, J., Schmid, G., Brandau, W., Simon, U., & Jahnen-Dechent, W. Gold Nanoparticles of Diameter 1.4 nm Trigger Necrosis by Oxidative Stress and Mitochondrial Damage. *Small* **5**, 2067-2076 (2009).

23. Pan, Y., Neuss, S., Leifert, A., Fischler, M., Wen, F., Simon, U., Schmid, G., Brandau, W., & Jahnen-Dechent, W. Size-Dependent Cytotoxicity of Gold Nanoparticles. *Small* **3**, 1941-1949 (2007).

24. Faulk, W. P., & Taylor, G. M. An immunocolloid method for the electron microscope. *Immunochemistry* **8**, 1081-& (1971).

25. Holgate, C. S., Jackson, P., Cowen, P. N., & Bird, C. C. Immunogold-silver staining: new method of immunostaining with enhanced sensitivity. *J. Histochem. Cytochem.* **31**, 938-944 (1983).

26. Hainfeld, J. F., Slatkin, D. N., Focella, T. M., & Smilowitz, H. M. Gold nanoparticles: a new X-ray contrast agent. *Brit. J. Radiol.* **79**, 248-253 (2006).

27. Hainfeld, J. F., Dilmanian, F. A., Zhong, Z., Slatkin, D. N., Kalef-Ezra, J. A., & Smilowitz, H. M. Gold nanoparticles enhance the radiation therapy of a murine squamous cell carcinoma. *Phys. Med. Biol.* **55**, 3045 (2010).

28. Dreaden, E. C., Austin, L. A., Mackey, M. A., & El-Sayed, M. A. Size Matters: Gold Nanoparticles in Targeted Cancer Drug Delivery. *Ther. Delivery (in press)* (2012).

29. Masuda, H., Tanaka, H., & Baba, N. Preparation of porous material by replacing microstructure of anodic alumina film with metal. *Chem. Lett.*, 621-622 (1990).

30. Martin, C. R. Template synthesis of polymeric and metal microtubules. *Adv. Mater.* **3**, 457-459 (1991).

31. Hartland, G. V. Optical Studies of Dynamics in Noble Metal Nanostructures. *Chem. Rev.* **111**, 3858-3887 (2011).

32. Payne, E. K., Shuford, K. L., Park, S., Schatz, G. C., & Mirkin, C. A. Multipole Plasmon Resonances in Gold Nanorods. *J. Phys. Chem. B* **110**, 2150-2154 (2006).

33. Yu, Y. Y., S. S. Chang, C. L. Lee, C. R. C. Wang Gold nanorods: electrochemical synthesis and optical properties. *J. Phys. Chem. B* **101**, 6661 (1997).

34. Gans, R. Über die Form ultramikroskopischer Goldteilchen. *Ann. Phys.* **342**, 881-900 (1912).

35. Jana, N. R., L. Gearheart, C. J. Murphy Seed-mediated growth approach for shape-controlled synthesis of spheroidal and rod-like gold nanoparticles using a surfactant template. *Adv. Mater.* **13**, 1389 (2001).

36. Nikoobakht, B., M. A. El-Sayed Preparation and growth mechanism of gold nanorods (NRs) using seed-mediated growth method. *Chem. Mater.* **15**, 1957 (2003).

37. Pérez-Juste, J., Liz-Marzán, L. M., Carnie, S., Chan, D. Y. C., & Mulvaney, P. Electric-Field-Directed Growth of Gold Nanorods in Aqueous Surfactant Solutions. *Adv. Funct. Mater.* **14**, 571-579 (2004).

38. Murphy, C. J., Thompson, L. B., Chernak, D. J., Yang, J. A., Sivapalan, S. T., Boulos, S. P., Huang, J., Alkilany, A. M., & Sisco, P. N. Gold nanorod crystal growth: From seed-

mediated synthesis to nanoscale sculpting. *Curr. Opin. Colloid Interface Sci.* **16**, 128-134 (2011).

39. Ha, T. H., Koo, H.-J., & Chung, B. H. Shape-Controlled Syntheses of Gold Nanoprisms and Nanorods Influenced by Specific Adsorption of Halide Ions. *J. Phys. Chem. C* **111**, 1123-1130 (2006).

40. Nikoobakht, B., & El-Sayed, M. A. Evidence for Bilayer Assembly of Cationic Surfactants on the Surface of Gold Nanorods. *Langmuir* **17**, 6368-6374 (2001).

41. Sau, T. K., & Murphy, C. J. Seeded High Yield Synthesis of Short Au Nanorods in Aqueous Solution. *Langmuir* **20**, 6414-6420 (2004).

42. Grzelczak, M., Perez-Juste, J., Mulvaney, P., & Liz-Marzan, L. M. Shape control in gold nanoparticle synthesis. *Chem. Soc. Rev.* **37**, 1783-1791 (2008).

43. Wang, Z. L., Mohamed, M. B., Link, S., & El-Sayed, M. A. Crystallographic facets and shapes of gold nanorods of different aspect ratios. *Surf. Sci.* **440**, L809-L814 (1999).

44. Carbó-Argibay, E., Rodríguez-González, B., Pacifico, J., Pastoriza-Santos, I., Pérez-Juste, J., & Liz-Marzán, L. M. Chemical Sharpening of Gold Nanorods: The Rod-to-Octahedron Transition. *Angew. Chem. Int. Ed.* **46**, 8983-8987 (2007).

45. Johnson, C. J., Dujardin, E., Davis, S. A., Murphy, C. J., & Mann, S. Growth and form of gold nanorods prepared by seed-mediated, surfactant-directed synthesis. *J. Mater. Chem.* **12**, 1765-1770 (2002).

46. Khanal, B. P., & Zubarev, E. R. Purification of High Aspect Ratio Gold Nanorods: Complete Removal of Platelets. *J. Am. Chem. Soc.* **130**, 12634-12635 (2008).

47. Aden, A. L., & Kerker, M. Scattering of Electromagnetic Waves from Two Concentric Spheres. *J. Appl. Phys.* **22**, 1242-1246 (1951).

48. Oldenburg, S. J., Averitt, R. D., Westcott, S. L., & Halas, N. J. Nanoengineering of optical resonances. *Chem. Phys. Lett.* **288**, 243-247 (1998).

49. Stöber, W., Fink, A., & Bohn, E. Controlled growth of monodisperse silica spheres in the micron size range. *J. Colloid Interface Sci.* **26**, 62-69 (1968).

50. Brinson, B. E., Lassiter, J. B., Levin, C. S., Bardhan, R., Mirin, N., & Halas, N. J. Nanoshells Made Easy: Improving Au Layer Growth on Nanoparticle Surfaces. *Langmuir* **24**, 14166-14171 (2008).

51. Wang, H., Brandl, D. W., Nordlander, P., & Halas, N. J. Plasmonic Nanostructures: Artificial Molecules. *Acc. Chem. Res.* **40**, 53-62 (2006).

52. Chen, J., McLellan, J. M., Siekkinen, A., Xiong, Y., Li, Z.-Y., & Xia, Y. Facile Synthesis of Gold/Silver Nanocages with Controllable Pores on the Surface. *J. Am. Chem. Soc.* **128**, 14776-14777 (2006).

53. Skrabalak, S. E., Chen, J., Sun, Y., Lu, X., Au, L., Cobley, C. M., & Xia, Y. Gold Nanocages: Synthesis, Properties, and Applications. *Acc. Chem. Res.* **41**, 1587-1595 (2008).

54. Lu, X., Au, L., McLellan, J., Li, Z.-Y., Marquez, M., & Xia, Y. Fabrication of Cubic Nanocages and Nanoframes by Dealloying Au/Ag Alloy Nanoboxes with an Aqueous Etchant Based on Fe(NO3)3 or NH4OH. *Nano Lett.* **7**, 1764-1769 (2007).

55. Liang, Z., Susha, A., & Caruso, F. Gold Nanoparticle-Based Core–Shell and Hollow Spheres and Ordered Assemblies Thereof. *Chem. Mater.* **15**, 3176-3183 (2003).

56. Liang, H.-P., Wan, L.-J., Bai, C.-L., & Jiang, L. Gold Hollow Nanospheres: Tunable Surface Plasmon Resonance Controlled by Interior-Cavity Sizes. *J. Phys. Chem. B* **109**, 7795-7800 (2005).

57. Kim, F., Connor, S., Song, H., Kuykendall, T., & Yang, P. Platonic Gold Nanocrystals. *Angew. Chem. Int. Ed.* **43**, 3673-3677 (2004).

58. Sau, T. K., & Murphy, C. J. Room Temperature, High-Yield Synthesis of Multiple Shapes of Gold Nanoparticles in Aqueous Solution. *J. Am. Chem. Soc.* **126**, 8648-8649 (2004).

59. Seo, D., Park, J. C., & Song, H. Polyhedral Gold Nanocrystals with Oh Symmetry: From Octahedra to Cubes. *J. Am. Chem. Soc.* **128**, 14863-14870 (2006).

60. Seo, D., Yoo, C. I., Park, J. C., Park, S. M., Ryu, S., & Song, H. Directed Surface Overgrowth and Morphology Control of Polyhedral Gold Nanocrystals. *Angew. Chem. Int. Ed.* **47**, 763-767 (2008).

61. Niu, W., Zheng, S., Wang, D., Liu, X., Li, H., Han, S., Chen, J., Tang, Z., & Xu, G. Selective Synthesis of Single-Crystalline Rhombic Dodecahedral, Octahedral, and Cubic Gold Nanocrystals. *J. Am. Chem. Soc.* **131**, 697-703 (2009).

62. Zhang, J., Langille, M. R., Personick, M. L., Zhang, K., Li, S., & Mirkin, C. A. Concave Cubic Gold Nanocrystals with High-Index Facets. *J. Am. Chem. Soc.* **132**, 14012-14014 (2010).

63. Ming, T., Feng, W., Tang, Q., Wang, F., Sun, L., Wang, J., & Yan, C. Growth of Tetrahexahedral Gold Nanocrystals with High-Index Facets. *J. Am. Chem. Soc.* **131**, 16350-16351 (2009).

64. Personick, M. L., Langille, M. R., Zhang, J., Harris, N., Schatz, G. C., & Mirkin, C. A. Synthesis and Isolation of {110}-Faceted Gold Bipyramids and Rhombic Dodecahedra. *J. Am. Chem. Soc.* **133**, 6170-6173 (2011).

65. Mantovani, A., Allavena, P., Sica, A., & Balkwill, F. Cancer-related inflammation. *Nature* **454**, 436-444 (2008).

66. Shankar, S. S., Rai, A., Ankamwar, B., Singh, A., Ahmad, A., & Sastry, M. Biological synthesis of triangular gold nanoprisms. *Nat. Mater.* **3**, 482-488 (2004).

67. Millstone, J. E., Park, S., Shuford, K. L., Qin, L., Schatz, G. C., & Mirkin, C. A. Observation of a Quadrupole Plasmon Mode for a Colloidal Solution of Gold Nanoprisms. *J. Am. Chem. Soc.* **127**, 5312-5313 (2005).

68. Nicewarner-Peña, S. R., Freeman, R. G., Reiss, B. D., He, L., Peña, D. J., Walton, I. D., Cromer, R., Keating, C. D., & Natan, M. J. Submicrometer Metallic Barcodes. *Science* **294**, 137-141 (2001).

69. Qin, L., Park, S., Huang, L., & Mirkin, C. A. On-Wire Lithography. *Science* **309**, 113-115 (2005).

70. Hao, F., Nehl, C. L., Hafner, J. H., & Nordlander, P. Plasmon Resonances of a Gold Nanostar. *Nano Lett.* **7**, 729-732 (2007).

71. Nehl, C. L., Liao, H., & Hafner, J. H. Optical Properties of Star-Shaped Gold Nanoparticles. *Nano Lett.* **6**, 683-688 (2006).

72. Guerrero-Martínez, A., Barbosa, S., Pastoriza-Santos, I., & Liz-Marzán, L. M. Nanostars shine bright for you: Colloidal synthesis, properties and applications of branched metallic nanoparticles. *Curr. Opin. Colloid Interface Sci.* **16**, 118-127 (2011).

73. Barbosa, S., Agrawal, A., Rodríguez-Lorenzo, L., Pastoriza-Santos, I., Alvarez-Puebla, R. n. A., Kornowski, A., Weller, H., & Liz-Marzán, L. M. Tuning Size and Sensing Properties in Colloidal Gold Nanostars. *Langmuir* **26**, 14943-14950 (2010).

74. Rodriguez-Lorenzo, L., Krpetic, Z., Barbosa, S., Alvarez-Puebla, R. A., Liz-Marzan, L. M., Prior, I. A., & Brust, M. Intracellular mapping with SERS-encoded gold nanostars. *Integr. Biol.* **3**, 922-926 (2011).

75. Khoury, C. G., & Vo-Dinh, T. Gold Nanostars For Surface-Enhanced Raman Scattering: Synthesis, Characterization and Optimization. *J. Phys. Chem. C* **112**, 18849-18859 (2008).

76. Rodríguez-Lorenzo, L., Álvarez-Puebla, R. n. A., de Abajo, F. J. G. a., & Liz-Marzán, L. M. Surface Enhanced Raman Scattering Using Star-Shaped Gold Colloidal Nanoparticles†. *J. Phys. Chem. C* **114**, 7336-7340 (2009).

77. Hrelescu, C., Sau, T. K., Rogach, A. L., Jäckel, F., Laurent, G., Douillard, L., & Charra, F. Selective Excitation of Individual Plasmonic Hotspots at the Tips of Single Gold Nanostars. *Nano Lett.* **11**, 402-407 (2011).

78. Senthil Kumar, P., Pastoriza-Santos, I., Rodríguez-González, B., Javier García de Abajo, F., & Liz-Marzán, L. M. High-yield synthesis and optical response of gold nanostars. *Nanotechnology* **19**, 015606 (2008).

79. Hulteen, J. C., & Van Duyne, R. P. Nanosphere lithography: A materials general fabrication process for periodic particle array surfaces. *J. Vac. Sci. Technol., A* **13**, 1553-1558 (1995).

80. Huang, W., Qian, W., & El-Sayed, M. A. The Optically Detected Coherent Lattice Oscillations in Silver and Gold Monolayer Periodic Nanoprism Arrays: The Effect of Interparticle Coupling. *J. Phys. Chem. B* **109**, 18881-18888 (2005).

81. Fromm, D. P., Sundaramurthy, A., Schuck, P. J., Kino, G., & Moerner, W. E. Gap-Dependent Optical Coupling of Single "Bowtie" Nanoantennas Resonant in the Visible. *Nano Lett.* **4**, 957-961 (2004).

82. Dreaden, E. C., Near, R. D., Abdallah, T., Talaat, M. H., & El-Sayed, M. A. Multimodal plasmon coupling in low symmetry gold nanoparticle pairs detected in surface-enhanced Raman scattering. *Appl. Phys. Lett.* **98**, 183115-183113 (2011).

83. Xu, Q., Rioux, R. M., Dickey, M. D., & Whitesides, G. M. Nanoskiving: A New Method To Produce Arrays of Nanostructures. *Acc. Chem. Res.* **41**, 1566-1577 (2008).

84. Zhang, H., Li, Z., & Mirkin, C. A. Dip-Pen Nanolithography-Based Methodology for Preparing Arrays of Nanostructures Functionalized with Oligonucleotides. *Adv. Mater.* **14**, 1472-1474 (2002).

85. Zhang, H., & Mirkin, C. A. DPN-Generated Nanostructures Made of Gold, Silver, and Palladium. *Chem. Mater.* **16**, 1480-1484 (2004).

86. Kim, P., Epstein, A. K., Khan, M., Zarzar, L. D., Lipomi, D. J., Whitesides, G. M., & Aizenberg, J. Structural Transformation by Electrodeposition on Patterned Substrates (STEPS): A New Versatile Nanofabrication Method. *Nano Lett.*, ASAP (2011).

87. Lu, Y., Liu, G. L., Kim, J., Mejia, Y. X., & Lee, L. P. Nanophotonic Crescent Moon Structures with Sharp Edge for Ultrasensitive Biomolecular Detection by Local Electromagnetic Field Enhancement Effect. *Nano Lett.* **5**, 119-124 (2005).

88. Liu, G. L., Lu, Y., Kim, J., Doll, J. C., & Lee, L. P. Magnetic Nanocrescents as Controllable Surface-Enhanced Raman Scattering Nanoprobes for Biomolecular Imaging. *Adv. Mater.* **17**, 2683-2688 (2005).

89. Lee, J., Hasan, W., Stender, C. L., & Odom, T. W. Pyramids: A Platform for Designing Multifunctional Plasmonic Particles. *Acc. Chem. Res.* **41**, 1762-1771 (2008).

90. Henzie, J., Kwak, E.-S., & Odom, T. W. Mesoscale Metallic Pyramids with Nanoscale Tips. *Nano Lett.* **5**, 1199-1202 (2005).

91. Shuford, K. L., Lee, J., Odom, T. W., & Schatz, G. C. Optical Properties of Gold Pyramidal Shells. *J. Phys. Chem. C* **112**, 6662-6666 (2008).

92. Hasan, W., Lee, J., Henzie, J., & Odom, T. W. Selective Functionalization and Spectral Identification of Gold Nanopyramids. *J. Phys. Chem. C* **111**, 17176-17179 (2007).

93. Sweeney, C. M., Stender, C. L., Nehl, C. L., Hasan, W., Shuford, K. L., & Odom, T. W. Optical Properties of Tipless Gold Nanopyramids. *Small* **7**, 2032-2036 (2011).

94. Luk'yanchuk, B., Zheludev, N. I., Maier, S. A., Halas, N. J., Nordlander, P., Giessen, H., & Chong, C. T. The Fano resonance in plasmonic nanostructures and metamaterials. *Nat. Mater.* **9**, 707-715 (2010).

95. Kroner, M., Govorov, A. O., Remi, S., Biedermann, B., Seidl, S., Badolato, A., Petroff, P. M., Zhang, W., Barbour, R., Gerardot, B. D., Warburton, R. J., & Karrai, K. The nonlinear Fano effect. *Nature* **451**, 311-314 (2008).

96. Hasan, W., Stender, C. L., Lee, M. H., Nehl, C. L., Lee, J., & Odom, T. W. Tailoring the Structure of Nanopyramids for Optimal Heat Generation. *Nano Lett.* **9**, 1555-1558 (2009).

97. Wust, P., Hildebrandt, B., Sreenivasa, G., Rau, B., Gellermann, J., Riess, H., Felix, R., & Schlag, P. M. Hyperthermia in combined treatment of cancer. *Lancet Oncol.* **3**, 487-497 (2002).

98. Alkilany, A. M., Nagaria, P. K., Hexel, C. R., Shaw, T. J., Murphy, C. J., & Wyatt, M. D. Cellular Uptake and Cytotoxicity of Gold Nanorods: Molecular Origin of Cytotoxicity and Surface Effects. *Small* **5**, 701-708 (2009).

99. Matsumura, Y., & Maeda, H. A New Concept for Macromolecular Therapeutics in Cancer Chemotherapy: Mechanism of Tumoritropic Accumulation of Proteins and the Antitumor Agent Smancs. *Cancer Res.* **46**, 6387-6392 (1986).

100. Maeda, H., Wu, J., Sawa, T., Matsumura, Y., & Hori, K. Tumor vascular permeability and the EPR effect in macromolecular therapeutics: a review. *J. Controlled Release* **65**, 271-284 (2000).

101. Sato, K., Hosokawa, K., Maeda, M. Rapid Aggregation of Gold Nanoparticles Induced by Non-Cross-Linking DNA Hybridization. *J. Am. Chem. Soc.* **125**, 8102-8103 (2003).

102. Iyer, A. K., Khaled, G., Fang, J., & Maeda, H. Exploiting the enhanced permeability and retention effect for tumor targeting. *Drug Discovery Today* **11**, 812-818 (2006).

103. Bain, C. D., Troughton, E. B., Tao, Y. T., Evall, J., Whitesides, G. M., & Nuzzo, R. G. Formation of monolayer films by the spontaneous assembly of organic thiols from solution onto gold. *J. Am. Chem. Soc.* **111**, 321-335 (1989).

104. Love, J. C., Estroff, L. A., Kriebel, J. K., Nuzzo, R. G., & Whitesides, G. M. Self-Assembled Monolayers of Thiolates on Metals as a Form of Nanotechnology. *Chem. Rev.* **105**, 1103-1170 (2005).

105. Bard, A. J., & Faulkner, L. R. *Electrochemical Methods: Fundamentals and Applications*. 2nd edn, (John Wiley & Sons, Inc., 2001).

106. Hu, K., & Bard, A. J. In Situ Monitoring of Kinetics of Charged Thiol Adsorption on Gold Using an Atomic Force Microscope. *Langmuir* **14**, 4790-4794 (1998).

107. Hostetler, M. J., Templeton, A. C., & Murray, R. W. Dynamics of Place-Exchange Reactions on Monolayer-Protected Gold Cluster Molecules. *Langmuir* **15**, 3782-3789 (1999).

108. Sardar, R., Funston, A. M., Mulvaney, P., & Murray, R. W. Gold Nanoparticles: Past, Present, and Future†. *Langmuir* **25**, 13840-13851 (2009).

109. Templeton, A. C., Wuelfing, M. P., & Murray, R. W. Monolayer protected cluster molecules. *Acc. Chem. Res.* **33**, 27-36 (2000).

110. Martin, B. R., Dermody, D. J., Reiss, B. D., Fang, M., Lyon, L. A., Natan, M. J., & Mallouk, T. E. Orthogonal Self-Assembly on Colloidal Gold-Platinum Nanorods. *Adv. Mater.* **11**, 1021-1025 (1999).

111. Walter, M., Akola, J., Lopez-Acevedo, O., Jadzinsky, P. D., Calero, G., Ackerson, C. J., Whetten, R. L., Grönbeck, H., & Häkkinen, H. A unified view of ligand-protected gold clusters as superatom complexes. *Proc. Natl. Acad. Sci. U.S.A.* **105**, 9157-9162 (2008).

112. Hou, W., Dasog, M., & Scott, R. W. J. Probing the Relative Stability of Thiolate- and Dithiolate-Protected Au Monolayer-Protected Clusters. *Langmuir* **25**, 12954-12961 (2009).

113. Zhao, Y., Perez-Segarra, W., Shi, Q. C., & Wei, A. Dithiocarbamate assembly on gold. *J. Am. Chem. Soc.* **127**, 7328-7329 (2005).

114. Daniel, M.-C., & Astruc, D. Gold Nanoparticles: Assembly, Supramolecular Chemistry, Quantum-Size-Related Properties, and Applications toward Biology, Catalysis, and Nanotechnology. *Chem. Rev.* **104**, 293-346 (2003).

115. Yee, C. K., Ulman, A., Ruiz, J. D., Parikh, A., White, H., & Rafailovich, M. Alkyl Selenide- and Alkyl Thiolate-Functionalized Gold Nanoparticles: Chain Packing and Bond Nature. *Langmuir* **19**, 9450-9458 (2003).

116. Cheng, Z. L., Skouta, R., Vazquez, H., Widawsky, J. R., Schneebeli, S., Chen, W., Hybertsen, M. S., Breslow, R., & Venkataraman, L. In situ formation of highly conducting covalent Au-C contacts for single-molecule junctions. *Nat. Nanotechnol.* **6**, 353-357 (2011).

117. Cheng, Y., Samia, A. C., Li, J., Kenney, M. E., Resnick, A., & Burda, C. Delivery and efficacy of a cancer drug as a function of the bond to the gold nanoparticle surface. *Langmuir* **26**, 2248-2255 (2010).

118. Cheng, Y., Meyers, J. D., Broome, A.-M., Kenney, M. E., Basilion, J. P., & Burda, C. Deep Penetration of a PDT Drug into Tumors by Noncovalent Drug-Gold Nanoparticle Conjugates. *J. Am. Chem. Soc.* **133**, 2583-2591 (2011).

119. Ulman, A. Formation and Structure of Self-Assembled Monolayers. *Chem. Rev.* **96**, 1533-1554 (1996).

120. Nuzzo, R. G., Zegarski, B. R., & Dubois, L. H. Fundamental studies of the chemisorption of organosulfur compounds on gold(111). Implications for molecular self-assembly on gold surfaces. *J. Am. Chem. Soc.* **109**, 733-740 (1987).

121. Tarazona-Vasquez, F., & Balbuena, P. B. Complexation of the Lowest Generation Poly(amidoamine)-NH2 Dendrimers with Metal Ions, Metal Atoms, and Cu(II) Hydrates: An ab Initio Study. *J. Phys. Chem. B* **108**, 15992-16001 (2004).

122. Greczynski, G., & Salaneck, W. R. Photoelectron spectroscopy of hybrid interfaces for light emitting diodes: Influence of the substrate work function. *Appl. Phys. Lett.* **79**, 3185-3187 (2001).

123. Orendorff, C. J., & Murphy, C. J. Quantitation of Metal Content in the Silver-Assisted Growth of Gold Nanorods. *J. Phys. Chem. B* **110**, 3990-3994 (2006).

124. Lee, J.-S., Stoeva, S. I., & Mirkin, C. A. DNA-Induced Size-Selective Separation of Mixtures of Gold Nanoparticles. *J. Am. Chem. Soc.* **128**, 8899-8903 (2006).

125. Zhu, Z.-J., Yeh, Y.-C., Tang, R., Yan, B., Tamayo, J., Vachet, R. W., & Rotello, V. M. Stability of quantum dots in live cells. *Nat. Chem.* **3**, 963-968 (2011).

126. Flynn, N. T., Tran, T. N. T., Cima, M. J., & Langer, R. Long-Term Stability of Self-Assembled Monolayers in Biological Media. *Langmuir* **19**, 10909-10915 (2003).

127. Dreaden, E. C., Mwakwari, S. C., Sodji, Q. H., Oyelere, A. K., & El-Sayed, M. A. Tamoxifen-Poly(ethylene glycol)-Thiol Gold Nanoparticle Conjugates: Enhanced Potency and Selective Delivery for Breast Cancer Treatment. *Bioconjugate Chem.* **20**, 2247-2253 (2009).

128. Dickerson, E. B., Dreaden, E. C., Huang, X. H., El-Sayed, I. H., Chu, H. H., Pushpanketh, S., McDonald, J. F., & El-Sayed, M. A. Gold nanorod assisted near-infrared plasmonic photothermal therapy (PPTT) of squamous cell carcinoma in mice. *Cancer Lett.* **269**, 57-66 (2008).

129. Harris, J. M., & Chess, R. B. Effect of pegylation on pharmaceuticals. *Nat. Rev. Drug Discovery* **2**, 214-221 (2003).

130. Zheng, M., Davidson, F., & Huang, X. Ethylene Glycol Monolayer Protected Nanoparticles for Eliminating Nonspecific Binding with Biological Molecules†. *J. Am. Chem. Soc.* **125**, 7790-7791 (2003).

131. Niidome, T., Yamagata, M., Okamoto, Y., Akiyama, Y., Takahashi, H., Kawano, T., Katayama, Y., & Niidome, Y. PEG-modified gold nanorods with a stealth character for in vivo applications. *J. Controlled Release* **114**, 343-347 (2006).

132. von Maltzahn, G., Park, J.-H., Agrawal, A., Bandaru, N. K., Das, S. K., Sailor, M. J., & Bhatia, S. N. Computationally Guided Photothermal Tumor Therapy Using Long-Circulating Gold Nanorod Antennas. *Cancer Res.* **69**, 3892-3900 (2009).

133. Liu, Z., Davis, C., Cai, W., He, L., Chen, X., & Dai, H. Circulation and long-term fate of functionalized, biocompatible single-walled carbon nanotubes in mice probed by Raman spectroscopy. *Proc. Natl. Acad. Sci. U.S.A.* **105**, 1410-1415 (2008).

134. Zalipsky, S., Hansen, C. B., Oaks, J. M., & Allen, T. M. Evaluation of blood clearance rates and biodistribution of poly(2-oxazoline)-grafted liposomes. *J. Pharm. Sci.* **85**, 133-137 (1996).

135. Gaertner, F. C., Luxenhofer, R., Blechert, B., Jordan, R., & Essler, M. Synthesis, biodistribution and excretion of radiolabeled poly(2-alkyl-2-oxazoline)s. *J. Controlled Release* **119**, 291-300 (2007).

136. Konradi, R., Pidhatika, B., Muhlebach, A., & Textor, M. Poly-2-methyl-2-oxazoline: A Peptide-like Polymer for Protein-Repellent Surfaces. *Langmuir* **24**, 613-616 (2008).

137. Kim, C. K., Ghosh, P., Pagliuca, C., Zhu, Z.-J., Menichetti, S., & Rotello, V. M. Entrapment of Hydrophobic Drugs in Nanoparticle Monolayers with Efficient Release into Cancer Cells. *J. Am. Chem. Soc.* **131**, 1360-1361 (2009).

138. Gibson, J. D., Khanal, B. P., & Zubarev, E. R. Paclitaxel-functionalized gold nanoparticles. *J. Am. Chem. Soc.* **129**, 11653-11661 (2007).

139. Gole, A., & Murphy, C. J. Azide-Derivatized Gold Nanorods: Functional Materials for "Click" Chemistry. *Langmuir* **24**, 266-272 (2007).

140. Oh, E., Susumu, K., Blanco-Canosa, J. B., Medintz, I. L., Dawson, P. E., & Mattoussi, H. Preparation of Stable Maleimide-Functionalized Au Nanoparticles and Their Use in Counting Surface Ligands. *Small* **6**, 1273-1278 (2010).

141. Demers, L. M., Mirkin, C. A., Mucic, R. C., Reynolds, R. A., Letsinger, R. L., Elghanian, R., & Viswanadham, G. A Fluorescence-Based Method for Determining the Surface Coverage and Hybridization Efficiency of Thiol-Capped Oligonucleotides Bound to Gold Thin Films and Nanoparticles. *Anal. Chem.* **72**, 5535-5541 (2000).

142. Link, S., & El-Sayed, M. A. Spectroscopic determination of the melting energy of a gold nanorod. *J. Chem. Phys.* **114**, 2362-2368 (2001).

143. Dass, A., Stevenson, A., Dubay, G. R., Tracy, J. B., & Murray, R. W. Nanoparticle MALDI-TOF mass spectrometry without fragmentation: Au25(SCH2CH2Ph)18 and mixed monolayer Au25(SCH2CH2Ph)(18-x)(L)(x). *J. Am. Chem. Soc.* **130**, 5940-5946 (2008).

144. Weisbecker, C. S., Merritt, M. V., & Whitesides, G. M. Molecular Self-Assembly of Aliphatic Thiols on Gold Colloids. *Langmuir* **12**, 3763-3772 (1996).

145. Bourg, M.-C., Badia, A., & Lennox, R. B. Gold–Sulfur Bonding in 2D and 3D Self-Assembled Monolayers: XPS Characterization. *J. Phys. Chem. B* **104**, 6562-6567 (2000).

146. Brown, S. D., Nativo, P., Smith, J.-A., Stirling, D., Edwards, P. R., Venugopal, B., Flint, D. J., Plumb, J. A., Graham, D., & Wheate, N. J. Gold Nanoparticles for the Improved Anticancer Drug Delivery of the Active Component of Oxaliplatin. *J. Am. Chem. Soc.* **132**, 4678-4684 (2010).

147. Rosi, N. L., Giljohann, D. A., Thaxton, C. S., Lytton-Jean, A. K. R., Han, M. S., & Mirkin, C. A. Oligonucleotide-Modified Gold Nanoparticles for Intracellular Gene Regulation. *Science* **312**, 1027-1030 (2006).

148. Seferos, D. S., Giljohann, D. A., Hill, H. D., Prigodich, A. E., & Mirkin, C. A. Nano-Flares: Probes for Transfection and mRNA Detection in Living Cells. *J. Am. Chem. Soc.* **129**, 15477-15479 (2007).

149. Agasti, S. S., Chompoosor, A., You, C. C., Ghosh, P., Kim, C. K., & Rotello, V. M. Photoregulated release of caged anticancer drugs from gold nanoparticles. *J. Am. Chem. Soc.* **131**, 5728-5729 (2009).

150. Gittins, D. I., & Caruso, F. Tailoring the Polyelectrolyte Coating of Metal Nanoparticles. *J. Phys. Chem. B* **105**, 6846-6852 (2001).

151. Gole, A., & Murphy, C. J. Polyelectrolyte-coated gold nanorods: Synthesis, characterization and immobilization. *Chem. Mater.* **17**, 1325-1330 (2005).

152. Murphy, C. J., Thompson, L. B., Alkilany, A. M., Sisco, P. N., Boulos, S. P., Sivapalan, S. T., Yang, J. A., Chernak, D. J., & Huang, J. Y. The Many Faces of Gold Nanorods. *J. Phys. Chem. Lett.* **1**, 2867-2875 (2010).

153. Singh, N., & Lyon, L. A. Au Nanoparticle Templated Synthesis of pNIPAm Nanogels. *Chem. Mater.* **19**, 719-726 (2007).

154. Obare, S. O., Jana, N. R., & Murphy, C. J. Preparation of Polystyrene- and Silica-Coated Gold Nanorods and Their Use as Templates for the Synthesis of Hollow Nanotubes. *Nano Lett.* **1**, 601-603 (2001).

155. Wood, K. C., Chuang, H. F., Batten, R. D., Lynn, D. M., & Hammond, P. T. Controlling interlayer diffusion to achieve sustained, multiagent delivery from layer-by-layer thin films. *Proc. Natl. Acad. Sci. U.S.A.* **103**, 10207-10212 (2006).

156. Kim, B. S., Smith, R. C., Poon, Z., & Hammond, P. T. MAD (Multiagent Delivery) Nanolayer: Delivering Multiple Therapeutics from Hierarchically Assembled Surface Coatings. *Langmuir* **25**, 14086-14092 (2009).

157. Smith, R. C., Riollano, M., Leung, A., & Hammond, P. T. Layer-by-Layer Platform Technology for Small-Molecule Delivery. *Angew. Chem. Int. Ed.* **48**, 8974-8977 (2009).

158. Su, X. F., Kim, B. S., Kim, S. R., Hammond, P. T., & Irvine, D. J. Layer-by-Layer-Assembled Multilayer Films for Transcutaneous Drug and Vaccine Delivery. *ACS Nano* **3**, 3719-3729 (2009).

159. Poon, Z., Lee, J. B., Morton, S. W., & Hammond, P. T. Controlling in Vivo Stability and Biodistribution in Electrostatically Assembled Nanoparticles for Systemic Delivery. *Nano Lett.* **11**, 2096-2103 (2011).

160. Liz-Marzán, L. M., Giersig, M., & Mulvaney, P. Synthesis of Nanosized Gold–Silica Core–Shell Particles. *Langmuir* **12**, 4329-4335 (1996).

161. Banholzer, M. J., Harris, N., Millstone, J. E., Schatz, G. C., & Mirkin, C. A. Abnormally Large Plasmonic Shifts in Silica-Protected Gold Triangular Nanoprisms. *J. Phys. Chem. C* **114**, 7521-7526 (2010).

162. Jana, N. R., Earhart, C., & Ying, J. Y. Synthesis of Water-Soluble and Functionalized Nanoparticles by Silica Coating. *Chem. Mater.* **19**, 5074-5082 (2007).

163. Mulvaney, S. P., Musick, M. D., Keating, C. D., & Natan, M. J. Glass-Coated, Analyte-Tagged Nanoparticles: A New Tagging System Based on Detection with Surface-Enhanced Raman Scattering. *Langmuir* **19**, 4784-4790 (2003).

164. Doering, W. E., & Nie, S. Spectroscopic Tags Using Dye-Embedded Nanoparticles and Surface-Enhanced Raman Scattering. *Anal. Chem.* **75**, 6171-6176 (2003).

165. Zavaleta, C. L., Smith, B. R., Walton, I., Doering, W., Davis, G., Shojaei, B., Natan, M. J., & Gambhir, S. S. Multiplexed imaging of surface enhanced Raman scattering nanotags in living mice using noninvasive Raman spectroscopy. *Proc. Natl. Acad. Sci. U.S.A.* **106**, 13511-13516 (2009).

CHAPTER 2

GOLD NANOPARTICLES IN BIOMEDICINE

While advances in the detection and treatment of cancer has resulted in dramatic improvements to human health in the US, reductions in cancer mortality rates have not kept pace with the large increase in incidence.[*3*] Today, 1 in 2 males and 1 in 3 females in the US will develop cancer at some point during their lifetime.[*4*] 1 in 4 males and 1 in 5 females in the US will die from the disease. There is a clear and urgent need for increasingly potent and selective methods with which to detect and treat cancers in their earliest stages.

Nanoparticles – materials with dimensions between 10^{-9} and 10^{-8} meters – have been systemically administered in humans since clinical approval of the first micellar drug Sandimmune® by the US Food and Drug Administration (FDA) in 1983 and the first polymer-drug nanoconjugate Adagen® later in 1990.[*5*] Since then, an explosion of research in nanoscale diagnostic and therapeutic agents has given rise to a range of biomedical nanotechnologies and platforms,[*2,6-12*] including protein-drug nanoconjugates,[*13*] micelles,[*14-17*] liposomes,[*18,19*] dendrimers,[*20-22*] inorganic nanoparticles,[*12,23-30*] and other polymer-drug nanoconjugates [*6,31-34*] (**Table 2.1**). More than two dozen biodiagnostic or therapeutic nanotechnologies have been approved for clinical use with roughly 250 others in clinical development. The global market share for biomedical nanotechnologies is expected to grow to $70-160 billion by 2015, rivaling the current worldwide market for biologics.[*35*] These nanoscale constructs provide a range of multiple, fundamentally new properties which can be exploited in ways that can improve our ability to detect, treat, and monitor disease states. Further, the unique interactions between these nanoscale materials and comparably sized physiological structures, proteins, organelles, DNA, etc. can also be leveraged to compliment

existing medical diagnostic/treatment strategies and to foster the development of new and potentially more efficacious approaches.

Gold nanoparticles exhibit a combination of physical, chemical, optical, and electronic properties unique from other biomedical nanotechnologies and provide a highly multifunctional platform with which to image and diagnose diseases,[*36-40*] to selectively deliver therapeutic agents, [*37,41-43*] to sensitize cells and tissues to treatment regimens,[*44,45*] to monitor and guide surgical procedures,[*26,46,47*] and to preferentially administer electromagnetic radiation [*46-49*] to disease sites (**Figure 2.1**). Because of their large size, circulating nanoparticles preferentially accumulate at tumor sites and in inflamed tissues due to the characteristically defective architecture of the vessels which supply oxygen and nutrients to these tissues (**Section 2.2**) [*50,51*]. Once circulating nanoparticles extravasate through the large vascular pores at these disease sites, they remain lodged due characteristically diminished lymphatic drainage and low diffusivity.[*52*] First termed by Maeda in 1986,[*53,54*] the enhanced permeability and retention (EPR) effect provides a basis for the selective accumulation of many high molecular weight drugs currently in clinical use. Gold nanoparticles can be used to deliver drugs or imaging contrast agents that otherwise exhibit poor solubility or pharmacokinetic profiles,[*55,56*] or to deliver agents which are intrinsically susceptible to enzymatic degradation and/or exhibit poor intracellular penetration such as small interfering RNA (siRNA).[*42,57-59*] Nanogold can be routinely surface functionalized at active ligand densities 10^2 – 10^3 fold higher than that achievable using liposomal or polymeric nanoparticles, respectively, allowing their binding affinity [*60*] to be optimized for a particular disease, type, stage, or patient. Because of their comparability in size to the distances between cell-surface targets, gold nanostructures can simultaneously engage multiple, adjacent receptor sites, achieving increased selectivity in their uptake through this multivalent avidity.[*61*]

Table 2.1. A Brief History of Nanoscale Drug Development. Adapted from Dreaden et al. [*1*].

nanoscale drug	initial dev.	seminal reference(s)	pharmaceutical	trade name*	carrier	drug	details	first FDA approval	disease	subsequent others in clincal use or development
micelle	1958, 1983	Stuttgen G, Wust H. Serum concentrations of vitamin A following variations in forms of application, dosage, and solubilizers. *Arzneim.-Forsch.* 8(161-162 (1958). Toronto Lung Transplant Group. Unilateral Lung Transplantation for Pulmonary Fibrosis. *New Engl. J. Med.* 314(18), 1140-1145 (1986)	cyclosporine emulsion	Sandimmune	Cremophor EL (polyoxyethylated castor oil)	cyclosporin	imparts water-solubility to cyclosporine for the prevention of organ transplant rejection; allowed 1st successful lung transplant in 1983	1983	n/a (immunosuppressive)	Genexol-PM (paclitaxel, metastatic breast cancer, 2006/S. Korea), NK012 (SN-38 topoisomerase I inhibitor, relapsed small cell lung cancer, Phase II complete, Phase I with Pt), NK105 (paclitaxel, gastric cancer, Phase II compete), NK911 (doxorubicin, solid tumors, Phase II), NC-6004 (cisplatin, pancreatic cancer, Phase II with gemcitabine)
polymer-drug nanoconjugate	1954, 1977	Jaizkewitz H. Incorporation of physiologically-active substances into a colloidal blood plasma substitute. I. Incorporation of mescaline peptide into polyvinylpyrrolidone. *Hoppe Seylers Z Physiol. Chem.* 297(3-6), 149-156 (1954). Abuchowski A, McCoy JR, Palczuk NC, van Es T, Davis FF. Effect of covalent attachment of polyethylene glycol on immunogenicity and circulating life of bovine liver catalase. *J. Biol. Chem.* 252(11), 3582-6 (1977).	pegademase bovine	Adagen	poly(ethylene glycol) (PEG)	adenosine deaminase (ADA)	(11–17) 5 kDa mPEG groups per ADA, 100x improved half life, diminished immune response	1990	severe combined immunodeficiency disease (SCID)	Zinostatin Stimalamer (hepatocellular carcinoma, Japan/1993), Oncospar (acute lymphoblastic leukemia; 1994/USA), PEG-Intron (chronic hepatitis C; 2000/EU, 2001/USA), Pegasys (chronic hepatitis C; 2002/USA & EU), Neulasta (febrile neutropenia; 2002/USA & EU), Somavert (acromegaly; 2002/EU, 2003/USA), Pegamotecan (topoisomerase I-inhibitor, gastric or gastro-oesophageal adenocarcinoma, Phase II complete), NKTR-102 (topoisomerase I-inhibitor, breast/ovarian cancer, Phase II complete)
liposome	1965	Bangham AD, Standish MM, Watkins JC. Diffusion of univalent ions across the lamellae of swollen phospholipids. *J. Mol. Biol.* 13(1), 238-252 (1965).	doxorubicin liposomal	Doxil	PEGylated phospholipid bilayer (artificial vesicle)	doxorubicin	ca. 3-fold increased drug half life, >90% drug retention in circulation, EPR tumor accumulation, granted orphan drug exclusivity Oct 2009-May 2014	1995	Kaposi's sarcoma	DaunoXome (daunorubicin, Kaposi's sarcoma, 1996/USA), Ambisome (amphotericin B, visceral leishmaniasis, USA/1997), Visudyne (verteporfin photodynamic therapy; age-related macular degeneration; 2000/USA & EU), Myocet (doxorubicin, breast/ovarian cancer & Kaposi's sarcoma 2000/EU, 2001/Canada), Thermodox (doxorubicin, liver/breast cancer, Phase III complete), Marqibo (vincristine, acute lymphoblastic leukemia, Phase III), Onco TCS (vincristine, non-Hodgkin's lymphoma, Phase III complete), ATI-1123 (docetaxel, ovarian cancer, AIDS-related Kaposi's sarcoma, & multiple myeloma, Phase I), MCC-465 (doxorubicin, stomach cancer, Phase I complete), MBP-426 (oxaliplatin, solid tumors, Phase I complete), SGT-53 (p53 gene plasmid, solid tumors, Phase I complete)
iron oxide	1985(6)	Olsson MRE, Persson BRR, Salford LG, Schröder U. Ferromagnetic particles as contrast agent in T2 NMR imaging. *Magn. Reson. Imaging* 4(5), 437-440 (1986).	imaging agent	Feridex	iron oxide	n/a	120 to 180 nm diameter, carboxydextran-coated superparamagnetic iron oxide (SPIO) for MRI of focal liver lesions	1996	n/a (imaging)	Resovist (40-60 nm HD, carboxydextran-SPIO, MRI of focal liver lesions, 2009/EU), Ferumoxtran-10 (20-50 nm HD, dextran-SPIO, liver MRI, limited experimental use in Netherlands)
protein-drug nanoconjugate	1975, 2000	Ringsdorf H. Structure and properties of pharmacologically active polymers. J. Polym. Sci. Pol. Sym. 51(1), 135-153 (1975). Desai NP, Louie L, Ron N, Magdassi S, Soon-Shiong P. Protein-based nanoparticles for drug delivery of paclitaxel. *Trans. World Biomater. Congr.* 1, 199 (2000).	nab-Paclitaxel	Abraxane	albumin	paclitaxel	hydrophobic association with human serum albumin (67 kDa); 33% increased tumor accumulation, higher MTD, reduced neutropenia; 130 nm diameter, -31 mV	2005	breast cancer	ABI-008 (nab-docetaxel, metastatic prostate cancer, Phase I), ABI-009 (nab-rapamycin, solid tumors, preclinical complete), ABI-010 (nab-17AAG, solid tumors, preclinical), ABI-011 (dual microtubule & topoisomerase-1 inhibitor, solid tumors, preclinical)
polymeric nanocarrier	1976, 1999	Langer RS, Folkman J. Polymers for the sustained release of proteins and other macromolecules. *Nature* 263(5580), 797-800 (1976). Gonzalez H, Hwang SJ, Davis ME. New Class of Polymers for the Delivery of Macromolecular Therapeutics. Bioconjugate Chem. 10(6), 1068-1074 (1999).	CRLX101, CALAA-01	n/a	poly(cyclodextrin)	camptothecin (CRLX101), siRNA (CALAA-01)	transferrin-targeted, PEG-stabilized, DNA topoisomerase I inhibitor or RNAi/Oligonucleotide Nanoparticle Delivery (RONDEL) system (siRNA for M2 subunit of ribonucleotide reductase, RRM2); CRLX101 ca. 20-50 nm & CALAA-01 ca. 70 nm diameter	Phase II (CRLX101), Phase I (CALAA-01)	solid tumors	XYOTAX (paclitaxel, non-small cell lung cancer, Phase III complete), CRLX101 (formerly IT-101; camptothecin nanoconjugate, solid tumors, Phase II), FCE28068 (PK1, doxorubicin, breast/colorectal/non-small cell lung cancer, Phase II complete), AP5280 (Pt4+, solid tumors, Phase I complete), AP5346 (Pt4+, solid tumors, Phase II), PNU166945 (paclitaxel, solid tumors, Phase I complete), MAG-CPT (camptothecin, solid tumors, Phase I complete), CT-2106 (camptothecin, colorectal/ovarian cancer, Phase I/II discontinued), FCE28069 (PK2, galactosamine, hepatocellular carcinoma, Phase I discontinued)
dendrimer	1978	Buhleier E, Wehner W, Vögtle F. "Cascade"- and "Nonskid-Chain-like" Syntheses of Molecular Cavity Topologies. Synthesis 1978(02), 155,158 (1978). Haensler J, Szoka FC. Polyamidoamine cascade polymers mediate efficient transfection of cells in culture. *Bioconjugate Chem.* 4(5), 372-379 (1993).	SPL7013	VivaGel	SPL7013 L-lysine dendrimer	intrinsic activity	L-lysine based SPL7013 dendrimer (16.5 kDa) inhibits viral incection (incl HIV and the genital herpes) and the growth of bacteria	Phase II (BV)	bacterial vaginosis (BV) & STIs	ATI-001 (G5 PAMAM dendrimer, <5 nm diameter, folate-targeted, methotrexate-loaded; solid tumors, preclinical complete)
gold	1954	Root SW, Andrews GA, Kniseley RM, Tyor MP. The distribution and radiation effects of intravenously administered colloidal Au198 in man. *Cancer* 7(5), 858-868 (1954). Paciotti GF, Myer LD, Kim TH et al. Colloidal gold: A novel colloidal nanoparticle vector for tumor directed drug delivery. *Clin. Cancer Res.* 7(11), 3607S-3674S (2001). Hirsch LR, Stafford RJ, Bankson JA et al. Nanoshell-mediated near-infrared thermal therapy of tumors under magnetic resonance guidance. *Proc. Natl. Acad. Sci. U.S.A.* 100(23), 13549-13554 (2003).	CYT-6091	Aurimune	solid gold nanoparticles	tumor necrosis factor α	systemic administration of 27 nm diameter spherical gold nanoparticles well tolerated; 3-fold increased drug MTD; tumor-accumulation of particles	Phase I complete	solid tumors	AuroLase (ca. 150 nm diameter silica-gold core-shell nanoparticles, laser photothermal ablation therapy of head & neck tumors, human pilot studies recruiting)
silica	1968	Stöber W, Fink A, Bohn E. Controlled growth of monodisperse silica spheres in the micron size range. *J. Colloid Interface Sci.* 26(1), 62-69 (1968). Yanagisawa T, Shimizu T, Kuroda K, Kato C. The Preparation of Alkyltrimethylammonium–Kanemite Complexes and Their Conversion to Microporous Materials. *Bul. Chem. Soc. Japan* 63(4), 988-992 (1990).	128I PET label	Cornell dots (C dots)	cRGDY-mesoporous silica	Cy5	cRGDY-labeled, Cy5-loaded, PEGylated mesoporous silica nanoparticles; 6.8 nm HD, renal clearance; FDA IND approved; tumor-selective accumulation; imaging of lymphatic drainage, nodal metastases, & tumor burden	n/a	solid tumors	Zink & Stoddart (100 nm diameter mesoporous silica nanoparticles with 2 nm nanopores & a pH-responsive release valve); Ferrari (3.5 nm diameter hemispherical mesoporous silica with 24.2 nm nanopores); both commercialization pending

abbreviations: DNA (Deoxyribonucleic acid), EPR (enhanced permeability and retention), G5 (generation 5), HD (hydrodynamic diameter), HIV (human immunodeficiency virus), IND (investigational new drug), MRI (magnetic resonance imaging), MTD (maximum tolerated dose), nm (nanometer), PAMAM (polyamido amine)), PET (positron emission tomography), Pt (platinum), SPIO (superparamagnetic iron oxide), STIs (sexually-transmitted infections)

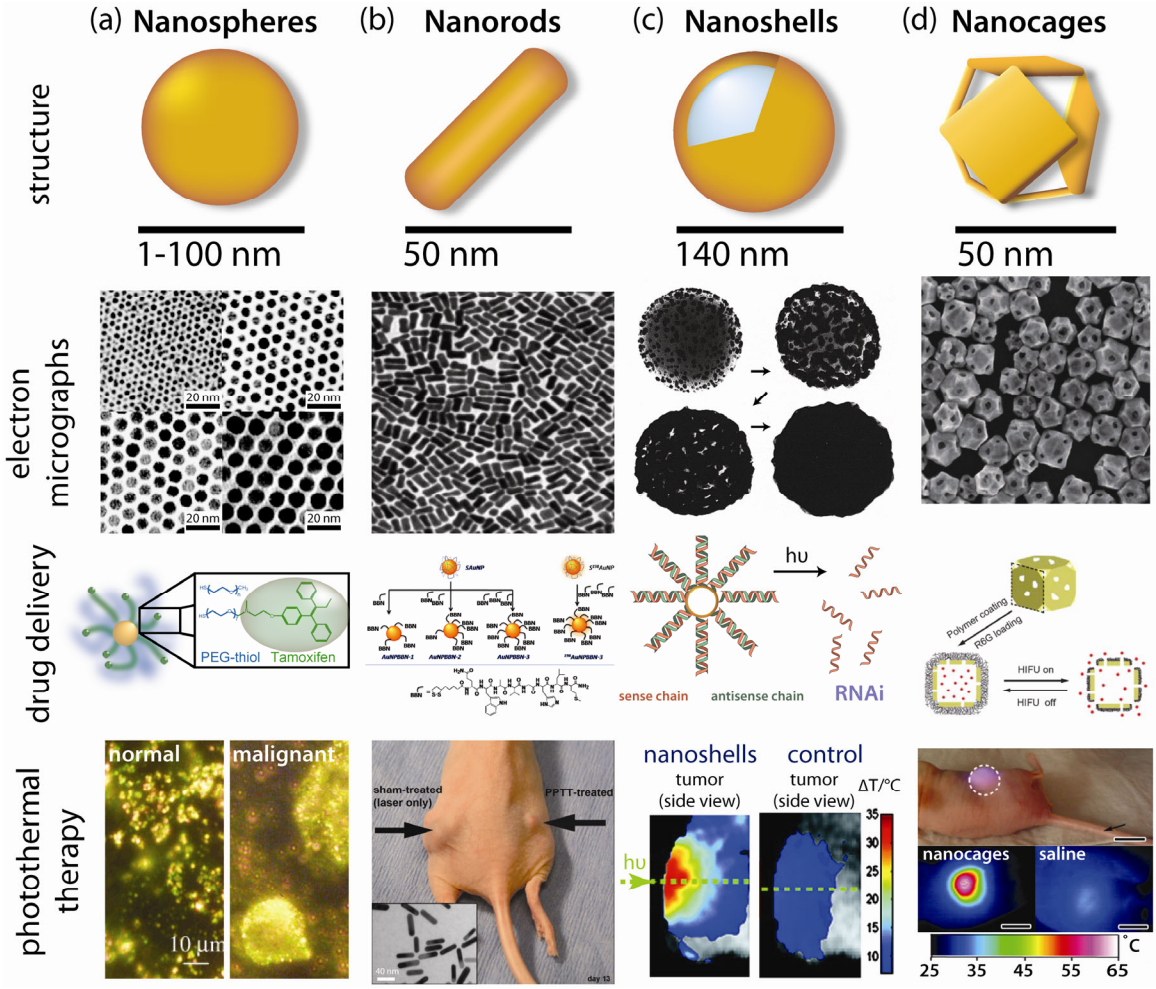

Figure 2.1. Applications of colloidal gold nanoparticles in drug delivery and laser photothermal therapy. A) Gold nanospheres, B) gold nanorods, C) gold nanoshells, and D) gold nanocages. Adapted from Dreaden et al. [*1*].

2.1 Photophysical Properties and Biomedical Applications of Gold Nanoparticles

Gold nanoparticles (**Table 2.2**) are particularly attractive platforms for targeted diagnostics and therapeutics (**Figure 2.2**) due to their unique optical and electronic properties. These structures can be conjugated at ligand densities [*62*] (1.0×10^6 μm^{-2}) that are 100- and 1000-fold higher than that achievable with conventional liposomes [*63*] or PLGA (poly(lactic-co-glycolic acid)) nanoparticles,[*64*] respectively, and the selective accumulation of gold nanoparticles at solid tumors can facilitate highly efficient photothermal ablation via non-invasive near-infrared (NIR) laser

exposure [*2,12,65-67*] (**Figure 2.3A**), high-Z enhanced X-ray computed tomography/radiotherapy,[*44,48*] non-invasive photoacoustic imaging/cytometry [*67-70*] (**Figure 2.3B**), contrast-enhanced optical coherence tomographic imaging [*71*] (OCT, **Figure 2.3C**), and electromagnetic enhancement in non-invasive spectroscopic biomarker detection schemes both in vitro [*72*] and in vivo [*73*] (**Figure 2.3D**).

Table 2.2. Selected reviews on gold nanotechnology and its use in biomedicine. Adapted from Dreaden et al. [*2*].

topic	reference
anisotropic nanoparticles	C. J. Murphy, T. K. Sau, A. M. Gole, C. J. Orendorff, J. Gao, L. Gou, S. E. Hunyadi and T. Li, Anisotropic Metal Nanoparticles: Synthesis, Assembly, and Optical Applications, *J. Phys. Chem. B*, 2005, **109**, 13857-13870.
biodiagnostics	N. L. Rosi, Mirkin, C. A., Nanostructures in biodiagnostics, *Chem. Rev.*, 2005, **105**, 1547-1562.
	J. N. Anker, Hall, W. P., Lyandres, O., Shah, N. C., Zhao, J., Van Duyne, R. P., Biosensing with plasmonic nanosensors, *Nat. Mater.*, 2008, **7**, 442-453.
	K. M. Mayer and J. H. Hafner, Localized Surface Plasmon Resonance Sensors, *Chem. Rev.*, 2011, **111**, 3828-3857.
biodistribution	N. Khlebtsov and L. Dykman, Biodistribution and toxicity of engineered gold nanoparticles: a review of in vitro and in vivo studies, *Chem. Soc. Rev.*, 2011, **40**, 1647-1671.
bio-nanotechnology	E. Katz and I. Willner, Integrated Nanoparticle–Biomolecule Hybrid Systems: Synthesis, Properties, and Applications, *Angew. Chem. Int. Ed.*, 2004, **43**, 6042-6108.
	X. Huang, P. K. Jain, I. H. El-Sayed and M. A. El-Sayed, Gold nanoparticles: Interesting optical properties and recent applications in cancer diagnostics and therapy, *Nanomedicine*, 2007, **2**, 681-693.
	C. J. Murphy, A. M. Gole, J. W. Stone, P. N. Sisco, A. M. Alkilany, E. C. Goldsmith and S. C. Baxter, Gold Nanoparticles in Biology: Beyond Toxicity to Cellular Imaging, *Acc. Chem. Res.*, 2008, **41**, 1721-1730.
	D. F. Moyano and V. M. Rotello, Nano Meets Biology: Structure and Function at the Nanoparticle Interface, *Langmuir*, 2011, **27** (17), 10376-10385.
bio-nanotechnology and nanomedicine	M. Hu, J. Chen, Z.-Y. Li, L. Au, G. V. Hartland, X. Li, M. Marquez and Y. Xia, Gold nanostructures: engineering their plasmonic properties for biomedical applications, *Chem. Soc. Rev.*, 2006, **35**, 1084-1094.
	E. Boisselier and D. Astruc, Gold nanoparticles in nanomedicine: preparations, imaging, diagnostics, therapies and toxicity, *Chem. Soc. Rev.*, 2009, **38**, 1759-1782.
	D. A. Giljohann, D. S. Seferos, W. L. Daniel, M. D. Massich, P. C. Patel and C. A. Mirkin, Gold Nanoparticles for Biology and Medicine, *Angew. Chem. Int. Ed.*, 2010, **49**, 3280-3294.
cancer nanotechnology	E. C. Dreaden, M. A. Mackey, X. Huang, B. Kang and M. A. El-Sayed, Beating cancer in multiple ways using nanogold, *Chem. Soc. Rev.*, 2011, **40**, 3391-3404.
clusters	A. C. Templeton, M. P. Wuelfing and R. W. Murray, Monolayer protected cluster molecules, *Acc. Chem. Res.*, 2000, **33**, 27-36.
	R. L. Whetten, M. N. Shafigullin, J. T. Khoury, T. G. Schaaff, I. Vezmar, M. M. Alvarez and A. Wilkinson, Crystal Structures of Molecular Gold Nanocrystal Arrays, *Acc. Chem. Res.*, 1999, **32**, 397-406.
drug delivery	P. Ghosh, G. Han, M. De, C. K. Kim and V. M. Rotello, Gold nanoparticles in delivery applications, *Adv. Drug Deliv. Rev.*, 2008, **60**, 1307-1315.
nano-biotechnology	C. M. Niemeyer, Nanoparticles, Proteins, and Nucleic Acids: Biotechnology Meets Materials Science, *Angew. Chem. Int. Ed.*, 2001, **40**, 4128-4158.
nanocages	S. E. Skrabalak, J. Chen, Y. Sun, X. Lu, L. Au, C. M. Cobley and Y. Xia, Gold Nanocages: Synthesis, Properties, and Applications, *Acc. Chem. Res.*, 2008, **41**, 1587-1595.
nanochemistry	R. Sardar, A. M. Funston, P. Mulvaney and R. W. Murray, Gold Nanoparticles: Past, Present, and Future, *Langmuir*, 2009, **25**, 13840-13851.
nanorods	J. Pérez-Juste, I. Pastoriza-Santos, L. M. Liz-Marzán and P. Mulvaney, Gold nanorods: Synthesis, characterization and applications, Coord. Chem. Rev., 2005, **249**, 1870-1901.
	A. Alekseeva, V. Bogatyrev, B. Khlebtsov, A. Mel'nikov, L. Dykman and N. Khlebtsov, Gold nanorods: Synthesis and optical properties, *Colloid J.*, 2006, **68**, 661-678.
	X. Huang, S. Neretina and M. A. El-Sayed, Gold Nanorods: From Synthesis and Properties to Biological and Biomedical Applications, *Adv. Mat.*, 2009, **21**, 4880-4910.
nanorods in medicine	A. M. Alkilany, L. B. Thompson, S. P. Boulos, P. N. Sisco and C. J. Murphy, Gold nanorods: Their potential for photothermal therapeutics and drug delivery, tempered by the complexity of their biological interactions, *Adv. Drug Deliv. Rev. (in press)*, 2011.
nanotechnology	M. C. Daniel and D. Astruc, Gold nanoparticles: assembly, supramolecular chemistry, quantum-size-related properties, and applications toward biology, catalysis, and nanotechnology, *Chem. Rev.*, 2004, **104**, 293-346.
pharmacokinetics	M. Longmire, P. L. Choyke and H. Kobayashi, Clearance properties of nano-sized particles and molecules as imaging agents: considerations and caveats, *Nanomedicine*, 2008, **3**, 703-717.
photochemistry	L. Brus, Noble Metal Nanocrystals: Plasmon Electron Transfer Photochemistry and Single-Molecule Raman Spectroscopy, *Acc. Chem. Res.*, 2008, **41**, 1742-1749.
photophysics	S. Link and M. A. El-Sayed, Shape and size dependence of radiative, non-radiative and photothermal properties of gold nanocrystals, *Int. Rev. Phys. Chem.*, 2000, **19**, 409-454.
	S. Eustis and M. A. El-Sayed, Why gold nanoparticles are more precious than pretty gold: Noble metal surface plasmon resonance and its enhancement of the radiative and nonradiative properties of nanocrystals of different shapes, *Chem. Soc. Rev.*, 2006, **35**, 209-217.
	G. V. Hartland, Optical Studies of Dynamics in Noble Metal Nanostructures, *Chem. Rev.*, 2011, **111**, 3858-3887.
photothermal therapy	S. Lal, S. E. Clare and N. J. Halas, Nanoshell-Enabled Photothermal Cancer Therapy: Impending Clinical Impact, *Acc. Chem. Res.*, 2008, **41**, 1842-1851.
plamonics	U. Kreibig and M. Vollmer, Optical properties of metal clusters, Springer, Berlin, 1995.
	C. F. Bohren and D. R. Huffman, Absorption and Scattering of Light by Small Particles, Wiley-VCH Verlag GmbH, Weinheim, 2007.
	K. L. Kelly, E. Coronado, L. L. Zhao and G. C. Schatz, The Optical Properties of Metal Nanoparticles: The Influence of Size, Shape, and Dielectric Environment, *J. Phys. Chem. B*, 2002, **107**, 668-677.
	H. Wang, D. W. Brandl, P. Nordlander and N. J. Halas, Plasmonic Nanostructures: Artificial Molecules, *Acc. Chem. Res.*, 2006, **40**, 53-62.
	S. A. Maier, Plasmonics: fundamentals and applications, Springer Verlag, New York, 2007.
purification and characterization	K. E. Sapsford, K. M. Tyner, B. J. Dair, J. R. Deschamps and I. L. Medintz, Analyzing Nanomaterial Bioconjugates: A Review of Current and Emerging Purification and Characterization Techniques, *Anal. Chem.*, 2011, **83**, 4453-4488.
self-assembly	M. Grzelczak, J. Vermant, E. M. Furst and L. M. Liz-Marzan, Directed Self-Assembly of Nanoparticles, *ACS Nano*, 2010, **4**, 3591-3605.
	L. M. Liz-Marzán, Tailoring Surface Plasmons through the Morphology and Assembly of Metal Nanoparticles, *Langmuir*, 2005, **22**, 32-41.
surface functionalization	J. C. Love, L. A. Estroff, J. K. Kriebel, R. G. Nuzzo and G. M. Whitesides, Self-Assembled Monolayers of Thiolates on Metals as a Form of Nanotechnology, *Chem. Rev.*, 2005, **105**, 1103-1170.
synthesis	M. Grzelczak, J. Perez-Juste, P. Mulvaney and L. M. Liz-Marzan, Shape control in gold nanoparticle synthesis, *Chem. Soc. Rev.*, 2008, **37**, 1783-1791.
toxicology	N. Lewinski, V. Colvin and R. Drezek, Cytotoxicity of Nanoparticles, *Small*, 2008, **4**, 26-49.
	A. Alkilany and C. Murphy, Toxicity and cellular uptake of gold nanoparticles: what we have learned so far?, *J. Nanopart. Res.*, 2010, **12**, 2313-2333.

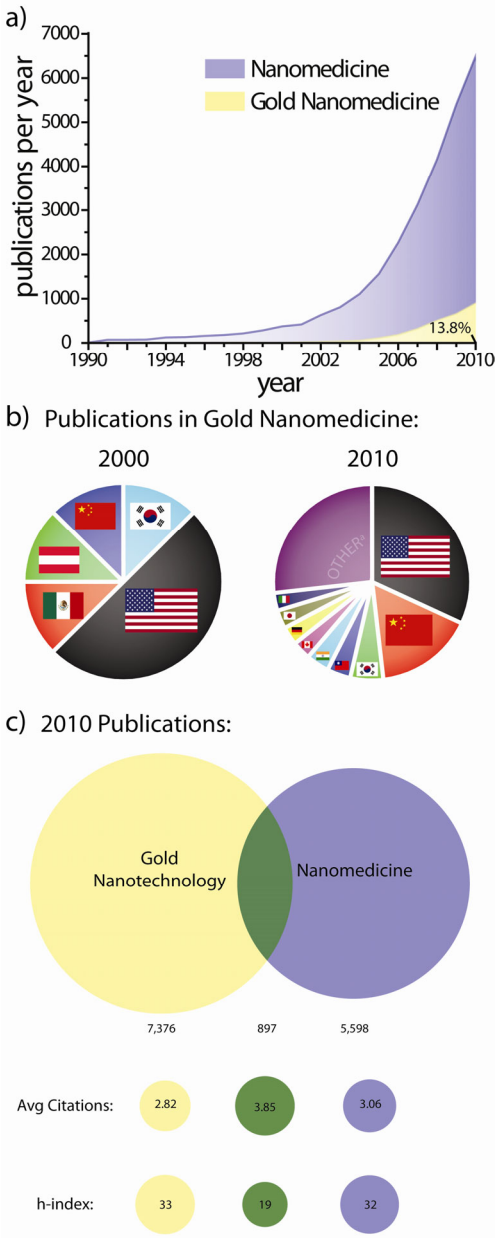

Figure 2.2. Exponential growth in the number of publications on gold nanotechnology and nanomedicine over the past two decades.[*74*] A) Annual publications in nanomedicine dramatically increased following award of the 1996 Nobel Prize in Chemistry to Kroto, Curl, and Smalley for their discovery of fullerenes. Medicinal applications of gold nanotechnologies further added to this growth following US President Bill Clinton's formation of the National Nanotechnology Infrastructure Network (NNIN) in 2000 and US President George H.W. Bush's expansion of the program in 2003 with the 21st Century Nanotechnology Research and Development Act. B) Contributions from various countries to publications on gold nanomedicine in 2000 and 2010. Publications in 2000 were limited to just 5 countries while those in 2010 included more than 50. [a]Other countries represent those with <2.9%. C) Overlap between publications on gold nanotechnology and nanomedicine in 2010 and comparison of their corresponding average number of citations and h-indices. Note that publication data in (A) is not cumulative. Adapted from Dreaden et al. [*2*].

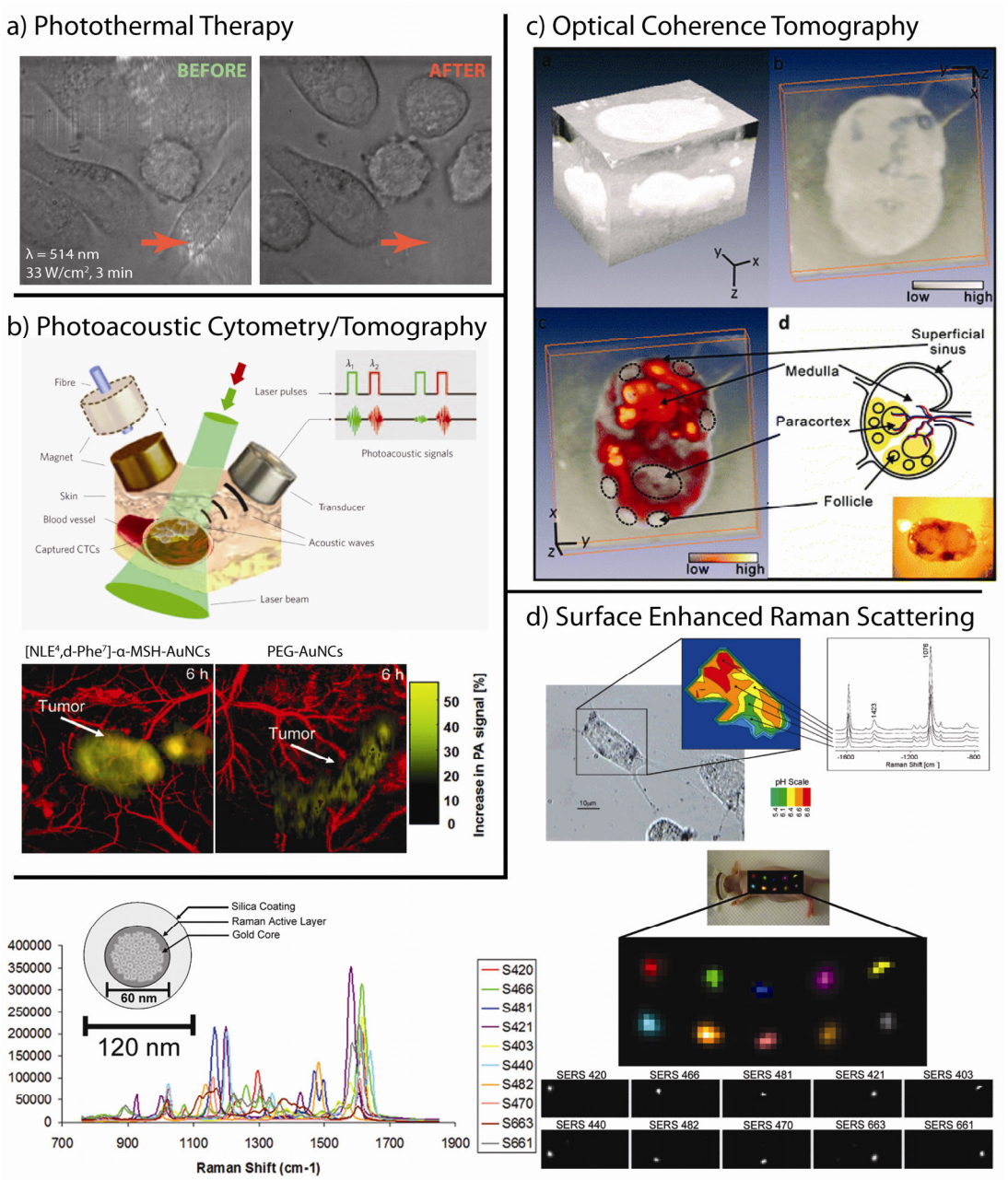

Figure 2.3. Properties of gold nanotechnologies that can be used to enhance therapeutic treatment and diagnostic imaging of cancer. A) Photothermal therapy: gold nanoparticles can serve as contrast agents for the selective laser photothermal ablation of tumor cells. Arrow indicates laser focus. Image obtained in collaboration with Prof. X. Huang (U of Memphis) and Prof. C.K. Payne (Georgia Tech). B) Photoacoustic cytometry/tomography: pulsed laser excitation of cells/tissues labeled with gold nanoparticles can be used to detect or sequester circulating tumor cells (CTCs, upper panel) or to non-invasively image/diagnose/stage tumors and guide surgical procedures (lower panel). C) Optical coherence tomography (OCT): the backscattering and photothermal properties of gold nanotechnologies can be used to enhance OCT contrast for monitoring disease metastasis to the lymphatic system. D) Surface enhanced Raman scattering (SERS): Electromagnetic near-field enhancements generated by gold nanoparticles can improve non-invasive in vitro (upper panel) and in vivo (lower panel) spectral cancer diagnostics. Adapted from Dreaden et al. [*75*].

The novel optical and electronic properties of gold nanoparticles are particularly attractive for use in multimodal drug delivery applications where these structures can afford enhanced drug pharmacokinetics/biodistribution (**Section 2.2**) and simultaneous hyperthermia,[*12,25,47,48,66,76*] and radiation therapy contrast,[*44,71,77-80*] as well as photo-imaging contrast,[*36,38,70,71,77,81-87*] spectrochemical diagnostic contrast,[*37,40,46,89-91*] and, when molecularly directed to specific sub-cellular sites, intrinsic pharmacodynamic [*2,12,88*] properties. The ability of these structures to act as photothermal therapeutic agents arises due to the delocalized nature of their free (conduction) electrons and the increasing polarizability of these charge carriers at the surfaces of these materials. These surface electrons exhibit collective modes of oscillation (surface plasmon modes) which vary in frequency depending on the size/shape of the nanoparticle and its dielectric environment.[*89*] Plasmon modes which result in a dipolar charge density distribution can couple with and resonantly absorb optical photons of the same frequency, resulting in a transient increase in the energy of these electrons equivalent to that of the photon (E_{Fermi}(Au) ca. -5.1 eV v. E_F^{VAC}) (**Table 2.3**) [*90*]. Plasmonic photothermal heat generation [*91*] can thus be simplified as a three step process: i) electron-electron coupling, ii) electron-phonon coupling, and iii) phonon-phonon coupling. Electron-electron coupling follows the energy absorption process, whereby the average (Fermi) energy of electrons in the nanoparticle is transiently increased for a few hundred femtoseconds. This increased electron energy decays via the coupled electronic and lattice heat capacities of the material (*i.e.* energy per unit temperature), resulting in a transient (ca. 1 ps) increase in the material's lattice temperature and thus, an increase in the volume of the nanoparticle. Volume expansion equilibrates through phonon "breathing" modes (phonon-phonon coupling) whereby coherent oscillations of the atomic lattice (phonon vibrations) dissipate energy, resulting in heat transfer to the surrounding media over several picoseconds. The extent of macroscopic heat generation depends on the incident

excitation power and the particle, but in most biomedical applications, photothermal heat generation often exceeds ΔT~20 °C [*2,12,46-49,67,76*].

Table 2.3. Useful physical parameters/relationships for plasmonic nanoparticles.

Photophysical parameter	Value	Reference
Bulk plasma (plasmon) frequency (ω_b)	Au: 1.30×10^{16} s^{-1}; Ag: 1.40×10^{16} s^{-1}	[*92*]
Spherical surface plasmon frequency (ω_{NP})	$\omega_b[\ell/(2\ell+1)]^{1/2}$	[*93*]
Cavity surface plasmon frequency (spherical, ω_C)	$\omega_b[(\ell+1)/(2\ell+1)]^{1/2}$	[*93*]

[a] ℓ = 1(dipole), 2(quadrupole),…; n.b. ℓ sometimes referred to as surface plasmon mode, order, symmetry, and/or angular momentum.

By changing the size/shape/surface of the gold nanoparticle, one can tune the wavelength of its plasmon absorption to coincide with spectral regions where the attenuation of photons by tissues and physiological fluids (*i.e.* water, oxy/deoxyhemoglobin, etc.) is minimal.[*12,94*] For example, in the near-infrared (NIR) window (ca. 650 – 900 nm; **Figure 2.4**), one can achieve upwards of 10 cm penetration depth through breast tissue even at low ($\mu W/cm^2$) laser power densities.[*2,12,95*] The local temperature increases attainable using plasmonic laser photothermal therapy (**Table 2.4**) are well sufficient to induce rapid tumor cell death (necrosis) with minimal damage to surrounding tissues. In milder, hyperthermic cases (ΔT~3-5 °C),[*96*] deleterious physiological responses such as cell membrane disruption, protein denaturation, metabolic signaling disruption, thrombosis, tumor ischemia, the induction of heat-shock proteins, signaling disruption, diminished membrane transport, and impaired DNA synthesis/repair can also lead to pro-apoptotoic responses in particle-labeled cells.[*97,98*] Other plasmonic metals include Li, Na, K, Mg, Al, Fe, Cu, Ag, and Pt.[*99*] Of these, gold is the only nanoscale metal which exhibits both inert reactivity and plasmon resonance which is red-shifted sufficient to avoid significant incident field attenuation by tissues and fluids in physiologically-relevant environments.

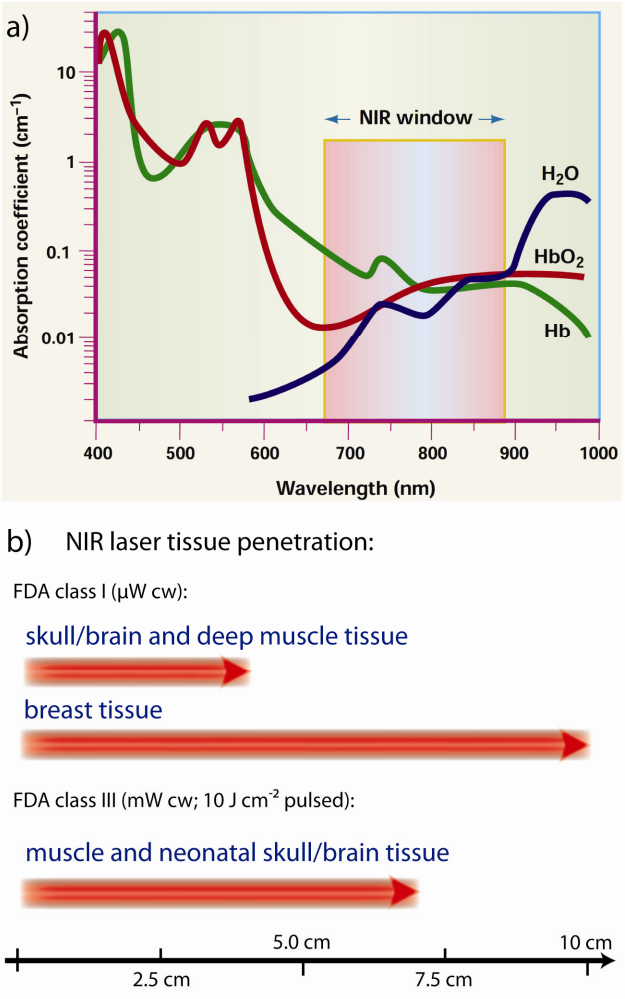

Figure 2.4. Wavelength range of the near-infrared (NIR) tissue transmission window. A) In the 650-900 nm spectral range, absorption from physiologic fluids such as oxy/deoxyhemoglobin and water is minimal, allowing (B) maximum penetration depths for external laser radiation. Photothermal therapy, photoacoustic tomography, and optical diagnostic imaging are most efficient in this range. Gold nanoparticle contrast agents are designed to optimally absorb in these regions. Adapted from Dreaden et al. [*12*].

Table 2.4. In vivo photothermal therapeutic studies using various gold nanoparticles. Adapted from Dreaden et al. [2].

gold nanoparticle class	particle size (nm)	targeting ligand	animal model: cancer type	admin. route	laser (λ, nm)	laser power (W/cm^2)	exposure time (min)	results
nanorods	AR=4	n/a; passive targeting with chitosan on surface	mice: squamous carcinoma (SCC7) tumors	i.v	808	41.5	4	20% of injected dose accumulated in tumor. Complete resorption of the tumor was achieved.
	33.7±3.5 X 9.1±1.4	n/a; passive targeting with PEGylated surface	mice: squamous carcinoma (SCC7) tumors	i.v	810	3.82	1	Second generation photosensitizer molecules were complexed to the surface of gold nanorods for dual therapy (photodynamic and plasmonic photothermal therapies). Dual therapy resulted in 95% reduction in tumor growth. Temperature at the tumor tissue reached 65 °C.
	50X12	n/a; passive targeting with PEGylated surface	mice: squamous cell carcinoma tumor	i.v & direct	808	1.7-1.9 (i.v.); 0.9-1.1 (direct)	10	Resorption of >57% of tumors treated with direct injection of nanoparticles to tumor site versus 25% of the intravenously-treated tumors.
	13X47	n/a; passive targeting with PEGylated surface	mice: MDA-MB-435 human tumors	i.v	810	2	5	Circulation $t_{1/2}$=17 hrs. 7% of injected dose in tumor site. Temprature at the tumor tissue reached 70 °C. Single i.v injection of gold nanorods coupled with laser irradiation eliminated all the induced tumor in mice.
gold/silica nanoshells	150	n/a; passive targeting with PEGylated surface	dogs: brain tumor	i.v	808	3.5	3	Temperature at the tumor tissue reached 56.8 °C
	130	n/a; passive targeting with PEGylated surface	mice: murine colon carcinoma cells	i.v	808	4	3	All treated animals were tumor-free without toxicity for more than 90 days after treatment.
	110±11	n/a; passive targeting with PEGylated surface	mice: Canine TVT cancer cells	i.v	820	4	<6	Average maximum Temperature at the tumor site reached ~70 °C. Irradiated tumor exhibited exhibited tissue damage
nanocages	48.0±3.5	n/a; passive targeting with PEGylated surface	athymic nude mice: U87MG glioma xenografts	i.v	808	0.7	10	Temperature at the tumor tissue reached 55 °C
gold/gold sulfide nanoshells	45 nm	n/a; passive targeting with PEGylated surface	BALBc mice: murine colon carcinoma cells	i.v	808	4	3	80% of tested mice survived with tumor free. Temperature at the tumor tissue reached 61 °C
hollow nanospheres	43.5±2.3	α-melanocyte-stimulating hormone analog and polyethylene glycol	mice: B16/F10 melanoma tumor	i.v	808	0.5	1	Nanoparticles were uptaken specifically by melanoma cells.12.9% of injected dose per organ weight, in tumor site.

Gold nanoparticles are also highly useful probes for microscopic imaging-based applications. For example, the resonant optical scattering intensity from a single 80 nm gold nanoparticle [*100*] is

equivalent to the emission intensity of 500,000 of the most efficient Alexa Fluor® dyes or 2,000 of the most efficient Qdot® 800 quantum dots.[*101*] While gold nanoparticles have been used for decades as labels in immunohistochemical and electron microscopic analysis of tissue sections,[*102*] Sokolov et al. first demonstrated in 2003 that the resonant scattering from gold nanoparticles could be used to image subcellular cancer biomarkers (EGFR) in vitro using confocal reflectance microscopy of immunolabeled gold nanoparticles (ca. 12 nm core diameter) for potential cancer diagnostics, staging, and treatment monitoring. Our labs have shown that simpler, less expensive, higher sensitivity cardioid dark-field optics can also be used to obtain high-contrast scattering images from immunolabeled gold nanoparticles in vitro, in this case in true-color, to achieve the identification and selective (photothermal) labeling of malignant cells.[*103,104*] Lin and coworkers first demonstrated the use of plasmonic nanoparticles (gold nanoparticles) for in vitro photothermal therapy in 2003, using 30 nm gold nanospheres conjugated with IgG antibodies for CD8 to label lymphocyte cells. Following exposure to a nanosecond pulse visible laser, 95% of cells treated with the gold nanospheres were killed.[*105*] Hirsch et al. first demonstrated the use of plasmonic nanoparticles for in vivo laser photothermal therapy in the same year, showing that interstitially-injected PEGylated gold nanoshells could selectively and efficiently ablate xenograft tumors in mice locally irradiated with a near-infrared laser.[*49*] Dickerson et al. were the first to demonstrate the use of increasingly efficient PEGylated gold nanorods in analogous therapeutic in vivo applications (**See Chapter 3**).[*46*] Bahatia and coworkers later showed that the intrinsic x-ray absorbing properties of gold nanorods (doubly greater than that of clinical iodine standards) can be used to guide NIR PTT and increase treatment efficacy.[*48*] Using x-ray computed tomography (CT) and contrast from tumor-accumulated gold nanorods, they were able to non-invasively image and three-dimensionally reconstruct tumor xenograft margins in mice models. Subsequent NIR PTT achieved complete

tumor resorption and 100% survival of the nanoparticle treated group, while tumors in sham-treated and control groups grew uncontrolled with ≤ 1 month survival (0.75 W cm^{-2}, 1 min, 1 cm spot dia).

In 2007, Xia and co-workers first demonstrated the use of gold nanocages for contrast in in vitro NIR PTT.[*106*] Nanocages conjugated to antibodies to human epidermal growth factor receptor 2 (anti-HER2) were used to selectively target breast cancer cells overexpressing cell surface HER2. Cell destruction using NIR laser exposure was observed at a minimum power density of 1.5 W cm^{-2} (5 min, 2 mm spot dia). The group later showed that intravenous (iv) administration of PEGylated gold nanocages and subsequent NIR laser exposure (λ~808 nm; 0.7 W cm^{-2}, 10 min) could significantly decreased (-70%) tumor metabolic activity as measured by ^{18}F-fluorodeoxyglucose positron emission tomography (^{18}F-FDG PET).[*47*] The nanocages exhibited ca. 5.7 % accumulation of the initial dose (g^{-1} tissue) at the tumor site with histologically verified tumor necrosis following laser exposure. Using similarly synthesized hollow-core, spherical gold nanoparticles, Li and coworkers have studied in vitro NIR PTT using anti-EGFR conjugates of the hollow gold nanoparticles, as well as their in vivo biodistribution following iv administration.[*107*] EGFR-overexpressing squamous cell carcinoma cells were found to be selectively labeled and photothermally destroyed following cw NIR laser exposure (40 W cm^{-2}, 5 min, 2 mm spot dia). Intravenous administration in tumor bearing nude mice resulted in predominant RES organ (*i.e.* liver, spleen, and kidney) accumulation. Tumor accumulation was found to be as high as 6.5% of the initial dose with predominant perivascular localization. Targeted NIR PTT of melanoma tumors using hollow gold nanoparticles was further studied in animal models by the same group using an agonist ligand of melanocortin type-1 receptor, overexpressed by melanoma cells.[*108*] Biodistribution studies following 24 h of intravenous circulation found significantly enhanced tumor accumulation by the active targeting strategy (13 v. 5 % initial dose g^{-1} tissue). Histological analysis

following NIR laser exposure determined significantly enhanced necrotic response from nanoparticle treated tumors (66% v. 8% sham, 0.5 W cm^{-2}, 1 min, 1 cm spot dia). PET imaging also indicated dramatically decreased (-89%) metabolic activity in nanoparticle treated tissues, but not in sham or control tumors. Xia and Wang have further demonstrated that the NIR absorption properties of nanocages and other plasmonic gold nanoparticles can be used to non-invasively image tumors for surgical or PTT guidance, as well as to assess the stage and location of primary melanoma tumors *in vivo* by photoacoustic tomographic imaging (**Figure 2.3B**).[*68*] Also using a ligand of melanocortin type-1 receptor, they showed that systemically administered nanocages can be preferentially targeted to melanoma tumors, allowing ca. 40% increased imaging contrast and actively-targeted tumor accumulation.

Determining the optimal gold nanostructure for NIR photothermal therapy (PTT) can be highly subjective due to the numerous ways in which such analyses can be performed. Structures can be compared based on their absorption cross sections, absorption efficiencies, or thermal transduction efficiencies on a per particle, per unit gold, per unit mass, or per unit extinction basis. Gold nanorods have been shown to exhibit much larger and narrower NIR absorption cross sections and efficiencies than either nanoshells or nanocages.[*109,110*] Experiments comparing NIR thermal transduction from solutions of equivalent optical density (*i.e.* extinction) found gold nanorods and AuS_2-Au nanoshells to be much more efficient photothermal contrast agents than SiO_2-Au nanoshells.[*110*] Per unit mass gold, nanorods have exhibited 1/3 the spectral bandwidth, *ca.* 3-fold higher extinction cross section, and 6 times greater heating capability than SiO_2-Au nanoshells in NIR laser photothermal experiments.[*48*]

One notable advantage for the use of PEGylated gold nanotechnologies in the clinic is their classification by the US FDA as a “medical device” in photothermal therapy applications, allowing for

substantially accelerated and less costly approval processes. Human pilot studies exploring the use of iv-administered PEGylated silica-gold core-shell nanoparticles for NIR laser photothermal ablation of recurrent and/or refractory head and neck tumors are currently ongoing in the US (NCT00848042; Nanospectra Biosciences, Inc.), with ongoing human pilot studies investigating the use of this technology for the treatment of primary prostate cancer in Mexico. Both studies are scheduled to be completed in the middle of this year. Because gold nanoparticles are comprised of a high atomic number (*i.e.* high-Z) element, they have also been shown to substantially to improve the efficacy of radiotherapy treatments via tumor-localized photoelectron and Auger electron ejection, which can damage the DNA of tumor cells in the local surrounding tissue.[*44*] Although hyperthermia is known to synergize with radiotherapy treatments, [*111*] reports of multimodal plasmonic laser photothermal therapy and high-Z enhanced radiotherapy using gold (and other plasmonic) nanoparticles has yet to be explored.

2.2 Pharmacokinetics, Biodistribution, and Cellular Uptake of Gold Nanoparticles

One of the earliest reports involving the use of gold nanoparticles in drug delivery applications came in 1954, when Root et al. investigated the clinical use of colloidal Au^{198} particles for radiotherapy treatment of liver cancer and leukemia, both with minimal success.[*112*] For the next 47 years, examples of peer-reviewed scientific studies involving biomedical applications of colloidal gold were scant at best. In 2001, Paciotti and Tamarkin began research studying the use of gold nanoparticles as a platform for the delivery of tumor necrosis factor α (TNFα) to solid tumor models in mice.[*113,114*] Subsequent Phase I clinical trials found that the PEGylated 27 nm (TEM diameter) gold nanoparticles were well tolerated in patients and able to safely deliver TNFα at dosages 3-fold higher than the previously reported maximum tolerable dose for the lone drug with no serious adverse side effects; Phase II trials are currently pending.[*115*]

Malignant cells require increasing amounts of nutrients in order to sustain their accelerated growth and division. To meet this demand, solid tumors stimulate the production of new vasculatures through which increasing amounts of blood can be supplied (i.e. angiogenesis). In contrast to normal vessels, the angiogenic neovasculature is characterized by a highly disordered endothelium with large gaps that permit the preferential penetration of nanosized conjugates (**Figure 2.5,6A**). Characteristically diminished lymphatic drainage from the tumor interstitium also serves to increase retention of such compounds at the tumor site, resulting in both augmented penetration and decreased clearance of circulating nanoconjugates. The EPR effect has been demonstrated using a variety of protein/DNA/polymer complexes, as well as nanoparticles including micelles, liposomes, metal nanostructures, and quantum dots.[*11*] As one would expect, the optimal size for EPR of a gold nanoparticle conjugate varies depending on the stage, location, and type of cancer, however non-deformable particles with a hydrodynamic diameter (HD) greater than the renal clearance threshold (ca. 6 nm HD, anionic; 6-8 nm, cationic [*116*]) and up to the 200 nm HD splenic clearance threshold [*116*] can be expected to exhibit preferential tumor accumulation. Although efficient renal (urinary) clearance is sometimes desirable, readers may note that polycationic nanoparticles can exhibit poor circulatory half lives due to electrostatic attraction with the negatively charged laminar surfaces of the blood vessels. Polyanionic nanoparticles, on the other hand, often exhibit decreased cell penetration due to electrostatic cell-surface repulsion. Nanoparticle opsonization and phagocytic uptake is typically lowest when particles are neutral in zeta potential and contain hydrophilic polymers which shield hydrophobic-hydrophobic and/or electrostatic interactions with IgG and serum proteins.[*117*] In contrast to orally administered drugs which optimally exhibit high lipophilicity (Log *P* ~ 3-5), optimal lipophilicity of a therapeutic nanoparticle

conjugate can be expected to lie over a range similar to iv administered drugs (median Log *P* ~ 1.92).[*118*]

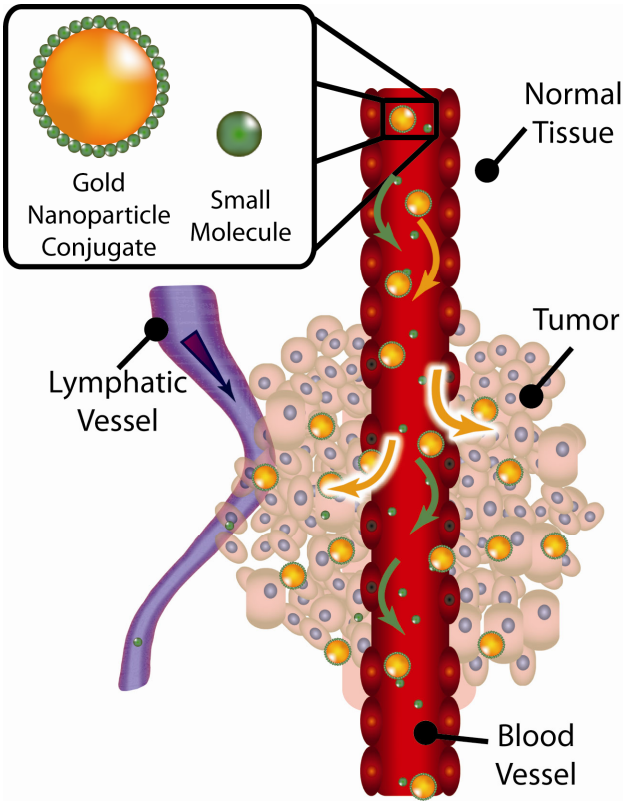

Figure 2.5. Graphic illustrating the size-selective preferential accumulation of circulating gold nanoparticle conjugates at tumor sites by the enhanced permeability and retention (EPR) effect. Large gold nanoparticle conjugates preferentially penetrate through blood vessels at tumor sites due to their disordered endothelial cells, while smaller molecules continue to circulate. Diminished lymphatic drainage at the tumor site also serves to reduce the clearance of these gold nanoparticle conjugates from the tumor interstitium. Adapted from Dreaden et al. [*12*].

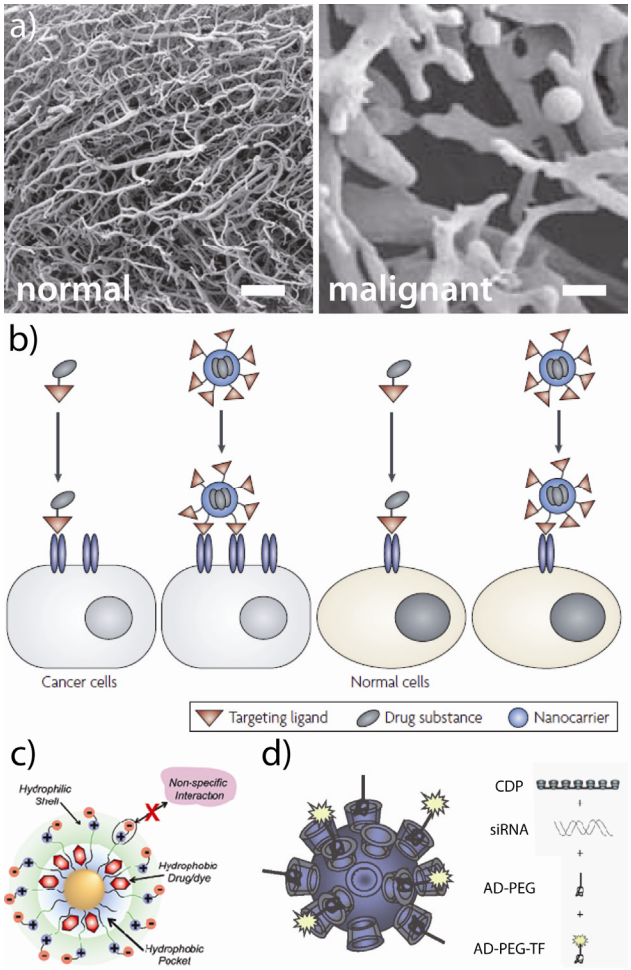

Figure 2.6. Properties of nanoscale technologies that can be leveraged to enhance the diagnosis and treatment of solid tumors. A) The EPR effect: Polymer cast replicas of blood vessels in normal (left) and malignant tissues (right) illustrate why high molecular weight compounds (i.e. nanoparticles) can preferentially accumulate at tumor sites supplied by disordered vasculatures. B) Multivalent avidity: unlike monovalent ligands, nanoscale constructs can simultaneously bind multiple adjacent receptors to augment uptake/selectivity. C,D) Enhanced stability: nanoscale carriers can enhance the solubility, circulatory half lives, biodistribution, and intracellular penetration of water-insoluble chemotherapeutics and proteins/nucleic acids (e.g. siRNA) which are susceptible to enzymatic degradation and subject to poor intracellular penetration rates. Scale bars represent 100 μm. Adapted from Dreaden et al. [*75*].

Numerous size-dependent blood half-lives and biodistribution profiles for spherical and rod-shaped gold nanoparticles have been reported. De Jong and coworkers detected gold nanoparticles, by inductively coupled plasma mass spectrometry (ICP-MS) in the blood, liver, spleen, lungs, kidneys, testis, thymus, heart and brain after iv administration in male rats with 10, 50, 100 and 250

nm spherical citrate-gold nanoparticles.[*119*] The highest amount of gold was detected in the blood, liver and spleen (24 h post-injection) with lower amounts in the lungs, kidneys, testis, thymus, heart and brain. 10 nm gold nanoparticles were the most widespread through different organs, with the highest gold content in the liver, and to a lesser extent, in the spleen. After 24 h, liver accumulation (%ID g^{-1} tissue) was found to be 46%, 21%, 44%, and 31% for 10, 50, 100 and 250 nm gold nanoparticles, respectively and 2.2%, 1.3%, 1.4%, and 1.2%., respectively, in the spleen. In contrast, Terentyuk et al. observed opposing trends using gold nanoparticles functionalized with poly(ethylene glycol) (PEG).[*120*] Following tail vein injection in white rats, the accumulation of gold in the liver and spleen was found to decrease with decreasing nanoparticle size from (50 to 15 nm), with 15 nm PEG-gold nanoparticles exhibiting the greatest blood residence times. Passively- (EPR-) targeted gold nanospheres have exhibited as much as 2 %ID g^{-1} and 5 %ID tumor accumulation in murine xenograft models (%ID g^{-1}, % initial dose per gram tissue);[*108,121*] actively-targeted gold nanoparticles have likewise exhibited upwards of 6-13 %ID g^{-1} tumor accumulation following systemic administration.[*107,108,121*]

It is apparent from the conflicting trends reported in the literature that systematic examinations of pharmacokinetic and biodistribution profiles for different nanoparticle sizes and surface chemistries is warranted. Chan and coworkers have performed a comprehensive examination of blood pharmacokinetics and biodistribution profiles for gold nanoparticles 25-119 nm in hydrodynamic diameter (HD), coated with varying molecular weights of PEG.[*122*] Decreasing nanoparticle size and increasing PEG molecular weight was found to increase the blood half-life of these nanoparticles following iv administration in CD1 mice (**Figure 2.7**). All nanoparticles exhibited increasing accumulation in the liver and spleen over time with greater apparent filtering capacity demonstrated by the spleen (%ID g^{-1} tissue). Passive tumor accumulation at subcutaneous

MDA-MB-435 xenografts following iv injection of the PEGylated gold nanospheres was found to be greatest for 61 nm HD PEGylated (5 kDa) gold nanoparticles with trends following: 61 > 83 > 99 > 40 > 22 nm HD at 24 h. Accumulation in the spleen and liver (24 h, %ID g^{-1}) likewise peaked for 61 nm HD particles. Size-dependent permeation of the tumor interstitium was evaluated after 8 h circulation of PEGylated nanoparticles, revealing decreasing intratumoral penetration with increasing nanoparticle size. 61 nm HD PEGylated gold nanoparticles (ca. 32-45 nm physical diameter with 5 kDa PEG) exhibited optimal blood half-life and tumor accumulation profiles with tumor accumulation, MPS biodistribution, and blood half life comparable for increasing PEG molecular weight. Due to their less optimal intratumoral penetration characteristics and relatively high MPS/RES organ uptake, administration of a combination of 61 nm HD PEGylated gold nanoparticles and sizes below may be well suited for future therapeutic applications.

(a)

	core diameter (nm) (±SD)	mPEG weight (Da)	hydrodynamic diameter (nm)	blood half-Life (h)	tumor AUC (particle mass (ug)·h/g)	tumor AUC (% ID·h/g)
particle set A	17.72 (1.47)	2000	25.2	4.0		
		5000	34.8	29.7		
		10000	63.5	51.1		
	31.28 (4.83)	2000	42.8	2.4		
		5000	62.6	19.3		
		10000	77.5	22.7		
	45.03 (4.83)	2000	53.8	0.4		
		5000	60.4	14.1		
		10000	83.9	16.1		
	66.54 (5.69)	2000	75.7	1.0		
		5000	85.6	9.2		
		10000	105.8	11.3		
	86.73 (7.74)	5000	105.4	3.3		
		10000	118.9	6.6		
particle set B	16.6 (1.80)	2000	22.4	2.5	0.45	0.3
	22.6 (2.68)	2000	39.6	4.0	18.89	15.8
	32.5 (5.16)	5000	61.3	16.5	39.05	26.5
	43.3 (5.08)	10000	82.6	11.6	39.33	20.4
	83.5 (8.29)	10000	99.4	7.2	170.42	17.9

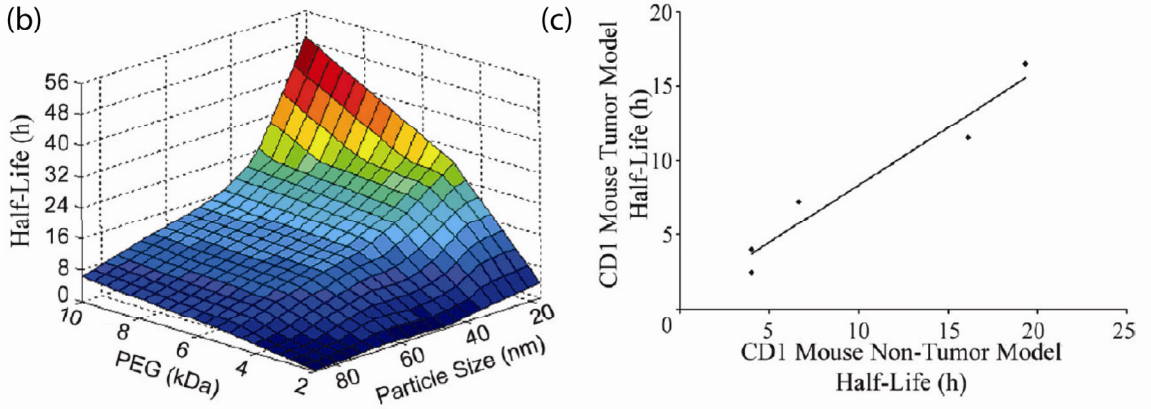

Figure 2.7. Pharmacokinetics of PEGylated gold nanoparticles. A) Relationship between circulatory half live, hydrodynamic diameter, and tumor accumulation for spherical gold nanoparticles of varying size and thiolated poly(ethylene glycol) (PEG) surface stabilizer molecular weight. B) Graph illustrating that circulatory half lives of PEGylated gold nanospheres is inversely proportional to particle size and PEG molecular weight (for particles >16 nm physical diameter). C) Graph illustrating similar pharmacokinetics of PEGylated gold nanoparticles in tumor-bearing and non-tumor-bearing mouse models. Adapted from Dreaden et al. [*1*].

The biodistribution profiles of rod-shaped gold nanoparticles are also of current interest as these structures have shown potential in drug and/or gene delivery applications [*123-126*] and photothermal therapy [*2,12,46-49,67,76*]. Systemically-administered, gold nanorods (55 x 13 nm) with no polymer functionalization have exhibited sustained circulation in the blood of Sprague-Dawley rats over periods as long as 14 days.[*127*] Accumulation in RES organs was observed with a plateau in gold nanorod accumulation in the liver at 1 d circulation. Retention in the liver over 28 d was also found, suggesting diminished capacity for hepatobiliary clearance/excretion of CTAB-

capped gold nanorods. Splenic accumulation exhibited a gradual increase over this time period, with lung, kidney, heart, brain, bone, and muscle accumulation likewise decreasing. CTAB-gold nanorods were observed by transmission electron microscopy (TEM) in the lysosomes of both the spleen and liver. Fecal excretion suggested some capacity for hepatobiliary clearance of these size gold nanorods, however due to their lack of adequate polymer stabilization, these results may not reflect those observable with PEGylated gold nanorods. Upon coating 65 x 11 nm gold nanorods with PEG, Niidome and coworkers observed no accumulation in major organs, with the exception of the liver, 72 h post injection. Here, PEGylation imparted dramatic improvements to both the pharmacokinetics and biodistribution profiles of systemically administered gold nanorods. Bhatia and coworkers found that PEGylated gold nanorods (5 kDa PEG-SH) can exhibit up to 17 h blood half life in nude mice with ca. 7 %ID g^{-1} tumor accumulation after 72 h.[*48*] Huang et al. have explored the active targeting of PEGylated gold nanorods by i) a single-chain variable fragment (ScFv) peptide that recognizes the epidermal growth factor receptor (EGFR), ii) an amino terminal fragment (ATF) peptide that recognizes the urokinase plasminogen activator receptor (uPAR), and iii) a cyclic RGD peptide that recognizes the a_vb_3 integrin receptor were also performed (hydrodynamic diameter 68-81 nm, zeta potential -5 to -25 mV).[*128*] As anticipated, active targeting was found to significantly improve the cellular accumulation of these nanoconjugates in vitro (A549 lung cancer cells); the blood half life of the PEGylated gold nanorods however, was reduced by 25 - 48% upon co-conjugation with these active targeting ligands and the tumor accumulation (24 h) of ATF- and ScFV anti-EGFR-targeted gold nanorods was enhanced ca. 67 and 46% relative to passively targeted PEGylated gold nanorods administered in mice models. Surprisingly, the tumor accumulation of cyclic RGD-targeted gold nanorods was significantly diminished (ca. -57 % relative to PEGylated gold nanorods), suggesting that laser photothermal therapy using this specific formulation may be

best suited to intratumoral injection schemes. Like other nanoparticles, the blood half life of PEGylated gold nanorods generally increases with PEG grafting density [*129*] and/or PEG molecular weight, both of which can augment subsequent passive tumor accumulation.

Although most gold nanoparticle conjugates are capable of exhibiting some degree of passive biodistribution, particle size, charge, and lipohilicity also play critical roles in determining the extent of cellular uptake once accumulated at a particular location. Chan and coworkers have studied the size-dependent cellular uptake of citrate-capped gold nanoparticles into cervical cancer cells (HeLa) and found that size-dependent internalization peaked at 50 nm (TEM diameter).[*130*] In another study using immunoglobulin G (IgG) antibody-gold nanoparticle conjugates, they found that ca. 40 nm (TEM diameter) particles conjugated to antibodies to human epidermal growth factor receptor 2 (anti-HER2; Herceptin®) exhibited the greatest uptake into breast cancer cells (SK-BR-3) and elicited the greatest therapeutic response (**Figure 2.8**).[*131*] Multivalent functionalization of smaller gold nanoparticles (ca. 2 nm TEM diameter) resulted in inefficient uptake due to the decreased ability of these small particles to occupy multiple receptor binding sites. Larger nanoparticles (ca. 70 nm TEM diameter), although capable of avid receptor binding, were too large to allow efficient membrane wrapping necessary for endocytotic uptake. Although the optimal particle size for intracellular penetration obviously varies depending on the cell size, type, receptor density, metabolic activity, etc., as well as the specific targeting strategy employed (i.e. IgG, fragments thereof, etc.), this study nonetheless highlights the importance of therapeutic nanoconjugate size in determining subsequent intracellular transport kinetics and anticipated treatment efficacy. Cationic zeta potential (i.e. positive surface charge) can also promote the uptake of nanoconjugates due to electrostatic attraction with anionic cell-surface proteoglycans. In some cases however, this attraction can result in significant cytotoxicity due to membrane disruption. Lipophilicity, as measured by octanol:water

partition coefficient (Log *P*) further promotes nanoparticle-cellular interaction and uptake by association with hydrophobic cell-surface and extracellular matrix domains. Due to poor aqueous stability and low circulatory half life however, highly lipophilic gold nanoparticles are typically co-conjugated with hydrophilic polymer stabilizers such as PEG.

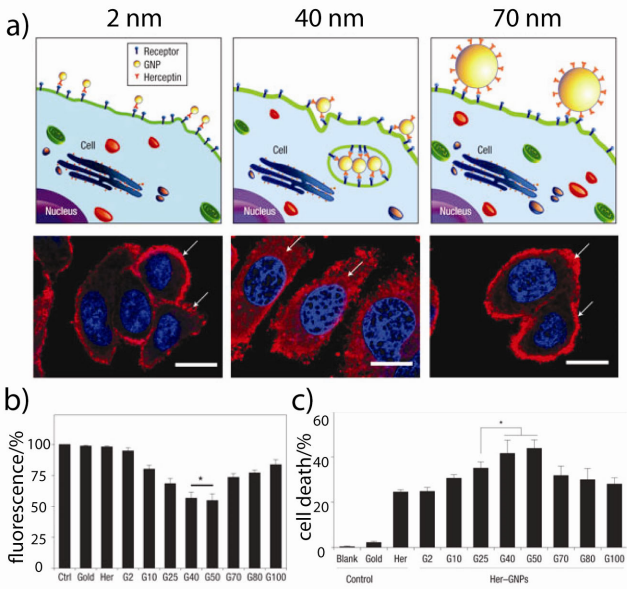

Figure 2.8. Size-dependent receptor-mediated endocytosis of antibody-gold nanoparticle conjugates. A) Schematic illustrating how nanoconjugate size and receptor density affect HER2-mediated uptake of herceptin-labeled gold nanoparticles into SK-BR-3 breast cancer cells. 2 nm gold nanoparticles were not efficiently internalized because multiple receptors could not be simultaneously bound. 70 nm particles exhibited multivalent binding; however they were too large for efficient membrane wrapping (i.e. endocytosis). B) Increased relative fluorescence intensity associated with nanoparticle uptake was found to correlate well with (C) subsequent therapeutic response. Nuclei are stained blue, scale bar = 10 μm, *$p < 0.05$, error bars ± SD, n = 4. Adapted from Dreaden et al. [*12*].

Given their utility in drug delivery and photothermal therapy, one might reasonably question whether gold nanospheres or nanorods are preferable for biomedical targeting/delivery. Although rod-shaped nanoparticles exhibit greater in vivo transvascular flux relative to spherical particles of equivalent hydrodynamic diameter [*132*], these particles have also exhibited diminished cellular uptake in vitro.[*132*] Fukumura, Bawendi, and Jain have examined the transmembrane

permeability, gel diffusivity, and transvascular flux of PEGylated semiconductor nanoparticles and nanorods of equivalent (33-35 nm) HD. They found that in all cases, nanorods exhibited optimal (per particle) transport properties and 4.1 times more rapid transvascular penetration, the latter presumed to be due to reduced steric hindrance from and viscous drag near vessel pore walls. Chan and coworkers have found that citrate-gold nanospheres (14 and 74 nm TEM diameter) exhibit higher intracellular accumulation (per particle) in HeLa cervical carcinoma cells than either 14×40 or 14×74 nm gold nanorods, with 50 nm spheres exhibiting the highest accumulation among a range of sizes/shapes. Readers may note however, that direct comparison between non-PEGylated gold nanospheres and nanorods can be difficult given the surface ligands present during their synthesis and the extent to which they can be exchanged and/or conjugated to match one another's physiochemical properties.

2.3 Challenges, Outlook, and Conclusions

While tremendous advances in the clinical translation of therapeutic gold nanotechnologies have been forged over the past decade, there remains a substantial body of work yet to be performed in order to realize broad acceptance of these platforms as first-line treatment modalities. One area of particularly pressing concern is the potential toxicity of these constructs and their unintended impacts on human health. In order to meet this urgent need, the National Institute of Standards and Technology (NIST), the U.S. Food and Drug Administration (FDA), the National Cancer Institute (NCI) have established the Nanotechnology Characterization Laboratory (NCL) to aid researchers in the regulatory review, preclinical testing/evaluation, and eventual translation of nanotechnologies intended for cancer therapies and diagnostics. While critically important in the near-term, clinical translation would also benefit from longer-term studies investigating potential deleterious effects from chronic inflammation [*133*] associated with diminished clearance of these particle constructs,

potential mutagenicity, and effects on reproductive health. Researchers in the field may also be better served to dispel many common misconceptions about gold nanoparticles, such as i) their presumed high cost of production, ii) the notion that humans have not been exposed to these materials until recent years, and iii) the perception that the avidity or efficacy of multivalent gold nanoparticles should not be directly compared with their monovalent molecular counterparts. As just three examples: i) the gold content present in a full-course dosage of TNF α-gold nanoparticles recently administered in a Phase I clinical trial (NCT00356980; CytImmune Sciences, Inc.) [*115*] currently costs less than 12¢ per patient and the quantity of gold salt used to produce the nanorods administered in Dickerson et al. [*46*] currently costs less than 23¢ per mouse.[*134*] In comparison, CHO cell–based manufacturing of biologics costs roughly $150 per gram (e.g. Amgen, Genentech [*135*]), while the price of gold and ionic its salts is roughly $50 per gram Au. ii) Contrary to popular belief, recent studies indicate that nanoscale silver particles can readily leach from both Ag nanoparticles and bulk Ag earrings over the course of just weeks,[*136*] suggesting that human exposure to noble metal nanoparticles may date as far back as the advent of modern currency. iii) While it is understandable that some may argue that binding affinity and/or drug potency of a multivalent nanoparticle should be compared on a per-ligand or per-drug molecule basis, such contentions appear to ignore efficacy. It would seem illogical for an oncologist to discount the effectiveness of cisplatin or Avastin® simply because they bear two distinct binding sites. Areas of research, such as high-throughput gold nanoconjugate synthesis/screening, low-cost models to predict excretion, and larger-scale in vivo characterization to allow direct side-by-side comparison of these constructs are currently underexplored and greatly needed. Going forward, one of the biggest challenges to systemically-deliverable gold nanotechnologies will be mass balance – that is – the demonstration of efficient clearance/excretion and accounting for the subsequent

accumulation/excretion of every μg of these drugs that are administered. Some areas of particular optimism include laser photothermal therapy for tumors in poorly accessible regions or those near vital organs/tissues (e.g. vocal cords, nerves, etc.), high-Z enhanced radiation therapy, isolated limb perfusion techniques, and intraoperative ablation of tumor margins. Given these challenges, those in the field should be mindful that although therapeutic gold nanotechnologies may have advanced quite rapidly into the clinic since their first proposed viable applications in biomedicine just 11 years ago,[*114*] compared with liposomal and monoclonal antibody technologies which took nearly 30 years since their first description as potential therapeutic agents to receive FDA approval (**See Table 2.1**), the field still has tremendous room for growth and further exploration of the new and exciting properties/functionality yet to be discovered and clinically applied.

2.4 References

1. Dreaden, E. C., Austin, L. A., Mackey, M. A., & El-Sayed, M. A. Size Matters: Gold Nanoparticles in Targeted Cancer Drug Delivery. *Ther. Delivery (in press)* (2012).

2. Dreaden, E. C., Alkilany, A. M., Huang, X., Murphy, C. J., & El-Sayed, M. A. The Golden Age: Gold Nanoparticles for Biomedicine. *Chem. Soc. Rev. (in press)* (2012).

3. Jemal, A., Siegel, R., Xu, J., & Ward, E. Cancer Statistics, 2010. *CA Cancer J. Clin.* **60**, 277-300 (2010).

4. *Surveillance Epidemiology and End Results (SEER) Database (2005-2007). US National Cancer Institute*, http://seer.cancer.gov).

5. Knop, K., Hoogenboom, R., Fischer, D., & Schubert, U. S. Poly(ethylene glycol) in Drug Delivery: Pros and Cons as Well as Potential Alternatives. *Angew. Chem. Int. Ed.* **49**, 6288-6308 (2010).

6. Peer, D., Karp, J. M., Hong, S., Farokhzad, O. C., Margalit, R., & Langer, R. Nanocarriers as an emerging platform for cancer therapy. *Nat. Nanotechnol.* **2**, 751-760 (2007).

7. Davis, M. E., Chen, Z., & Shin, D. M. Nanoparticle therapeutics: an emerging treatment modality for cancer. *Nat. Rev. Drug Discov.* **7**, 771-782 (2008).

8. Shi, J., Votruba, A. R., Farokhzad, O. C., & Langer, R. Nanotechnology in Drug Delivery and Tissue Engineering: From Discovery to Applications. *Nano Lett.* **10**, 3223-3230 (2010).

9. Petros, R. A., & DeSimone, J. M. Strategies in the design of nanoparticles for therapeutic applications. *Nat. Rev. Drug Discov.* **9**, 615-627 (2010).

10. Kim, B. Y. S., Rutka, J. T., & Chan, W. C. W. Nanomedicine. *New Engl. J. Med.* **363**, 2434-2443 (2010).

11. Jain, R. K., & Stylianopoulos, T. Delivering nanomedicine to solid tumors. *Nat. Rev. Clin. Oncol.* **7**, 653-664 (2010).

12. Dreaden, E. C., Mackey, M. A., Huang, X., Kang, B., & El-Sayed, M. A. Beating cancer in multiple ways using nanogold. *Chem. Soc. Rev.* **40**, 3391-3404 (2011).

13. Torchilin, V. P., & Lukyanov, A. N. Peptide and protein drug delivery to and into tumors: challenges and solutions. *Drug Discovery Today* **8**, 259-266 (2003).

14. Bae, Y., & Kataoka, K. Intelligent polymeric micelles from functional poly(ethylene glycol)-poly(amino acid) block copolymers. *Adv. Drug Del. Rev.* **61**, 768-784 (2009).

15. Oerlemans, C., Bult, W., Bos, M., Storm, G., Nijsen, J. F. W., & Hennink, W. E. Polymeric Micelles in Anticancer Therapy: Targeting, Imaging and Triggered Release. *Pharm. Res.* **27**, 2569-2589 (2010).

16. Lukyanov, A. N., & Torchilin, V. P. Micelles from lipid derivatives of water-soluble polymers as delivery systems for poorly soluble drugs. *Adv. Drug Del. Rev.* **56**, 1273-1289 (2004).

17. Zhang, L., Chan, J. M., Gu, F. X., Rhee, J.-W., Wang, A. Z., Radovic-Moreno, A. F., Alexis, F., Langer, R., & Farokhzad, O. C. Self-Assembled Lipid–Polymer Hybrid Nanoparticles: A Robust Drug Delivery Platform. *ACS Nano* **2**, 1696-1702 (2008).

18. Torchilin, V. P. Recent advances with liposomes as pharmaceutical carriers. *Nat. Rev. Drug Discov.* **4**, 145-160 (2005).

19. Kaasgaard, T., & Andresen, T. L. Liposomal cancer therapy: exploiting tumor characteristics. *Expert Opin. Drug Deliv.* **7**, 225-243 (2010).

20. Astruc, D., Boisselier, E., & Ornelas, C. Dendrimers Designed for Functions: From Physical, Photophysical, and Supramolecular Properties to Applications in Sensing, Catalysis, Molecular Electronics, Photonics, and Nanomedicine. *Chem. Rev.* **110**, 1857-1959 (2010).

21. Medina, S. H., & El-Sayed, M. E. H. Dendrimers as Carriers for Delivery of Chemotherapeutic Agents. *Chem. Rev.* **109**, 3141-3157 (2009).

22. Mintzer, M. A., & Grinstaff, M. W. Biomedical applications of dendrimers: a tutorial. *Chem. Soc. Rev.* **40**, 173-190 (2011).

23. Ghosh, P., Han, G., De, M., Kim, C. K., & Rotello, V. M. Gold nanoparticles in delivery applications. *Adv. Drug Del. Rev.* **60**, 1307-1315 (2008).

24. Giljohann, D. A., Seferos, D. S., Daniel, W. L., Massich, M. D., Patel, P. C., & Mirkin, C. A. Gold Nanoparticles for Biology and Medicine. *Angew. Chem. Int. Ed.* **49**, 3280-3294 (2010).

25. Lal, S., Clare, S. E., & Halas, N. J. Nanoshell-Enabled Photothermal Cancer Therapy: Impending Clinical Impact. *Acc. Chem. Res.* **41**, 1842-1851 (2008).

26. Jokerst, J. V., & Gambhir, S. S. Molecular Imaging with Theranostic Nanoparticles. *Acc. Chem. Res.* **44**, 1050-1060 (2011).

27. Trewyn, B. G., Slowing, I. I., Giri, S., Chen, H.-T., & Lin, V. S. Y. Synthesis and Functionalization of a Mesoporous Silica Nanoparticle Based on the Sol–Gel Process and Applications in Controlled Release. *Acc. Chem. Res.* **40**, 846-853 (2007).

28. Bonacchi, S., Genovese, D., Juris, R., Montalti, M., Prodi, L., Rampazzo, E., & Zaccheroni, N. Luminescent Silica Nanoparticles: Extending the Frontiers of Brightness. *Angew. Chem. Int. Ed.* **50**, 4056-4066 (2011).

29. Xie, J., Huang, J., Li, X., Sun, S., & Chen, X. Iron Oxide Nanoparticle Platform for Biomedical Applications. *Curr. Med. Chem.* **16**, 1278-1294 (2009).

30. Thakor, A. S., Jokerst, J., Zavaleta, C., Massoud, T. F., & Gambhir, S. S. Gold Nanoparticles: A Revival in Precious Metal Administration to Patients. *Nano Lett.* **11**, 4029-4036 (2011).

31. Harris, J. M., & Chess, R. B. Effect of pegylation on pharmaceuticals. *Nat. Rev. Drug Discovery* **2**, 214-221 (2003).

32. Duncan, R. Polymer conjugates as anticancer nanomedicines. *Nat. Rev. Cancer* **6**, 688-701 (2006).

33. Napier, M. E., & DeSimone, J. M. Nanoparticle Drug Delivery Platform. *Polymer Rev.* **47**, 321-327 (2007).

34. Hammond, P. T. Form and Function in Multilayer Assembly: New Applications at the Nanoscale. *Adv. Mater.* **16**, 1271-1293 (2004).

35. Aggarwal, S. What's fueling the biotech engine-2008. *Nat. Biotechnol.* **27**, 987-993 (2009).

36. Wang, H., Huff, T. B., Zweifel, D. A., He, W., Low, P. S., Wei, A., & Cheng, J.-X. In vitro and in vivo two-photon luminescence imaging of single gold nanorods. *Proc. Natl. Acad. Sci. U.S.A.* **102**, 15752-15756 (2005).

37. Zavaleta, C. L., Smith, B. R., Walton, I., Doering, W., Davis, G., Shojaei, B., Natan, M. J., & Gambhir, S. S. Multiplexed imaging of surface enhanced Raman scattering nanotags in living mice using noninvasive Raman spectroscopy. *Proc. Natl. Acad. Sci. U.S.A.* **106**, 13511-13516 (2009).

38. Lu, W., Huang, Q., Geng, K. B., Wen, X. X., Zhou, M., Guzatov, D., Brecht, P., Su, R., Oraevsky, A., Wang, L. V., Li, C. Photoacoustic imaging of living mouse brain vasculature using hollow gold nanospheres. *Biomaterials* **31**, 2617-2626 (2010).

39. Kim, D., Jeong, Y. Y., & Jon, S. A drug-loaded aptamer-gold nanoparticle bioconjugate for combined CT imaging and therapy of prostate cancer. *ACS Nano* **4**, 3689-3696 (2010).

40. von Maltzahn, G., Centrone, A., Park, J.H., Ramanathan, R., Sailor, M.J., Hatton, T.A., Bhatia, S.N. SERS-coded gold nanorods as a multifunctional platform for densely multiplexed near-infrared imaging and photothermal heating. *Adv. Mater.* **21**, 1-6 (2009).

41. Dreaden, E. C., Mwakwari, S. C., Sodji, Q. H., Oyelere, A. K., & El-Sayed, M. A. Tamoxifen-Poly(ethylene glycol)-Thiol Gold Nanoparticle Conjugates: Enhanced Potency and Selective Delivery for Breast Cancer Treatment. *Bioconjugate Chem.* **20**, 2247-2253 (2009).

42. Giljohann, D. A., Seferos, D. S., Prigodich, A. E., Patel, P. C., & Mirkin, C. A. Gene regulation with polyvalent siRNA-nanoparticle conjugates. *J. Am. Chem. Soc.* **131**, 2072-2073 (2009).

43. Dhar, S., Daniel, W. L., Giljohann, D. A., Mirkin, C. A., & Lippard, S. J. Polyvalent oligonucleotide gold nanoparticle conjugates as delivery vehicles for platinum(IV) warheads. *J. Am. Chem. Soc.* **131**, 14652-14653 (2009).

44. Hainfeld, J. F., Dilmanian, F. A., Zhong, Z., Slatkin, D. N., Kalef-Ezra, J. A., & Smilowitz, H. M. Gold nanoparticles enhance the radiation therapy of a murine squamous cell carcinoma. *Phys. Med. Biol.* **55**, 3045 (2010).

45. Chithrani, D. B., Jelveh, S., Jalali, F., van Prooijen, M., Allen, C., Bristow, R. G., Hill, R. P., & Jaffray, D. A. Gold Nanoparticles as Radiation Sensitizers in Cancer Therapy. *Radiat. Res.* **173**, 719-728 (2010).

46. Dickerson, E. B., Dreaden, E. C., Huang, X., El-Sayed, I. H., Chu, H., Pushpanketh, S., McDonald, J. F., & El-Sayed, M. A. Gold nanorod assisted near-infrared plasmonic photothermal therapy (PPTT) of squamous cell carcinoma in mice. *Cancer Lett.* **269**, 57-66 (2008).

47. Chen, J., Glaus, C., Laforest, R., Zhang, Q., Yang, M., Gidding, M., Welch, M. J., & Xia, Y. Gold nanocages as photothermal transducers for cancer treatment. *Small* **6**, 811-817 (2010).

48. von Maltzahn, G., Park, J.-H., Agrawal, A., Bandaru, N. K., Das, S. K., Sailor, M. J., & Bhatia, S. N. Computationally Guided Photothermal Tumor Therapy Using Long-Circulating Gold Nanorod Antennas. *Cancer Res.* **69**, 3892-3900 (2009).

49. Hirsch, L. R., Stafford, R. J., Bankson, J. A., Sershen, S. R., Rivera, B., Price, R. E., Hazle, J. D., Halas, N. J., & West, J. L. Nanoshell-mediated near-infrared thermal therapy of tumors under magnetic resonance guidance. *Proc. Natl. Acad. Sci. U.S.A.* **100**, 13549-13554 (2003).

50. Yuan, F., Dellian, M., Fukumura, D., Leunig, M., Berk, D. A., Torchilin, V. P., & Jain, R. K. Vascular Permeability in a Human Tumor Xenograft: Molecular Size Dependence and Cutoff Size. *Cancer Res.* **55**, 3752-3756 (1995).

51. Yuan, F., Leunig, M., Huang, S. K., Berk, D. A., Papahadjopoulos, D., & Jain, R. K. Mirovascular Permeability and Interstitial Penetration of Sterically Stabilized (Stealth) Liposomes in a Human Tumor Xenograft. *Cancer Res.* **54**, 3352-3356 (1994).

52. Pluen, A., Boucher, Y., Ramanujan, S., McKee, T. D., Gohongi, T., di Tomaso, E., Brown, E. B., Izumi, Y., Campbell, R. B., Berk, D. A., & Jain, R. K. Role of tumor–host interactions in interstitial diffusion of macromolecules: Cranial vs. subcutaneous tumors. *Proc. Natl. Acad. Sci. U.S.A.* **98**, 4628-4633 (2001).

53. Matsumura, Y., & Maeda, H. A New Concept for Macromolecular Therapeutics in Cancer Chemotherapy: Mechanism of Tumoritropic Accumulation of Proteins and the Antitumor Agent Smancs. *Cancer Res.* **46**, 6387-6392 (1986).

54. Maeda, H. Tumor-Selective Delivery of Macromolecular Drugs via the EPR Effect: Background and Future Prospects. *Bioconjugate Chem.* **21**, 797-802 (2010).

55. Kim, C. K., Ghosh, P., Pagliuca, C., Zhu, Z.-J., Menichetti, S., & Rotello, V. M. Entrapment of Hydrophobic Drugs in Nanoparticle Monolayers with Efficient Release into Cancer Cells. *J. Am. Chem. Soc.* **131**, 1360-1361 (2009).

56. Zhang, X.-Q., Xu, X., Lam, R., Giljohann, D., Ho, D., & Mirkin, C. A. Strategy for Increasing Drug Solubility and Efficacy through Covalent Attachment to Polyvalent DNA–Nanoparticle Conjugates. *ACS Nano* **5**, 6962-6970 (2011).

57. Lee, S. K., Han, M. S., Asokan, S., & Tung, C. H. Effective gene silencing by multilayered siRNA-coated gold nanoparticles. *Small* **7**, 364-370 (2011).

58. Lu, W., Zhang, G., Zhang, R., Flores, L. G., Huang, Q., Gelovani, J. G., & Li, C. Tumor Site–Specific Silencing of NF-κB p65 by Targeted Hollow Gold Nanosphere–Mediated Photothermal Transfection. *Cancer Res.* **70**, 3177-3188 (2010).

59. Guo, S., Huang, Y., Jiang, Q., Sun, Y., Deng, L., Liang, Z., Du, Q., Xing, J., Zhao, Y., Wang, P. C., Dong, A., & Liang, X. J. Enhanced gene delivery and siRNA silencing by gold nanoparticles coated with charge-reversal polyelectrolyte. *ACS Nano* **4**, 5505-5511 (2010).

60. Tassa, C., Duffner, J. L., Lewis, T. A., Weissleder, R., Schreiber, S. L., Koehler, A. N., & Shaw, S. Y. Binding Affinity and Kinetic Analysis of Targeted Small Molecule-Modified Nanoparticles. *Bioconjugate Chem.* **21**, 14-19 (2009).

61. Jiang, W., Kim, B. Y. S., Rutka, J. T., & Chan, W. C. W. Nanoparticle-mediated cellular response is size-dependent. *Nat. Nanotechnol.* **3**, 145-150 (2008).

62. Bard, A. J., & Faulkner, L. R. *Electrochemical Methods: Fundamentals and Applications*. 2nd edn, (John Wiley & Sons, Inc., 2001).

63. Torchilin, V. P., Rammohan, R., Weissig, V., & Levchenko, T. S. TAT peptide on the surface of liposomes affords their efficient intracellular delivery even at low temperature and in the presence of metabolic inhibitors. *Proc. Natl. Acad. Sci. U.S.A.* **98**, 8786-8791 (2001).

64. Park, J., Mattessich, T., Jay, S. M., Agawu, A., Saltzman, W. M., & Fahmy, T. M. Enhancement of surface ligand display on PLGA nanoparticles with amphiphilic ligand conjugates. *J. Control. Release* **156**, 109-115 (2011).

65. Dickerson, E. B., Dreaden, E. C., Huang, X. H., El-Sayed, I. H., Chu, H. H., Pushpanketh, S., McDonald, J. F., & El-Sayed, M. A. Gold nanorod assisted near-infrared plasmonic photothermal therapy (PPTT) of squamous cell carcinoma in mice. *Cancer Lett.* **269**, 57-66 (2008).

66. Oyelere, A. K., El-Sayed, M. A., & Dreaden, E. C. Targeted Cellular Delivery of Nanoparticles. U.S. patent 12/890,519 pending (2010).

67. Dreaden, E. C., El-Sayed, M. A., & El-Sayed, I. H. in *Nanomedicine and Cancer Nanoscience Applied to Health and Medicine Series* (eds V.R. Preedy & R. Srirajaskanthan) (Science Publishers, 2011).

68. Kim, C., Cho, E. C., Chen, J., Song, K. H., Au, L., Favazza, C., Zhang, Q., Cobley, C. M., Gao, F., Xia, Y., & Wang, L. V. In Vivo Molecular Photoacoustic Tomography of Melanomas Targeted by Bioconjugated Gold Nanocages. *ACS Nano* **4**, 4559-4564 (2010).

69. Dreaden, E. C., Near, R. D., Abdallah, T., Talaat, M. H., & El-Sayed, M. A. Multimodal plasmon coupling in low symmetry gold nanoparticle pairs detected in surface-enhanced Raman scattering. *Appl. Phys. Lett.* **98**, 183115-183113 (2011).

70. Galanzha, E. I., Shashkov, E. V., Kelly, T., Kim, J.-W., Yang, L., & Zharov, V. P. In vivo magnetic enrichment and multiplex photoacoustic detection of circulating tumour cells. *Nat. Nanotechnol.* **4**, 855-860 (2009).

71. Jung, Y., Reif, R., Zeng, Y., & Wang, R. K. Three-Dimensional High-Resolution Imaging of Gold Nanorods Uptake in Sentinel Lymph Nodes. *Nano Lett.* **11**, 2938-2943 (2011).

72. Pallaoro, A., Braun, G. B., & Moskovits, M. Quantitative ratiometric discrimination between noncancerous and cancerous prostate cells based on neuropilin-1 overexpression. *Proc. Natl. Acad. Sci. U. S. A.* **108**, 16559-16564 (2011).

73. Zavaleta, C. L., Smith, B. R., Walton, I., Doering, W., Davis, G., Shojaei, B., Natan, M. J., & Gambhir, S. S. Multiplexed imaging of surface enhanced Raman scattering nanotags in

living mice using noninvasive Raman spectroscopy. *Proc. Natl. Acad. Sci. U. S. A.* **106**, 13511-13516 (2009).

74. Barbosa, S., Agrawal, A., Rodríguez-Lorenzo, L., Pastoriza-Santos, I., Alvarez-Puebla, R. n. A., Kornowski, A., Weller, H., & Liz-Marzán, L. M. Tuning Size and Sensing Properties in Colloidal Gold Nanostars. *Langmuir* **26**, 14943-14950 (2010).

75. Dreaden, E. C., & El-Sayed, M. A. Detecting and Destroying Cancer Cells in More than One Way with Noble Metals and Different Confinement Properties on the Nanoscale. *Acc. Chem. Res. (in press)* (2012).

76. Lu, W., Xiong, C., Zhang, G., Huang, Q., Zhang, R., Zhang, J. Z., & Li, C. Targeted Photothermal Ablation of Murine Melanomas with Melanocyte-Stimulating Hormone Analoge-Conjugated Hollow Gold Nanospheres. *Clin. Cancer Res.* **15**, 876-886 (2009).

77. Gobin, A. M., Lee, M. H., Halas, N. J., James, W. D., Drezek, R. A., & West, J. L. Near-Infrared Resonant Nanoshells for Combined Optical Imaging and Photothermal Cancer Therapy. *Nano Lett.* **7**, 1929-1934 (2007).

78. Suneil, J., Jonathan, A. C., Alan, R. H., Karl, T. B., Stephen, J. M., Wendy, B. H., Mark, F. M., Glenn, R. D., Kevin, M. P., Fred, J. C., Joe, M. O. S., & David, G. H. Cell-specific Radiosensitization by Gold Nanoparticles at Megavoltage Radiation Energies. *Int. J. Radiat. Oncol. Biol. Phys.* (2010).

79. Roa, W., Zhang, X., Guo, L., Shaw, A., Hu, X., Xiong, Y., Gulavita, S., Patel, S., Sun, X., Chen, J., Moore, R., & Xing, J. Z. Gold nanoparticle sensitize radiotherapy of prostate cancer cells by regulation of the cell cycle. *Nanotechnol.* **20**, 375101 (2009).

80. Hainfeld, J. F., Slatkin, D. N., & Smilowitz, H. M. The use of gold nanoparticles to enhance radiotherapy in mice. *Phys. Med. Biol.* **49**, N309 (2004).

81. Tong, L., He, W., Zhang, Y. S., Zheng, W., Cheng, J. X. Visualizing Systemic Clearance and Cellular Level Biodistribution of Gold Nanorods by Intrinsic Two-Photon Luminescence. *Langmuir* **25**, 12454-12459 (2009).

82. Park, J., Estrada, A., Sharp, K., Sang, K., Schwartz, J. A., Smith, D. K., Coleman, C., Payne, J. D., Korgel, B. A., Dunn, A. K., Tunnell, J. W. Two-photon-induced photoluminescence imaging of tumors using near-infrared excited gold nanoshells. *Opt. Express* **16**, 1590-1599 (2008).

83. Durr, N. J., T. Larson, D. K. Smith, B. A. Korgel, K. Sokolov, A. Ben-Yakar Two-photon luminescence imaging of cancer cells using molecularly targeted gold nanorods. *Nano Lett.* **7**, 941-945 (2007).

84. Hainfeld, J. F., Slatkin, D. N., Focella, T. M., & Smilowitz, H. M. Gold nanoparticles: a new X-ray contrast agent. *Brit. J. Radiol.* **79**, 248-253 (2006).

85. Cai, Q. Y., Kim, S.H., Choi, K.S., Kim, S.Y., Byun, S.J., Kim, K.W., Park, S.H., Juhng, S.K., Yoon, K.H. Colloidal gold nanoparticles as a blood-pool contrast agent for X-ray computed tomography in mice. *Invest. Radiol.* **42**, 797-806 (2007).

86. Sun, I.-C., Eun, D.-K., Na, J. H., Lee, S., Kim, I.-J., Youn, I.-C., Ko, C.-Y., Kim, H.-S., Lim, D., Choi, K., Messersmith, P. B., Park, T. G., Kim, S. Y., Kwon, I. C., Kim, K., & Ahn, C.-H. Heparin-Coated Gold Nanoparticles for Liver-Specific CT Imaging. *Chem. Eur. J.* **15**, 13341-13347 (2009).

87. Kim, D., Park, S., Lee, J. H., Jeong, Y. Y., & Jon, S. Antibiofouling Polymer-Coated Gold Nanoparticles as a Contrast Agent for in Vivo X-ray Computed Tomography Imaging. *J. Am. Chem. Soc.* **129**, 7661-7665 (2007).

88. Kang, B., Mackey, M. A., & El-Sayed, M. A. Nuclear Targeting of Gold Nanoparticles in Cancer Cells Induces DNA Damage, Causing Cytokinesis Arrest and Apoptosis. *J. Am. Chem. Soc.* **132**, 1517-1519 (2010).

89. Kelly, K. L., Coronado, E., Zhao, L. L., & Schatz, G. C. The Optical Properties of Metal Nanoparticles: The Influence of Size, Shape, and Dielectric Environment. *J. Phys. Chem. B* **107**, 668-677 (2002).

90. Greczynski, G., & Salaneck, W. R. Photoelectron spectroscopy of hybrid interfaces for light emitting diodes: Influence of the substrate work function. *Appl. Phys. Lett.* **79**, 3185-3187 (2001).

91. Hartland, G. V. Optical Studies of Dynamics in Noble Metal Nanostructures. *Chem. Rev.* **111**, 3858-3887 (2011).

92. Noguez, C. Surface plasmons on metal nanoparticles: The influence of shape and physical environment. *J. Phys. Chem. C* **111**, 3806-3819 (2007).

93. Wang, H., Brandl, D. W., Nordlander, P., & Halas, N. J. Plasmonic Nanostructures: Artificial Molecules. *Acc. Chem. Res.* **40**, 53-62 (2007).

94. Weissleder, R. A clearer vision for in vivo imaging. *Nat. Biotechnol.* **19**, 316-317 (2001).

95. Ntziachristos, V., Yodh, A. G., Schnall, M., & Chance, B. Concurrent MRI and diffuse optical tomography of breast after indocyanine green enhancement. *Proc. Natl. Acad. Sci. U.S.A.* **97**, 2767-2772 (2000).

96. Wust, P., Hildebrandt, B., Sreenivasa, G., Rau, B., Gellermann, J., Riess, H., Felix, R., & Schlag, P. M. Hyperthermia in combined treatment of cancer. *Lancet Oncol.* **3**, 487-497 (2002).

97. Bert, H., Peter, W., Olaf, A., Annette, D., Geetha, S., Thoralf, K., Roland, F., & Hanno, R. The cellular and molecular basis of hyperthermia. *Crit. Rev. Oncol. Hematol.* **43**, 33-56 (2002).

98. Huff, T. B., Tong, L., Zhao, Y., Hansen, M. N., Cheng, J. X., & Wei, A. Hyperthermic effects of gold nanorods on tumor cells. *Nanomedicine* **2**, 125-132 (2007).

99. Bohren, C. F., & Huffman, D. R. *Absorption and Scattering of Light by Small Particles*. (Wiley–Interscience, 1983).

100. Jain, P. K., K. S. Lee, I. H. El-Sayed, M. A. El-Sayed Calculated absorption and scattering properties of gold nanoparticles of different size, shape, and composition: applications in biological imaging and biomedicine. *J. Phys. Chem. B* **110**, 7238-7248 (2006).

101. Bross, P. F., Beitz, J., Chen, G., Chen, X. H., Duffy, E., Kieffer, L., Roy, S., Sridhara, R., Rahman, A., Williams, G., & Pazdur, R. Approval summary: Gemtuzumab ozogamicin in relapsed acute myeloid leukemia. *Clin. Cancer Res.* **7**, 1490-1496 (2001).

102. Holgate, C. S., Jackson, P., Cowen, P. N., & Bird, C. C. Immunogold-silver staining: new method of immunostaining with enhanced sensitivity. *J. Histochem. Cytochem.* **31**, 938-944 (1983).

103. El-Sayed, I. H., Huang, X., El-Sayed, M. A. Surface plasmon resonance scattering and absorption of anti-EGFR antibody conjugated gold nanoparticles in cancer diagnostics: applications in oral cancer. *Nano Lett.* **5**, 829-834 (2005).

104. Huang, X. H., El-Sayed, I. H., Qian, W., & El-Sayed, M. A. Cancer cell imaging and photothermal therapy in the near-infrared region by using gold nanorods. *J. Am. Chem. Soc.* **128**, 2115-2120 (2006).

105. Pitsillides, C. M., Joe, E. K., Wei, X., Anderson, R. R., & Lin, C. P. Selective Cell Targeting with Light-Absorbing Microparticles and Nanoparticles. *Biophys. J.* **84**, 4023-4032 (2003).

106. Chen, J., D. Wang, J. Xi, L. Au, A. Siekkinen, A. Warsen, Z. Y. Li, H. Zhang, Y. Xia, X. Li Immuno gold nanocages with tailored optical properties for targeted photothermal destruction of cancer cells. *Nano Lett.* **7**, 1318 (2007).

107. Melancon, M. P., W. Lu, Z. Yang, R. Zhang, Z. Cheng, A. M. Elliot, J. Stafford, T. Olson, J. Z. Zhang, C. Li In vitro and in vivo targeting of hollow gold nanoshells directed at epidermal growth factor receptor for photothermal ablation therapy. *Mol. Cancer Ther.* **7**, 1730 (2008).

108. Lu, W., Xiong, C., Zhang, G., Huang, Q., Zhang, R., Zhang, J. Z., & Li, C. Targeted Photothermal Ablation of Murine Melanomas with Melanocyte-Stimulating Hormone Analogâ€"Conjugated Hollow Gold Nanospheres. *Clin. Cancer Res.* **15**, 876-886 (2009).

109. Hu, M., Chen, J., Li, Z.-Y., Au, L., Hartland, G. V., Li, X., Marquez, M., & Xia, Y. Gold nanostructures: engineering their plasmonic properties for biomedical applications. *Chem. Soc. Rev.* **35**, 1084-1094 (2006).

110. Cole, J. R., Mirin, N. A., Knight, M. W., Goodrich, G. P., & Halas, N. J. Photothermal Efficiencies of Nanoshells and Nanorods for Clinical Therapeutic Applications. *J. Phys. Chem. C* **113**, 12090-12094 (2009).

111. Kampinga, H. H. Cell biological effects of hyperthermia alone or combined with radiation or drugs: A short introduction to newcomers in the field. *Int J. Hyperther.* **22**, 191-196 (2006).

112. Root, S. W., Andrews, G. A., Kniseley, R. M., & Tyor, M. P. The distribution and radiation effects of intravenously administered colloidal Au^{198} in man. *Cancer* **7**, 856-866 (1954).

113. Paciotti, G. F., Myer, L., Weinreich, D., Goia, D., Pavel, N., McLaughlin, R. E., & Tamarkin, L. Colloidal gold: A novel nanoparticle vector for tumor directed drug delivery. *Drug Deliv.* **11**, 169-183 (2004).

114. Paciotti, G. F., Myer, L. D., Kim, T. H., Wang, S., Alexander, H. R., Weinreich, D., & Tamarkin, L. Colloidal gold: A novel colloidal nanoparticle vector for tumor-directed drug delivery. *Clin. Cancer Res.* **7**, 3673S-3674S (2001).

115. Libutti, S. K., Paciotti, G. F., Byrnes, A. A., Alexander, H. R., Gannon, W. E., Walker, M., Seidel, G. D., Yuldasheva, N., & Tamarkin, L. Phase I and Pharmacokinetic Studies of CYT-6091, a Novel PEGylated Colloidal Gold-rhTNF Nanomedicine. *Clin. Cancer Res.* **16**, 6139-6149 (2010).

116. Longmire, M., Choyke, P. L., & Kobayashi, H. Clearance properties of nano-sized particles and molecules as imaging agents: considerations and caveats. *Nanomedicine* **3**, 703-717 (2008).

117. Owens Iii, D. E., & Peppas, N. A. Opsonization, biodistribution, and pharmacokinetics of polymeric nanoparticles. *Int. J. Pharm.* **307**, 93-102 (2006).

118. Obach, R. S., Lombardo, F., & Waters, N. J. Trend Analysis of a Database of Intravenous Pharmacokinetic Parameters in Humans for 670 Drug Compounds. *Drug Metab. Dispos.* **36**, 1385-1405 (2008).

119. De Jong, W. H., Hagens, W. I., Krystek, P., Burger, M. C., Sips, A. J. A. M., & Geertsma, R. E. Particle size-dependent organ distribution of gold nanoparticles after intravenous administration. *Biomaterials* **29**, 1912-1919 (2008).

120. Terentyuk, G. S., Maslyakova, G. N., Suleymanova, L. V., Khlebtsov, B. N., Kogan, B. Y., Akchurin, G. G., Shantrocha, A. V., Maksimova, I. L., Khlebtsov, N. G., & Tuchin, V. V. Circulation and distribution of gold nanoparticles and induced alterations of tissue morphology at intravenous particle delivery. *J. Biophotonics* **2**, 292-302 (2009).

121. Choi, C. H. J., Alabi, C. A., Webster, P., & Davis, M. E. Mechanism of active targeting in solid tumors with transferrin-containing gold nanoparticles. *Proc. Natl. Acad. Sci. U. S. A.* **107**, 1235-1240 (2010).

122. Perrault, S. D., Walkey, C., Jennings, T., Fischer, H. C., & Chan, W. C. W. Mediating Tumor Targeting Efficiency of Nanoparticles Through Design. *Nano Lett.* **9**, 1909-1915 (2009).

123. Salem, A. K., Searson, P. C., & Leong, K. W. Multifunctional nanorods for gene delivery. *Nat. Mater.* **2**, 668-671 (2003).

124. Chen, C. C., Lin, Y. P., Wang, C. W., Tzeng, H. C., Wu, C. H., Chen, Y. C., Chen, C. P., Chen, L. C., & Wu, Y. C. DNA-gold nanorod conjugates for remote control of localized gene expression by near infrared irradiation. *J. Am. Chem. Soc.* **128**, 3709-3715 (2006).

125. Park, J.-H., von Maltzahn, G., Ong, L. L., Centrone, A., Hatton, T. A., Ruoslahti, E., Bhatia, S. N., & Sailor, M. J. Cooperative Nanoparticles for Tumor Detection and Photothermally Triggered Drug Delivery. *Adv. Mater.* **22**, 880-885 (2010).

126. Park, J.-H., von Maltzahn, G., Xu, M. J., Fogal, V., Kotamraju, V. R., Ruoslahti, E., Bhatia, S. N., & Sailor, M. J. Cooperative Nanomaterial System to Sensitize, Target, and Treat Tumors. *Proc. Natl. Acad. Sci. U.S.A.* **107**, 981-986 (2010).

127. Wang, L. M., Li, Y. F., Zhou, L. J., Liu, Y., Meng, L., Zhang, K., Wu, X. C., Zhang, L. L., Li, B., & Chen, C. Y. Characterization of gold nanorods in vivo by integrated analytical techniques: their uptake, retention, and chemical forms. *Anal. Bioanal. Chem.* **396**, 1105-1114 (2010).

128. Huang, X., Peng, X., Wang, Y., Shin, D. M., El-Sayed, M. A., & Nie, S. A reexamination of active and passive tumor targeting by using rod-shaped gold nanocrystals and covalently conjugated peptide ligands. *ACS Nano* **4**, 5887-5896 (2010).

129. Akiyama, Y., Mori, T., Katayama, Y., & Niidome, T. The effects of PEG grafting level and injection dose on gold nanorod biodistribution in the tumor-bearing mice. *J. Controlled Release* **139**, 81-84 (2009).

130. Chithrani, B. D., Ghazani, A. A., & Chan, W. C. W. Determining the Size and Shape Dependence of Gold Nanoparticle Uptake into Mammalian Cells. *Nano Lett.* **6**, 662-668 (2006).

131. Jiang, W., KimBetty, Y. S., Rutka, J. T., & Chan, C. W. Nanoparticle-mediated cellular response is size-dependent. *Nat. Nanotechnol.* **3**, 145-150 (2008).

132. Chauhan, V. P., Popović, Z., Chen, O., Cui, J., Fukumura, D., Bawendi, M. G., & Jain, R. K. Fluorescent Nanorods and Nanospheres for Real-Time In Vivo Probing of Nanoparticle Shape-Dependent Tumor Penetration. *Angew. Chem. Int. Ed.* **50**, 11417-11420 (2011).

133. Cho, W.-S., Cho, M., Jeong, J., Choi, M., Cho, H.-Y., Han, B. S., Kim, S. H., Kim, H. O., Lim, Y. T., Chung, B. H., & Jeong, J. Acute toxicity and pharmacokinetics of 13 nm-sized PEG-coated gold nanoparticles. *Toxicol. Appl. Pharmacol.* **236**, 16-24 (2009).

134. Estimation for humans based on the Nov 29, 2011 price of gold ($1713.40 USD per 1 troy oz = 31.1034768 g) obtained from http://www.marketwatch.com/investing/future/GOLD and the maximum full-couse 1.2 mg/m^2 dosage administered in Libutti et al. (doi 10.1158/1078-0432.CCR-10-0978) for an average adult cancer patient (1.79[a] m^2). Estimation for mice models based on the Nov 29, 2011 price of gold chloride trihydrate ($96.90 USD) obtained from http://www.sigmaaldrich.com, the systemic dosage of gold nanorods administerd in Dickerson et al. (100 μL of OD_{800}=120, doi 10.1016/j.canlet.2008.04.026), and a conservative synthetic yield of 5.078 L of OD_{800}=1 per gram of gold salt. [a]Sacco, J. J.; Botten, J.; Macbeth, F.; Bagust, A.; Clark, P. The Average Body Surface Area of Adult Cancer Patients in the UK: A Multicentre Retrospective Study. PLoS ONE 2010, 5, e8933.

135. Dove, A. Uncorking the biomanufacturing bottleneck. *Nat. Biotechnol.* **20**, 777-779 (2002).

136. Glover, R. D., Miller, J. M., & Hutchison, J. E. Generation of Metal Nanoparticles from Silver and Copper Objects: Nanoparticle Dynamics on Surfaces and Potential Sources of Nanoparticles in the Environment. *ACS Nano* **5**, 8950-8957 (2011).

CHAPTER 3

LASER PHOTOTHERMAL CANCER THERAPY

The application of nanotechnology in medicine has been a rapidly growing field in recent years.[1-8] A variety of structures with unique structural,[*9,10*] optical,[*11,12*] electronic,[13] magnetic,[14] and catalytic [15] properties have been exploited in the areas of cancer imaging,[*2,16-19*] diagnostics,[*6,20,21*] and treatment.[22-30] Noble metal nanoparticles provide remarkable opportunities in these applications due to their inherently low toxicity [31-33] and strongly enhanced optical properties associated with localized surface plasmon resonance.[34-36] The enhanced electromagnetic field surrounding such particles gives rise to large absorption, Rayleigh (Mie) scattering, raman scattering, and two-photon luminescence cross-sections, properties which have been utilized in photothermal cancer therapy (PTT),[24-30] surface enhanced Raman detection (SERS), [37-39] and diagnostic imaging [17-20] applications.

While surgical excision of tumors is a highly effective method of cancer treatment, curative strategies for primary tumors located in vital or poorly accessible tissues remain a challenge. In cases of recurrent tumors or those with ill-defined margins, alternative and multimodal oncological approaches are employed. The primary [40-42] and adjunctive [43-46] treatment of cancers by induced hyperthermia is a well established but burgeoning field of medical research. Here, temperatures in tumor-loaded tissues are elevated to 40-43°C [47] and above by selective or non-selective application of microwave, radio, ultrasound, alternating magnetic, infrared, or visible radiation. At temperatures greater than 43°C, protein denaturation and disruption of the cellular membrane is known to occur and ablation of tumor tissues has been shown in numerous cases.[*42,48,49*] Under mild temperature increases, clinical studies indicate an acceleration of both

perfusion and reoxygenation [*50,51*] of tumor tissues, thereby increasing the efficacy of cytostatic drug delivery (*chemosensitization*) and radiotherapy (*radiosensitization*), respectively. In all cases, clinical studies indicate statistically significant benefits to local tumor control and overall survival rates for primary [40-42] and conjunctive hyperthermia.[52-56] Although promising, conventional non-invasive hyperthermic strategies are often less selective than those based-on or used in combination with thermal contrast agents, in many cases, causing damage to surrounding healthy tissues, as well as significant discomfort. Moreover, hyperthermic treatments using commercially available instruments are often limited to shallow penetration depths [46] (<3 cm), lower treatment temperatures, and regions of the body with regular surface composition. Invasive approaches using microwave antennas are highly susceptible to interference, while magnetic particle treatments require large doses.

Photothermal therapy [*49,57-59*] is a minimally-invasive treatment method in which photon energy is converted to thermal energy sufficient to induce cellular hyperthermia. Selectivity is achieved by focused directional control or invasive [40-42] (fiber optic) positioning of the incident radiation, often pulsed [28-30] or continuous wave [*24-28,30,48*] (cw) laser, and is typically accompanied by preferential administration of photoactive molecules [60-62] or nano-scale particles. Photoexcitation of the latter two results in non-radiative relaxation by local heat transfer to the surrounding tumor environment. In contrast, photodynamic therapy (PDT),[63-65] relies on non-radiative relaxation through local formation of cytotoxic singlet oxygen species. While PTT and PDT treatments have garnered significant attention, such methods are inherently limited by photobleaching effects and absorption cross sections several times weaker than those of noble metal nanoparticles.

Recent advances in the field of plasmonics present new opportunities for both primary and multimodal PTT strategies using noble metal nanoparticles. By photo-exciting conduction electrons which oscillate at the surfaces of such structures (surface plasmons), highly efficient local heating can be achieved by non-radiative relaxation through electron-phonon and subsequent phonon-phonon coupling processes.[35] While several materials and spherical nanoparticles exhibit surface plasmon resonance in the visible region, opportunities for *in vivo* plasmonic photothermal therapy [8] (PPTT) are restricted due to a high degree of absorption by tissues at visible wavelengths. Such ablative treatments are therefore limited to shallow depths.[66] In contrast, PPTT of deep tissue malignancies may be accomplished by laser exposure and plasmon absorption in the near-infrared region (NIR). Due to minimal attenuation by water and hemoglobin at these wavelengths, NIR transmission [7] in soft tissues may be achieved at depths exceeding 10 cm. By chemically varying the shape or composition of noble metal nanoparticles,[*9,21,24,67-69*] surface plasmon absorption can be tuned from ultraviolet (UV) to infrared (IR) wavelengths. The enhanced nonlinear optical properties of spherical metal nanoparticles have also been used by our group in *in vitro* near-infrared pulsed laser PPTT by second harmonic generation.[*29,70,71*]

The potential uses of gold nanoparticles in near-infrared PPTT have been published using a variety of noble metal nanostructures, including gold nanoshells,[*26,48*] gold nanorods,[*8,27,72*] and recently, gold nanocages.[73] Studies using nanoshell-mediated PPTT indicate significantly improved local tumor control and survival times in animal models, while surface plasmon absorption of gold nanocages have been used in diagnostic imaging and *in vitro* therapy.[24]

One of the simplest and widely used methods to obtain plasmonic nanoparticles involves the seed-mediated growth of colloidal gold nanorods.[68] The use of such particles in near-infrared PPTT is highly attractive due to their rapid synthesis, facile bioconjugation, strong absorption cross-

section, and tunable optical extinction. Recent calculations by discrete dipole approximation (DDA) show the absorption cross section of nanorod structures to be nominally larger than that of nanocages and more than twice that of nanoshell structures at their NIR plasmon resonance.[73] By synthetically varying the aspect ratio of the nanorods, longitudinal plasmon absorption can be shifted throughout the visible, NIR, and IR regions.[*68,74-76*]

Our previous work [27] showed that gold nanorods conjugated to epithelial growth factor receptor antibodies (anti-EGFR) can serve as contrast agents for *in vitro* biodiagnostics. Moreover, due to overexpression of the EGF receptor on cancer cell surfaces and the specificity of antibody binding, malignant cells were found to require half the energy necessary to destroy normal cells when both were incubated with the same concentration of nanorod bioconjugates, a key feature of selective PPTT.

In the present work, the feasibility of *in vivo* near-infrared PPTT is demonstrated using colloidal gold nanorods in an animal model. Subcutaneous squamous cell carcinoma xenografts were grown in nude (*nu/nu*) mice and gold nanoparticles were selectively delivered to tumors by both direct and intravenous injection. Thiolated poly (ethylene) glycol (5 kDa) was covalently bound to the gold nanorod surface to increase biocompatibility,[77-80] suppress immunogenic responses, and to decrease adsorption to the negatively charge luminal surface of blood vessels. Near-infrared PPTT was performed extracorporally using a small, portable, inexpensive, continuous wave diode laser. Making use of the enhanced permeability and retention (EPR) effect,[*81,82*] preferential accumulation of PEGylated gold nanorods in tumor tissues was achieved due to the high density, extensive extravasation, and inherently defective architecture of the tumor vasculature, as well as the diminished lymphatic clearance from associated interstitial spaces. Significant decreases in tumor growth were observed for both direct tumor injection ($P<0.0001$) and intravenous ($P<0.0008$)

treatments. Inhibition of average tumor growth for both delivery methods was observed over a 13-day period, with resorption of >57% of the directly-injected tumors and 25% of the intravenously-treated tumors.

3.1 Design and Development of Plasmonic Photothermal Cancer Therapy

Synthesis and PEGylation of gold nanorods. Seed-mediated growth was performed at 25 °C from freshly prepared aqueous solutions (18 MΩ) following methods of Nikoobakht and El-Sayed.[68] Briefly, 2.50 mL of 1.00 mM $HAuCl_4$ (Aldrich, 24459-7) was added to 5.00 mL of 0.200 M cetyltrimethylammonium bromide (CTAB, Aldrich). 600 µL of ice-cold 10 mM $NaBH_4$ (Aldrich, 480886) was added to the stirred solution and allowed to react for several minutes, forming the pale brown gold seed solution. Next, 100.0 mL of 1.00 mM $HAuCl_4$ was added to 100.0 mL of 0.200 M CTAB and 4.50 mL of 4.00 mM $AgNO_3$ (Fischer). 1.40 mL of 78.8 mM ascorbic acid (Aldrich, A-7506) was added, followed by gentle mixing to form the transparent growth solution. 160 µL of the seed solution was added to the unstirred growth solution and allowed to react for 2 hours. Nanorods synthesized by this method are approximately 12 nm in width and 50 nm length (4.0 aspect ratio), with a longitudinal plasmon absorption maximum at 800 nm.

Gold nanorod solutions were centrifuged twice at 20,000 x *g* for 15 min and re-dispersed in deionized water to remove excess CTAB molecules. mPEG-SH (Nektar Therapeutics, 5 kDa) was added to the ~1 nM colloidal nanorod solution at a final concentration of 10 mM. Rods were sonicated overnight and centrifuged at 20,000 x *g* for 15 min and redispersed in deionized water to remove excess PEG molecules. The PEGylated gold nanorods were again centrifuged at 20,000 x *g* for 15 min, sterile filtered, and re-dispersed in 10 mM phosphate-buffered saline (PBS, Mediatech) to the desired optical density at 800 nm. Extinction spectra of the PEGylated nanorod saline suspensions showed no peak shift, broadening, or reduction over a 1 week period prior to injection.

Cell culture and inoculation of mice with tumor cells. HSC-3 human squamous carcinoma cells (courtesy of Dr. Ivan H. El-Sayed - UCSF Dept of Otolaryngology) were cultured in DMEM (Mediatech) supplemented with 10% v/v heat-inactivated fetal bovine serum (Invitrogen), 2 mM L-glutamine (Sigma), penicillin (100 U/ml) (Sigma), and streptomycin (100 µg/ml) (Sigma) in a 5% CO_2 humidified atmosphere. Female *nu/nu* mice, 7-8 weeks of age, were obtained from Taconic (Hudson, NY). Mice were injected subcutaneously in the flank with 100 µL (3×10^6) HSC-3 cells suspended in 10 mM PBS. Near-infrared PPTT began once tumor burden reached 3 mm in diameter (7-9 days). All experiments were conducted with the approval of the Institutional Animal Care and Use Committee (IACUC) of the Georgia Institute of Technology (Atlanta, GA).

Intratumoral nanoparticle accumulation, temperature, and imaging. Tumor bearing mice were injected with gold nanorods ($OD_{\lambda=800}$ = 120, 100 µl) via the tail vein, and euthanized at specified time points. Tumor tissues was excised, fixed in 10% formalin for 24 hours, and embedded in paraffin blocks. Blocks were sectioned (5 microns) and stained using the Silver Enhancer Kit SE-100 (Sigma-Aldrich) according to the manufacturer's instructions. Incubation time for optimal visualization was determined to be 10 minutes. Silver staining of the tissue sections were examined using a BX60 Olympus microscope, and photographed using an Olympus Camedia digital camera.

Thermal transient measurements of HSC-3 tumor interstitia were obtained using a 33 gauge hypodermic thermocouple (Omega). The tip of the thermistor was positioned at the tumor center-of-mass and temperatures were recorded in 15 second intervals prior to, during, and following NIR exposure for direct (15 µL, $OD_{\lambda=800}$=40, 10 min, 0.9-1.1 W/cm^2, 6 mm dia) and intravenously (100 µL, $OD_{\lambda=800}$=120, 10 min, 1.7-1.9 W/cm^2, 6 mm dia) administered gold nanorods, as well as for comparably exposed sham/NIR treatments (15 µL direct intratumoral injection of 10 mM PBS).

In vivo imaging of PEGylated gold nanorod accumulation was monitored by attenuation of near-infrared transmission (808 nm diode laser, Power Technologies) using a custom-built CCD device array. Control measurements were taken from images obtained by 15 μL direct intratumoral injection of 10 mM PBS, while directly and intravenously administered measurements were obtained using previously mentioned dosages.

In vivo near-infrared PPTT. Mice were anesthetized with ketamine/xylazine/acepromazine. 15 μL of PEGylated gold nanorods ($OD_{\lambda=800}$ = 40) were directly injected into the tumor interstitium or 100 μL of PEGylated gold nanorods ($OD_{\lambda=800}$ = 120) were intravenously (tail) injected. Control tumor sites were injected with 15 μL of 10 mM PBS with no NIR exposure. For direct administration, mouse tumors were extracorporeally exposed to NIR radiation (0.9-1.1 W/cm^2, 6 mm dia, 10 min) within 2 minutes of injection to limit particle diffusion beyond the tumor boundaries. For intravenous administration, nanorods were allowed 24 hour circulation to maximize intratumoral particle accumulation prior to NIR exposure (1.7-1.9 W/cm^2, 6 mm dia,10 min). Ellipsoidal tumor volume was calculated as $V = (d)^2(D)(\pi/6)$. Statistical hypothesis testing was performed using Welch's t test and non-parametric analysis of variance was performed by the Kruskal-Wallis test. Due to the unusually rapid growth rates observed in the HSC-3 xenograft model, tumors and vital organs were harvested at day 14 for use in separate, ongoing toxicological investigations.

3.2 Gold Nanorods as Highly Efficient Near-Infrared Photothermal Contrast Agents

Intratumoral particle accumulation. PEGylated gold nanorods were intravenously injected (tail vein) to assess optimal intratumoral particle accumulation. Following injection, HSC-3 tumors were excised at varying time intervals, fixed, sectioned, and stained with silver to visualize the extent of particle loading. Nanorods directly injected into tumors were used as a positive control (data not

shown). **Figure 3.1A** shows a typical histological section from a HSC-3 tumor injected with 15 μL of 10 mM PBS (control). **Figures 3.1B,C** illustrate representative tumor sections following 2 and 6 hours of accumulation, respectively. At these time points, no appreciable accumulation of particles was observed. In contrast, high particle loading was observed following 24 hours of circulation (**Figure 3.1D**). Because the highest accumulation, and therefore PPTT selectivity, was observed at 24 hours, this time point was used for subsequent intravenous near-infrared PPTT treatments.

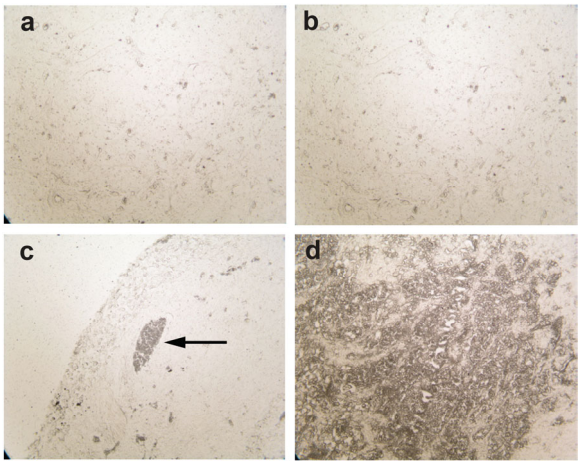

Figure 3.1. Histological sections of silver stained HSC-3 tumor xenografts from female *nu/nu* mice intravenously (tail) injected with (A) 100 μL of 10 mM PBS following 24 hr circulation and PEGylated gold nanorods (100 μL, $OD_{\lambda=800}$=120) following (B) 2 hr (C), 6 hr, and (D) 24 hr accumulation. Direct injection of particles to the tumor interstitium was used as a positive staining control (data not shown). Arrow indicates staining of red blood cells (observed in all tumors). Adapted from Dickerson et al. [*83*].

Transient particle accumulation following direct and intravenous administration was monitored by NIR transmission imaging (**Figure 3.2**). Intensity line-scans of NIR extinction showed marginal diffusion of directly injected particles over 3 min, with no subsequent change observed over several hours. Intensity line-scans from NIR transmission images of HSC-3 tumor sites directly injected with 15 μL of 10 mM PBS show nominal extinction due to increased tissue density, while line-scans obtained following intravenous nanorod delivery at 24 hr accumulation showed extinction

2.00 times that observed for control sites. Directly injected tumor sites showed NIR extinction (2 min) more than 2.18 times greater than that observed by intravenous administration and 4.35 times that observed at control sites.

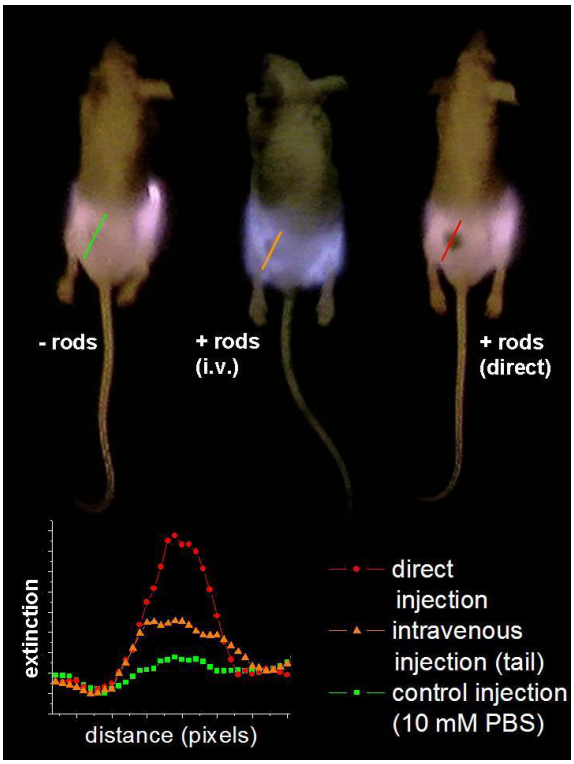

Figure 3.2. NIR transmission images of mice prior to PPTT treatments. Inset shows intensity line-scans of NIR extinction at tumor sites for control (■), intravenous (▲), and direct (●) administration of PEGylated gold nanorods. Control mice were interstitially injected with 15 µL 10 mM PBS alone, while directly administered mice received interstitial injections of 15 µL PEGylated gold nanorods ($OD_{\lambda=800}$=40, 2 min accumulation), and intravenously administered mice recieved 100 µL PEGylated gold nanorod ($OD_{\lambda=800}$=120, 24 hr accumulation) injections. Adapted from Dickerson et al. [*83*].

Thermal response measurements and nanorod accumulation. Thermal transient measurements for direct (**Figure 3.3A**) and intravenous (**Figure 3.3B**) near-infrared PPTT treatments show thermal equilibrium conditions prior to NIR irradiation. Rapid heating was observed upon exposure, followed by steady-state equilibrium. Note that >90% of the observed temperature increase occurred

within the first 3 minutes. Upon removal of NIR exposure, tissues displayed expected Newtonian cooling behavior.

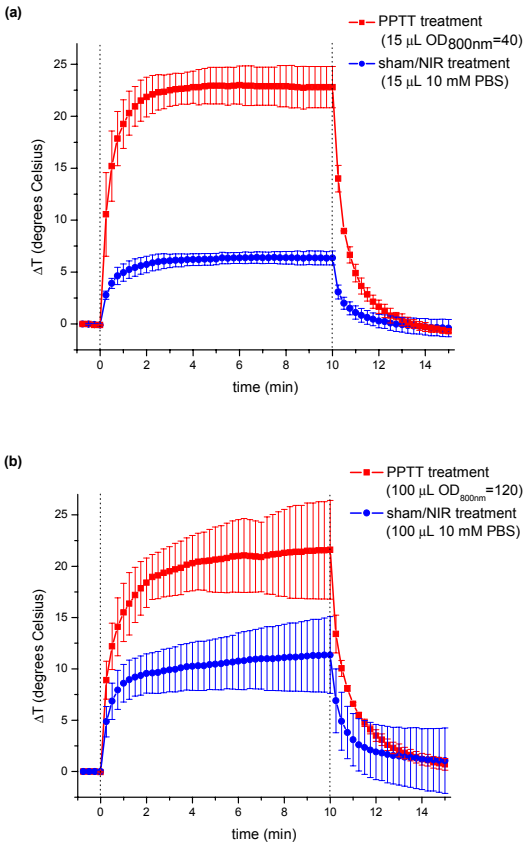

Figure 3.3. Thermal transient measurements of HSC-3 tumor interstitia during (A) direct and (B) intravenous near-infrared PPTT (■) and sham/NIR (●) treatments using PEGylated gold nanorods. Direct PPTT treatments were performed by administration of 15 µL PEGylated gold nanorods ($OD_{\lambda=800}$=40, 2 min accumulation) followed by 10 min of 0.9-1.1 W/cm^2 NIR laser exposure. Intravenous PPTT treatments were performed by administration of 100 µL PEGylated gold nanorods ($OD_{\lambda=800}$=120, 24 hr accumulation) followed by 10 min of 1.7-1.9 W/cm^2 NIR laser exposure. Sham/NIR treatments were performed by administration of 15 µL 10 mM PBS and NIR laser exposure of comparable time and power density. Errors reported as SD. Adapted from Dickerson et al. [*83*].

Heating efficiencies of PPTT treatments (the ratio of steady-state temperature change in the presence of plasmonic particles to that in their absence) were found to be 3.59±0.5 for direct-injection and 1.90±0.4 for intravenous injection of PEGylated gold nanorods. The former value is

remarkably similar to that observed during *in vivo* near-infrared PPTT treatments reported by Hirsch et al. [26] by direct injection of gold nanoshells. Observed increases in temperature change for sham/NIR treatments using comparable exposure times and power densities as direct and intravenous administration conditions correlate well with increases in power density. Disparity of direct and intravenous PPTT heating efficiency scales proportionately with observed increases in NIR extinction (4.35 and 2.00 times greater than control extinction, respectively) and is attributed to decreased particle loading by intravenous delivery. Although particle volume and concentration was significantly higher for intravenous injections, accumulation is likely limited by the extent of tumor angiogenesis and uptake by the reticuloendothelial system (RES). Treatment selectivity and efficacy was most apparent for direct injections; however, both methods showed significantly improved local tumor control.

Tumor growth suppression: direct versus intravenous injection. Groups of four to six mice were initially used to establish optimal conditions for near-infrared PPTT treatment of HSC-3 tumor xenografts. 15 µl of PEGylated gold nanorods ($OD_{\lambda=800}$=40) were directly administered at three sites within the tumor interstitium or 100 µL ($OD_{\lambda=800}$=120) were intravenously injected (tail). After two minutes, tumors directly injected with nanorods were subjected to extracorporeal NIR exposure (808 nm, 6 mm dia) and it was determined that 10-15 minutes of irradiation at 0.9-1.1 W/cm^2 was necessary for significant tumor response and minimal damage to surrounding tissues. After 24 hours, tumors intravenously administered with nanorods were also subjected to extracorporeal NIR exposure (808 nm, 6 mm dia) and it was determined that 10-15 minutes of irradiation at 1.7-1.9 W/cm^2 was necessary for significant tumor response and minimal damage to surrounding tissues. In addition, no statistically significant differences in tumor growth were observed for direct nanorod injections without NIR exposure, sham/NIR exposure alone, and PBS intratumoral injections alone (P=0.427

at day 9) (**Figure 3.4**). **Figure 3.5** illustrates typically observed tumor resorption and growth inhibition following direct injection of PEGylated gold nanorods and near-infrared PPTT versus sham/NIR treatments.

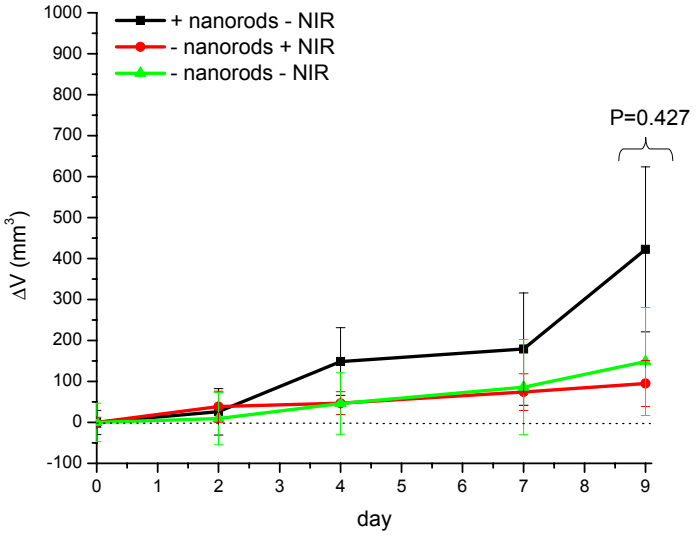

Figure 3.4. Observed changes in HSC-3 xenograft growth for 15 µL $OD_{\lambda=800}$=40 intratumoral PEGylated gold nanorod injections in female *nu/nu* mice without NIR exposure (■), 15 min 1.7-1.9 W/cm^2 NIR exposure alone (●), and 15 µL 10 mM PBS intratumoral injections (▲) alone (P=0.427 at day 9). Adapted from Dickerson et al. [*83*].

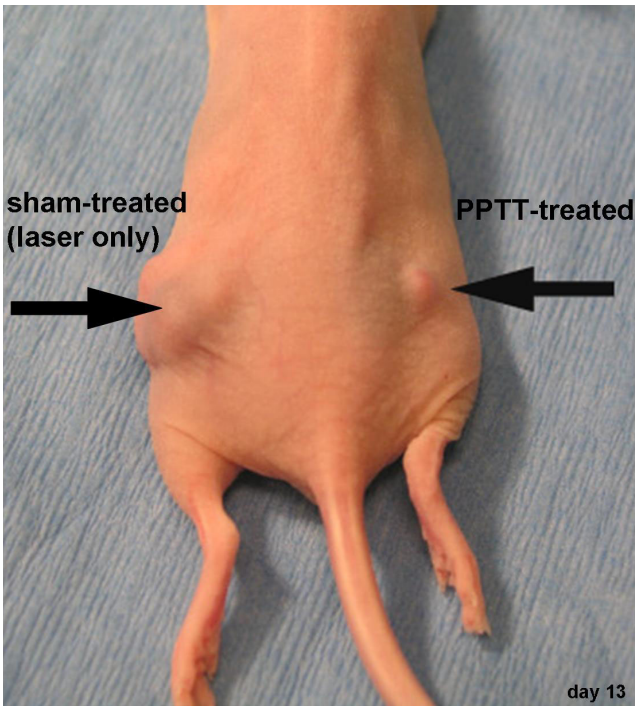

Figure 3.5. Representative HSC-3 tumor resorption and growth inhibition in female *nu/nu* mice at day 13 following direct injection of EPGylated gold nanorods (15 μL, $OD_{\lambda=800}$=40) and a single near-infrared PPTT treatment (10 min, 0.9-1.1 W/cm^2, 6 mm dia) versus sham/NIR treatment (15 μL, 10 mM PBS) at the same NIR laser exposure power density and duration. Adapted from Dickerson et al. [*83*].

Using previously established treatment conditions, change in tumor volume was recorded over a 13 day period for control mice, as well as those treated by intravenous and direct nanorod injections followed by PPTT (**Figure 3.6**). Here, control mice were subjected to 15 μL direct injection of 10 mM PBS to the tumor interstitium, with no NIR exposure. Average change in tumor volume for each group was plotted (**Figure 3.7**) and statistical hypothesis testing for differences in average tumor growth was performed (**Table 3.1**). **Figure 3.7** shows a >96% decrease in average tumor growth for directly treated HSC-3 xenografts and a >74% decrease in average tumor growth for intravenously treated HSC-3 xenografts at day 13 (relative to control tumors). Moreover, resorption of >57% of the directly treated tumors and 25% of the intravenously treated tumors was observed over the monitoring period.

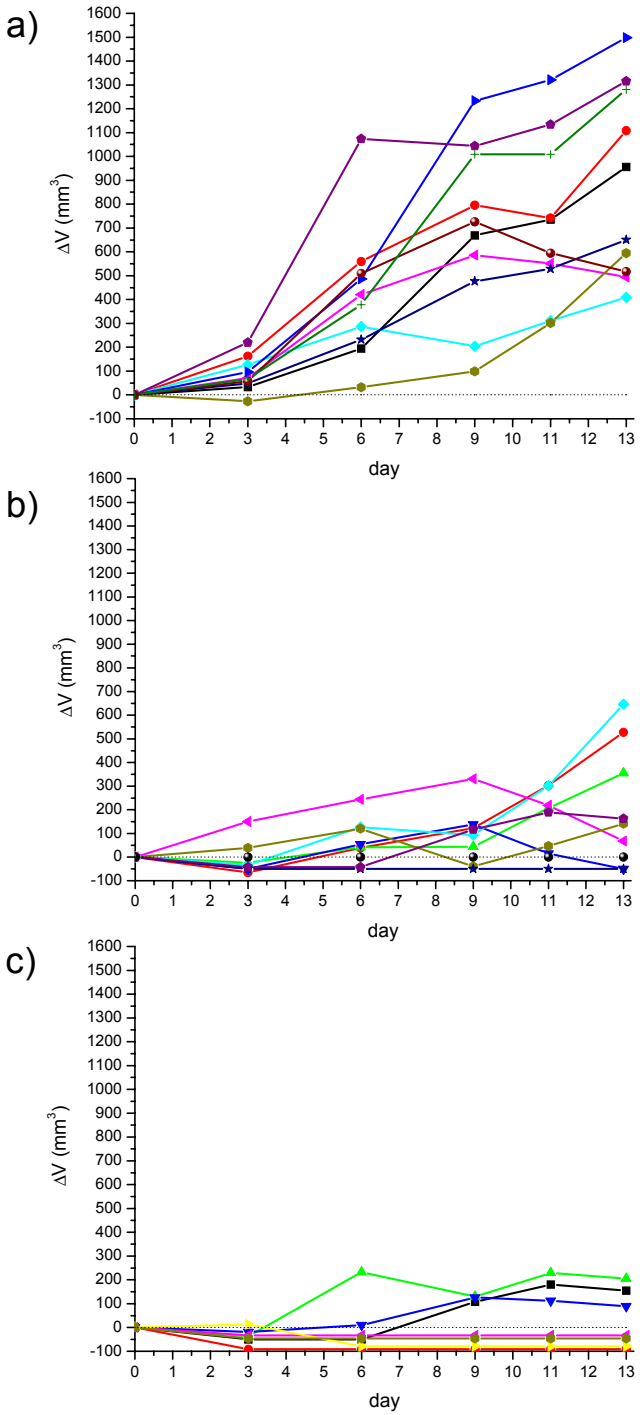

Figure 3.6. Change in tumor volume following near-infrared PPTT treatment of HSC-3 xenografts by (A) control, (B) intravenous, and (C) direct injections of PEGylated gold nanorods. Control mice were treated by interstitial injection of 15 µL 10 mM PBS alone, while direct PPTT treatments were performed by administration of 15 µL PEGylated gold nanorods ($OD_{\lambda=800}$=40, 2 min accumulation) followed by 10 min of 0.9-1.1 W/cm^2 NIR laser exposure. Intravenous PPTT treatments were performed by administration of 100 µL PEGylated gold nanorods ($OD_{\lambda=800}$=120, 24 hr accumulation) followed by 10 min of 1.7-1.9 W/cm^2 NIR laser exposure. Adapted from Dickerson et al. [*83*].

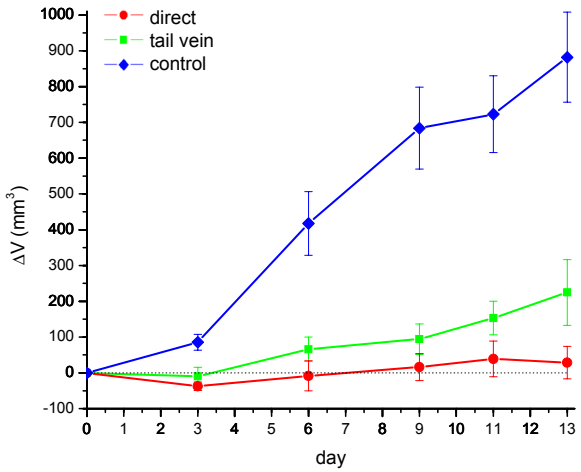

Figure 3.7. Average change in tumor volume for HSC-3 xenografts following near-infrared PPTT treatment by control (♦), intravenous (■), and direct (●) injection of PEGylated gold nanorods. Errors for control (n=10), direct injection (n=8), and intravenous injection (n=7) groups reported as standard error of the means. Control mice were treated by interstitial injection of 15 µL 10 mM PBS alone, while intravenous PPTT treatments were performed by administration of 100 µL PEGylated gold nanorods ($OD_{\lambda=800}$=120, 24 hr accumulation) followed by 10 min of 1.7-1.9 W/cm^2 NIR laser exposure. Direct PPTT treatments were performed by administration of 15 µL PEGylated gold nanorods ($OD_{\lambda=800}$=40, 2 min accumulation) followed by 10 min of 0.9-1.1 W/cm^2 NIR laser exposure. Adapted from Dickerson et al. [*83*].

Table 3.1. P-values for average volume change in HSC-3 tumors following near-infrared PPTT by 808 nm irradiation of PEGylated gold nanorods. Adapted from Dickerson et al. [*83*].

	day 0	day 3	day 6	day 9	day 11	day 13
direct vs control	-	0.0003	0.001	0.0002	0.0001	0.0001
tail vein vs control	-	0.0136	0.0037	0.0005	0.0004	0.0008
direct vs tail	-	0.3415	0.1896	0.1936	0.1205	0.084

Average tumor growth at day 13 for directly and intravenously treated tumors was significantly less than that observed in untreated control groups (P<0.0001 and P<0.0008, respectively). Differences in observed efficacy for direct and intravenous treatments gradually increased during the experiment, reaching statistical significance at the 8% level on day 13. Non-parametric analysis of variance for the treated and untreated groups (**Table 3.2**) found statistically

significant differences at the 2% level and below for the duration of the experiment. These results clearly indicate both the selectivity and specificity of near-infrared PPTT.

Table 3.2. Non-parametric analysis of variance for near-infrared PPTT treatment (2) and control groups. Adapted from Dickerson et al. [*83*].

day 0	day 3	day 6	day 9	day 11	day 13
-	0.0024	0.0009	0.0008	0.0001	0.0005

The dramatic changes in observed HSC-3 tumor growth are attributed to selective hyperthermia of malignant tissues treated with PEGylated gold nanorods by near-infrared PPTT. Preferential accumulation of PEGylated gold nanorods within the tumor interstitium occurs due to the EPR effect.[81] Because of their rapid metabolic rates, tumor cells are regarded as increasingly vulnerable to hyperthermic effects [*44,72*] such as disruption of metabolic signaling processes, protein denaturation, and the onset of acidosis or apoptosis caused by the production of heat-shock proteins [*84*] and other immunostimulants. Small increases in local temperature are known to result in disruption of nuclear and cytoskeletal assemblies and indeed, previous [*44,85*] and recent reports [*29,72*] indicate significant membrane blebbing [*86-88*] under hyperthermic conditions. Under severe conditions, hyperthermic damage can result in impaired vasculature supply, endothelial swelling,[44] and microthrombosis associated with homeostatic disruption.[*89*] *In vitro,* mild hyperthermia has been shown to impede the function of cell surface receptors, membrane transport, and RNA- and DNA-polymerization during protein synthesis. Repair of sublethal cell damage by DNA-polymerase-α and -β, such as that incurred during radiotherapy, has also been shown to be inhibited by hyperthermia. While tumor growth suppression and resorption is likely a cumulative result of the previously mentioned effects, it is presumed here that ablation of the tumor vasculature and localized membrane disruption predominates.

3.3 Outlook and Conclusions

Although the mechanism of cellular response in the present case is yet to be determined, the specificity of hyperthermic effects on tumor growth from both direct and intravenous near-infrared PPTT treatments is unmistakable ($P<0.0001$ and $P<0.0008$, respectively). Inhibition of average tumor growth and minimal damage to surrounding tissues is observed for both methods. Resorption of >57% of the directly-injected tumors and 25% of the intravenously-treated tumors clearly indicates the potential curative and adjunctive applications of NIR plasmonic photothermal therapy (PPTT) in pre-clinical settings.

3.4 References

1. Ferrari, M. Cancer nanotechnology: Opportunities and challenges. *Nat. Rev. Cancer* **5**, 161-171 (2005).

2. Gao, X. H., Cui, Y. Y., Levenson, R. M., Chung, L. W. K., & Nie, S. M. In vivo cancer targeting and imaging with semiconductor quantum dots. *Nat. Biotechnol.* **22**, 969-976 (2004).

3. Katz, E., & Willner, I. Integrated nanoparticle-biomolecule hybrid systems: Synthesis, properties, and applications. *Angew. Chem. Int. Edit.* **43**, 6042-6108 (2004).

4. Moghimi, S. M., Hunter, A. C., & Murray, J. C. Long-circulating and target-specific nanoparticles: Theory to practice. *Pharmacol. Rev* **53**, 283-318 (2001).

5. Niemeyer, C. M. Nanoparticles, proteins, and nucleic acids: Biotechnology meets materials science. *Angew. Chem. Int. Ed.* **40**, 4128-4158 (2001).

6. Rosi, N. L., & Mirkin, C. A. Nanostructures in biodiagnostics. *Chem. Rev.* **105**, 1547-1562 (2005).

7. Weissleder, R. A clearer vision for in vivo imaging. *Nat. Biotechnol.* **19**, 316-317 (2001).

8. Huang, X., Jain, P. K., El-Sayed, I. H., & El-Sayed, M. A. Gold nanoparticles and nanorods in medicine: From cancer diagnostics to photothermal therapy. *Nanomedicine* **2**, 681-693 (2007).

9. Burda, C., Chen, X. B., Narayanan, R., & El-Sayed, M. A. Chemistry and properties of nanocrystals of different shapes. *Chem. Rev.* **105**, 1025-1102 (2005).

10. Liz-Marzan, L. M. Tailoring surface plasmons through the morphology and assembly of metal nanoparticles. *Langmuir* **22**, 32-41 (2006).

11. Noguez, C. Surface plasmons on metal nanoparticles: The influence of shpae and physical environment. *J. Phys. Chem. C* **111**, 3806-3819 (2007).

12. Pileni, M. P. Self-assembly of inorganic nanocrystals: Fabrication and collective intrinsic properties. *Acc. Chem. Res.* **40**, 685-693 (2007).

13. Adams, D. M., Brus, L., Chidsey, C. E. D., Creager, S., Creutz, C., Kagan, C. R., Kamat, P. V., Lieberman, M., Lindsay, S., Marcus, R. A., Metzger, R. M., Michel-Beyerle, M. E., Miller, J. R., Newton, M. D., Rolison, D. R., Sankey, O., Schanze, K. S., Yardley, J., & Zhu, X. Y. Charge transfer on the nanoscale: Current status. *J. Phys. Chem. B* **107**, 6668-6697 (2003).

14. Thomas, L., Lionti, F., Ballou, R., Gatteschi, D., Sessoli, R., & Barbara, B. Macroscopic quantum tunnelling of magnetization in a single crystal of nanomagnets. *Nature* **383**, 145-147 (1996).

15. Daniel, M. C., & Astruc, D. Gold nanoparticles: Assembly, supramolecular chemistry, quantum-size-related properties, and applications toward biology, catalysis, and nanotechnology. *Chem. Rev.* **104**, 293-346 (2004).

16. Huh, Y. M., Jun, Y. W., Song, H. T., Kim, S., Choi, J. S., Lee, J. H., Yoon, S., Kim, K. S., Shin, J. S., Suh, J. S., & Cheon, J. In vivo magnetic resonance detection of cancer by using multifunctional magnetic nanocrystals. *J. Am. Chem. Soc.* **127**, 12387-12391 (2005).

17. Durr, N. J., Larson T, Smith DK, Korgel BA, Sokolov K, Ben-Yakar A Two-photon luminescence imaging of cancer cells using molecularly targeted gold nanorods. *Nano Lett.* **7**, 941-945 (2007).

18. Sokolov, K., Follen, M., Aaron, J., Pavlova, I., Malpica, A., Lotan, R., & Richards-Kortum, R. Real-time vital optical imaging of precancer using anti-epidermal growth factor receptor antibodies conjugated to gold nanoparticles. *Cancer Res.* **63**, 1999-2004 (2003).

19. Wang, H., Huff TB, Zweifel DA, He W, Low PS, Wei, A, Cheng JX In vitro and in vivo two-photon luminescence imaging of single gold nanorods. *Proc. Natl. Acad. Sci. U.S.A.* **102**, 15752-15756 (2005).

20. El-Sayed, I. H., Huang X, El-Sayed MA Surface plasmon resonance scattering and absorption of anti-EGFR antibody conjugated gold nanoparticles in cancer diagnostics: applications in oral cancer. *Nano Lett.* **5**, 829-834 (2005).

21. Loo, C., Lowery, A., Halas, N., West, J., & Drezek, R. Immunotargeted nanoshells for integrated cancer imaging and therapy. *Nano Lett.* **5**, 709-711 (2005).

22. Johannsen, M., Gneveckow, U., Eckelt, L., Feussner, A., Waldofner, N., Scholz, R., Deger, S., Wust, P., Loening, S. A., & Jordan, A. Clinical hyperthermia of prostate cancer using

magnetic nanoparticles: Presentation of a new interstitial technique. *Int. J. Hyperthermia* **21**, 637-647 (2005).

23. Kam, N. W. S., O'Connell, M., Wisdom, J. A., & Dai, H. J. Carbon nanotubes as multifunctional biological transporters and near-infrared agents for selective cancer cell destruction. *Proc. Natl. Acad. Sci. U.S.A.* **102**, 11600-11605 (2005).

24. Chen, J., Wang D, Xi J, Au L, Siekkinen A, Warsen A, Li ZY, Zhang H, Xia Y, Li X Immuno gold nanocages with tailored optical properties for targeted photothermal destruction of cancer cells. *Nano Lett.* **7**, 1318-1322 (2007).

25. El-Sayed, I. H., Huang X, El-Sayed MA Selective laser photo-thermal therapy of epithelial carcinoma using anti-EGFR antibody conjugated gold nanoparticles. *Cancer Lett.* **239**, 129-135 (2006).

26. Hirsch, L. R., Stafford, R. J., Bankson, J. A., Sershen, S. R., Rivera, B., Price, R. E., Hazle, J. D., Halas, N. J., & West, J. L. Nanoshell-mediated near-infrared thermal therapy of tumors under magnetic resonance guidance. *Proc. Natl. Acad. Sci. U.S.A.* **100**, 13549-13554 (2003).

27. Huang, X., El-Sayed IH, El-Sayed MA Cancer cell imaging and photothermal therapy in the near-infrared region by using gold nanorods. *J. Am. Chem. Soc.* **128**, 2115-2120 (2006).

28. Pitsillides, C. M., Joe EK, Wei X, Anderson RR, Lin CP Selective cell targeting with light-absorbing microparticles and nanoparticles. *Biophys. J.* **84**, 4023-4032 (2003).

29. Tong, L., Zhao, Y., Huff, T. B., Hansen, M. N., Wei, A., & Cheng, J. X. Gold Nanorods Mediate Tumor Cell Death by Compromising Membrane Integrity. *Adv. Mater.* **19**, 3136-3141 (2007).

30. Zharov, V. P., Galitovsky V, Viegas M Photothermal detection of local thermal effects during selective nanophotothermolysis. *Appl. Phys. Lett.* **83**, 4897-4899 (2003).

31. Connor, E. E., Mwamuka, J., Gole, A., Murphy, C. J., & Wyatt, M. D. Gold nanoparticles are taken up by human cells but do not cause acute cytotoxicity. *Small* **1**, 325-327 (2005).

32. Khan, J. A., Pillai, B., Das, T. K., Singh, Y., & Maiti, S. Molecular effects of uptake of gold nanoparticles in HeLa cells. *Chembiochem* **8**, 1237-1240 (2007).

33. Shukla, R., Bansal, V., Chaudhary, M., Basu, A., Bhonde, R. R., & Sastry, M. Biocompatibility of gold nanoparticles and their endocytotic fate inside the cellular compartment: A microscopic overview. *Langmuir* **21**, 10644-10654 (2005).

34. El-Sayed, M. A. Some interesting properties of metals confined in time and nanometer space of different shapes. *Acc. Chem. Res.* **34**, 257-264 (2001).

35. Link, S., & El-Sayed, M. A. Shape and size dependence of radiative, non-radiative and photothermal properties of gold nanocrystals. *Int. Rev. Phys. Chem.* **19**, 409-453 (2000).

36. Mie, G. Contribution to the optics of turbid media, especially colloidal metal suspensions. *Ann. Phys.* **25**, 377-445 (1908).

37. Huang, X., El-Sayed IH, Qian W, El-Sayed MA Cancer Cells Assemble and Align Gold Nanorods Conjugated to Antibodies to Produce Highly Enhanced, Sharp and Polarized Surface Raman Spectra: A Potential Cancer Diagnostic Marker. *Nano Lett.* **7**, 1591-1597 (2007).

38. Moskovits, M. Surface-Enhanced Spectroscopy. *Rev. Mod. Phys.* **57**, 783-826 (1985).

39. Stuart, D. A., Yuen, J. M., Lyandres, N. S. O., Yonzon, C. R., Glucksberg, M. R., Walsh, J. T., & Van Duyne, R. P. In vivo glucose measurement by surface-enhanced Raman spectroscopy. *Anal. Chem.* **78**, 7211-7215 (2006).

40. Amin, Z., Donald, J. J., Masters, A., Kant, R., Steger, A. C., Bown, S. G., & Lees, W. R. Hepatic Metastases - Interstitial Laser Photocoagulation with Real-Time Us Monitoring and Dynamic Ct Evaluation of Treatment. *Radiology* **187**, 339-347 (1993).

41. Eichler, K., Mack, M. G., Straub, R., Engelmann, K., Zangos, S., Woitaschek, D., & Vogl, T. J. Oligonodular hepatocellular carcinoma (HCC): MR-guided laser-induced thermotherapy (LITT). *Radiologe* **41**, 915-922 (2001).

42. Nolsoe, C. P., Torppedersen, S., Burcharth, F., Horn, T., Pedersen, S., Christensen, N. E. H., Olldag, E. S., Andersen, P. H., Karstrup, S., Lorentzen, T., & Holm, H. H. Interstitial Hyperthermia of Colorectal Liver Metastases with a Us-Guided Nd-Yag Laser with a Diffuser Tip - a Pilot Clinical-Study. *Radiology* **187**, 333-337 (1993).

43. Falk, M. H., & Issels, R. D. Hyperthermia in oncology. *Int. J. Hyperthermia* **17**, 1-18 (2001).

44. Hildebrandt, B., Wust, P., Ahlers, O., Dieing, A., Sreenivasa, G., Kerner, T., Felix, R., & Riess, H. The cellular and molecular basis of hyperthermia. *Crit. Rev. Oncol. Hematol.* **43**, 33-56 (2002).

45. Horsman, M. R., & Overgaard, J. Hyperthermia: a potent enhancer of radiotherapy. *Clin. Oncol.* **19**, 418-426 (2007).

46. Wust, P., Hildebrandt, B., Sreenivasa, G., Rau, B., Gellermann, J., Riess, H., Felix, R., & Schlag, P. M. Hyperthermia in combined treatment of cancer. *Lancet Oncol.* **3**, 487-497 (2002).

47. Dewey, W. C. Arrhenius Relationships from the Molecule and Cell to the Clinic. *Int. J. Hyperthermia* **10**, 457-483 (1994).

48. O'Neal, D. P., Hirsch LR, Halas NJ, Payne JD, West JL Photothermal Tumor Ablation in mice using near infrared absorbing nanoshells. *Cancer Lett.* **209**, 171-176 (2004).

49. Sultan, R. A. Tumour ablation by laser in general surgery. *Lasers Med. Sci.* **5**, 185-193 (1990).

50. Rau, B., Wust, P., Tilly, W., Gellermann, J., Harder, C., Riess, H., Budach, V., Felix, R., & Schlag, P. M. Preoperative radiochemotherapy in locally advanced or recurrent rectal cancer: Regional radiofrequency hyperthermia correlates with clinical parameters. *Int. J. Radiat. Oncol. Biol. Phys.* **48**, 381-391 (2000).

51. Song, C. W., Shakil, A., Osborn, J. L., & Iwata, K. Tumour oxygenation is increased by hyperthermia at mild temperatures. *Int. J. Hyperthermia* **12**, 367-373 (1996).

52. Issels, R. D., Abdel-Rahman, S., Wendtner, C. M., Falk, M. H., Kurze, V., Sauer, H., Aydemir, U., & Hiddemann, W. Neoadjuvant chemotherapy combined with regional hyperthermia (RHT) for locally advanced primary or recurrent high-risk adult soft-tissue sarcomas (STS) of adults: long-term results of a phase II study. *Eur. J. Cancer* **37**, 1599-1608 (2001).

53. Overgaard, J., Gonzalez, D. G., Hulshof, M., Arcangeli, G., Dahl, O., Mella, O., & Bentzen, S. M. Randomized Trial of Hyperthermia as Adjuvant to Radiotherapy for Recurrent or Metastatic Malignant-Melanoma. *Lancet* **345**, 540-543 (1995).

54. Rau, B., Wust, P., Hohenberger, P., Loffel, J., Hunerbein, M., Below, C., Gellermann, J., Speidel, A., Vogl, T., Riess, H., Felix, R., & Schlag, P. M. Preoperative hyperthermia combined with radiochemotherapy in locally advanced rectal cancer - A phase II clinical trial. *Ann. Surg.* **227**, 380-389 (1998).

55. van der Zee, J., Gonzalez, D. G., van Rhoon, G. C., van Dijk, J. D. P., van Putten, W. L. J., & Hart, A. A. M. Comparison of radiotherapy alone with radiotherapy plus hyperthermia in locally advanced pelvic tumours: a prospective, randomised, multicentre trial. *Lancet* **355**, 1119-1125 (2000).

56. Vernon, C. C., Hand, J. W., Field, S. B., Machin, D., Whaley, J. B., vanderZee, J., vanPutten, W. L. J., vanRhoon, G. C., vanDijk, J. D. P., Gonzalez, D. G., Liu, F. F., Goodman, P., & Sherar, M. Radiotherapy with or without hyperthermia in the treatment of superficial localized breast cancer: Results from five randomized controlled trials. *Int. J. Radiat. Oncol. Biol. Phys.* **35**, 731-744 (1996).

57. McKenziei, A. L., Carruth JAS Lasers in surgery and medicine. *Phys. Med. Biol.* **29**, 619-641 (1984).

58. Svaasand, L. O., Gomer CJ, Morinelli EA On the physical rationale of laser induced hyperthermia. *Lasers Med. Sci.* **5**, 121-128 (1990).

59. Brunetaud, J. M., Mordon S, Maunoury V, Beacco C Non-PDT uses of lasers in oncology. *Lasers Med. Sci* **10**, 3-8 (1995).

60. Chen, W. R., Adams, R. L., Bartels, K. E., & Nordquist, R. E. Chromophore-Enhanced in-Vivo Tumor-Cell Destruction Using an 808-Nm Diode-Laser. *Cancer Lett.* **94**, 125-131 (1995).

61. Chen, W. R., Adams, R. L., Carubelli, R., & Nordquist, R. E. Laser-photosensitizer assisted immunotherapy: A novel modality for cancer treatment. *Cancer Letters* **115**, 25-30 (1997).

62. Chen, W. R., Adams, R. L., Higgins, A. K., Bartels, K. E., & Nordquist, R. E. Photothermal effects on murine mammary tumors using indocyanine green and an 808-nm diode laser: An in vivo efficacy study. *Cancer Lett.* **98**, 169-173 (1996).

63. Dolmans, D., Fukumura, D., & Jain, R. K. Photodynamic therapy for cancer. *Nat. Rev. Cancer* **3**, 380-387 (2003).

64. Dougherty, T. J., Gomer, C. J., Henderson, B. W., Jori, G., Kessel, D., Korbelik, M., Moan, J., & Peng, Q. Photodynamic therapy. *J. Natl. Cancer Inst.* **90**, 889-905 (1998).

65. Henderson, B. W., & Dougherty, T. J. How Does Photodynamic Therapy Work. *Photochem. Photobiol.* **55**, 145-157 (1992).

66. Elisseeff, J., Anseth, K., Sims, D., McIntosh, W., Randolph, M., & Langer, R. Transdermal photopolymerization for minimally invasive implantation. *Proc. Natl. Acad. Sci. U.S.A.* **96**, 3104-3107 (1999).

67. Murphy, C. J., San, T. K., Gole, A. M., Orendorff, C. J., Gao, J. X., Gou, L., Hunyadi, S. E., & Li, T. Anisotropic metal nanoparticles: Synthesis, assembly, and optical applications. *J. Phys. Chem. B* **109**, 13857-13870 (2005).

68. Nikoobakht, B., & El-Sayed, M. A. Preparation and growth mechanism of gold nanorods (NRs) using seed-mediated growth method. *Chem. Mat.* **15**, 1957-1962 (2003).

69. Wiley, B., Sun, Y., & Xia, Y. Synthesis of Silver Nanostructures with Controlled Shapes and Properties. *Acc. Chem. Res.* **40**, 1067-1076 (2007).

70. Huang, X., Jain PK, El-Sayed IH, El-Sayed MA Plasmonic photothermal therapy using gold nanoparticles. *Lasers Med. Sci.* **ASAP** (2007).

71. Huang, X., El-Sayed IH, Qian W, El-Sayed MA The potential use of the enhanced nonlinear properties of gold nanospheres in photothermal cancer therapy. *Lasers Surg. Med.* **39**, 747-753 (2007).

72. Huff, T. B., Tong, L., Zhao, Y., Hansen, M. N., Cheng, J. X., & Wei, A. Hyperthermic effects of gold nanorods on tumor cells. *Nanomedicine* **2**, 125-132 (2007).

73. Hu, M., Chen, J. Y., Li, Z. Y., Au, L., Hartland, G. V., Li, X. D., Marquez, M., & Xia, Y. N. Gold nanostructures: engineering their plasmonic properties for biomedical applications. *Chem. Soc. Rev.* **35**, 1084-1094 (2006).

74. Gans, R. Form of ultramicroscopic particles of silver. *Ann. Phys.* **47**, 270-284. (1915).

75. Gole, A., & Murphy, C. J. Seed-mediated synthesis of gold nanorods: Role of the size and nature of the seed. *Chem. Mater.* **16**, 3633-3640 (2004).

76. Perez-Juste, J., Pastoriza-Santos, I., Liz-Marzan, L. M., & Mulvaney, P. Gold nanorods: Synthesis, characterization and applications. *Coord. Chem. Rev.* **249**, 1870-1901 (2005).

77. Harris, J. M., & Chess, R. B. Effect of pegylation on pharmaceuticals. *Nat. Rev. Drug Discov.* **2**, 214-221 (2003).

78. Huff, T. B., Hansen, M. N., Zhao, Y., Cheng, J. X., & Wei, A. Controlling the cellular uptake of gold nanorods. *Langmuir* **23**, 1596-1599 (2007).

79. Liao, H. W., & Hafner, J. H. Gold nanorod bioconjugates. *Chem. Mater.* **17**, 4636-4641 (2005).

80. Niidome, T., Yamagata, M., Okamoto, Y., Akiyama, Y., Takahashi, H., Kawano, T., Katayama, Y., & Niidome, Y. PEG-modified gold nanorods with a stealth character for in vivo applications. *J. Controlled Release* **114**, 343-347 (2006).

81. Maeda, H. The enhanced permeability and retention (EPR) effect in tumor vasculature: The key role of tumor-selective macromolecular drug targeting. *Adv. Enzyme Reg.* **41**, 189-207 (2001).

82. Jain, R. K. Transport of Molecules in the Tumor Interstitium: A Review. *Cancer Res.* **47**, 3039-3051 (1987).

83. Dickerson, E. B., Dreaden, E. C., Huang, X., El-Sayed, I. H., Chu, H., Pushpanketh, S., McDonald, J. F., & El-Sayed, M. A. Gold nanorod assisted near-infrared plasmonic photothermal therapy (PPTT) of squamous cell carcinoma in mice. *Cancer Lett.* **269**, 57-66 (2008).

84. Li, G. C., Mivechi, N. F., & Weitzel, G. Heat-Shock Proteins, Thermotolerance, and Their Relevance to Clinical Hyperthermia. *Int. J. Hyperthermia* **11**, 459-488 (1995).

85. Borrelli, M. J., Wong, R. S. L., & Dewey, W. C. A Direct Correlation between Hyperthermia-Induced Membrane Blebbing and Survival in Synchronous G1 Cho Cells. *J. Cel. Physiol.* **126**, 181-190 (1986).

86. Coleman, M. L., Sahai, E. A., Yeo, M., Bosch, M., Dewar, A., & Olson, M. F. Membrane blebbing during apoptosis results from caspase-mediated activation of ROCK I. *Nat. Cell Biol.* **3**, 339-345 (2001).

87. Sebbagh, M., Renvoize, C., Hamelin, J., Riche, N., Bertoglio, J., & Breard, J. Caspase-3-mediated cleavage of ROCK I induces MLC phosphorylation and apoptotic membrane blebbing. *Nat. Cell Biol.* **3**, 346-352 (2001).

88. Mills, J. C., Stone, N. L., Erhardt, J., & Pittman, R. N. Apoptotic membrane blebbing is regulated by myosin light chain phosphorylation. *J. Cell Bio.* **140**, 627-636 (1998).

89. Kowal-Vern, A., McGill, V., Walenga, J. M., & Gamelli, R. L. Antithrombin III concentrate in the acute phase of thermal injury. *Burns* **26**, 97-101 (2000).

CHAPTER 4

GOLD NANOPARTICLES FOR THE TARGETED DIAGNOSIS/TREATMENT OF HORMONE-DEPENDENT TUMORS

4.1 Antiestrogen Gold Nanoparticles

4.1.1 Estrogen Receptor, Membrane Association, and Cancer

Binding of the steroidal hormone 17β-estradiol (E_2) to estrogen receptor (ER) is a process essential to normal cell proliferation and differentiation in women. E_2 binding induces a conformational change in ER which allows it to recruit cofactors necessary for the transcription of various genes commonly upregulated in malignant cells [*1*] (e.g. transforming growth factor alpha,[*2*] *c-myc*,[*3*] and cathepsin D [*4*]. Accordingly, hormone receptors such as ER or progesterone receptor are overexpressed in 75–80% of all breast cancers.[*5*] Antiestrogen compounds, such as the small molecule breast cancer treatment drug tamoxifen (TAM) compete with E_2 for binding to ER, conformationally preventing adoption of associated transcription cofactors and subsequently initiating programmed cell death.[*6-9*]

Diagnostic and therapeutic applications of functionalized nanoparticles are highly attractive due to the inherently multivalent nature of their surface.[*10-15*] Like divalent antibodies, the binding affinity of a nanoparticle conjugate is enhanced proportional to the density of its binding sites. Receptor-mediated therapeutic response (i.e. potency) is similarly increased as a function of local ligand concentration and in cases where intracellular drug transport relies on passive diffusion, uptake of nanoparticle conjugates can greatly increase delivery rates.[*16,17*] Enhanced permeability and retention (EPR) of nano-sized drug conjugates can also lead to augmented and preferential

accumulation at tumor sites in vivo.[*18,19*] Due to their biocompatibility,[*20,21*] stability,[*22*] and potential use in photothermal laser treatments,[*19,23-27*] gold nanoparticles are excellent candidates for such ligand-receptor targeting strategies of cancer treatment.

Selective targeting and delivery of gold nanoparticles functionalized with ligands of cell surface receptors overexpressed by malignant cells has been well documented. Huang et al. have shown that oral cancer cells that upregulate human epidermal growth factor receptor (EGFR, HER1, ErbB1) can be selectively labeled and photothermally destroyed by gold nanospheres and nanorods targeted with IgG antibodies.[*25,28*] ScFv fragments of anti-EGFR have also been used to selectively target and accumulate gold nanoparticles at tumor sites in vivo.[*29*] The folate receptor has been employed to selectively deliver gold nanospheres to malignant cells in vitro,[*30*] while Wei and coworkers have similarly demonstrated selective uptake and photothermal therapy of cancer cells using gold nanorods functionalized with a thiol-polyethylene glycol folate derivative.[*26,31*]

Like several members of the hormone receptor family, ER isoforms are located both intracellularly and on the cell membrane.[*11,32,33*] Gold nanoparticle analogs of the commercial pharmaceutical tamoxifen could therefore act not only as, selective targeting agents, but also as increasingly potent endocrine treatments for malignancies which overexpress ER (e.g. breast cancer). To this aim, a thiol-polyethylene glycol (PEG-SH) tamoxifen derivative was synthesized for subsequent gold nanoparticle (AuNP) conjugation (**Figure 4.1**). A biocompatible [*19,34*] PEG-SH linker was employed (i) to enable covalent attachment to the AuNP surface (Au-S 126 kJ mol^{-1}), [*35,36*] (ii) to minimize opsonin binding and reticulo-endothelial system uptake,[*37*] (iii) to suppress non-specific cell binding/uptake [*38*] and protein adsorption,[*19,22*] and (iv) to afford stability [*22*] over a wide range of temperature, ionic strength, and pH.

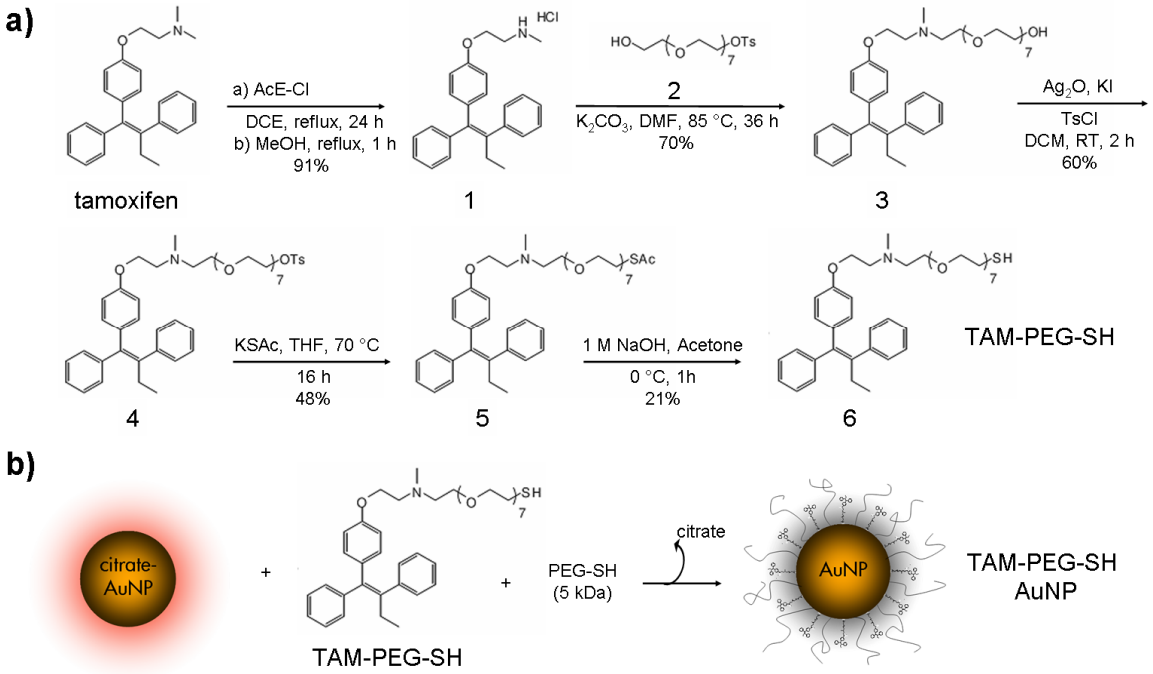

Figure 4.1. A) Synthesis of thiol-PEGylated tamoxifen (TAM-PEG-SH) and (B) covalent attachment to 25 nm gold nanoparticles (AuNPs). Adapted from Dreaden et al. [*39*].

Our results have shown enhanced potency and selective intracellular delivery of tamoxifen-targeted gold nanoparticles to ER(+) breast cancer cells in vitro. Particle uptake was observed in both a receptor- and ligand- dependent fashion with up to 2.7 –fold enhanced drug potency versus the free drug. Both delivery and therapeutic response were shown to be suppressed by estrogen competition. Optical microscopy/spectroscopy and cell viability indicate that augmented growth inhibition versus the free drug can be attributed to increased rates of intracellular TAM transport by cellular uptake of the nanoparticle conjugate. Receptor- and ligand- dependent nanoparticle delivery suggests that the plasma membrane localized estrogen receptor alpha may facilitate selective particle uptake and presents future opportunities for co-administration of laser photothermal therapy.[*19,23-27*]

4.1.2 Design and Development of Antiestrogen and Antiangrogen Gold Nanoparticles

Synthesis of thiol-pegylated tamoxifen (TAM-PEG-SH). Octaethylene glycol (OEG), Tamoxifen, and all chemicals used in the synthesis were purchased from Sigma Aldrich. Anhydrous solvents and other reagents were purchased and used without further purification. Analtech silica gel plates (60 F_{254}) were used for analytical TLC, and Analtech preparative TLC plates (UV 254, 2000 μm) were used for purification. UV light was used to examine the spots. 200-400 Mesh silica gel was used in column chromatography. NMR spectra were recorded on a Varian-Gemini 400 magnetic resonance spectrometer. ^{1}H and ^{13}C NMR spectra were recorded in parts per million (ppm) relative to the peaks of $CDCl_3$, (7.24 and 77.0 ppm, respectively). Mass spectra were recorded at the Georgia Institute of Technology mass spectrometry facility in Atlanta, GA.

Synthesis of N-Desmethyl tamoxifen **(1)**. The synthetic procedure was adapted from Olofson et al.;[*40*] briefly, tamoxifen (0.53 g, 1.43 mmol) was dissolved in anhydrous CH_2Cl_2 (15 ml) at 0 °C followed by addition of α-chloroethyl chloroformate (0.17 ml, 1.49 mmol). After 15 min at 0 °C, the reaction was refluxed for 24 h. The solvent was evaporated off to obtain a yellowish oil, to which methanol (10 ml) was added and refluxed for approximately 3 h. The solvent was evaporated off, and purification performed by gel filtration using CH_2Cl_2, then 10:1 CH_2Cl_2/CH_3OH to obtain 0.52 g (91 %) of N-desmethyl tamoxifen **2**. ^{1}H NMR (DMSO, 400 MHz) δ 0.89 (3H, t, J = 7.2 Hz), 2.43 (2H, q, J = 14.8, 7.6 Hz), 2.56 (3H, s), 3.12 (2H, t, J = 4.0 Hz), 4.08 (2H, t, J = 4.8 Hz), 6.57 (2H, d, J = 8.8 Hz), 6.76 (2H, d, J = 8.8 Hz), 7.03 – 7.31 (10H, m), 9.56 (1H, br); HRMS [FAB, mnba] $(C_{25}H_{27}NO)^{+}$ calcd, 358.2171; found, 358.2198.

Synthesis of Tosyl octaethylene glycol **(2)**. The synthetic procedure was adapted from Bouzide and Sauvé.[*41*] Briefly, octaethylene glycol (0.50 g, 1.35 mmol) was dissolved in anhydrous CH_2Cl_2 (7 ml) at 0 °C, followed by addition of freshly prepared Ag_2O (0.47 g, 2.02 mmol), KI (0.09 g, 0.50 mmol), and then TsCl (0.26 g, 1.35 mmol). The reaction mixture was left to stir at 0 °C, under

argon for 30 min, after which TLC deemed the reaction complete. Ag_2O was filtered off over a pad of celite cake washing with 12:1 CH_2Cl_2/CH_3OH. The filtrate was concentrated and purified on a silica column using 3:2, then gradually 1:4 CH_2Cl_2/acetone to yield the title compound as a colorless oil (0.55 g, 78 %). ^{1}H NMR ($CDCl_3$, 400 MHz) δ 2.44 (3H, s), 2.81 (1H, br), 3.58 – 3.70 (30H, m), 4.15 (2H, t, J = 4.8 Hz), 7.35 (2H, d, J = 8.4 Hz), 7.80 (2H, d, J = 8.4 Hz); HRMS [ESI] $(C_{23}H_{40}O_{11}S + H)^+$ calcd, 525.2364; found, 525.2377.

Synthesis of Tamoxifen-OEG-OH (**3**). N-Desmethyl tamoxifen (**1**) (0.27 g, 0.68 mmol) and tosyl octaethylene glycol (**2**) (0.54 g, 1.05 mmol) were dissolved in anhydrous DMF (10 ml), followed by addition of K_2CO_3 (0.95 g, 6.85 mmol), and stirred under argon at ~ 85 °C for 24 h. DMF was evaporated off. Ethyl acetate was added to the residue and the resulting suspension was filtered off to remove excess K_2CO_3. Solvent was evaporated from the filtrate and the crude was purified by preparatory TLC using 12:1:0.1 $CH_2Cl_2/CH_3OH/NH_4OH$ to obtain 0.342 g (70 %) of compound **3** as an oil. ^{1}H NMR ($CDCl_3$, 400 MHz) δ 0.90 (3H, t, J = 7.2 Hz), 1.85 (1H, br), 2.31 (3H, s), 2.44 (2H, q, J = 14.0, 7.2 Hz), 2.64 (2H, t, J = 6.0 Hz), 2.76 (2H, t, J = 6.0 Hz), 3.53 – 3.72 (30H, m), 3.91 (2H, t, J = 6.4 Hz), 6.54 (2H, m), 6.76 (2H, m), 7.10 – 7.40 (10H, m); ^{13}C NMR ($CDCl_3$, 100 MHz) δ 13.8, 29.2, 43.3, 50.7, 56.6, 57.2, 61.7, 65.6, 69.1, 70.3, 70.5, 70.6, 70.7, 70.8, 73.0, 113.6, 126.2, 126.7, 128.0, 128.3, 129.7, 129.9, 132.1, 135.8, 138.4, 141.5, 142.6, 144.0, 156.8; HRMS [ESI] $(C_{41}H_{59}NO_9 + H)^+$ calcd, 710.4262; found, 710.4253.

Synthesis of Tamoxifen-OEG-Tosylate (**4**). Tamoxifen-OEG-OH (**3**) (0.33 g, 0.46 mmol) was dissolved in anhydrous CH_2Cl_2 (10 ml) at 0 °C, followed by addition of Ag_2O (0.16 g, 0.69 mmol), KI (0.03 g, 0.18 mmol), and then TsCl (0.096 g, 0.5 mmol). Stirring was continued for 2 h at 0 °C, then at room temperature, overnight. Ag_2O was filtered off through a pad of celite cake washing with ethyl acetate. Purification was performed on silica column eluting with 12:1 CH_2Cl_2/CH_3OH

yielding the title compound as oil (0.24 g, 60 %). ^{1}H NMR ($CDCl_3$, 400 MHz) δ 0.91 (3H, t, J = 7.2 Hz), 2.31 – 2.46 (8H, m), 2.71 (2H, br), 2.83 (2H, br), 3.57 – 3.70 (28H, m), 3.95 (2H, br), 4.15 (2H, t, J = 4.4 Hz), 6.53 (2H, d, J = 8.4 Hz), 6.76 (2H, d, J = 8.8 Hz), 7.10 – 7.34 (12H, m), 7.80 (2H, d, J = 8.4 Hz); LRMS [ESI] ($C_{48}H_{65}NO_{11}S$ + H)$^+$ calcd, 864.1; found, 864.5.

Synthesis of Tamoxifen-OEG-SAc (**5**). KSAc (0.079 g, 0.69 mmol) was added to tamoxifen-OEG-Tosylate (**4**) (0.12 g, 0.14 mmol) dissolved in anhydrous THF and refluxed under argon at ~ 75 °C for 16 h. TLC analysis indicated a substantial consumption of the starting material. THF was evaporated off, and the crude product dissolved in ethyl acetate. Decolorizing carbon was added and then filtered. Solvent was evaporated from the filtrate and the crude was purified by preparatory TLC using 12:1 CH_2Cl_2/CH_3OH to obtain 50 mg (48 %) of **5** as reddish oil. ^{1}H NMR ($CDCl_3$, 400 MHz) δ 1.03 (3H, t, J = 7.2 Hz), 2.45 (3H, s), 2.47 (3H, s), 2.56 (2H, q, J = 15.2, 7.6 Hz), 2.80 (2H, t, J = 6.0 Hz), 2.91 (2H, t, J = 5.6 Hz), 3.21 (2H, t, J = 6.0 Hz), 3.70 – 3.80 (28H, m), 4.05 (2H, t, J = 6.0 Hz), 6.66 (2H, d, J = 8.0 Hz), 6.88 (2H, d, J = 8.0 Hz), 7.22 – 7.46 (10H, m); HRMS [ESI] ($C_{43}H_{61}NO_9S$ + H)$^+$ calcd, 768.4139; found, 768.4118.

Synthesis of Thiol-peglated tamoxifen **(6)**. Tamoxifen-OEG-SAc (**5**) (0.05 g, 0.065 mmol) was dissolved in acetone (1.5 ml) at 0 °C, followed by addition of 1M NaOH (1.5 ml) and stirring continued at 0 °C for 7 h. The reaction mixture was quenched with water (20 ml), and then extracted with 20 % CH_3OH in CH_2Cl_2 (4 × 15 mL). The organic layers were combined, dried under sodium sulfate, evaporated and purified on preparatory TLC using 11:1 CH_2Cl_2/CH_3OH to give 10 mg (21 %) of the title compound as reddish semi-solid. ^{1}H NMR ($CDCl_3$, 400 MHz) δ 0.90 (3H, t, J = 7.2 Hz), 2.32 (3H, s), 2.44 (2H, q, J = 8.0,7.6 Hz), 2.65 (2H, t, J = 6.0 Hz), 2.76 (2H, t, J = 6.4 Hz), 2.85 (2H, t, J = 6.8 Hz), 3.53 – 3.72 (28H, m), 3.91 (2H, t, J = 6.0 Hz), 6.52 (2H, d, J = 8.8 Hz), 6.74 (2H, d, J = 8.8 Hz), 7.08 – 7.32 (10H, m); ^{13}C NMR ($CDCl_3$, 100 MHz) δ 13.5, 28.9, 29.6,

38.3, 43.3, 56.4, 57.0, 65.6, 69.2, 69.6, 70.3, 70.4, 70.5, 70.6, 113.3, 125.9, 126.4, 127.8, 128.0, 129.4, 129.6, 131.8, 135.4, 138.1, 141.2, 142.3, 143.7, 156.6; HRMS [ESI] $(C_{41}H_{59}NO_8S]^+$ calcd, 725.3961; found, 725.4011.

Gold nanoparticle synthesis and TAM-PEG-SH conjugation. Gold nanoparticles (25 nm dia) were synthesized by Turkevich reduction of chloroauric acid.[*42*] Briefly, 20 mL of 3.5 mg/mL aqueous sodium citrate was added to 200 mL of 1.0 mM aqueous $HAuCl_4$ under reflux, with stirring. The solution was refluxed for 15 min, then removed from the heat and stirred for an additional 30 min. Excess sodium citrate was removed from the crude AuNP solution by centrifugation (13,000 × g).

TAM-PEG-SH (5 mg) was solubilized in 100 μL ethanol and diluted to 0.5 mM in deionized water. 0.5 mM PEG-SH (5 kDa, Lysan Bio) was solubilized in deioninized water and PEG-SH or a 1:1 ratio TAM-PEG-SH and PEG-SH were added at a 1.4×10^4 -fold molar excess to a concentrated solution of citrate-capped AuNPs followed by overnight sonication. Particle concentration was estimated using the molar extinction coefficient for 23 nm citrate-capped gold nanospheres determined by Orendorff and Murphy (1.3×10^9 $M^{-1}cm^{-1}$).[*43*] TAM-PEG-SH AuNP conjugates were dispersed in DMEM growth media supplanted with 10% v/v heat-inactivated fetal bovine serum, penicillin (100 U/ml), streptomycin (100 μg/ml), 4.5 g/L glucose, 4.5 g/L sodium pyruvate, without L-glutamine and phenol red to final *ligand* concentrations of 0.1, 0.5, 1, 2, 5, 10, and 20 μM and used immediately.

Gold Nanoparticle and Bioconjugate Characterization. Gold nanoparticles were analyzed by diffraction-contrast Transmission Electron Microscopy (TEM, JEOL 100CX II) and UV-Vis absorption spectroscopy (Ocean Optics, HR4000CG-UV-NIR). Absorption of TAM-PEG-SH at 280 nm was used to quantify the number of bound TAM-PEG-SH ligands per nanoparticle. An

aqueous solution of gold nanospheres was incubated with a 1.4×10^4 -fold molar excess of both TAM-PEG-SH and PEG-SH overnight with sonication. Nanoparticle-conjugates were removed from solution by centrifugation (45 min, 13,000 × g) and the observed change in UV absorption (280 nm) before and after nanoparticle conjugation was used to approximate the number of bound ligands. No contribution to absorption by PEG-SH was observed at these wavelengths and it assumed to occupy the majority of the remaining surface sites.

Zeta potential of the gold nanoparticles and conjugates was measured using a NanoZS Zetasizer particle analyzer (Malvern) equipped with a 633 nm laser.

Cell culture and nanoparticle incubation. ERα(-) MDA-MB-231 and ERα(+) MCF-7 breast cancer cells (human adenocarcinoma, ATCC) or ERα(+) human squamous cell carcinoma [*44-46*] (HSC-3) cells were cultured to 10^5 cells/cm^2 in DMEM growth media supplanted with 10% v/v heat-inactivated fetal bovine serum, penicillin (100 U/ml), streptomycin (100 μg/ml), 4.5 g/L glucose, 4.5 g/L sodium pyruvate, without L-glutamine and phenol red at 37 °C in a 5% CO_2 humidified atmosphere. Growth media was removed from the cell cultures and replaced with identical media containing gold nanoparticle conjugates heated to 37 °C at time = 0 h.

Cell viability assay. Following incubation, growth media containing gold nanoparticle conjugates was removed and cells were rinsed twice in sterile Dulbecco's phosphate buffered saline (DPBS). Mitochondrial dehydrogenase activity was assessed by MTT or XTT spectrophotometric assay (Sigma TOX1, TOX2) following the manufacturer's instructions. The assay was performed using a SpectraMax Plus 384 microplate reader and statistical analysis was performed by t-test.

Selected-area absorption microspectrometry and dark-field scattering microscopy. Collagen-coated growth substrates were prepared by immersion of 18 mm dia glass coverslips in ethanol, followed by 30 min UV sterilization. Coverslips were immersed in a 0.22 μm filtered 0.04 mg/mL collagen

(Roche) solution - prepared by solubilization in 5 mL 1% v/v aqueous acetic acid and dilution in 250 mL sterile DPBS for 6 h at 37 °C in a 5% CO_2 humidified atmosphere. The coated substrates were rinsed in sterile DPBS and placed in 12-well plates immediately prior to cell passage. Following incubation with gold nanoparticle conjugates, substrates were twice rinsed in sterile DPBS buffer and cells were fixed in cold 4 % wt/wt paraformaldehyde in DPBS buffer for 15 min. Coverslips were coated in glycerol, then mounted and sealed onto glass slides.

Dark-field microscopy was performed using an inverted objective Olympus IX70 microscope fitted with a dark-field condenser (U-DCW), 100x/1.35 oil Iris objective (UPLANAPO), tungsten lamp, and a Nikon D200 digital SLR camera. Optical extinction spectra were obtained in a transmission configuration using a SEE110 absorption microspectrometer fitted with a pinhole aperture, fiber optic-coupled CCD array detector, 50 × objective, and tungsten lamp. Periodic oscillations observed in some spectra are the result of interference between adjacent surfaces of the glass slides.

4.1.3 Preclinical Evaluation of Antiestrogen and Antiandrogen Gold Nanoparticles

The crude AuNP colloid (ca. 3 nM) was found by TEM to be predominantly comprised of 25 nm gold spheres exhibiting an extinction maximum at 530 nm (**Figure 4.2**). Based on the change in UV absorption (280 nm) of TAM solutions following nanoparticle conjugation and removal, we estimate 12,000 TAM-PEG-SH ligands per particle - 41 % of the maximum theoretical surface coverage for a 25 nm dia Au (111) surface. A change in zeta potential from -38.4 mV to -5.79 mV was also observed following TAM-PEG-SH functionalization. To preserve aqueous stability, TAM-PEG-SH AuNPs were not centrifuged prior to in vitro experiments, leaving 13 % of free drug in solution. *For comparison, concentrations for the nanoparticle conjugate are reported as effective ligand concentration (i.e. TAM-PEG-SH) throughout.*

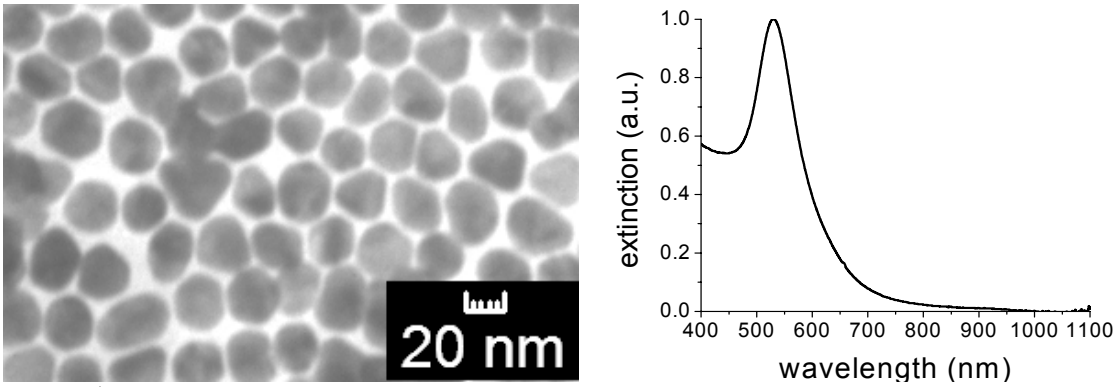

Figure 4.2. Transmission electron microscopy (left) and optical extinction (right) of gold nanoparticles used in tamoxifen-targeting experiments. Adapted from Dreaden et al. [*39*].

Dark-field scattering microscopy was performed to assess intracellular nanoparticle uptake. **Figure 4.3** illustrates representative images of ERα(+) [MCF-7, top] and ERα(-) [MDA-MB-231, bottom] breast cancer cells incubated for 24 h with 1 μM TAM-PEG-SH AuNPs and PEG-SH AuNPs. ERα(+) breast cancer cells displayed a high degree of intracellular and perinuclear localization of TAM-PEG-SH AuNPs, while ER(-) breast cancer cells showed no such labeling. These findings are consistent with both reported expression levels and cellular localization [*47*] of ERα in MCF-7 [*48-50*] and MDA-MB-231 [*49,51*] cell lines. As anticipated,[*38*] AuNPs labeled only with PEG-SH exhibited no apparent cellular labeling or uptake for either ERα(+) or ERα(-) breast cancer cells. Uptake of TAM-PEG-SH AuNPs by ERα(+) breast cells was observed to be time-dependent, with marginal cell surface labeling at 2-6 h and a high degree of perinuclear and cytoplasmic localization at 24 h (**Figure 4.4**). To further demonstrate ER expression-dependent targeting, ERα(+) human squamous [HSC-3] oral cancer cells were incubated for 24 h in the presence of 1 μM TAM-PEG-SH AuNPs and PEG-SH AuNPs. Dark-field scattering images from HSC-3 cells show selective uptake of the TAM-PEG-SH AuNPs in a manner similar to that obtained from MCF-7 breast cancer cells (**Figure 4.5**). Selected-area optical extinction spectra obtained from the ERα(+) and ERα(-) breast cells exhibited AuNP surface plasmon extinction exclusively from

perinuclear regions of ERα(+) cells incubated with TAM-PEG-SH AuNPs (s/n~10) (**Figure 4.6**).

Extinction from PEG-SH AuNPs was not observed from either cell line.

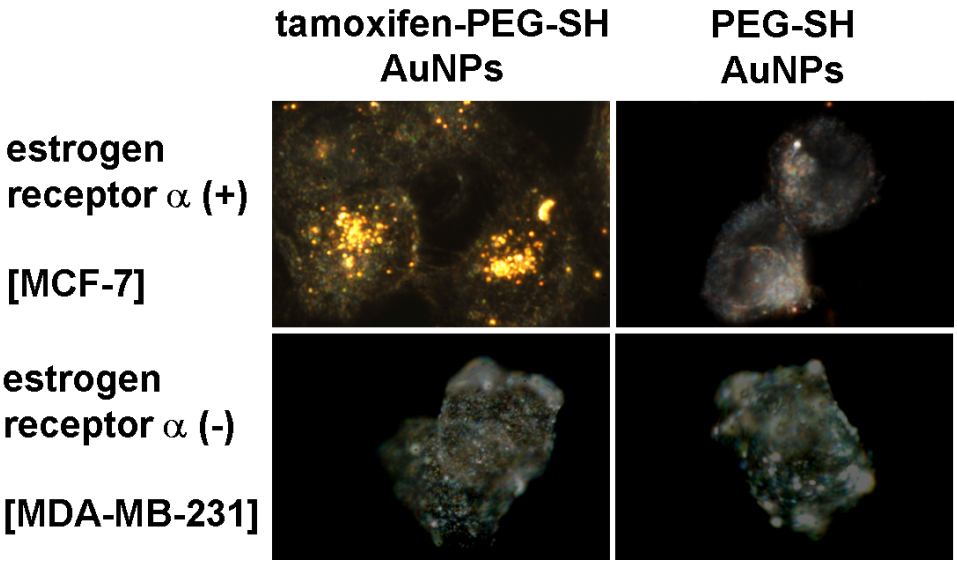

Figure 4.3. Dark-field scattering microscopy showing ligand- and receptor- dependent intracellular targeting of breast cancer cells by gold nanoparticle conjugates. Representative dark-field scattering images of ERα(+) [MCF-7, top] and ERα(-) [MDA-MB-231, bottom] human adenocarcinoma cells incubated for 24 h with 1 μM TAM-PEG-SH AuNP (left) and PEG-SH AuNP (right) conjugates (ca. 1.2×10^4 TAM-PEG-SH per AuNP). Adapted from Dreaden et al. [*39*].

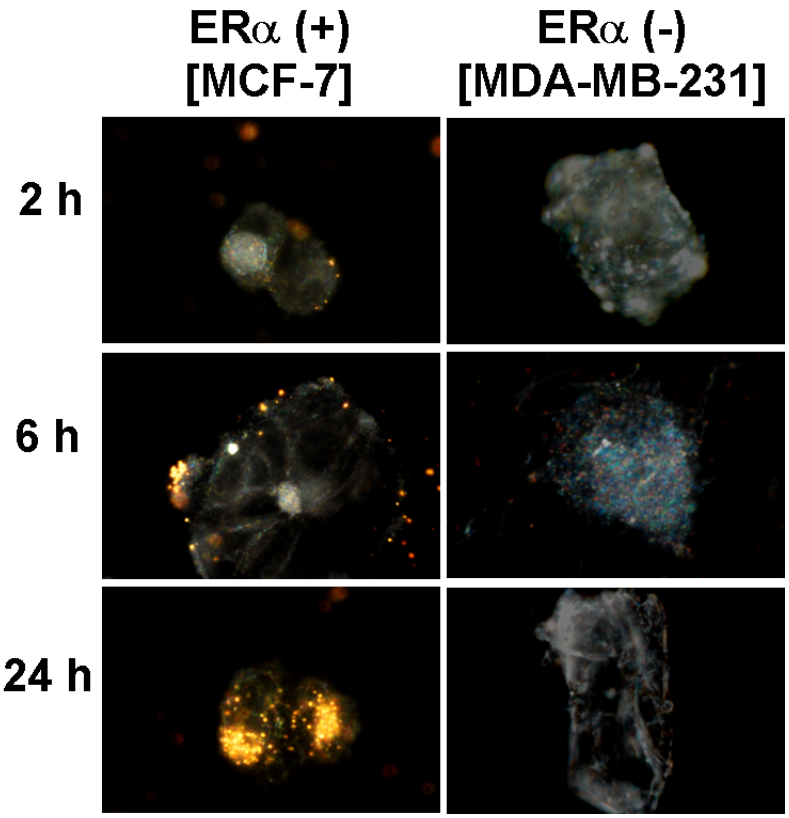

Figure 4.4. Dark-field scattering images of time- and ERα expression- dependent intracellular delivery of TAM-PEG-SH AuNPs (1 μM) to ERα(+) (MCF-7, left) and ERα(-) (MDA-MB-231, right) breast cancer cells. Adapted from Dreaden et al. [39].

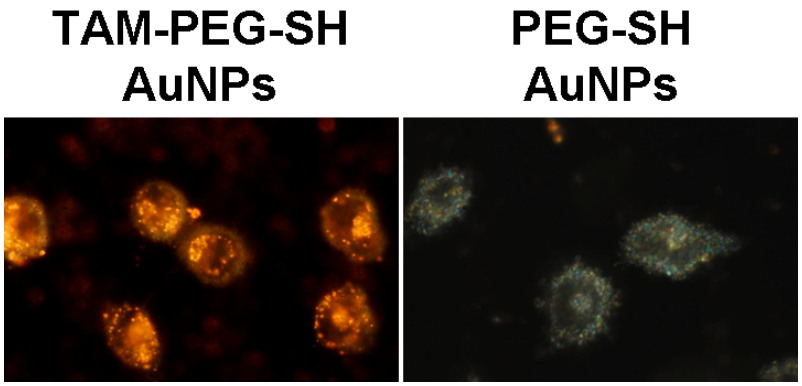

Figure 4.5. Comparison of ligand-dependent intracellular targeting selectivity with estrogen receptor positive oral cancer cells. Representative dark-field scattering images of human squamous cell carcinoma (HSC-3) cells incubated for 24 h with 1 μM TAM-PEG-SH AuNPs (left) and PEG-SH AuNPs (right). Adapted from Dreaden et al. [39].

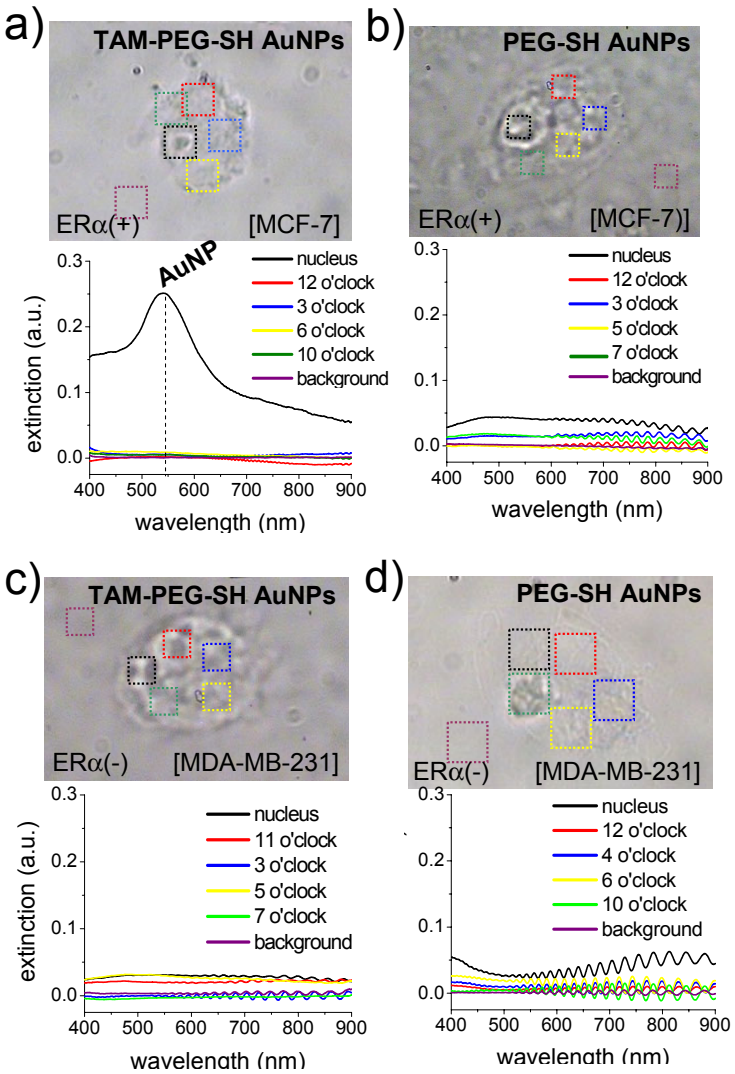

Figure 4.6. Optical imaging and spectroscopy showing receptor- and ligand- dependent perinuclear localization of tamoxifen-gold nanoparticle conjugates in breast cancer cells (s/n~10). Representative microscopic images and selected-area optical extinction spectra obtained from ERα(+) MCF-7 breast cancer cells incubated for 24 h with (A) 1 μM TAM-PEG-SH AuNPs and (B) unfunctionalized (PEG-SH) AuNPs, as well as ERα(-) MDA-MB-231 breast cancer cells incubated for 24 h with (C) 1 μM TAM-PEG-SH AuNPs and (D) unfunctionalized (PEG-SH) AuNPs. Adapted from Dreaden et al. [*39*].

Figures 4.7A,B illustrate time-dependent dose-response curves for cell viability of ERα(+) MCF-7 breast cancer cells incubated with equivalent concentrations of TAM-PEG-SH as the free drug and the nanoparticle conjugate, respectively. A comparison of the time-dependent IC_{50} (50% inhibitory concentration) values obtained for the free drug and its AuNP conjugate indicate 1.3 - 2.7

fold enhanced potency (**Figure 4.7C**) for TAM-PEG-SH AuNPs. While IC_{50} values for TAM-PEG-SH alone are comparable to or better than those previously reported for MCF-7 breast cancer cells treated with both tamoxifen [*44*] and its active metabolite,[*52*] a much more dramatic improvement is observed upon nanoparticle ligation, in contrast to the free drug, with significant growth inhibition observed for TAM-PEG-SH AuNPs at both 6 and 12 h incubation (6.4 and 2.4 μM IC_{50}, respectively). In accordance with previous studies,[*20*] no cytotoxic effects were observed in MCF-7 cells treated with PEG-SH AuNPs at the highest concentrations and incubation times used in the present study ($P>0.75$). Moreover, cytotoxic effects were not observed in ERα(-) MDA-MB-231 breast cancer cells incubated with TAM-PEG-SH alone, PEG-SH AuNPs, or TAM-PEG-SH AuNPs at the highest concentrations and incubation times used in the present study ($P>0.28$, 0.33, and 0.11, respectively). Although differences in sensitivity to and rates of particle/drug uptake and metabolism for ERα(+) and (-) cell lines may contribute to variation in apparent cytotoxicity, the observed ligand-dependency correlates well with levels of cellular ER expression, particularly under the conditions of extended incubation time and excess concentration used. In addition, cell viability following incubation with TAM-PEG-SH AuNPs in the absence of free drug was found statistically insignificant in difference from that observed in its presence. Here, AuNPs functionalized with TAM-PEG-SH equivalent to that present at the 24 h IC_{50} of the conjugate in the presence of free drug subsequently exhibited 57 $\pm$ 14 % cell viability ($P>0.6$). The lack of significant growth inhibition by the free drug at short incubation times, together with an observed decrease in the disparity between IC_{50} values of the free drug and the AuNP conjugate over time, and the apparent ligand-dependent response indicate increased rates of TAM-PEG-SH transport by the AuNP conjugate.

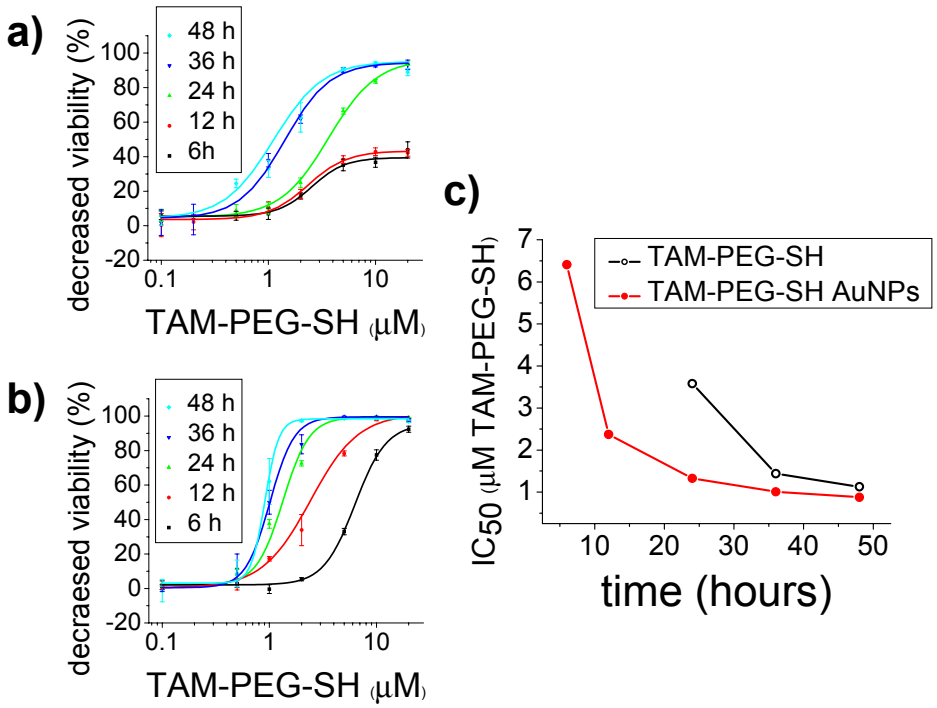

Figure 4.7. Time-dependent dose-response curves for cell viability of estrogen receptor alpha positive [MCF-7] breast cancer cells incubated with equivalent concentrations of TAM-PEG-SH (A) as a free drug and (B) as a gold nanoparticle conjugate. C) Time-dependent IC50 (50% inhibitory concentration) values showing 1.3 – 2.7 times enhanced potency from the nanoparticle conjugate versus the free drug. Error bars represent SD. 3.6, 1.4, 1.1 μM TAM-PEG-SH IC50 (24, 36, 48 h, respectively) versus 6.4, 2.4, 1.3, 1.0, 0.88 μM TAM-PEG-SH AuNP IC50 (6, 12, 24, 36, 48 h, respectively). Adapted from Dreaden et al. [*39*].

Although our results with the HSC-3 cell line, an ERα(+) oral cancer cell line, further attested to the role of ERα in nanoaprticle uptake, it is however conceivable that particle lipophilicity could also contribute to differences cellular uptake and cytotoxicity. In light of this possibility, blocking experiments were performed using ERα's endogenous ligand 17β-estradiol (estrogen) to further confirm receptor-dependent targeting and therapeutic response. ERα(+) MCF-7 breast cells were incubated overnight with increasing concentrations of estrogen, followed by 24 h incubation with 10 μM TAM-PEG-SH AuNPs. Image overlays from bright-field transmission and dark-field scattering microscopy of these cells (**Figure 4.8,9**) indicate near complete suppression of TAM-PEG-SH AuNP intracellular localization at estrogen concentrations as low as 20 nM. Decreased cell

surface labeling was also observed with increasing estrogen concentration. Such competitive effects are in agreement with previous reports indicating 1-2 orders of magnitude greater ERα binding affinity for 17β-estradiol versus TAM.[*53*] Cell viability experiments with ERα(+) breast cells incubated for 24 h with 10 μM TAM-PEG-SH AuNPs and previously blocked overnight with equimolar concentrations of estrogen were also performed (**Figure 4.10**). As in previous studies with the free drug,[*8*] the cytotoxic activity of TAM-labeled AuNPs was near completely suppressed following pre-exposure of the cells to estrogen ($P>0.87$), while they retained optimal potency in the absence of estrogen ($P<0.0001$). These findings correlate ERα binding with both TAM-PEG-SH AuNP intracellular localization and subsequent cell death.

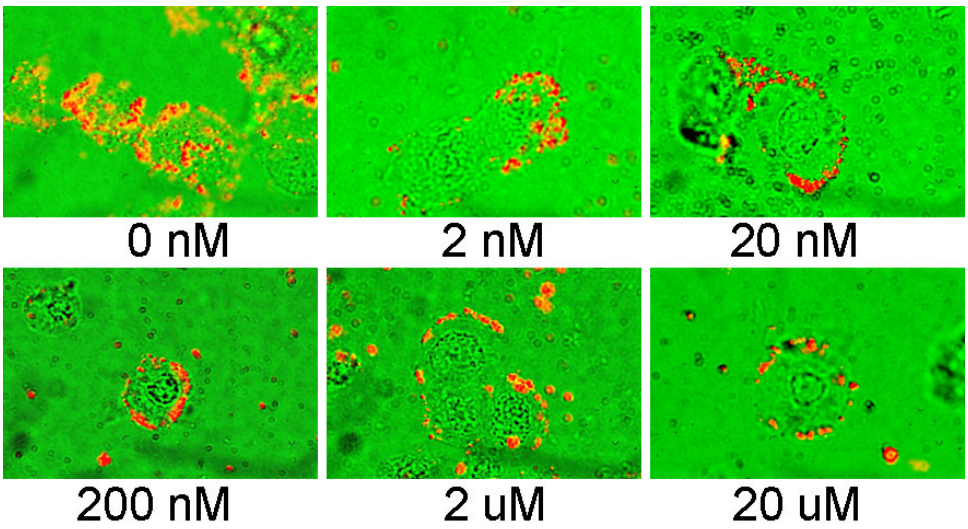

Figure 4.8. Representative dark-field scattering (red) and bright-field transmission (green) image overlays of TAM-PEG-SH AuNP competitive binding following 24 h incubation with 17β-estradiol. ERα(+) breast cancer cells [MCF-7] were incubated overnight with increasing concentrations of estrogen, followed by 24 h incubation with 10 μM tamoxifen-gold nanoparticle conjugates. Adapted from Dreaden et al. [*39*].

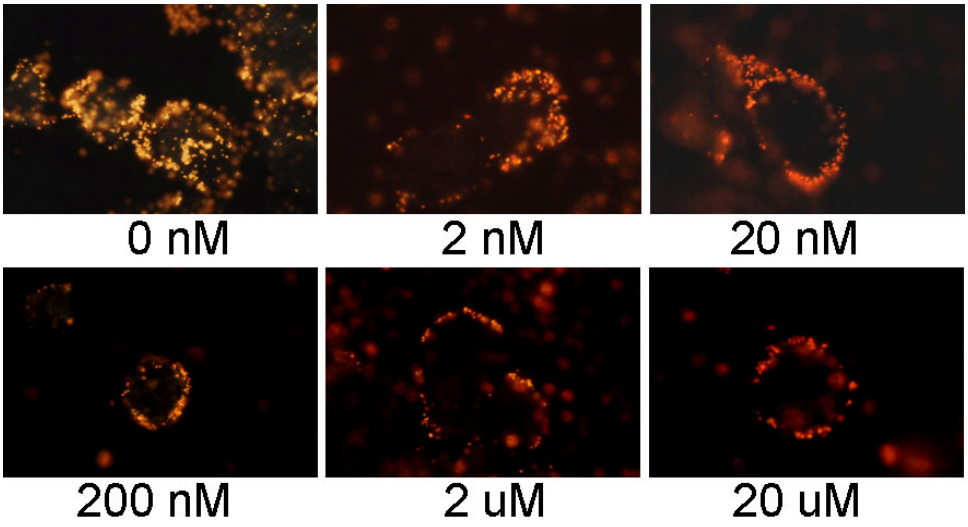

Figure 4.9. Representative dark-field scattering images of TAM-PEG-SH AuNP competitive binding following overnight incubation with estrogen. ERα(+) breast cancer cells [MCF-7] were incubated overnight with increasing concentrations of 17β-estradiol, followed by 24 h incubation with 10 μM TAM-PEG-SH AuNPs. Adapted from Dreaden et al. [*39*].

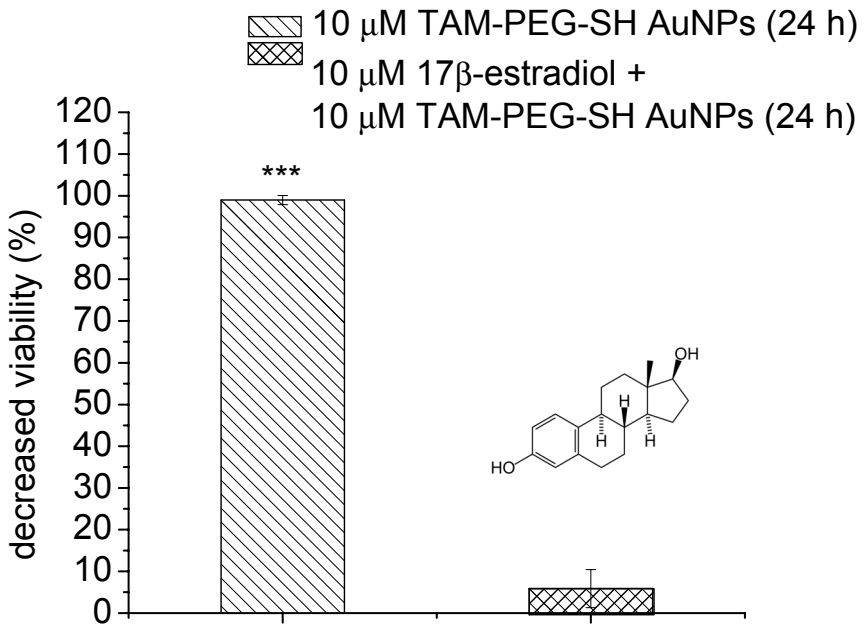

Figure 4.10. Suppression of TAM-PEG-SH AuNP activity by estrogen competition in ERα(+) breast cancer cells. Growth inhibition of MCF-7 cells incubated for 24 h with 10 μM TAM-PEG-SH AuNPs when previously untreated (left) and treated overnight with 10 μM 17β-estradiol (right). Adapted from Dreaden et al. [*39*].

The ERα expression-dependent uptake observed here also suggests that the cell membrane-associated receptor may facilitate intracellular nanoparticle transport. Indeed, plasma membrane localized ERα is well documented, as is its recognition of both antibody epitopes for the nuclear receptor and 17β-estradiol in mammalian cells.[*11,32*] The functions of membrane ERα beyond classical gene transcription, and more recently membrane-initiated signaling, are however less understood.[*54*] Comprehensive studies by Levin and coworkers indicate intracellular transport and caveolar localization of ERα in the plasma membrane of MCF-7 cells in vitro (via caveolin-1 and -2 association).[*50*] In order to determine whether plasma membrane localized ERα could contribute to receptor-mediated endocytosis of TAM-PEG-SH AuNP conjugates, cytotoxicity was examined under conditions of negligible endocytotic activity. MCF-7 cell viability was shown to increase by 87 $\pm$ 2 % following incubation with 20 μM TAM-PEG-SH AuNPs for 6 h at 4 °C versus 37 °C ($P<0.04$), indicating that endocytosis – in addition to ERα binding and intracellular particle delivery – is required for therapeutic response from tamoxifen-labeled AuNP conjugates.

4.1.4 Outlook and Conclusions

In summary, tamoxifen-gold nanoparticle conjugates were shown to selectively target estrogen receptor alpha in human breast cancer cells with up to 2.7 times enhanced potency in vitro. Optical microscopy and spectroscopy indicate a high degree of perinuclear and cytoplasmic localization of the targeted particles, while neither localization nor cytotoxic effects were observed from the untargeted nanoparticles. Time-dependent dose-response studies show that augmented potency results from increased rates of drug transport by nanoparticle uptake versus passive diffusion of the free drug. Receptor-selective and estrogen-competitive cytotoxicity/uptake of the nanoparticle conjugates indicates no additive effects associated with the gold particles themselves and suggests that

plasma membrane-localized ERα may facilitate selective endocytotic transport of these and other therapeutic nanoparticle conjugates. Increased potency and selective intracellular delivery of tamoxifen-gold nanoparticle conjugates provides opportunities for further enhancement by co-functionalization or adjunctive laser photothermal therapy.

4.2 Antiandrogen Gold Nanoparticles

4.2.1 Androgen Receptor, Membrane Association, and Cancer

Prostate cancer is the most commonly diagnosed cancer among men in developed countries.[*55*] One in six males in the US [*56*] and one in nine males in the UK [*57*] will develop the disease at some point during their lifetime. Despite tremendous advances in prostate cancer screening, more than a quarter million men die from the disease every year [*55*] due primarily to treatment-resistance and metastasis. Colloidal nanotechnologies can provide tremendous enhancements to existing targeting/treatment strategies for prostate cancer to which malignant cells are less sensitive. Here, we show that antiandrogen gold nanoparticles – multivalent analogs of antiandrogens currently used in clinical therapy for prostate cancer – selectively engage two distinct receptors involved in treatment-resistant prostate cancer. These particles were found to preferentially accumulate in hormone-insensitive and chemotherapy-resistant prostate cancer cells and exhibited $>10^4$-fold enhanced drug potency versus antiandrogens currently in clinical use. These antiandrogen gold nanoparticles bound androgen receptor with the highest affinity reported to-date (to our knowledge) and showed for the first time that multivalent antiandrogens can act as agonists for a newly discovered G protein-coupled receptor involved in prostate cancer risk, progression, and survival.

Androgen deprivation therapy (ADT) is currently recommended for the treatment of advanced/metastatic prostate cancer.[*58*] Nonsteroidal antiandrogens such as flutamide (Eulexin®), bicalutamide (Casodex®), and nilutamide (Nilandron®) are some of the most commonly prescribed ADT drugs and diminish androgenic effects by competitively inhibiting androgen-androgen receptor binding associated with prostate cancer growth, division, and survival. While most advanced or metastatic prostate cancers initially respond well to ADT, malignant cells that survive 2–3 years will typically enter an antiandrogen-resistant [*59*] (i.e. castration-resistant) state and subsequently exhibit chemotherapy-resistance as well.[*60*] Without further intervention, median survival following this period is just 18–24 months. Increasingly selective and potent drugs are urgently needed to treat these prostate cancers.

Nanoscale drug conjugates can provide improved targeting selectivity for prostate cancer treatments via multivalent ligand display (augmented affinity and avidity) and size-dependent passive accumulation; they can also realize increasing potency through high drug loading capacity and enhanced intracellular transport rates (endocytosis versus passive diffusion). Langer, Farokhzad, and Lippard have shown that PLGA nanoparticles targeted with aptamers towards prostate-specific membrane antigen can deliver platinum prodrug chemotherapeutics to prostate cancer cells with substantially greater drug potency than untargeted carriers or cisplatin alone.[*61,62*] Folate-targeted lipid nanoparticles have also been applied in gene therapy [*63*] and RNA interference [*64*] for prostate cancer in vivo. Katti and Kannan have shown that gold nanoparticles targeted with bombesin peptides directed towards gastrin-releasing peptide receptor (overexpressed on prostate cancer cells) selectively target prostate cancer cells in vitro/vivo with multivalent affinity and can provide enhanced contrast for x-ray computed tomography (CT) imaging.[*65*] Neoadjuvant administration of gold nanoparticles has been further shown to sensitize prostate cancer cells towards

external beam radiation therapy [*66*] and to facilitate in vivo laser photothermal ablation therapy in animal models of prostate cancer.[*67*]

We hypothesized that derivatives of commercially-available antiandrogen chemotherapeutics could serve as combined targeting and therapeutic agents for tissue-selective drug delivery of nanoscale drug carriers to prostate cancers expressing membrane androgen receptor [*68,69*] and/or a recently deorphaned androgen-sensing G protein-coupled receptor, GPRC6A,[*70*] involved in increased prostate cancer risk, growth, and poor survival. We found that multivalent antiandrogen gold nanoparticles selectively target and engage both androgen receptor and GPRC6A and facilitate cell death in antiandrogen treatment-resistant prostate cancer cells at concentrations more than four orders of magnitude lower than their corresponding free drugs. Antiandrogen gold nanoparticles bound androgen receptor with the highest affinity reported to-date (to our knowledge). These platforms provide opportunities for further increased treatment efficacy via drug co-conjugation, laser photothermal ablation, radiotherapy sensitization, and imaging-based treatment guidance/monitoring.[*71,72*]

4.2.2 Design and Development of Antiestrogen and Antiangrogen Gold Nanoparticles

Nanoparticle Synthesis and Characterization. Gold nanoparticles were synthesized using the methods of Turkevich[*42*] and Frens.[*73*] Briefly, 10 mL of 16.6 mM trisodium citrate was rapidly added to 190 mL of 0.638 mM aqueous chloroauric acid solution under reflux with stir. The solution was allowed to react for 20 min and the crude nanoparticle product was centrifuged (4185 × g) for 20 min. Particle sizing was performed using transmission electron microscopy (TEM, JEOL 100CX II) and image analysis software (ImageJ). Octanol/water partition coefficient (log P) was determined using the shake-flask method and experimentally determined particle molar extinction cross sections reported by Liu et al. for a 26 ± 6 nm diameter gold nanoparticle.[*74*] Hydrodynamic

diameter was measured using a NanoZS Zetasizer particle analyzer (Malvern, 633 nm). Optical extinction was characterized by UV-Vis absorption spectroscopy (Ocean Optics, HR4000CG-UV-NIR). Particles used in these studies were 29 ± 4 nm in diameter (λ_{max}~532 nm).

Conjugation of the Nanoparticles. Thiol-PEGylated antiandrogen ligands were solubilized in DMSO and added to aqueous solutions of purified gold nanoparticles at varying molar excesses and allowed to react overnight under sonication, in dark, at 30 ºC. The conjugates were purified by centrifugation (30 min, 4185 × g) and stored at 4 ºC prior to use. Surface adsorbate coverages were determined by UV absorption assay (α-Bic, 280 nm; β-Bic, 262 nm) using experimentally determined cross sections for the particle [*74*] and ligand. α-Bic and β-Bic nanoconjugates used in these studies were functionalized with 95% PEG-thiol (5 kDa, Lysan Bio) and 5% antiangrogen ligand (2.25 ± 0.02 × 10^3 α-Bic particle^{-1}; 1.56 ± 0.08 × 10^3 β-Bic particle^{-1}) and were conjugated at a 1.0378 × 10^4 and 1.5567 × 10^4 molar excess of thiolated ligands, respectively. Control particles were fully PEGylated.

Cell Culture and In Vitro Analysis. DU-145 human prostate carcinoma cells (ATCC) were subcultured in Dulbecco's modified eagle's medium (DMEM) supplanted with 10% v/v fetal bovine serum (FBS), 20 I.U./mL penicillin, 100 ug/mL streptomycin, and 250 ng/mL amphotericin B at 37 ºC in a 5% CO_2 humidified atmosphere. Cell viability was determined from mitochondrial dehydrogenase activity by tetrazolium assay (XTT, Sigma). All experiments were performed on cells passaged 12 h prior. Unless otherwise noted, nanoparticle concentration indicates particle molarity.

Radioligand Binding. Radioligand binding (Ricerca Biosciences) was performed using rat androgen receptor and [^{3}H]mibolerone (PanVera) in triphosphate buffer (pH 7.4). 78 ng of AR was incubated with 1.5 nM [^{3}H]mibolerone for 4 h at 4 ºC, then incubated with a hydroxyapatite slurry

over 15 minutes and filtered. The filters are washed 3 times and counted to determine [^{3}H]mibolerone specifically bound.

GPRC6A Expression and Stimulation. PC-3, 22Rv1, and LNCaP prostate carcinoma cells (ATCC) and non-malignant RWPE-1 prostate cells (ATCC) were subcultured in RPMI 1640 supplemented with 10% v/v fetal bovine serum (Gibco). Cells (10^3 well^{-1}) were cultured in triplicate in 96-well flat-bottomed microculture dishes in the presence and absence of various compounds for 72 hr. *Gprc6a* expression levels were analyzed by total RNA levels isolated using a quantitative real-time polymerase chain reaction RT-PCR protocol (Perkin-Elmer), as described previously.[*70*] Briefly, PCR reactions contained 100 ng of template (cDNA or RNA), 300 nM each of forward and reverse primer, and 1× iQ SYBR Green Supermix (Bio-Rad, Hercules, CA, USA) in 50 µL. Samples were amplified for 40 cycles in an iCycler iQ Real-Time PCR Detection System (Bio-Rad) with an initial melt at 95°C for 10 minutes, followed by 40 cycles of 95°C for 15 seconds and 60°C for 1 minute. PCR product accumulation was monitored at multiple points during each cycle by measuring the increase in fluorescence caused by the binding of SybrGreen I to dsDNA. The threshold cycle (C_t) of tested-gene product from the indicated genotype was normalized to the C_t for cyclophilin A. The primers for human *Gprc6a* consisted of hGPRC6A.F130: cataattggaggtttgtttgc and hGPRC6A.R346: cactgtgacttctgtacaagtgtc. Dissociation analysis was used to confirm the presence of a single transcript and lack of primer-dimer amplification in all PCR reactions.

Cyclic adenosine monophosphate (cAMP) accumulation in response to GPRC6A stimulation was determined via spectrophotometric enzyme-linked immunosorbent assay (EIA kit, Cayman Chemical) of GPRC6A$^-$/AR$^-$ HEK-293 (ATCC) and transfected [*75*] GPRC6A$^+$/AR$^-$ HEK-293.mGPRC6A cell extracts according to the manufacturer's instructions. HEK-293 (ATCC) and HEK-293.mGPRC6A cells (10^5 well^{-1}) were subcultured in triplicate in DMEM containing 10% v/v

fetal calf serum and 1% v/v penicillin/streptomycin (Gibco). Quiescent cells were treated overnight with stimulators as indicated, then100 nM forskolin for 30 minutes at 37 °C. Treatment was stopped and the cells were lysed by replacing media with 0.5 ml 0.1 N HCl. cAMP levels were measured following the manufactory's protocol.

Imaging. Nanoconjugate localization was determined by optical dark-field scattering microscopy. Sterile glass coverslips (18 mm dia) were incubated with 0.04 mg/mL rat tail collagen/DPBS for 6 h at 37 °C in a 5% CO_2 humidified atmosphere and rinsed in DPBS. Cells were passaged onto the coverslips and after 12 h, growth solutions were replaced with fresh media containing 0.2 nM gold nanoparticle conjugates. After incubation (24 h), cell monolayers were rinsed in DPBS and fixed in 4 % paraformaldehyde/DPBS at 4 °C for 15 min. The fixed coverslips were coated with glycerol, mounted, and sealed onto glass slides. Optical dark-field scattering microscopy was performed using an inverted objective Olympus IX70 microscope fitted with a dark-field condenser (U-DCW), 100x/1.35 oil Iris objective (UPLANAPO), (white light) tungsten lamp, and a Nikon D200 digital SLR camera. Please note that dark-field scattering optics are distinct from confocal optics and that fluorescence images were obtained on a separate instrument.

Fluorescence microscopy was performed on a Zeiss NLO META confocal microscope. Antiandrogen nanoparticles were labeled with a carboxyfluorescein-terminal PEG-SH (5 kDa). 5-(and-6)-carboxyfluorescein succinimidyl ester (Molecular Probes) was reacted with amine-terminal PEG-SH (5 kDa, Lysan Bio) in pH 7.4 DPBS buffer for 24 h in dark, with sonication. Fluorescently-labeled PEG-SH was dialyzed twice (5 Da MWCO, Spectra/Por) at a 10^3 volume excess for 24 h with three solvent exchanges. Carboxyfluorescein-terminal PEG-SH was incubated with the antiandrogen nanoparticles for 12 h with sonication at RT and purified by centrifugation (6000 rpm, 15 min). Cell cultures were incubated with 5.0 μM Alexa Fluor 647-dextran (10 kDa) to

label endo/lysosomal compartments and 0.33 nM of the fluorescently-labeled nanoconjugates. After 12 h, DAPI was added to 300 nM and allowed to incubate for 15 min. The cell monolayers were then twice rinsed with DPBS and fixed in 4 % paraformaldehyde/DPBS at 4 °C for 30 min. The microscopy samples were again twice rinsed with DPBS and incubated with 1 mg/mL $NaBH_4$ at 4 °C to minimize fixative-induced fluorescence. After 5 min, the borohydride solution was replaced with fresh solution and allowed to incubate for another 5 min at 4 °C. The samples were then rinsed three times with DPBS and imaged.

4.2.3 Preclinical Evaluation of Antiestrogen and Antiandrogen Gold Nanoparticles

Gold nanoparticles (AuNPs, 29 ± 4 nm diameter, **Figure 4.11A**) were synthesized by Turkevich/Frens reduction of chloroauric acid and conjugated with a mixed self-assembled monolayer of 5% thiol PEGylated antiandrogen and 95% thiolated poly(ethylene glycol) stabilizer (PEG-SH, 5 kDa). Antiandrogen ligands used in these studies were employed to reflect structural homology between antiandrogens in clinical use with α- and β-Bicalutamide (α-Bic, β-Bic; **Figure 4.11A**) both bearing an aromatic α-anilide ring characteristic of flutamide, bicalutamide, and nilutamide, as well as a five-membered imidazolidinedione ring characteristic of nilutamide and the H-bonded structure of bicalutamide and/or the active metabolite of flutamide. β-Bic contains an additional β-aromatic ring characteristic of bicalutamide which binds the hydrophobic pocket formed by helix 12 residues on androgen receptor and confers it enhanced potency [*76*] (**Figure 4.11B**). Antiandrogen ligands were synthesized by Cu(I)-catalyzed Huisgen cycloaddition (i.e. click, azide-alkyne coupling) with PEGylated lipoic acid. Thiol anchoring groups were used to enable stable Au surface bond formation and PEG stabilizer/spacer groups were employed to sterically stabilize the subsequent nanoparticle constructs in physiological media and to resist protein adsorption and/or

immunogenic response. α-Bic- and β-Bic-AuNPs contained 2.25 ± 0.02 × 10^3 and 1.56 ± 0.08 × 10^3 antiandrogen ligands per particle, respectively (**Figure 4.12**).

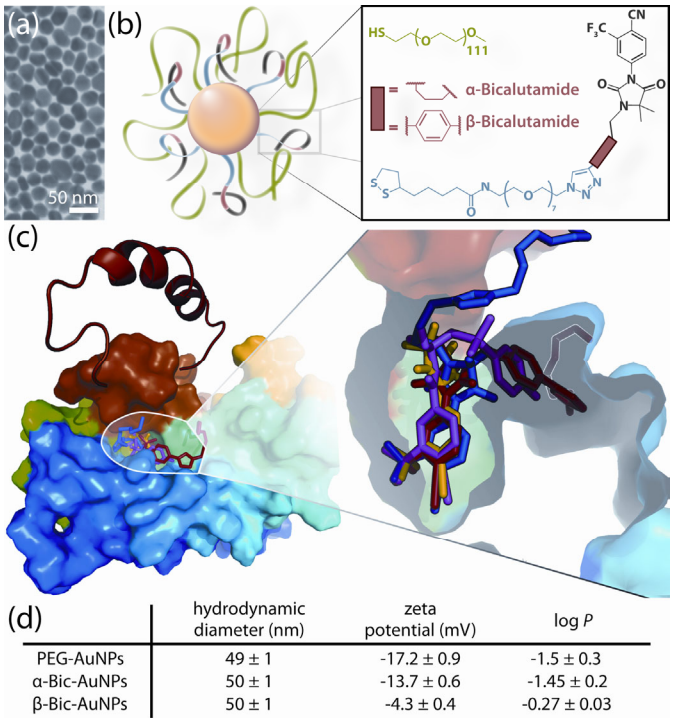

(d)

	hydrodynamic diameter (nm)	zeta potential (mV)	log *P*
PEG-AuNPs	49 ± 1	-17.2 ± 0.9	-1.5 ± 0.3
α-Bic-AuNPs	50 ± 1	-13.7 ± 0.6	-1.45 ± 0.2
β-Bic-AuNPs	50 ± 1	-4.3 ± 0.4	-0.27 ± 0.03

Figure 4.11. Multivalent antiandrogen gold nanoparticles for the treatment of castration-resistant prostate cancer. A) Electron micrographs of the as-synthesized 29 ± 4 nm diameter gold nanoparticles. B) Illustration of the antiandrogen nanoconjugates with receptor binding groups shown groups in grey/red. C) Molecular docking of the antiandrogen ligands with androgen receptor showing outward orientation of the thiol PEGylated nanoparticle linker groups and maintenance of contact points within the androgen receptor binding pocket by the bicalutamide ligand (β-Bic, red) and its β ring-deficient analog (α-Bic, blue), as compared to their precursor drugs bicalutamide (magenta) and its nilutamide analog (yellow). D) Physiochemical properties of the antiandrogen gold nanoparticles. Adapted from Dreaden et al. [*77*].

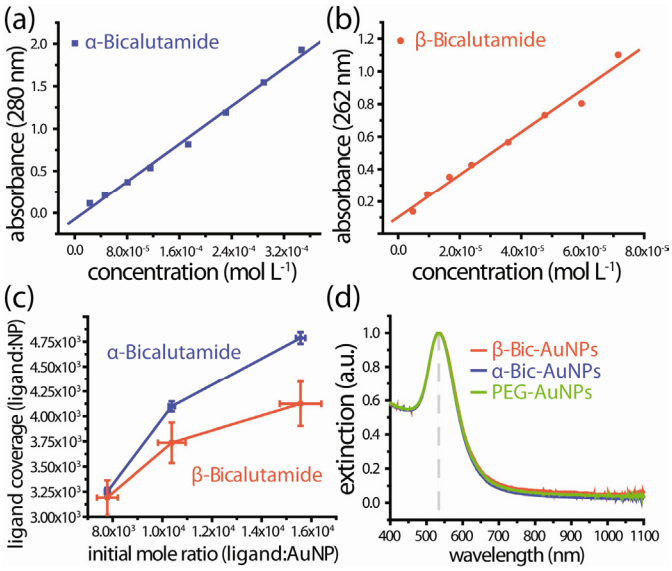

Figure 4.12. Conjugation of the antiandrogen gold nanoparticles. UV absorption calibration curves for (A) α-Bicalutamide and (B) β-bicalutamide antiandrogen ligands in water. C) Antiandrogen ligand coverages on 29 ± 4 nm diameter gold nanoparticles as a function of ligand excess present during conjugation. D) Normalized optical extinction spectra of the purified antiandrogen and PEGylated gold nanoparticles in water. Error bars represent SD. Adapted from Dreaden et al. [*77*].

α-Bic and β-Bic AuNPs were found to be 50 ± 1 nm in hydrodynamic diameter, which recent studies by Chan and coworkers indicate to the be within the optimal size range for both tumor accumulation and cellular internalization of AuNPs [*78,79*] (**Figure 4.11D**). PEGylated control nanoparticles were found to be 49 ± 1 nm. The octanol:water partition coefficient of α-Bic- and β-Bic-AuNPs was found to be -1.4 ± 0.2 and -0.27 ± 0.03, respectively, both below that expected from an intravenously administered drug (1.92) with acceptable pharmacokinetics.[*80*]

Molecular docking of the antiandrogen ligands with androgen receptor (AR) show that the contact points of their parent drugs within the AR binding pocket are maintained by the ligands and that their thiol PEGylated linker groups face outwards to enable accessibility by nanoparticle-bound ligands (**Figure 4.11C**). Receptor binding competition with radiolabeled androgen (**Figure 4.13A**) shows that the AR binding affinities (Ki) of α-Bic and β-Bic are enhanced 25,000- and 8,400-fold, respectively, when displayed as a multivalent nanoparticle construct (**Figure 4.13B**), binding AR

with greater affinity than its endogenous hormone dihydroxytestosterone (DHT, 0.28 – 2 nM) [*76,81*] and yielding, to our knowledge, the highest reported K_i for a non-steroidal antiandrogen. α-Bic- and β-Bic bound AR with affinities comparable to those previously reported for bicalutamide,[*82*] while their nanoparticle conjugates did so at concentrations 11- and 5.4-fold less than a nanoparticle-equivalent quantity of free antiandrogen ligands, respectively (**Figure 4.13A**, inset; **Figure 4.13B**). Because membrane AR (mAR) binds antibodies [*68*] and endogenous androgens [*83*] for intracellular AR, and because antiandrogens can diminish the effects of androgenic mAR stimulation,[*84*] these data suggest that antiandrogen gold nanoparticles can selectively target mAR which is preferentially overexpressed by human prostate cancer cells and whose expression levels correlate with poor prognosis (Gleason score) [*85*] and total AR levels [*68*] found in 80-90% of all prostate cancers.[*86*]

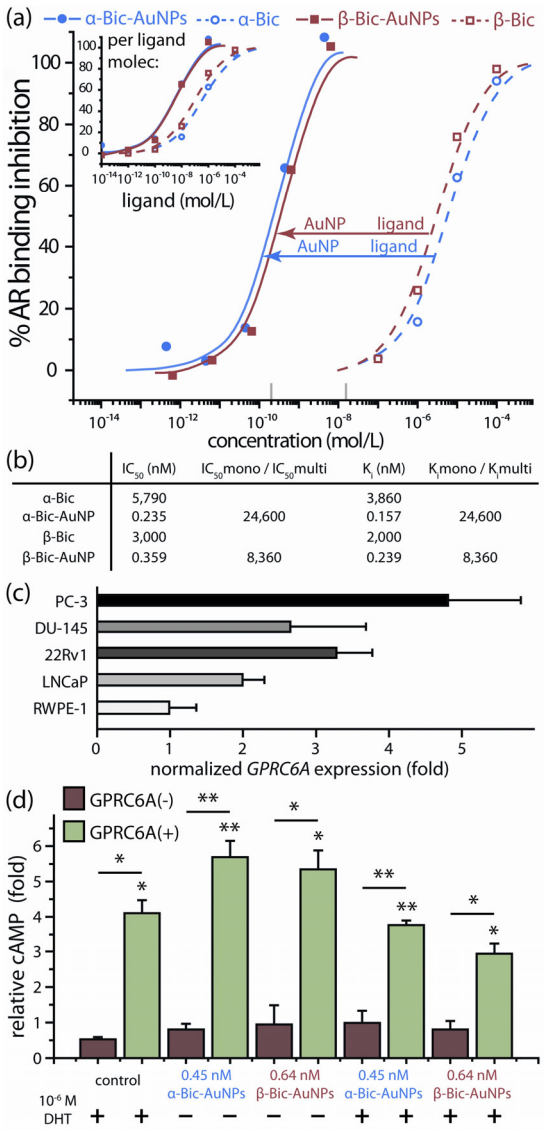

Figure 4.13. Antiandrogen gold nanoparticles selectively engage androgen receptor (AR) and G protein-coupled receptor GPRC6A targets. A) AR binding competition between radiolabeled androgen and antiandrogen nanoparticles (solid) or antiandrogen ligands (dashed) showing multivalency-enhanced AR binding affinity (K_i) from the nanoparticle constructs. Antiandrogen nanoparticles displaced [^{3}H]androgen from AR with 8,400–25,000 fold greater affinity than free antiandrogens (main panel, a) and did so at concentrations lower than expected from an equivalent number of nanoparticle ligands (inset, A). Grey hash marks denote lower and upper limits reported for AR's endogenous high affinity ligand, dihydrotestosterone (DHT). B) Half maximal inhibitory concentration (IC_{50}) and binding affinity (K_i) for antiandrogen nanoparticles and ligands with their corresponding multivalency-enhanced values. C) Upregulated GPRC6A mRNA expression levels measured from various prostate cancer cell lines relative to non-malignant RWPE-1 prostate cells. D) Androgen-competitive downstream production of cyclic adenosine monophosphate (cAMP) accumulated in response to overnight GPRC6A stimulation by α-Bic- and β-Bic-AuNPs in an $AR^-/GPRC6A^-$ and $AR^-/GPRC6A^+$ transfected cell line. DHT, dihydrotestosterone. Error bars represent SEM. P for individual values relative to untreated controls or as indicated; *P<0.05, **P<0.01. Adapted from Dreaden et al. [*77*].

GPRC6A is a membrane-associated C family G protein-coupled receptor recently discovered through genomic homology search.[*87*] GPRC6A senses androgens and is a positive regulator of testosterone and a negative regulator of estrogen; its expression has been shown to contribute to prostate cancer growth, malignancy (**Figure 4.13C**), and poor survival in animal models of prostate cancer.[*70*] Polymorphism at its GPRC6A gene was recently associated with significantly altered susceptibility to prostate cancer in a genome-wide association study among Japanese men ($P=1.6 \times 10-12$).[*70,88*] Downstream production of cyclic adenosine monophosphate (cAMP) in response to GPRC6A stimulation was assessed using an established AR-/GPRC6A- and AR-/GPRC6A+ transfected cell line.[*75*] α-Bic- and β-Bic-AuNPs significantly stimulated GPRC6A in an androgen-competitive manner (**Figure 4.13D**), eliciting cAMP production at sub-nM concentrations. GPRC6A stimulation by α-Bic- and β-Bic-AuNPs was 2.0- and 1.9-fold greater than that by an equivalent or greater concentration of PEGylated-AuNPs ($P=0.06$ & 0.15, respectively) and was 2.3- and 3.5-fold greater than their nanoparticle-equivalent concentrations of free ligands ($P=0.003$ & 0.03, respectively) (**Figure 4.14**). These data show that antiandrogen gold nanoparticles can selectively engage GPRC6A with multivalent affinity and in a manner independent of AR/mAR.

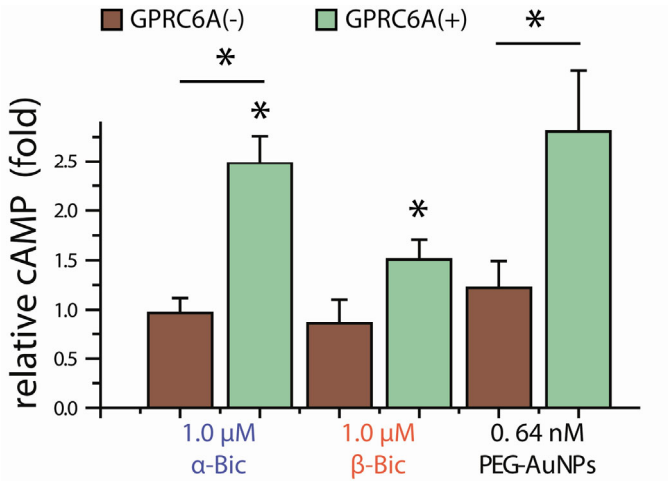

Figure 4.14. Nanoparticle-equivalent concentrations of antiandrogen ligands and PEGylated control nanoparticles engage GPRC6A significantly less than antiandrogen gold nanoparticles. Downstream cyclic adenosine monophosphate (cAMP) accumulated in response to GPRC6A stimulation by α-Bic/β-Bic ligands and PEGylated control nanoparticles showing significantly lower GPRC6A engagement/stimulation by α-Bic (2.3-fold, P=0.003), β-Bic (3.5-fold, P=0.03), and PEGylated gold nanoparticles (2.0-fold v. α-Bic-AuNPs, P=0.06; 1.9-fold v. β-Bic-AuNPs, P=0.15). Error bars represent SEM. P for individual values relative to untreated controls or as indicated; *P<0.05. Adapted from Dreaden et al. [*77*].

Binding/uptake selectivity of the antiandrogen gold nanoparticles was assessed in a membrane-AR+ and GPRC6A^{+} prostate carcinoma cell line [*83*] whose response to chemotherapy and antiandrogen therapy reflects that of castration-resistant prostate cancer,[*60*] DU-145 (**Figure 4.15A**). Fluorescently-labeled antiandrogen gold nanoparticles exhibited high intracellular accumulation in DU-145 cells and localized in a manner similar to that reported for AR,[*89*] while PEGylated nanoparticles exhibited no significant accumulation. Uptake and localization patterns of both targeted and untargeted nanoparticles in an AR null [*90*] squamous cell carcinoma cell line showed only non-specific cell surface binding (**Figure 4.16**). We hypothesized that androgen-stimulated upregulation of AR in DU-145,[*91*] and correspondingly increased mAR expression,[*68*] may augment antiandrogen nanoparticle accumulation in prostate cancer cells. Particle uptake/localization was imaged using a technique termed optical dark-field scattering microscopy which can achieve sensitivity orders of magnitude higher than conventional fluorescence-based

methods.[*71,72*] Testosterone (T, 10^{-6} M) stimulation of DU-145 had no effect on PEGylated nanoparticle accumulation (**Figure 4.17**), but significantly increased α-Bic- and β-Bic-AuNP accumulation, consistent with previous reports of 1.5–2 fold testosterone-induced receptor upregulation in DU-145 [*91*] (**Figure 4.15B**). These imaging data show that antiandrogen gold nanoparticles selectively accumulate in antiandrogen treatment-resistant AR^+/$GPRC6A^+$ prostate cancer cells and do so in an AR-dependent manner.

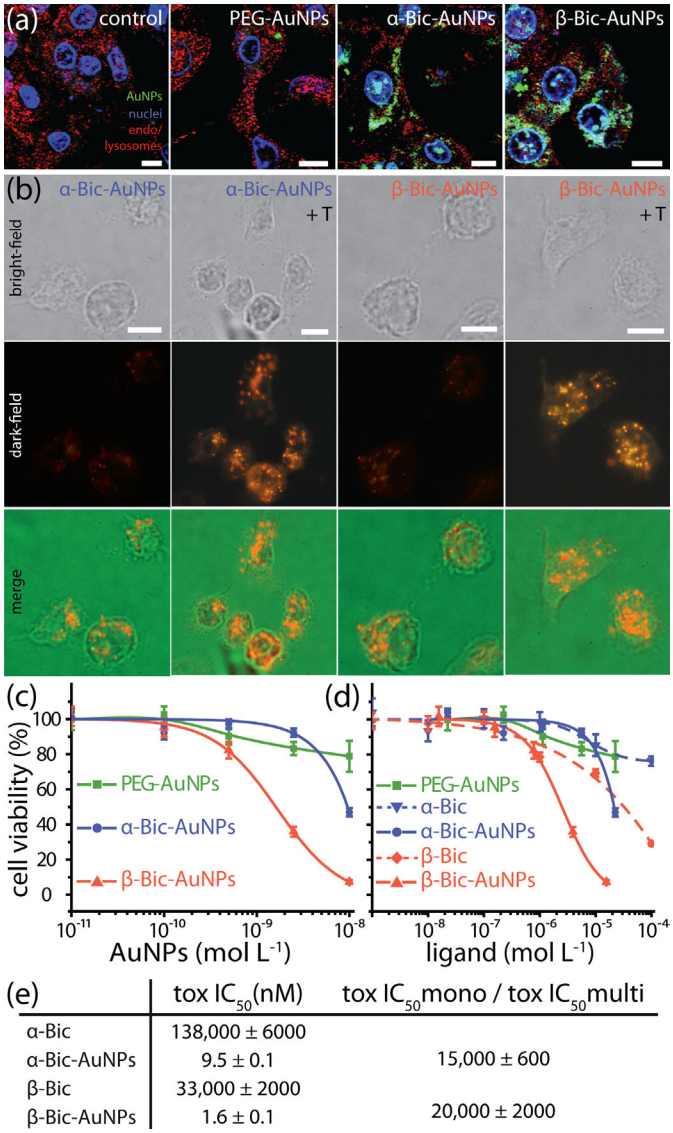

(e)	tox IC_{50}(nM)	tox IC_{50}mono / tox IC_{50}multi
α-Bic	138,000 ± 6000	
α-Bic-AuNPs	9.5 ± 0.1	15,000 ± 600
β-Bic	33,000 ± 2000	
β-Bic-AuNPs	1.6 ± 0.1	20,000 ± 2000

Figure 4.15. Antiandrogen gold nanoparticles selectively accumulate in chemotherapy- and antiandrogen-resistant prostate cancer cells expressing membrane-androgen receptor (mAR) and G protein-coupled receptor GPRC6A and induce cell death with 10^4-fold increased drug potency. A) Confocal fluorescence images of selective antiandrogen nanoparticle intracellular localization (green) in $mAR^+/GPRC6A^+$ DU-145 prostate cancer cells. Endo/lysosomes were labeled with dextran (red) and nuclei were stained with DAPI (blue). B) Optical dark-field scattering microscopy of DU-145 cells showing augmented antiandrogen gold nanoparticle accumulation in response to androgen-stimulated mAR-upregulation by testosterone (T, 10^{-6} M). Note that images in (A) and (B) were obtained using different instruments. C) Dose-dependent cell viability (%) of antiandrogen treatment-resistant DU-145 prostate cancer cells incubated with antiandrogen gold nanoparticles and (D) antiandrogen ligands (24 h). Nanoparticle equivalent ligand concentrations are plotted in (D) for comparison, showing (E) 1.5×10^4- and 2.0×10^4-fold enhanced drug potency. Scale bars represent 10 μm. Error bars represent SD. Adapted from Dreaden et al. [*77*].

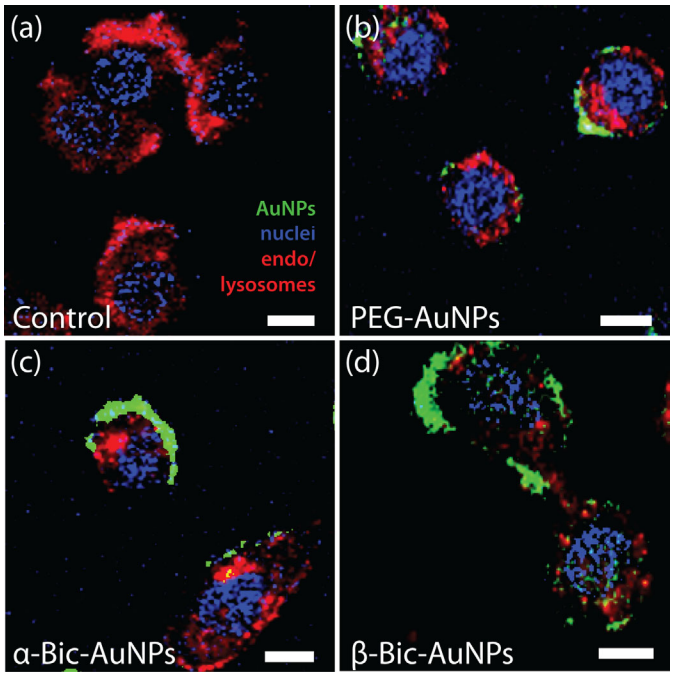

Figure 4.16. Nonspecific cell surface binding of antiandrogen gold nanoparticles with an androgen receptor null cancer cell line. Confocal fluorescence microscopy of androgen receptor negative human squamous cell carcinoma (SCC) cells illustrating non-specific membrane binding antiandrogen gold nanoparticle conjugates. HSC-3 cells were incubated with antiandrogen- or control-gold nanoparticles (green) and a dextran endo/lysosomal marker (red) for 12 h. Nuclei were stained with DAPI (blue). Scale bar represents 10 μm. Adapted from Dreaden et al. [*77*].

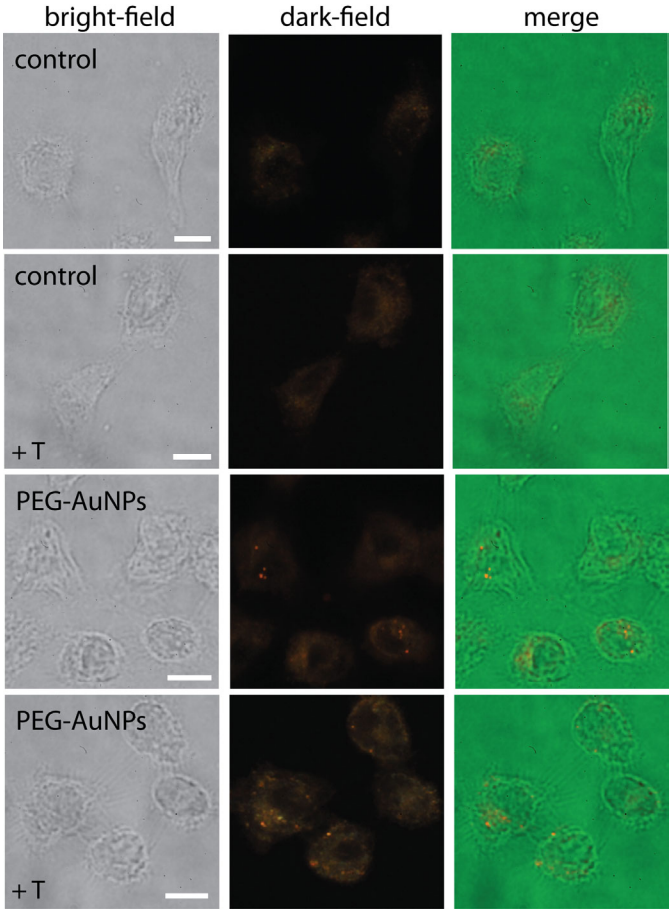

Figure 4.17. PEGylated gold nanoparticles exhibit low, androgen stimulation-independent accumulation in antiandrogen treatment-resistant prostate cancer cells expressing membrane-androgen receptor (mAR) and G protein-coupled receptor GPRC6A. Optical dark-field scattering microscopy of DU-145 prostate cancer cells showing baseline accumulation levels of PEGylated control gold nanoparticles both in the presence and absence of androgen-stimulated mAR-upregulation by testosterone (T, 10^{-6} M). Scale bars represent 10 μm. Adapted from Dreaden et al. [*77*].

Cytotoxicity of the antiandrogen nanoparticles and their ligands to chemotherapy- and antiandrogen-resistant [*60*] $mAR^+/GPRC6A^+$ DU-145 prostate carcinoma cells was investigated by tetrazolium assay (24 h). α-Bic- and β-Bic-AuNPs induced half maximal cytotoxicity (IC50) at 9.5 and 1.5 nM, respectively, exhibiting potency 1.5×10^4- and 2.0×10^4-fold greater than their corresponding free drugs, respectively (6- and 13-fold greater than expected from a nanoparticle-equivalent concentration of free ligands, respectively) (**Figure 4.15C-E**). Free α-Bic- and β-Bic

cytotoxicity was comparable to that previously reported for bicalutamide and OH-flutamide with DU-145,[*92*] while PEGylated gold nanoparticles exhibited no significant toxicity over the therapeutically-relevant AuNP concentration ranges. Together, these data correlate selective AR and GPRC6A engagement (vide infra) with enhanced drug potency and cell death by antiandrogen gold nanoparticles.

4.2.4 Outlook and Conclusions

In summary, we found that antiandrogen gold nanoparticles selectively engaged two distinct receptors involved in prostate cancer growth and progression. These particles selectively accumulated in castration- and chemotherapy-resistant prostate cancer cells and induced cell death at nanomolar concentrations, more than four orders of magnitude lower than antiandrogens currently in clinical use. Further, antiandrogen gold nanoparticles bound androgen receptor with the highest affinity reported to-date (to our knowledge) and selectively agonized a newly discovered G-protein coupled receptor involved in prostate carcinogenesis and disease risk. These platforms provide opportunities for increasingly potent and selective therapy of treatment-resistant prostate cancers and may exhibit further enhanced therapeutic efficacy via drug co-conjugation, image-based treatment guidance/monitoring, concurrent laser photothermal ablation therapy, and/or high-Z enhanced radiotherapy.

4.3 References

1. Obrero, M., Yu, D. V., & Shapiro, D. J. Estrogen receptor-dependent and estrogen receptor-independent pathways for tamoxifen and 4-hydroxytamoxifen-induced programmed cell death. *J. Biol. Chem.* **277**, 45695-45703 (2002).

2. Bates, S. E., Davidson, N. E., Valverius, E. M., Freter, C. E., Dickson, R. B., Tam, J. P., Kudlow, J. E., Lippman, M. E., & Salomon, D. S. Expression of Transforming Growth Factor-Alpha and Its Messenger Ribonucleic-Acid in Human-Breast Cancer - Its Regulation by Estrogen and Its Possible Functional-Significance. *Mol. Endocrinol.* **2**, 543-555 (1988).

3. Dubik, D., Dembinski, T. C., & Shiu, R. P. C. Stimulation of c-Myc Oncogene Expression Associated With Estrogen-Induced Proliferation of Human-Breast Cancer-Cells. *Cancer Res.* **47**, 6517-6521 (1987).

4. Krishnan, V., Wang, X. H., & Safe, S. Estrogen Receptor-SP1 Complexes Mediate Estrogen-Induced Cathepsin-D Gene-Expression in MCF-7 Human Breast-Cancer Cells. *J. Biol. Chem.* **269**, 15912-15917 (1994).

5. Cleator, S., Heller, W., & Coombes, R. C. Triple-negative breast cancer: therapeutic options. *Lancet Oncol.* **8**, 235-244 (2007).

6. Jordan, V. C. Chemoprevention of breast cancer with selective oestrogen-receptor modulators. *Nat. Rev. Cancer* **7**, 46-53 (2007).

7. Shiau, A. K., Barstad, D., Loria, P. M., Cheng, L., Kushner, P. J., Agard, D. A., & Greene, G. L. The structural basis of estrogen receptor/coactivator recognition and the antagonism of this interaction by tamoxifen. *Cell* **95**, 927-937 (1998).

8. Coezy, E., Borgna, J.-L., & Rochefort, H. Tamoxifen and Metabolites in MCF7 Cells: Correlation between Binding to Estrogen Receptor and Inhibition of Cell Growth. *Cancer Res.* **42**, 317-323 (1982).

9. Jordan, V. C. Tamoxifen: A most unlikely pioneering medicine. *Nat. Rev. Drug Discovery* **2**, 205-213 (2003).

10. Weissleder, R., Kelly, K., Sun, E. Y., Shtatland, T., & Josephson, L. Cell-specific targeting of nanoparticles by multivalent attachment of small molecules. *Nat. Biotechnol.* **23**, 1418-1423 (2005).

11. Zivadinovic, D., Gametchu, B., & Watson, C. S. Membrane estrogen receptor-alpha levels in MCF-7 breast cancer cells predict cAMP and proliferation responses. *Breast Cancer Res.* **7**, R101-R112 (2005).

12. Montet, X., Funovics, M., Montet-Abou, K., Weissleder, R., & Josephson, L. Multivalent Effects of RGD Peptides Obtained by Nanoparticle Display. *J. Med. Chem.* **49**, 6087-6093 (2006).

13. Gestwicki, J. E., Cairo, C. W., Strong, L. E., Oetjen, K. A., & Kiessling, L. L. Influencing Receptor-Ligand Binding Mechanisms with Multivalent Ligand Architecture. *J. Am. Chem. Soc.* **124**, 14922-14933 (2002).

14. Goodman, C. M., & Rotello, V. M. Biomacromolecule surface recognition using nanoparticles. *Mini-Rev. Org. Chem.* **1**, 103-114 (2004).

15. Gibson, J. D., Khanal, B. P., & Zubarev, E. R. Paclitaxel-functionalized gold nanoparticles. *J. Am. Chem. Soc.* **129**, 11653-11661 (2007).

16. Cho, K., Wang, X., Nie, S., Chen, Z., & Shin, D. M. Therapeutic Nanoparticles for Drug Delivery in Cancer. *Clin. Cancer Res.* **14**, 1310-1316 (2008).

17. Chawla, J. S., & Amiji, M. M. Biodegradable poly([var epsilon]-caprolactone) nanoparticles for tumor-targeted delivery of tamoxifen. *Int. J. Pharm.* **249**, 127-138 (2002).

18. Maeda, H. The enhanced permeability and retention (EPR) effect in tumor vasculature: The key role of tumor-selective macromolecular drug targeting. *Adv. Enzyme Reg.* **41**, 189-207 (2001).

19. von Maltzahn, G., Park, J.-H., Agrawal, A., Bandaru, N. K., Das, S. K., Sailor, M. J., & Bhatia, S. N. Computationally Guided Photothermal Tumor Therapy Using Long-Circulating Gold Nanorod Antennas. *Cancer Res.* **69**, 3892-3900 (2009).

20. Connor, E. E., Mwamuka, J., Gole, A., Murphy, C. J., & Wyatt, M. D. Gold nanoparticles are taken up by human cells but do not cause acute cytotoxicity. *Small* **1**, 325-327 (2005).

21. Khan, J. A., Pillai, B., Das, T. K., Singh, Y., & Maiti, S. Molecular effects of uptake of gold nanoparticles in HeLa cells. *Chembiochem* **8**, 1237-1240 (2007).

22. Zhang, F., Skoda, M. W. A., Jacobs, R. M. J., Zorn, S., Martin, R. A., Martin, C. M., Clark, G. F., Goerigk, G., & Schreiber, F. Gold nanoparticles decorated with oligo(ethylene glycol) thiols: Protein resistance and colloidal stability. *J. Phys. Chem. A* **111**, 12229-12237 (2007).

23. Dickerson, E. B., Dreaden, E. C., Huang, X., El-Sayed, I. H., Chu, H., Pushpanketh, S., McDonald, J. F., & El-Sayed, M. A. Gold nanorod assisted near-infrared plasmonic photothermal therapy (PPTT) of squamous cell carcinoma in mice. *Cancer Lett.* **269**, 57-66 (2008).

24. O'Neal, D. P., Hirsch, L. R., Halas, N. J., Payne, J. D., & West, J. L. Photothermal Tumor Ablation in mice using near infrared absorbing nanoshells. *Cancer Lett.* **209**, 171-176 (2004).

25. Huang, X., El-Sayed, I. H., & El-Sayed, M. A. Cancer cell imaging and photothermal therapy in the near-infrared region by using gold nanorods. *J. Am. Chem. Soc.* **128**, 2115-2120 (2006).

26. Huff, T. B., Tong, L., Zhao, Y., Hansen, M. N., Cheng, J. X., & Wei, A. Hyperthermic effects of gold nanorods on tumor cells. *Nanomedicine* **2**, 125-132 (2007).

27. Hirsch, L. R., Stafford, R. J., Bankson, J. A., Sershen, S. R., Rivera, B., Price, R. E., Hazle, J. D., Halas, N. J., & West, J. L. Nanoshell-mediated near-infrared thermal therapy of tumors under magnetic resonance guidance. *Proc. Natl. Acad. Sci. USA* **100**, 13549-13554 (2003).

28. El-Sayed, I. H., X., H., & El-Sayed, M. A. Selective laser photo-thermal therapy of epithelial carcinoma using anti-EGFR antibody conjugated gold nanoparticles. *Cancer Lett.* **239**, 129-135 (2006).

29. Qian, X. M., Peng, X. H., Ansari, D. O., Yin-Goen, Q., Chen, G. Z., Shin, D. M., Yang, L., Young, A. N., Wang, M. D., & Nie, S. M. In vivo tumor targeting and spectroscopic detection with surface-enhanced Raman nanoparticle tags. *Nat. Biotechnol.* **26**, 83-90 (2008).

30. Dixit, V., Van den Bossche, J., Sherman, D. M., Thompson, D. H., & Andres, R. P. Synthesis and Grafting of Thioctic Acid-PEG-Folate Conjugates onto Au Nanoparticles for Selective Targeting of Folate Receptor-Positive Tumor Cells. *Bioconjugate Chem.* **17**, 603-609 (2006).

31. Tong, L., Zhao, Y., Huff, T. B., Hansen, M. N., Wei, A., & Cheng, J. X. Gold Nanorods Mediate Tumor Cell Death by Compromising Membrane Integrity. *Adv. Mater.* **19**, 3136-3141 (2007).

32. Levin, E. R. Integration of the Extranuclear and Nuclear Actions of Estrogen. *Mol. Endocrinol.* **19**, 1951-1959 (2005).

33. Campbell, C. H., Bulayeva, N., Brown, D. B., Gametchu, B., & Watson, C. S. Regulation of the membrane estrogen receptor-alpha: role of cell density, serum, cell passage number, and estradiol. *FASEB J.* **16**, 1917-1927 (2002).

34. Niidome, T., Yamagata, M., Okamoto, Y., Akiyama, Y., Takahashi, H., Kawano, T., Katayama, Y., & Niidome, Y. PEG-modified gold nanorods with a stealth character for in vivo applications. *J. Controlled Release* **114**, 343-347 (2006).

35. Jang, S. S., Jang, Y. H., Kim, Y.-H., Goddard, W. A., Flood, A. H., Laursen, B. W., Tseng, H.-R., Stoddart, J. F., Jeppesen, J. O., Choi, J. W., Steuerman, D. W., DeIonno, E., & Heath, J. R. Structures and Properties of Self-Assembled Monolayers of Bistable [2]Rotaxanes on Au (111) Surfaces from Molecular Dynamics Simulations Validated with Experiment. *J. Am. Chem. Soc.* **127**, 1563-1575 (2005).

36. Lavrich, D. J., Wetterer, S. M., Bernasek, S. L., & Scoles, G. Physisorption and Chemisorption of Alkanethiols and Alkyl Sulfides on Au(111). *J. Phys. Chem. B* **102**, 3456-3465 (1998).

37. Gref, R., Domb, A., Quellec, P., Blunk, T., Muller, R. H., Verbavatz, J. M., & Langer, R. The Controlled Intravenous Delivery of Drugs Using PEG-Coated Sterically Stabilized Nanospheres. *Adv. Drug Delivery Rev.* **16**, 215-233 (1995).

38. Nativo, P., Prior, I. A., & Brust, M. Uptake and Intracellular Fate of Surface-Modified Gold Nanoparticles. *ACS Nano* **2**, 1639-1644 (2008).

39. Dreaden, E. C., Mwakwari, S. C., Sodji, Q. H., Oyelere, A. K., & El-Sayed, M. A. Tamoxifen-Poly(ethylene glycol)-Thiol Gold Nanoparticle Conjugates: Enhanced Potency and Selective Delivery for Breast Cancer Treatment. *Bioconjugate Chem.* **20**, 2247-2253 (2009).

40. Olofson, R. A., Martz, J. T., Senet, J. P., Piteau, M., & Malfroot, T. A New Reagent for the Selective, High-Yield N-Dealkylation of Tertiary-Amines - Improved Syntheses of Naltrexone and Nalbuphine. *J. Org. Chem.* **49**, 2081-2082 (1984).

41. Bouzide, A., & Sauve, G. Silver(I) oxide mediated highly selective monotosylation of symmetrical diols. Application to the synthesis of polysubstituted cyclic ethers. *Org. Lett.* **4**, 2329-2332 (2002).

42. Turkevich, J., Stevenson, P. C., & Hillier, J. A Study of the Nucleation and Growth Processes in the Synthesis of Colloidal Gold. *Discuss. Faraday Soc.*, 55-75 (1951).

43. Orendorff, C. J., & Murphy, C. J. Quantitation of Metal Content in the Silver-Assisted Growth of Gold Nanorods. *J. Phys. Chem. B* **110**, 3990-3994 (2006).

44. Guthrie, N., Gapor, A., Chambers, A. F., & Carroll, K. K. Inhibition of Proliferation of Estrogen Receptor-Negative MDA-MB-435 and -Positive MCF-7 Human Breast Cancer Cells by Palm Oil Tocotrienols and Tamoxifen, Alone and in Combination. *J. Nutr.* **127**, 544S-548S (1997).

45. Jordan, V. C. New insights into the metabolism of tamoxifen and its role in the treatment and prevention of breast cancer. *Steroids* **72**, 829-842 (2007).

46. Nozoe, T., Oyama, T., Takenoyama, M., Hanagiri, T., Sugio, K., & Yasumoto, K. Significance of immunohistochemical expression of estrogen receptors alpha and beta in squamous cell carcinoma of the esophagus. *Clin. Cancer Res.* **13**, 4046-4050 (2007).

47. Htun, H., Holth, L. T., Walker, D., Davie, J. R., & Hager, G. L. Direct visualization of the human estrogen receptor alpha reveals a role for ligand in the nuclear distribution of the receptor. *Mol. Biol. Cell* **10**, 471-486 (1999).

48. Brooks, S. C., Locke, E. R., & Soule, H. D. Estrogen Receptor in a Human Cell Line (MCF-7) from Breast Carcinoma. *J. Biol. Chem.* **248**, 6251-6253 (1973).

49. Horwitz, K. B., Zava, D. T., Thilagar, A. K., Jensen, E. M., & McGuire, W. L. Steroid Receptor Analyses of Nine Human Breast Cancer Cell Lines. *Cancer Res.* **38**, 2434-2437 (1978).

50. Razandi, M., Oh, P., Pedram, A., Schnitzer, J., & Levin, E. R. ERs associate with and regulate the production of caveolin: Implications for signaling and cellular actions. *Mol. Endocrinol.* **16**, 100-115 (2002).

51. Chen, X. M., Danes, C., Lowe, M., Herliczek, T. W., & Keyomarsi, K. Activation of the estrogen-signaling pathway by p21(WAF1/CIP1) in estrogen receptor-negative breast cancer cells. *J. Natl. Cancer Inst.* **92**, 1403-1413 (2000).

52. Seeger, H., Diesing, D., Gückel, B., Wallwiener, D., Mueck, A. O., & Huober, J. Effect of tamoxifen and 2-methoxyestradiol alone and in combination on human breast cancer cell proliferation. *J. Steroid Biochem. Mol. Biol.* **84**, 255-257 (2003).

53. Rich, R. L., Hoth, L. R., Geoghegan, K. F., Brown, T. A., LeMotte, P. K., Simons, S. P., Hensley, P., & Myszka, D. G. Kinetic analysis of estrogen receptor/ligand interactions. *Proc. Natl. Acad. Sci. U.S.A.* **99**, 8562-8567 (2002).

54. Qing, L., Pallas, D. C., Surks, H. K., Baur, W. E., Mendelsohn, M. E., & Karas, R. H. Striatin assembles a membrane signaling complex necessary for rapid, nongenomic activation of endothelial NO synthase by estrogen receptor alpha. *Proc. Natl. Acad. Sci. U.S.A.* **101**, 17126-17131 (2004).

55. Ferlay, J., Shin, H.-R., Bray, F., Forman, D., Mathers, C., & Parkin, D. M. Estimates of worldwide burden of cancer in 2008: GLOBOCAN 2008. *Int. J. Cancer* **127**, 2893-2917 (2010).

56. Siegel, R., Ward, E., Brawley, O., & Jemal, A. Cancer Statistics, 2011. *CA Cancer J. Clin.* **61**, 212-236 (2011).

57. Cancer Research UK. *Statistics on the risk of developing cancer*, <http://info.cancerresearchuk.org/cancerstats/incidence/risk/> (accessed 7 December, 2011).

58. Chen, Y., Clegg, N. J., & Scher, H. I. Anti-androgens and androgen-depleting therapies in prostate cancer: new agents for an established target. *Lancet Oncol.* **10**, 981-991 (2009).

59. Attar, R. M., Takimoto, C. H., & Gottardis, M. M. Castration-Resistant Prostate Cancer: Locking Up the Molecular Escape Routes. *Clin. Cancer Res.* **15**, 3251-3255 (2009).

60. Borsellino, N., Belldegrun, A., & Bonavida, B. Endogenous Interleukin 6 Is a Resistance Factor for cis-Diamminedichloroplatinum and Etoposide-mediated Cytotoxicity of Human Prostate Carcinoma Cell Lines. *Cancer Res.* **55**, 4633-4639 (1995).

61. Dhar, S., Gu, F. X., Langer, R., Farokhzad, O. C., & Lippard, S. J. Targeted delivery of cisplatin to prostate cancer cells by aptamer functionalized Pt(IV) prodrug-PLGA–PEG nanoparticles. *Proc. Natl. Acad. Sci. U.S.A.* **105**, 17356-17361 (2008).

62. Dhar, S., Kolishetti, N., Lippard, S. J., & Farokhzad, O. C. Targeted delivery of a cisplatin prodrug for safer and more effective prostate cancer therapy in vivo. *Proc. Natl. Acad. Sci. U.S.A.* (2011).

63. Hattori, Y., & Maitani, Y. Folate-linked nanoparticle-mediated suicide gene therapy in human prostate cancer and nasopharyngeal cancer with herpes simplex virus thymidine kinase. *Cancer Gene Ther.* **12**, 796-809 (2005).

64. Xue, H.-Y., & Wong, H.-L. Solid Lipid–PEI Hybrid Nanocarrier: An Integrated Approach To Provide Extended, Targeted, and Safer siRNA Therapy of Prostate Cancer in an All-in-One Manner. *ACS Nano* **5**, 7034-7047 (2011).

65. Chanda, N., Kattumuri, V., Shukla, R., Zambre, A., Katti, K., Upendran, A., Kulkarni, R. R., Kan, P., Fent, G. M., Casteel, S. W., Smith, C. J., Boote, E., Robertson, J. D., Cutler, C., Lever, J. R., Katti, K. V., & Kannan, R. Bombesin functionalized gold nanoparticles

show in vitro and in vivo cancer receptor specificity. *Proc. Natl. Acad. Sci. U.S.A.* **107**, 8760-8765 (2010).

66. Roa, W., Zhang, X., Guo, L., Shaw, A., Hu, X., Xiong, Y., Gulavita, S., Patel, S., Sun, X., Chen, J., Moore, R., & Xing, J. Z. Gold nanoparticle sensitize radiotherapy of prostate cancer cells by regulation of the cell cycle. *Nanotechnol.* **20**, 375101 (2009).

67. Stern, J. M., Stanfield, J., Kabbani, W., Hsieh, J.-T., & Cadeddu, J. A. Selective Prostate Cancer Thermal Ablation With Laser Activated Gold Nanoshells. *J. Urol.* **179**, 748-753 (2008).

68. Pedram, A., Razandi, M., Sainson, R. C. A., Kim, J. K., Hughes, C. C., & Levin, E. R. A conserved mechanism for steroid receptor translocation to the plasma membrane. *J. Biol. Chem.* **282**, 22278-22288 (2007).

69. Hatzoglou, A., Kampa, M., Kogia, C., Charalampopoulos, I., Theodoropoulos, P. A., Anezinis, P., Dambaki, C., Papakonstanti, E. A., Stathopoulos, E. N., Stournaras, C., Gravanis, A., & Castanas, E. Membrane Androgen Receptor Activation Induces Apoptotic Regression of Human Prostate Cancer Cells in Vitro and in Vivo. *J. Clin. Endocrinol. Metab.* **90**, 893-903 (2005).

70. Pi, M., & Quarles, L. D. GPRC6A regulates prostate cancer progression. *Prostate (ASAP)* (2011).

71. Dreaden, E. C., Mackey, M. A., Huang, X., Kang, B., & El-Sayed, M. A. Beating cancer in multiple ways using nanogold. *Chem. Soc. Rev.* **40**, 3391-3404 (2011).

72. Dreaden, E. C., Alkilany, A. M., Huang, X., Murphy, C. J., & El-Sayed, M. A. The Golden Age: Gold Nanoparticles for Biomedicine. *Chem. Soc. Rev. (in press)* (2012).

73. Frens, G. Controlled Nucleation for the Regulation of the Particle Size in Monodisperse Gold Suspensions. *Nature* **241**, 20-22 (1973).

74. Liu, X., Atwater, M., Wang, J., & Huo, Q. Extinction coefficient of gold nanoparticles with different sizes and different capping ligands. *Coll. Surf. B* **58**, 3-7 (2007).

75. Pi, M., Parrill, A. L., & Quarles, L. D. GPRC6A Mediates the Non-genomic Effects of Steroids. *J. Biol. Chem.* **285**, 39953-39964 (2010).

76. Bohl, C. E., Gao, W., Miller, D. D., Bell, C. E., & Dalton, J. T. Structural basis for antagonism and resistance of bicalutamide in prostate cancer. *Proc. Natl. Acad. Sci. U.S.A.* **102**, 6201-6206 (2005).

77. Dreaden, E. C., Gryder, B. E., Austin, L. A., Tene Defo, B. A., Hayden, S. C., Pi, M., Quarles, L. D., Oyelere, A. K., & El-Sayed, M. A. Antiandrogen Gold Nanoparticles Dual-Target and Overcome Treat-ment Resistance in Hormone-Insensitive Prostate Cancer Cells. *submitted to Nat. Nanotechnol.* (2012).

78. Jiang, W., Kim, B. Y. S., Rutka, J. T., & Chan, W. C. W. Nanoparticle-mediated cellular response is size-dependent. *Nat. Nanotechnol.* **3**, 145-150 (2008).

79. Perrault, S. D., Walkey, C., Jennings, T., Fischer, H. C., & Chan, W. C. W. Mediating Tumor Targeting Efficiency of Nanoparticles Through Design. *Nano Lett.* **9**, 1909-1915 (2009).

80. Obach, R. S., Lombardo, F., & Waters, N. J. Trend Analysis of a Database of Intravenous Pharmacokinetic Parameters in Humans for 670 Drug Compounds. *Drug Metab. Dispos.* **36**, 1385-1405 (2008).

81. He, Y., Yin, D., Perera, M., Kirkovsky, L., Stourman, N., Li, W., Dalton, J. T., & Miller, D. D. Novel nonsteroidal ligands with high binding affinity and potent functional activity for the androgen receptor. *Euro. J. Med. Chem.* **37**, 619-634 (2002).

82. Kirkovsky, L., Mukherjee, A., Yin, D., Dalton, J. T., & Miller, D. D. Chiral Nonsteroidal Affinity Ligands for the Androgen Receptor. 1. Bicalutamide Analogues Bearing Electrophilic Groups in the B Aromatic Ring1. *J. Med. Chem.* **43**, 581-590 (2000).

83. Papadopoulou, N., Charalampopoulos, I., Anagnostopoulou, V., Konstantinidis, G., Foller, M., Gravanis, A., Alevizopoulos, K., Lang, F., & Stournaras, C. Membrane androgen receptor activation triggers down-regulation of PI-3K/Akt/NF-kappaB activity and induces apoptotic responses via Bad, FasL and caspase-3 in DU145 prostate cancer cells. *Mol. Cancer* **7** (2008).

84. Gu, S., Papadopoulou, N., Gehring, E.-M., Nasir, O., Dimas, K., Bhavsar, S., Föller, M., Alevizopoulos, K., Lang, F., & Stournaras, C. Functional membrane androgen receptors in colon tumors trigger pro-apoptotic responses in vitro and reduce drastically tumor incidence in vivo. *Mol. Cancer* **8**, 1-14 (2009).

85. Kampa, M., Kogia, C., Theodoropoulos, P. A., Anezinis, P., Charalampopoulos, I., Papakonstanti, E. A., Stathopoulos, E. N., Hatzoglou, A., Stournaras, C., Gravanis, A., & Castanas, E. Activation of membrane androgen receptors potentiates the antiproliferative effects of paclitaxel on human prostate cancer cells. *Mol. Cancer Ther.* **5**, 1342-1351 (2006).

86. Heinlein, C. A., & Chang, C. Androgen Receptor in Prostate Cancer. *Endocr. Rev.* **25**, 276-308 (2004).

87. Wellendorph, P., & Bräuner-Osborne, H. Molecular cloning, expression, and sequence analysis of GPRC6A, a novel family C G-protein-coupled receptor. *Gene* **335**, 37-46 (2004).

88. Takata, R., Akamatsu, S., Kubo, M., Takahashi, A., Hosono, N., Kawaguchi, T., Tsunoda, T., Inazawa, J., Kamatani, N., Ogawa, O., Fujioka, T., Nakamura, Y., & Nakagawa, H. Genome-wide association study identifies five new susceptibility loci for prostate cancer in the Japanese population. *Nat. Genetics* **42**, 751-754 (2010).

89. Whitaker, H. C., Hanrahan, S., Totty, N., Gamble, S. C., Waxman, J., Cato, A. C. B., Hurst, H. C., & Bevan, C. L. Androgen Receptor Is Targeted to Distinct Subcellular Compartments in Response to Different Therapeutic Antiandrogens. *Clin. Cancer Res.* **10**, 7392-7401 (2004).

90. Virolainen, E., Vanharanta, R., & Carey, T. E. Steroid hormone receptors in human squamous carcinoma cell lines. *Int. J. Cancer* **33**, 19-25 (1984).

91. Alimirah, F., Chen, J., Basrawala, Z., Xin, H., & Choubey, D. DU-145 and PC-3 human prostate cancer cell lines express androgen receptor: Implications for the androgen receptor functions and regulation. *FEBS Lett.* **580**, 2294-2300 (2006).

92. Kreis, W., Budman, D. R., & Calabro, A. A reexamination of PSC 833 (Valspodar) as a cytotoxic agent and in combination with anticancer agents. *Cancer Chemother. Pharmacol.* **47**, 78-82 (2001).

CHAPTER 5

MACROPHAGE-MEDIATED DELIVERY OF GOLD NANORODS

5.1 Macrophage-Targeting Nanoparticles for Tissue-Selective Delivery to Solid Tumors

Gold nanoparticles have demonstrated tremendous utility and multifunctionality for the diagnosis and treatment of cancer.[1-6] Not only can these structures serve as targeted drug delivery vehicles,[7] they can also act as contrast agents for near-infrared (NIR) laser photothermal tumor ablation [8-12] and as platforms in a range of other biomedical diagnostic [1,13,14] and therapeutic [15-18] applications. The uptake and removal of circulating nanoparticles by the mononuclear phagocyte system (MPS),[19] represents one of the most significant impediments to the efficient delivery of nanoscale structures to solid tumors and to-date, the majority of tumor-targeting strategies for nanoparticles attempt to evade the MPS and increase circulation time. Here, we show that colloidal gold nanorods (AuNRs) can be actively-targeted towards phagocytic macrophages that exhibit high intrinsic accumulation and infiltration into solid tumors. Macrolide-functionalized gold nanorods were preferentially delivered to tumor-associated macrophage (TAM) cells and selectively induced TAM-dependent cytotoxicity towards breast cancer cells in co-culture. Because TAMs migrate freely in circulation, bypass the blood-brain-barrier, and extensively accumulate/infiltrate into breast tumors, these data show that macrophage-targeting gold nanoparticles can serve as promising candidates for targeted cancer therapy.

Although the MPS plays an important physiological function in removing foreign material, cellular debris, and pathogens from circulation, its cells also play a principal role in anti-tumor immunity [20] and as such, TAMs readily accumulate and infiltrate into solid tumors, comprising up to 50% of tumor mass in breast carcinomas.[21] A limited number of studies have investigated the

ability of macrophages to deliver nanoscale drugs and imaging agents to solid tumors. Badie and coworkers have shown that TAMs can serve as efficient carriers of cyclodextrin-based nanoparticles (CDPs; fluorescent analogues of IT-101) into glioma tumors.[22] CDPs were found to preferentially accumulate in TAMs that subsequently migrated into circulation and localized at distant tumor sites. Because TAMs are able to bypass the blood-brain-barrier during pathogenesis,[23] increasingly-specific delivery of camptothecin (IT-101) to brain tumors is expected from CDPs. Jackson et al. found that circulating, PEG-labeled quantum dots are similarly uptaken by TAMs that readily infiltrate glial tumors.[24] TAMs have also been actively targeted by nanoparticle ligands to facilitate increasingly-specific delivery. Mannan-conjugated lipid nanoparticles have achieved selective gene delivery to alveolar macrophages;[25] folate-targeted iron oxide nanoparticles have exhibited TAM-exclusive accumulation in breast tumors [26] and glutamine-functionalized liposomes have demonstrated TAM-dependent translocation into neuroblastoma tumors.[27] Hirschberg and coworkers have further exploited TAMs to preferentially deliver photothermal contrast agents to tumor cells,[28,29] finding that TAMs efficiently take up PEGylated gold nanoshells and subsequently infiltrate glial tumor spheroids to allow selective NIR laser photothermal ablation therapy (810 nm, ≥7 W cm^{-2}, 10 min).

Macrolides are a class of structurally-homologous antibiotics widely administered for more than four decades for the treatment of microbial infections in humans, particularly those of the respiratory tract and soft tissues. In addition to their broad-spectrum antibiotic activity, one notable hallmark of macrolides is their exceptionally high accumulation in phagocytic cells (macrophages) that facilitate increasingly specific delivery of these drugs to sites of inflammation (infection).[30,31] We hypothesized that macrolide ligands could also facilitate the preferential delivery of gold nanoparticles to inflamed tumor tissues via TAMs, allowing for enhanced TAM anti-tumor

potential,[32-34] increasingly effective laser photothermal therapy,[8-12] and/or heat shock protein-induced activation of macrophage-mediated anti-tumor immunity.[35] To this end, gold nanorods (AuNRs) were synthesized via seed-mediated growth from chloroauric acid and conjugated with PEG-thiol or mixed self-assembled monolayers of (9:1) PEG-thiol and thiol-PEGylated azithromycin (Zithromax®), clarithromycin (Biaxin®), or tricyclic ketolide (TE-802) (**Figure 5.1A,B**; **Figure 5.2**). Each of the nanorods, abbreviated hereafter as PEG-AuNRs, Azith-AuNRs, Clarith-AuNRs, and TriKeto-AuNRs, respectively, were conjugated such that they displayed 1×10^3 macrolide ligands and 9×10^3 PEG-thiol molecules per particle, as well as a NIR absorption maximum ca. 818 nm. PEG-AuNRs displayed 10×10^3 PEG-thiol molecules per particle.

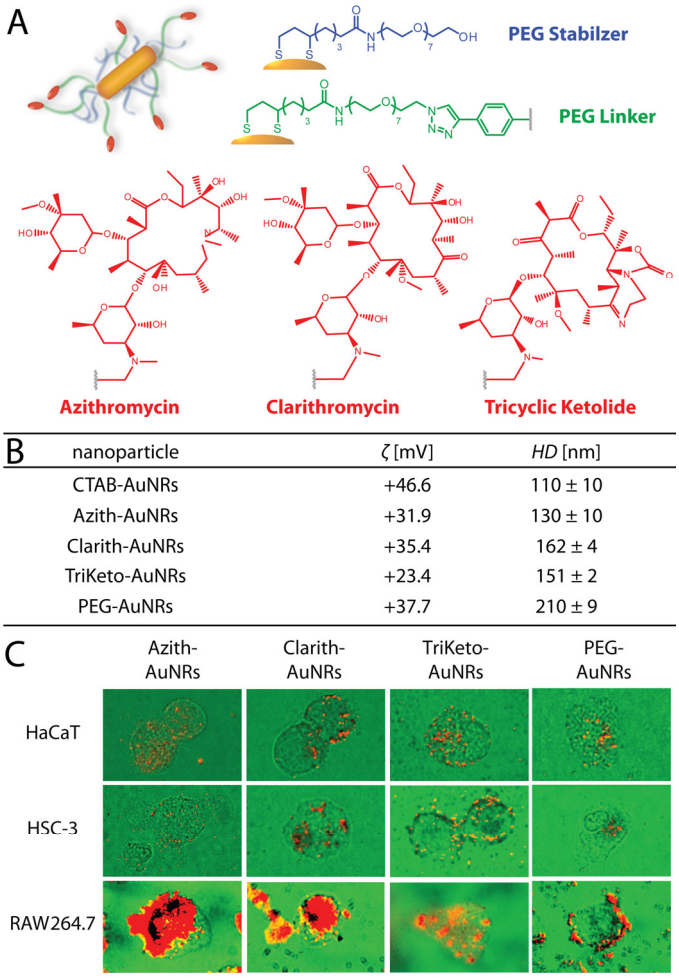

B

nanoparticle	ζ [mV]	*HD* [nm]
CTAB-AuNRs	+46.6	110 ± 10
Azith-AuNRs	+31.9	130 ± 10
Clarith-AuNRs	+35.4	162 ± 4
TriKeto-AuNRs	+23.4	151 ± 2
PEG-AuNRs	+37.7	210 ± 9

Figure 5.1. A) Schematic representation and (B) physiochemical characteristics of the macrolide-gold nanorods used herein. C) Cardioid immersion dark-field scattering microscopy (DFSM) of cell cultures (green) illustrating preferential uptake/accumulation of macrolide-gold nanorods (red) into tumor-associated macrophage cells (RAW 264.7) relative to squamous cell carcinoma (HSC-3) and keratinocyte cells (HaCaT). PEGylated gold nanorods exhibited only nominal cell-surface binding with TAMs. Images in (C) are false color. Adapted from Dreaden et al. [*36*].

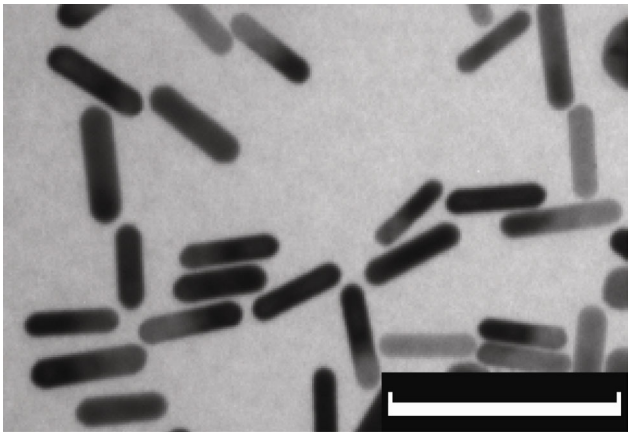

Figure 5.2. Transmission electron microscopy (TEM) image of the as-synthesized colloidal gold nanorods. Scale bar represents 100 μm. Adapted from Dreaden et al. [*36*].

5.1.1 Design and Development of Near-Infrared Absorbing, Macrophage-Targeting Gold Nanorods

Synthesis and Characterization of Macrolide-Gold Nanorods. Thiol PEGylated macrolide ligands were synthesized as described in Dreaden et al. (**See Section 5.21**).[*37*] Gold nanorods (AuNRs) were synthesized as described in Dickerson et al. with slight modifications.[*9*] Briefly, $NaBH_4$ (600 μL, 10 mM; 4 °C) was rapidly added to a stirred 7.5 mL solution containing 0.333 mM $HAuCl_4•(H_2O)_3$ (Sigma) and 0.133 M cetyltrimethylammonium bromide (CTAB, Sigma). The reaction was allowed to proceed for 5 min, then 320 μL of the as-formed seed solution was rapidly injected into a 420 mL growth solution containing 0.479 mM $HAuCl_4•(H_2O)_3$, 95.7 mM CTAB, 86.2 μM $AgNO_3$ (Fischer), and 0.528 mM ascorbic acid (Sigma). The seeded growth solution was gently mixed and allowed to react overnight. The crude nanorod solution was purified and concentrated by centrifugation (30 min, 4185 × *g*) and stored at 4 °C until use. All reactions were performed at room temperature under aseptic conditions in aqueous solutions (18 MΩ). Particle size was analyzed via transmission electron microscopy (TEM, JEOL 100CX II). Hydrodynamic diameter (*HD*) and zeta potential (ζ) measurements were performed using a NanoZS Zetasizer particle

analyzer (Malvern, 633 nm). Optical extinction measurements were performed using an Ocean Optics HR4000CG-UV-NIR spectrometer.

Nanoparticle ligand coverages were determined as described in Dreaden et al. with slight modifications.[*38*] Briefly, purified gold nanorod concentrates were rapidly injected into aqueous solutions containing PEG-thiol or 9:1 mole ratios of PEG-thiol and macrolide ligands Azith, Clarith, or TriKeto (PEG-thiol, hydroxy octa(ethylene glycol)-lipoic amide). Molar excesses of ligands relative to AuNRs were adjusted until comparable grafting densities were achieved for each of the macrolide-AuNR conjugates following centrifugal purification (15 min, 4185 × g; twice). Azith- Clarith- and TriKeto-AuNRs contained 1×10^3 macrolide ligands and 9×10^3 PEG-thiol ligands per nanorod, obtained by incubating with solutions containing 1.3, 1.6, and 3.9×10^5-fold ligand excesses, respectively, at 30 *°C*, under sonication for 12 h. Adsorbate coverages of Azith, Clarith, TriKeto were determined via UV absorption assay (260 nm) of centrifugal supernatants; coverages for PEG-thiol were determined via Ellman's assay (Pierce/Thermo Scientific). Molar extinction cross sections for thiol PEGylated Azith, Clarith, and TriKeto [UV-vis (water): $\varepsilon_{260\ nm}$] were found to be 1.08 ± 0.03, 0.841 ± 0.03, and $1.26 \pm 0.02 \times 10^4$ L mol^{-1} cm^{-1}, respectively. Molar extinction cross sections of the nanorods were interpolated from experimental data in Orendorff and Murphy.[*39*] Nanoparticle supernatants used in coverage assays were centrifuged at 18,000 × g for 1 h to remove any trace particles. Gold nanorods used in these studies were ca. 50 ± 8 nm in length and 13 ± 2 nm in width (4.0 ± 0.9 aspect ratio) as measured by TEM (**Figure 5.2**) and were stably dispersed in complete growth media over 24 h [UV-vis (water): λ_{max}~818 nm].

Cell Culture and Laser Photothermal Therapy. RAW 264.7 alveolar TAMs, MCF7 human breast adenocarcinoma cells, HSC-3 human oral squamous cell carcinoma cells, and HaCaT non-malignant human epithelial keratinocyte cells were subcultured in Dulbecco's modified Eagle's

medium (DMEM) supplanted with 10% v/v fetal bovine serum (FBS), 20 I.U./mL penicillin, 100 ug/mL streptomycin, and 250 ng/mL amphotericin B at 37 ^{o}C in a 5% CO_2 humidified atmosphere. RAW 264.7 and MCF7 cells were obtained from ATCC; HSC-3 and HaCaT cells were a gift from Dr. Ivan H. El-Sayed (UCSF Otolaryngology). Cells were passaged using 0.25% trypsin containing 2.21 mM EDTA in Hank's Buffered Salt Solution (HBSS, Mediatech) and pelleted via centrifugation (RAW 264.7, 2000 rpm; MCF7, 1750 rpm; HSC-3/HaCaT, 1500 rpm). All experiments were performed on cells passaged 12 h prior. Cells were counted via hemacytometry and passaged to surface area-equivalent confluences. Spectroscopic and microscopic measurements were performed in complete media lacking phenol red. Co-cultures were constructed by passaging RAW 264.7 TAMs onto 12-well tissue culture plates (BD). Culture media was removed following overnight incubation and replaced with complete media containing 10 pM AuNR conjugates. Following 24 h incubation with the nanoconjugates, adherent cells were washed with DPBS, trypsinized, pelleted, triturated, and seeded onto DPBS-rinsed MCF7 cultures passaged onto 96-well tissue culture plates (BD) 12 h prior. TAMs were allowed to adhere for 12 h, after which adherent cells in co-culture were washed with DPBS and incubated with 50 μL DPBS (ca. 1.6 mm depth). Monolayers were irradiated using a fiber optic-coupled near-infrared (NIR) diode laser (λ=808 nm, Power Technologies) for 10 min (646 mW cm^{-2}) and positioned atop a 5 mm copper plate heated to 37 ºC (n = 3; non-irradiated, n=6). TAM-only photothermal experiments were similarly performed in 96-well plates and irradiated after 24 h AuNR incubation and washing with PBS (n=3 non-irradiated, n=6). Each plate contained an independent set of control cells. Following treatment, cultures were allowed to incubate in complete growth media for 24 h and viability was analyzed by tetrazolium assay (XTT, Sigma) following the manufacture's instructions. TAM proliferation assays in response to macrolide and macrolide-AuNR exposure were similarly performed (**Figure 5.3**).

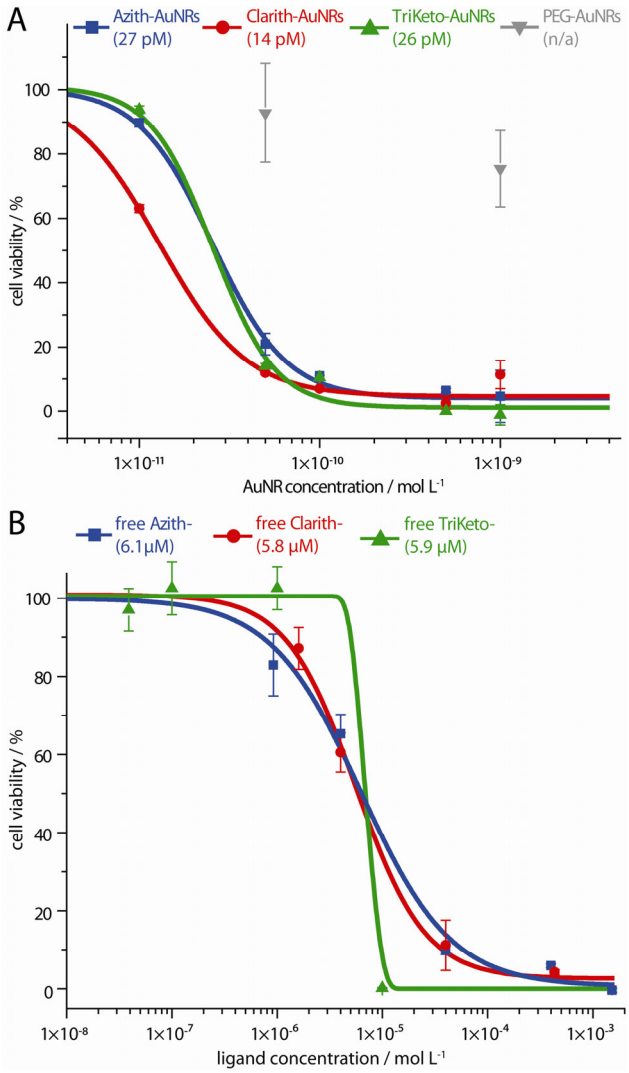

Figure 5.3. Effects of macrolide-gold nanorods and macrolide ligands on RAW 264.7 tumor-associated macrophage (TAM) proliferation. A) Macrolide-gold nanorods and (B) thiol-PEGylated macrolide ligands diminished TAM proliferation in a dose-dependent manner (24 h). Values in parentheses indicate half maximal inhibitory concentrations. Error bars represent SD. Adapted from Dreaden et al. [*36*].

Dark-Field Scattering Microscopy. Nanoparticle uptake/accumulation was assessed via dark-field scattering optical microscopy (DFSM) using an inverted-objective Olympus IX70 microscope fitted with a cardioid immersion dark-field optical condenser (U-DCW), 100x/1.35na oil iris objective (UPLANAPO), tungsten lamp illumination, and a Nikon D200 digital SLR camera. Round glass coverslips (18 mm; Fischer) were sterilized by ethanol immersion and UV exposure (30

min), followed by immersion in 0.04 mg/mL rat tail collagen/DPBS (Roche) for 6 h at 37 °C in a 5% CO_2 humidified atmosphere. The collagen-coated coverslips were next rinsed in DPBS and cells were passaged onto the coverslips. After 12 h, growth solutions were replaced with media containing 0.5 nM of the nanoconjugates and the cells were allowed to incubate for 24 h. Cell monolayers were rinsed in DPBS and fixed in 4 % paraformaldehyde/DPBS for 15 min at 4 °C. The fixed coverslips were coated in glycerol, mounted and sealed onto glass slides, and imaged immediately.

Laser Scanning Confocal Microscopy. RAW 264.7 TAMs were passaged onto 12-well tissue culture plates. Following overnight incubation, growth media was removed and replaced with complete media containing 10 pM AuNR conjugates. Following 24 h incubation with the nanoconjugates, adherent cells were washed with DPBS and incubated with 500 μL of 300 nM 4',6-diamidino-2-phenylindole (DAPI; Molecular Probes; DPBS, 37 °C), a membrane-permeable fluorescent nuclear marker, for 10 min. DAPI-labeled, AuNR-loaded TAMs were rinsed twice with DPBS (37 °C), trypsinized, pelleted, triturated, and seeded onto DPBS-rinsed MCF7 cultures passaged onto 12-well tissue culture plates containing sterile 18 mm round glass coverslips at their base. TAMs were allowed to adhere for 12 h, after which adherent cells in co-culture were washed with DPBS (37 °C) and incubated with 1 mL of 4 μM ethidium homodimer-1 (EthD-1; Molecular Probes, DPBS, 37 °C), a membrane-impermeable fluorescent nuclear marker for apoptotic/necrotic cells, for 45 min. After 12 h, co-culture medium was removed and replaced with fresh growth media. Following an additional 24 h of incubation, adherent co-culture cells were mounted and sealed onto 75 x 25 mm glass slides using 10 μL of 4 μM EthD-1 and 5 μL of Crystal Mount™ mounting medium (Sigma). Labeled co-cultures were immediately imaged via confocal fluorescence microscopy using an inverted-objective Zeiss Axiovert 200M microscope equipped with a Neofluor 40x/1.3na oil objective and Zeiss ZEN 2009 software.

5.1.2 Macrolide-Gold Nanorods Selectively Target and Induce Macrophage Cytotoxicity Towards Breast Cancer Cells

Preferential uptake/accumulation of the macrolide-AuNRs into TAM cells was assessed via cardioid immersion dark-field scattering microscopy (DFSM). TAM cells (RAW 264.7) exhibited substantially higher levels of macrolide-AuNR uptake than either squamous cell carcinoma (HSC-3) or keratinocyte cells (HaCaT) cells (**Figure 5.1C**) and showed only nominal cell-surface binding by PEG-AuNRs.[*37*] Based on these findings, phototoxicity from NIR laser exposure (λ=808 nm) was assessed using TAMs treated with sub-lethal concentrations of macrolide-AuNRs (10 pm, 24 h; **Figures 5.3,4**). NIR laser exposure of TAM cultures washed/immersed in buffer (1.6 mm) showed modest phototoxicity from Azith- and TriKeto-AuNRs, but no significant effects from Clarith-AuNRs, PEG-AuNRs, or laser treatment alone (10 min, 646 mW cm^{-2}). We then evaluated the effects of AuNR-loaded TAMs and NIR laser exposure on cell viability in breast adenocarcinoma co-cultures. TAM cultures were again loaded with sub-lethal concentrations of macrolide-AuNRs (10 pm, 24 h), washed with buffer, and seeded onto MCF7 breast cultures at 50% plating densities to reflect physiological levels of TAM infiltration into breast carcinomas (**Figure 5.5**).[21] After 12 h, co-cultures were washed and immersed in buffer (1.6 mm), NIR laser-exposed (10 min, 646 mW cm^{-2}), and allowed to incubate in complete growth media for an additional 24 h. While no statistically significant cytotoxic effects from NIR laser exposure were observed, we found substantial cytotoxicity in co-cultures containing macrolide-AuNR-treated TAMs and significant, but notably diminished cytotoxicity in those containing PEG-AuNR-treated TAMs (ca. 55%; **Figure 5.4B**).

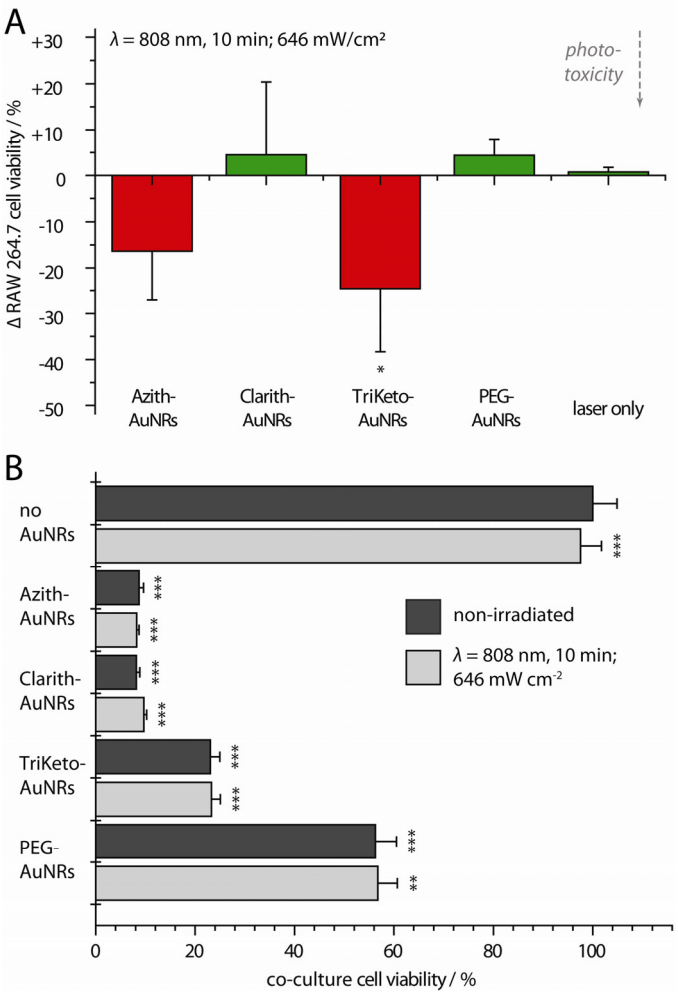

Figure 5.4. A) Near-infrared laser photothermal ablation of tumor-associated macrophage (TAM) cells loaded with macrolide-gold nanorods (AuNRs). B) Selective cytotoxicity of AuNR-loaded TAMs co-cultured with MCF7 breast adenocarcinoma cells. Error bars represent SD. P-values in (A) reported relative to non-irradiated RAW 264.7 cells; P-values in (B) reported relative to non-irradiated, non-AuNR-treated co-cultures. *P<0.05, **P<0.01, ***P<0.001. Adapted from Dreaden et al. [*36*].

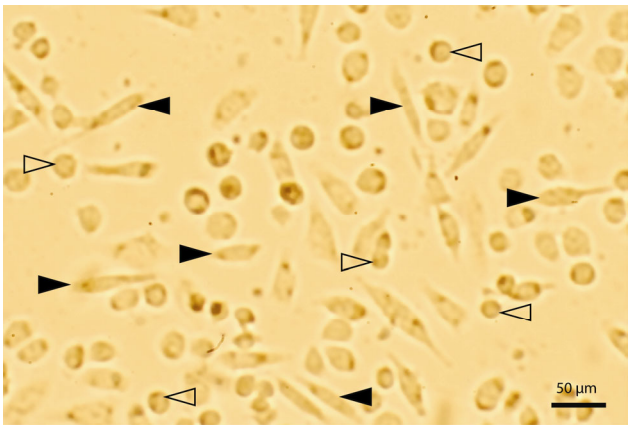

Figure 5.5. Microscopic image of breast carcinoma:macrophage co-cultures. MCF7 human breast adenocarcinoma cells are indicated by solid arrowheads and RAW 264.7 tumor-associated macrophage cells (TAMs) are indicated by open arrowheads. Adapted from Dreaden et al. [*36*].

In order to delineate which cells contributed to co-culture cell death, AuNR-treated TAMs were labeled with 4',6-diamidino-2-phenylindole (DAPI), a membrane-permeable fluorescent nuclear marker, prior to passage into co-culture. DAPI-labeled, AuNR-loaded TAM cells were thoroughly rinsed with buffer and again seeded at 50% plating densities with MCF7 breast adenocarcinoma cells. After 12 h, culture media was removed and replaced with fresh growth media. Following an additional 24 h of incubation, adherent co-culture cells were labeled with ethidium homodimer-1 (EthD-1), a membrane-impermeable fluorescent nuclear marker for apoptotic/necrotic cells. Confocal fluorescence microscopy of the co-cultures revealed that MCF7 breast cancer cells contributed near exclusively to the observed cell death, with no colocalization of DAPI-labeled TAM fluorescence with the EthD-1 apoptotic/necrotic cell marker (**Figure 5.6**).

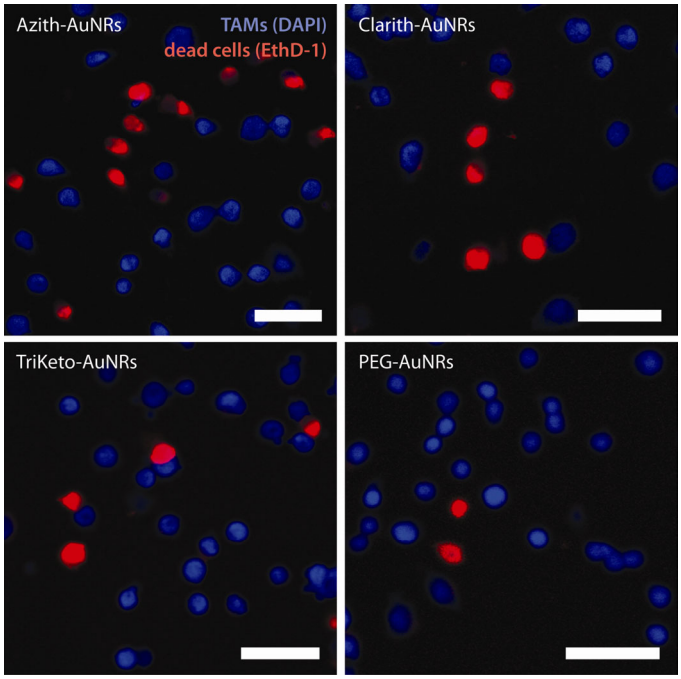

Figure 5.6. Tumor-associated macrophages (TAMs) treated with macrolide-gold nanorods (AuNRs) induce cell death in co-cultured breast adenocarcinoma cells. Macrolide-AuNR-loaded TAM nuclei were labeled with 4',6-diamidino-2-phenylindole (DAPI, blue) and seeded onto MCF7 breast cell cultures at 50% plating densities. Confocal fluorescence microscopy using the apoptotic/necrotic nuclear marker, ethidium homodimer-1 (EthD-1, red), shows cytotoxicity exclusive to breast adenocarcinoma cells. Scale bar represents 25 μm. Adapted from Dreaden et al. [*36*].

Although macrophage cytokine activation by gold nanoparticles (AuNPs) is well-documented,[32-34] we believe this to be the first report on the subsequent effects of AuNP-activated macrophages on nearby cells. Tsai and coworkers observed upregulation of cytotoxic tumor necrosis factor (TNF-α) and interlukin (IL) 1/6 in response to the administration of untargeted AuNPs.[32] In a study by Puntes and coworkers, enhanced upregulation of cytotoxic TNF-α and IL-1/6 was also observed in macrophage cells treated with peptide-conjugated gold nanoparticles designed to mimic virus-like particles through epitope repetition.[33] Groll and coworkers more recently observed that PEGylated AuNRs can likewise increase cytotoxic TNF-α and IL-1/6 protein levels in AuNR-treated macrophages.[34] Together, these findings suggest that AuNP-activated macrophages may enhance the innate cytotoxic responses of TAMs towards the tumors which they

infiltrate. Moreover, macrolide-AuNRs that actively target TAMs may further augment anti-tumor response and achieve increasingly preferential delivery due to the size-dependent enhanced permeability and retention (EPR) effect.[*40*] Clinical trials involving the systemic administration of therapeutic TNF-α-AuNPs may additionally synergize with tumor-specific cytotoxic effects from AuNP-activated TAMs (CYT-6091, CytImmune Sciences, Inc.).[7]

Unwanted MPS uptake of nanostructures can be mitigated in a variety of ways including saturation by "decoy" nanoparticles (e.g. 3.4-8.5 nmol dosages in rats),[24] transient depletion of circulating macrophages (e.g. by anti-αCSF1 [26] and/or liposomal clodronate [20]), and surface-functionalization with protein-repellant polymers (e.g. PEG, POx),[*41,42*] complement inhibitors (e.g. heparin),[*43*] and/or "markers of self" (e.g. CD47[*41*] and CD200). In spite of these efforts, biodistribution profiles of "stealth" AuNPs typically remain high in MPS organs such as the spleen and liver.[*2,45*] Jeong and coworkers observed that intravenously administered PEG-AuNPs sequester in splenic macrophages and neutrophil-infiltrated liver tissues, resulting in tissue-specific inflammation (i.e. upregulation of TNF-α, IL-1/6/10/12).[*42*] While potentially beneficial in tumor tissues, the deleterious effects of AuNP-activated TAMs described here could result in significant impacts to healthy tissues and warrant further investigation.

5.1.3 Outlook and Conclusions

In conclusion, we have synthesized a novel gold nanoparticle conjugate which targets and activates anti-tumor potential in macrophage cells that exhibit high accumulation and infiltration into solid tumors. Macrolide-gold nanorods (AuNRs) preferentially accumulated in tumor-associated macrophage cells (TAMs) that exhibited selectively-enhanced cytotoxicity towards breast adenocarcinoma cells in co-culture. Although modest near-infrared photothermal ablation response was observed in monocultures of AuNR-activated TAMs, we observed no additive cytotoxic effects

from photothermally-treated TAMs in co-culture over the time course of these experiments – as would be expected from heat-shock protein-induced activation or photothermal ablation. Taken together, the ability of TAMs to migrate freely in circulation, bypass the blood-brain-barrier, and preferentially accumulate and infiltrate into solid tumors make macrolide-functionalized gold nanoparticles promising candidates for targeted cancer drug delivery to breast and brain tumors. Enhanced anti-tumor potential by tumor-localized, AuNR-activated TAMs may further synergize with chemotherapeutic treatment regimens and warrant further investigation.

5.2 Ligand-Dependent Susceptibility of Macrolide-Gold Nanorods to Multiple Drug Resistance

Forty percent of all human tumors develop resistance to chemotherapy.[*43*] This treatment resistance can be drug-specific; however, it is often accompanied by wide-ranging drug insensitivity, or multiple drug resistance (MDR), which is responsible for treatment failure in more than 90% of all metastatic cancer cases.[*44*] The transmembrane drug efflux pump MDR1 P-glycoprotein (P-gp, **Figure 5.7A**) is considered to be the most prevalent and single most important cause of MDR in humans.[*48,49*] Nanoscale drug carriers can overcome MDR in many cases and are widely believed to be less susceptible to drug efflux due to endocytotic uptake/protection.[*45-47*] The intrinsic vulnerability of nanoparticles to P-gp-mediated efflux is, however, poorly understood and it is currently unclear whether nanoscale drug carriers, as a whole, are subject to P-gp efflux. We hypothesized that nanoparticles covalently conjugated with various substrates of P-gp may be able to circumvent P-gp-mediated efflux, thereby increasing their therapeutic potential. We found that the cellular accumulation of nanoparticles conjugated with MDR-evasive substrates was unaffected by competitive inhibitors for P-gp, but that the accumulation of those conjugated with MDR-susceptible substrates was significantly enhanced. These findings suggest, for the first time, that

nanoscale drug carriers, themselves, can be susceptible to MDR and that P-gp-mediated drug efflux depends directly on the extent to which the nanoparticles' surface ligands are recognized by P-gp and other MDR proteins. These data further provide opportunities for the design of increasingly efficacious drugs and imaging agents in the future.

Polymeric nanoparticles, liposomes, iron oxide nanoparticles, micelles, polysaccharide nanoparticles, and diamond nanoparticles have all demonstrated increasing efficacy in treating MDR cells in vitro/vivo,[*45,48*] but differentiating effects attributable to nanoparticle-accelerated delivery kinetics from direct interactions with P-gp is difficult. Further, many components of nanoscale drug carriers, as well as their excipients/solubilizing agents, can likewise diminish drug:P-gp interactions and obfuscate direct comparisons. For example, Kabanov and coworkers have shown that nonionic triblock copolymers (Pluronic®) that self-assemble to form micellar drug carriers can, themselves, transiently deplete ATP, diminishing P-gp-mediated efflux of the drugs that they deliver.[*54*] Mumper and coworkers have shown that polyoxyethylene oleyl ethers (Brij® 78) used to produce nanoscale drug emulsions can similarly diminish P-gp-mediated drug efflux by transient ATP depletion.[*49*] When non-bonded to a nanocarrier, many common components of nanoscale drug carriers such as Cremophor® EL, Tween® 80, PEG (0.4-20 kDa), TPGS, Myrj® 52, sucrose monolaurate, and Triton® X-100, can also inhibit efflux by P-gp.[*50*] Neutral phospholipids of which many liposomes/micelles are comprised (e.g. phosphatidylcholine [*51*]) can also act as competitive substrates for P-gp.

Gold nanoparticles are promising candidates for targeted anti-cancer drug delivery and laser photothermal therapies. Phase I clinical trials have been successfully completed for the former [*7*] and human pilot studies [*52*] are currently in progress for the latter, both for the treatment of solid tumors in the US. To investigate the hypothesis that nanoparticle ligation may diminish P-gp-

mediated drug efflux, we synthesized a series of colloidal gold nanorods covalently conjugated with structurally homologous substrates of P-gp that exhibit varying degrees of susceptibility to P-gp-medited efflux, as reported previously.[*53-58*] **Figure 5.7B** illustrates the composition of these model nanoscale drug carriers, each comprised of a ca. 50 × 13 nm gold nanorod (**Figure 5.7C**) covalently conjugated with PEG or a mixed self-assembled monolayer of PEG stabilizer and one of three PEG-anchored macrolide antibiotics: azithromycin (Zithromax®), clarithromycin (Biaxin®), or tricyclic ketolide (TE-802). These gold nanorod (AuNR) conjugates are abbreviated hereafter as PEG-AuNRs, Azith-AuNRs, Clarith-AuNRs, and TriKeto-AuNRs, respectively. Macrolides were used as model substrates here due to their known biocompatibility, widespread use as broad-spectrum antibiotics, and well-characterized interactions with P-gp and the specific inhibitors and cell lines employed in this study.[*59-64*] Trends in efficacy between these macrolides (TriKeto>Clarith>Azith) correspond directly with their reported susceptibility to P-gp-mediated efflux (Azith>Clarith>TriKeto),[*53-58*] with second-generation Azith and Clarith exhibiting diminished therapeutic response relative to third-generation TriKeto, due in large part to its decreased recognition by P-gp.[*58*] Nanorods were used here due to their high absorption at tissue-penetrating, near-infrared (NIR) frequencies (**Figure 5.7D**), often useful in adjunctive therapeutic applications.[*9*] **Figure 5.7C** conceptually illustrates how nanocarrier/drug accumulation could be diminished by MDR via P-gp-mediated efflux and/or exocytosis of the gold nanoconjugates through its flippase activity.[*59*]

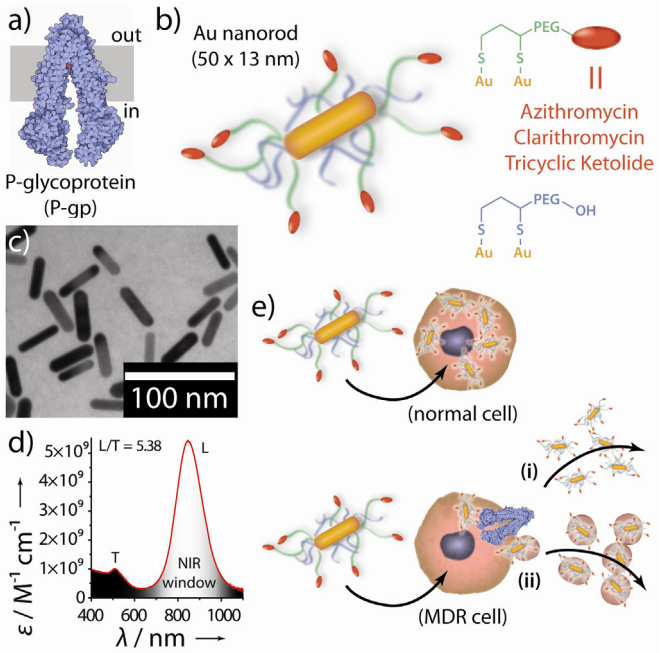

Figure 5.7. A) Structure of the multiple drug resistance (MDR) protein, MDR1 P-glycoprotein (P-gp). B) Illustration of the model nanoscale drug carriers employed herein: colloidal gold nanorods (AuNRs) covalently bonded with structurally homologous macrolide antibiotic substrates for P-gp that exhibit varying degrees of recognition/efflux (TriKeto<Clarith<Azith). C) Electron microscopy and D) extinction spectrum of the gold nanorods. E) Schematic illustrating how the accumulation of nanoscale drug carriers could be diminished by MDR via P-gp-mediated (i) efflux and/or (ii) exocytosis of the gold nanoconjugates through P-gp flippase activity. Adapted from Dreaden et al. [*37*].

5.2.1 Design and Development of Nanoscale Substrates for MDR1 P-glycoprotein

Summary. Thiol PEGylated macrolides were synthesized by Huisgen cycloaddition of azido octa(ethylene glycol)-lipoic amide (**7**) with 3'-ethynylbenzyl derivatized azithromycin (**8**), clarithromycin (**10**), and tricyclic ketolide TE-802 (**12**). Gold nanorods were synthesized by seed-mediated growth [*9*] and spectrophotometric accumulation assays (24 h) were performed as described by Cho and Xia [*60*] using nanoparticle molar extinction cross sections interpolated from Orendorff and Murphy [*39*] with corrections for optical extinction from P-gp inhibitors (100 μM) and growth media, as well as diffuse scattering from cellular debris. Adherent cells were counted manually in triplicate from 0.603 mm^2 images obtained immediately prior to each assay. Nanorods used in these

studies were functionalized with 1×10^3 macrolide and 9×10^3 PEG-thiol ligands particle^{-1} (as determined by UV-absorption and Ellman's assay, respectively) and were purified by centrifugation prior to conjugation and twice prior to use in cell culture. Dark-field scattering microscopy (DFSM) was performed following 24 h incubation with 0.5 nM nanoparticle-supplanted complete growth media. Fluorescence microscopy was performed following 24 h incubation with 0.5 nM nanoparticle-supplanted complete growth media containing Alexa Fluor 647-dextran (Invitrogen) to lable endocytotic vesicles. Nanoconjugates were fluorescently-labeled by substituting 11% of their polymer layer with carboxyfluorescein-terminal PEG-SH (5 kDa) during conjugation. Efflux experiments were performed using P-gp(+) J774.2 (ATCC) [*53*] and P-gp(-) COLO 205 (ATCC) [*61*] cells. Tetrazolium assay (Sigma, XTT) found no significant toxicity for the nanoconjugates or P-gp inhibitors at these concentrations. Electron microscopy was performed using a JEOL 100CX II transmission electron microscope and extinction spectra were obtained using an Ocean Optics, HR4000CG-UV-NIR spectrometer.

Experimental Materials/Methods. All commercially available starting materials were used without further purification. Octaethylene glycol (OEG) was purchased from Sigma Aldrich. Reaction solvents were either high performance liquid chromatography (HPLC) grade or American Chemical Society (ACS) grade and used without further purification. Analtech silica gel plates (60 F_{254}) were used for analytical thin layer chromatography (TLC), and Analtech preparative TLC plates (UV 254, 2000 μm) were used for purification. UV light and anisaldehyde/iodine stain were used to visualize the spots. 200-400 Mesh silica gel was used in column chromatography. Nuclear magnetic resonance (NMR) spectra were recorded on a Varian-Gemini 400 magnetic resonance spectrometer. ^{1}H NMR spectra were recorded in parts per million (ppm) relative to the peak of $CDCl_3$, (7.24 ppm).^{13}C spectra were recorded relative to the central peak of the $CDCl_3$ triplet (77.0 ppm) and were

recorded with complete hetero-decoupling. High-resolution mass spectra (HR-MS) were recorded at the Georgia Institute of Technology mass spectrometry facility in Atlanta. 3'-ethynylbenzylazithromycin **8**, 3'-ethynylbenzylclarithromycin **10**, and 3'-ethynylbenzyltricyclic ketolide **12**, were synthesized as we previously reported.[*62,63*]

*Synthesis of Tosyl octa(ethylene glycol) (***1***).* The synthetic procedure was adapted from Sauvé and co-workers.[*64*] Octa(ethylene glycol) (0.50 g, 1.35 mmol) was dissolved in anhydrous methylene chloride (7 mL) at 0°C, followed by addition of freshly prepared Ag_2O (0.47 g, 2.02 mmol), KI (0.09 g, 0.50 mmol), and then TsCl (0.26 g, 1.35 mmol). The reaction mixture was left to stir at 0°C, under argon for 30 min, after which TLC deemed the reaction complete. Ag_2O was filtered off over a pad of celite cake washing with 12:1 CH_2Cl_2/CH_3OH. The filtrate was concentrated and purified on a silica column using 3:2 CH_2Cl_2/acetone. Gradually increasing polarity to 1:4, yielded the title compound as a colorless oil (0.58 g, 78%). ^{1}H NMR (400 MHz, $CDCl_3$): δ=2.44 (3H, s), 2.81 (1H, br), 3.58 – 3.70 (30H, m), 4.15 (2H, t, *J* = 4.8 Hz), 7.35 (2H, d, *J* = 8.4 Hz), 7.80 ppm (2H, d, *J* = 8.4 Hz); HR-MS (ESI): *m/z* calcd for $[C_{23}H_{40}O_{11}S + H]^+$: 525.2364; found 525.2377. ESI=electrospray ionization.

*Synthesis of Azido octa(ethylene glycol) (***2***.* To a solution of tosyl octa(ethylene glycol) **1** (0.5 g, 0.95 mmol) in DMF (10 mL), was added sodium azide (0.25 g, 3.81 mmol) and the reaction mixture stirred at 85°C under argon gas for 6 h. TLC confirmed completion of reaction. DMF was evaporated off and the residue dissolved in ethyl acetate (25 mL). Excess sodium azide was filtered off and the product purified on silica plug eluting with 12:1 CH_2Cl_2/MeOH, affording the title compound as colorless oil in 84% (0.44 g) yield. ^{1}H NMR (400 MHz, $CDCl_3$): δ=3.38 (2H, t, *J* = 5.2 Hz), 3.58-3.73 ppm (30H, m). DMF=dimethylformamide.

*Synthesis of Azido monotosyl octa(ethylene glycol) (**3**).* Reaction of azido octa(ethylene glycol) **2** (0.33 g, 0.82 mmol), Ag_2O (0.29 g, 1.23 mmol), KI (0.054 g, 0.33 mmol), TsCl (0.17 g, 0.90 mmol) in DCM (10 mL) as described for the protocol of compound **1**, afforded 0.39 g (87%) of the desired product. ^{1}H NMR (400 MHz, $CDCl_3$): δ=2.44 (3H, s), 3.38 (2H, t, *J* = 4.0 Hz), 3.57-3.70 (28H, m), 4.15 (2H, t, *J* = 4.0 Hz), 7.35 (2H, d, *J* = 8.0 Hz), 7.80 ppm (2H, d, *J* = 8.0 Hz). Ts=tosyl.

*Synthesis of Azido phthalimide octa(ethylene glycol) (**4**).* A solution of compound **3** (0.45 g, 0.81 mmol) and phthalimide potassium salt (0.15 g, 0.81 mmol) in anhydrous DMF (10 mL) was stirred at 50°C for 12 h under argon. DMF was evaporated off, redissolved the crude mixture in ethyl acetate (40 mL), and filtered off excess salt. Purification by silica preparative TLC eluting with 20:1 CH_2Cl_2/MeOH yielded 79% (0.34 g) of the title compound. ^{1}H NMR (400 MHz, $CDCl_3$): δ=3.37 (2H, t, *J* = 4.8 Hz), 3.57-3.74 (28H, m), 3.88 (2H, t, *J* = 6.0 Hz), 7.70 (2H, m), 7.83 ppm (2H,m); HR-MS (FAB): *m/z* calcd for $C_{24}H_{36}N_4O_9$ $[M+H]^+$: 525.2560; found 525.2609. FAB=fast atom bombardment.

*Synthesis of Amino azido octa(ethylene glycol) (**5**).* A mixture of compound **4** (0.28 g, 0.53 mmol) and methylamine solution (40 wt% in water, 3.2 mL, 40.6 mol) was stirred at room temperature for 64 h. Excess methylamine was evaporated off. The crude product was dissolved in 1 N HCl (10 mL) and extracted with CH_2Cl_2 (4 x 5 mL). The aqueous layer was basified with 1 M NaOH and then extracted with 10% MeOH/CH_2Cl_2 (4 x 5 mL), dried over anhydrous sodium sulfate and evaporated to dryness to give 0.14 g (68%) of the title compound as oil. ^{1}H NMR (400 MHz, $CDCl_3$): δ=2.87 (2H, m), 3.38 (2H, t, *J* = 4.8 Hz), 3.50 (2H, t, *J* = 4.8 Hz), 3.62-3.68 ppm (26H, m); HR-MS (FAB): *m/z* calcd for $C_{16}H_{34}N_4O_7$ $[M+H]^+$: 395.2506; found 395.2522.

*Synthesis of Azido octa(ethylene glycol)-Lipoic Amide (***7**, **Figure 5.8***)*. To a solution of compound **5** (0.20 g, 0.50 mmol) and lipoic acid **6** (0.11 g, 0.50 mmol) in dry CH_2Cl_2 (7 mL) were added EDCI (0.095 g, 0.50 mmol) and DMAP (0.003 g, 0.023 mmol). The reaction was allowed to stir under argon for 4.5 h at room temperature. The solvent was concentrated under reduced pressure and the residue was purified by silica preparative TLC eluting with 12:1 CH_2Cl_2/MeOH to afford **7** as yellow oil (0.27 g, 91%). ^{1}H NMR (400 MHz, $CDCl_3$): δ=1.38-1.52 (2H, m), 1.58-1.72 (4H, m), 1.87-1.93 (1H, m), 2.19 (2h, t, *J* = 7.6 Hz), 2.41-2.5 (1H, m), 3.07-3.22 (2H, m), 3.37 (2H, t, *J* = 4.8 Hz), 3.45 (2H, m), 3.55 (2H, t, *J* = 5.2 Hz), 3.57-3.69 ppm (28H, m); HR-MS (FAB): *m/z* calcd for $C_{24}H_{46}N_4O_8S_2$ $[M+H]^+$: 583.2835; found 583.2858. EDCI=1-ethyl-3-(3-dimethylaminopropyl) carbodiimide, DMAP=4-Dimethylaminopyridine, ME=methyl.

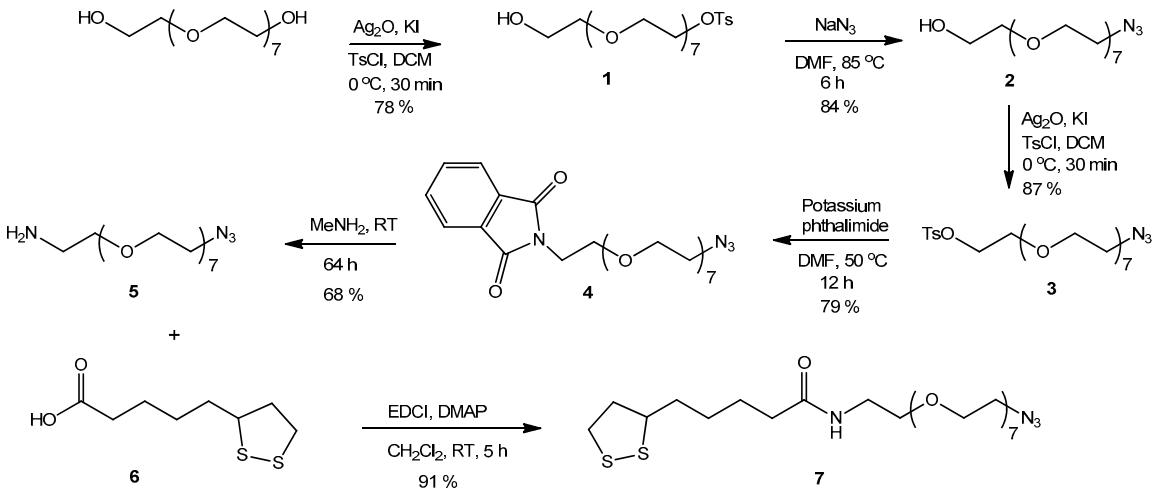

Figure 5.8. Synthesis of Azido octa(ethylene glycol)-Lipoic Amide (**7**). Adapted from Dreaden et al. [*37*].

*Synthesis of Azithromycin-PEG Thiol (***9**, **Figure 5.9***)*. 3'-Ethynylbenzylazithromycin **8** (0.057 g, 0.059 mmol) and compound **7** (0.045 g, 0.059 mmol) were dissolved in anhydrous THF (5 mL) and stirred under argon at room temperature. Copper (I) iodide (0.008 g, 0.042 mmol) and Hunig's

base (0.6 mL) were then added to the reaction mixture with continued stirring for 26 h. A solution of 4:1 saturated NH_4Cl/NH_4OH (30 mL) was added to the reaction mixture and extracted with 20% $MeOH/CH_2Cl_2$ (3 x 30 mL). The organic layer was dried over Na_2SO_4 and concentrated in vacuo. The crude product was purified by preparative TLC (silica, 12:1:0.05 CH_2Cl_2/MeOH/Et_3N) to give 80 mg (83%) of compound **9** as yellow foam. ^{1}H NMR (400 MHz, $CDCl_3$): δ=0.84-1.01 (9H, m), 1.07-2.00 (37H, m), 2.07-2.66 (16H, m), 2.83-3.25 (8H, m), 3.34-3.65 (32H, m), 3.73-3.97 (3H, m), 4.19 (1H, m), 4.40 (1H , d, *J* = 7.2 Hz), 4.56 (2H, t, *J* = 4.0 Hz), 4.75 (1H, m), 5.04 (1H, m), 6.38 (1H, br), 7.35 (2H, br), 7.78 (2H, d, *J* = 8.0 Hz), 7.97 ppm (1H, s); ^{13}C NMR (100 MHz, $CDCl_3$): δ=8.9, 9.3, 11.5, 12.3, 15.0, 16.6, 18.4, 21.6, 21.7, 22.3, 25.6, 26.8, 27.4, 29.1, 29.9, 34.9, 36.5, 36.6, 37.1, 38.7, 39.3, 40.4, 42.2, 42.4, 45.8, 46.1, 49.5, 50.6, 53.7, 53.9, 56.6, 58.1, 64.6, 65.7, 68.9, 69.7, 70.1, 70.4, 70.7, 70.8, 73.0, 74.2, 74.5, 78.0, 78.3, 83.4, 95.0, 102.6, 121.1, 125.9, 129.5, 130.3, 139.4, 147.5, 173.0, ppm 178.7; HR-MS (MALDI): *m/z* calcd for $C_{70}H_{122}N_6O_{20}S_2$ $[M+H]^+$: 1431.8228; found 1431.8233. THF=tetrahydrofuran, Hunig's base=DIPEA= *N*,*N*-diisopropylethylamine, Et=ethyl, MALDI=matrix-assisted laser desorption ionization.

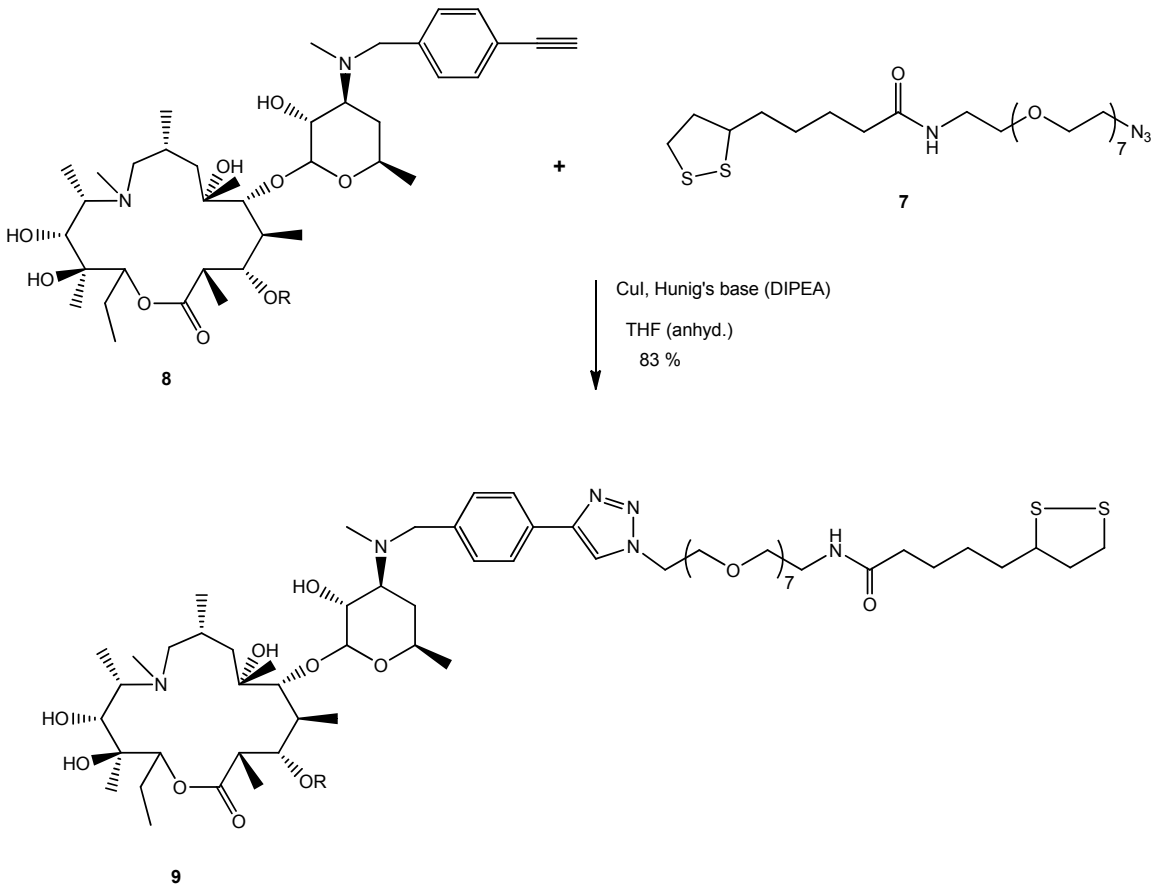

8 7 9

Figure 5.9. Synthesis of Azithromycin-PEG Thiol (**9**). Adapted from Dreaden et al. [*37*].

*Synthesis of Clarithromycin-PEG Thiol (***11**, **Figure 5.10***).* Reaction of 3'-ethynylbenzylclarithromycin **10** (0.050 g, 0.021 mmol) and compound **7** (0.034 g, 0.021 mmol) according to the protocol described for the synthesis of compound **9**, followed by similar preparative TLC conditions gave 58 mg (69%) of **11** as yellow foam. ^{1}H NMR (400 MHz, $CDCl_3$): δ=0.83 (6H, m), 1.03-1.90 (33H, m), 2.10-2.60 (12H, m), 2.81-3.16 (14H, m), 3.40-3.72 (35H, m), 3.89-3.93 (4H, m), 4.43 (1H, d, *J* = 6.8 Hz), 4.58 (2H, m), 4.86 (1H, m), 5.03 (1H , d, *J* = 9.6 Hz), 6.50 (1H, br), 7.60 (2H, br), 7.85 (2H, m), 8.03 ppm (1H, s); ^{13}C NMR (100 MHz, $CDCl_3$): δ=9.3, 10.6, 12.0, 12.3, 14.1, 15.9, 16.0, 17.4, 18.0, 18.6, 19.8, 21.0, 22.6, 25.4, 28.9, 29.3, 29.4, 29.6, 30.1, 31.9, 34.6, 34.8, 36.2, 37.3, 38.4, 38.9, 39.1, 40.2, 42.0, 44.9, 45.1, 49.3, 50.4, 50.5, 53.7,

56.4, 65.8, 69.1, 69.5, 69.9, 70.1, 70.4, 70.5, 70.6, 72.6, 74.2, 76.6, 76.8, 77.7, 78.2, 81.1, 95.9, 105.0, 121.4, 126.1, 130.0, 146.8, 172.9, 175.6, 220.9 ppm; HR-MS (MALDI): *m/z* calcd for $C_{70}H_{119}N_5O_{21}S_2$ $[M+H]^+$: 1430.791; found 1430.7833.

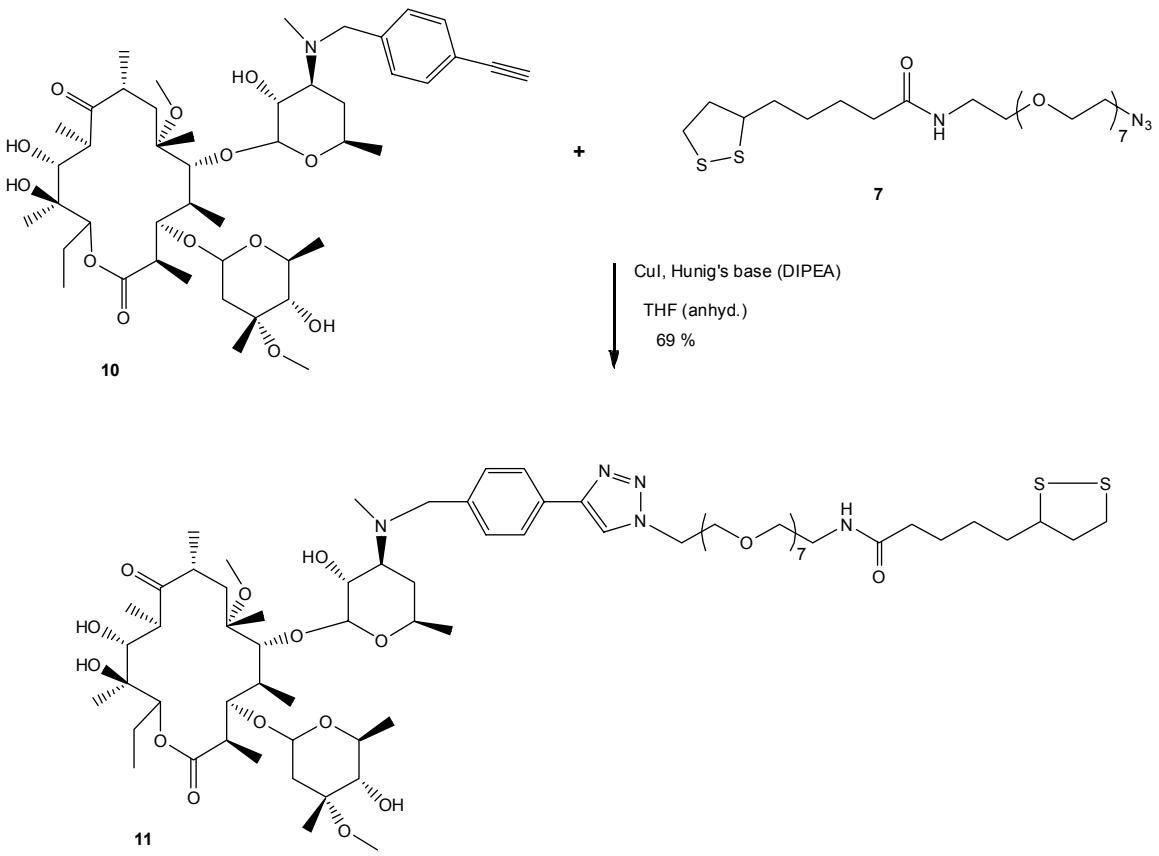

Figure 5.10. Synthesis of Clarithromycin-PEG Thiol (**11**). Adapted from Dreaden et al. [*37*].

*Synthesis of Tricyclic Ketolide-PEG Thiol (***13**, **Figure 5.11***).* Reaction of 3'-ethynylbenzyltricyclic ketolide **12** (0.052 g, 0.07 mmol) and compound **7** (0.047 g, 0.08 mmol) according to the protocol described for the synthesis of compound **9**, followed by similar preparative TLC conditions gave 65 mg (71%) of **13** as yellow foam. ^{1}H NMR (400 MHz, $CDCl_3$): δ=0.82 (3H, t, *J* = 7.2 Hz), 1.03 (3H, d, *J* = 6.4 Hz), 1.17-1.90 (35H, m), 2.10-2.44 (5H, m), 2.57-2.98 (5H, m), 3.11-3.97 (42H, m), 4.20 (1H, d, *J* = 8.0 Hz), 4.28 (1H, d, *J* = 8.0 Hz), 4.56 (2H, t, *J* =

4.0 Hz), 4.92 (1H, d, *J* = 8.0 Hz), 6.64 (1H, br), 7.30 (2H, d, *J* = 8.0 Hz), 7.77 (2H, d, *J* = 7.6 Hz), 7.98 ppm (1H, s); ^{13}C NMR (100 MHz, $CDCl_3$): δ=10.6, 11.3, 13.1, 14.3, 14.6, 16.5, 19.3, 19.8, 21.4, 22.3, 25.6, 29.1, 29.6, 29.9, 31.8, 34.9, 36.4, 36.6, 37.0, 38.7, 38.8, 39.4, 40.4, 42.5, 42.7, 48.2, 56.7, 65.7, 69.7, 70.2, 70.3, 70.5, 70.7, 76.7, 78.7, 79.2, 81.8, 104.0, 121.2, 126.0, 129.4, 130.1, 138.8, 147.5, 156.2, 169.8, 173.2, 204.4 ppm; HR-MS (MALDI): *m/z* calcd for $C_{65}H_{105}N_7O_{17}S_2$ $[M+H]^+$: 1320.7081; found 1320.6881.

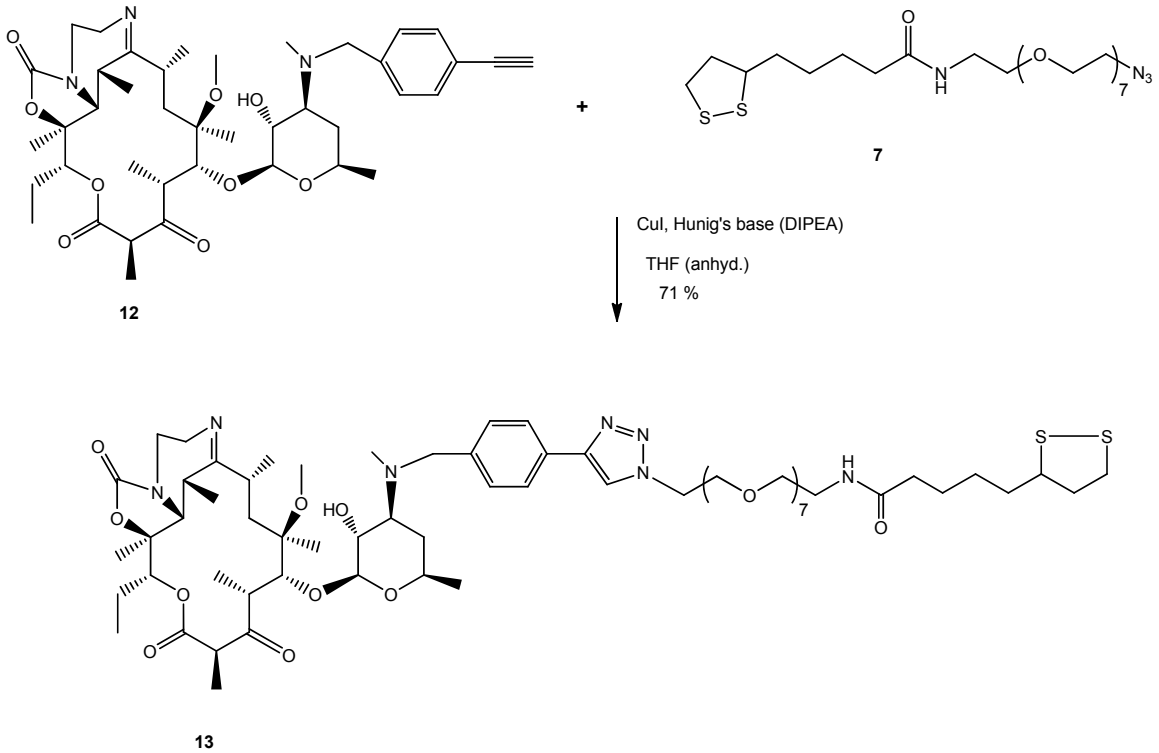

Figure 5.11. Synthesis of Tricyclic Ketolide-PEG Thiol (**13**). Adapted from Dreaden et al. [*37*].

Synthesis and Characterization of Macrolide-Gold Nanorods. Colloidal gold nanorods were synthesized by seed-mediated growth as described previously.[*9*] Briefly, 600 μL of ice-cold 10 mM $NaBH_4$ was rapidly injected into a stirred 7.5 mL aqueous solution of 0.333 mM $HAuCl_4$ and 0.133 M cetyltrimethylammonium bromide (CTAB). The mixture was allowed to react for 5 min, after

which 320 μL was aliquoted into a 420 mL aqueous solution of 0.479 mM $HAuCl_4$, 95.7 mM CTAB, 86.2 μM $AgNO_3$, and 0.528 mM ascorbic acid. The seeded growth solution was gently mixed and allowed to react overnight. The crude nanorod product was purified by centrifugation (30 min, 4185 × g) and stored at 4 °C until use. All reactions were performed at room temperature under aseptic conditions. Particle sizing was performed by transmission electron microscopy (TEM, JEOL 100CX II). Hydrodynamic diameter (HD) and zeta potential (ζ) was measured using a NanoZS Zetasizer particle analyzer (Malvern, 633 nm). Gold nanorods used in these studies were 50 ± 8 nm in length and 13 ± 2 nm in width (4.0 ± 0.9 aspect ratio; λ_{max}~818 nm; HD = 110 ± 10 nm, ζ = +46.6 mV). Azith-, Clarith-, TriKeto-, and PEG-AuNRs exhibited HD values of 130 ± 10, 162 ± 4, 151 ± 2, and 210 ± 9 nm, respectively, and ζ values of +31.9, +35.4, +23.4, and +37.7 mV, respectively.

Nanoparticle ligand coverages were determined as described in Dreaden et al. with slight modifications.[*38*] Briefly, purified gold nanorod concentrates were rapidly injected into aqueous solutions containing PEG-thiol or PEG-thiol and macrolide ligands **9**, **11**, or **13** (PEG-thiol, hydroxy octa(ethylene glycol)-lipoic amide). Nanorod/ligand solutions were incubated at 30 °C, under sonication for 12 h, and purified via centrifugation (15 min, 4185 × g; twice). Adsorbate coverages of **9**, **11**, **13**, and PEG-thiol were quantified by UV absorption assay (260 nm) and Ellman's assay (Pierce/Thermo Scientific), respectively, using experimentally derived molar extinction cross sections for the thiol PEGylated macrolides: $\varepsilon_{260\ nm}$ = 1.08 ± 0.03 × 10^4 L mol^{-1} cm^{-1} (azithromycin, **9**), 0.841 ± 0.03 × 10^4 L mol^{-1} cm^{-1} (clarithromycin, **11**), 1.26 ± 0.02 × 10^4 L mol^{-1} cm^{-1} (tricyclic ketolide, **13**). Molar extinction cross sections of the nanorods were interpolated from experimental data in Orendorff and Murphy.[*39*] Nanoparticles used in coverage assays were centrifuged at 18,000 × g for 1 h to remove any trace particles present in the supernatant. Optical

extinction measurements were obtained using an Ocean Optics HR4000CG-UV-NIR spectrometer. Nanoconjugates used in these studies were functionalized with 1×10^3 macrolide ligands and 9×10^3 PEG-thiol ligands per nanorod, each obtained by incubating with solutions containing 1.3, 1.6, and 3.9×10^5-fold ligand excesses (**9**, **11**, **13**, respectively) (**Figure 5.12**). Functionalized nanoparticles were stably dispersed in growth media over the time course of the experiments (**Figure 5.13**).

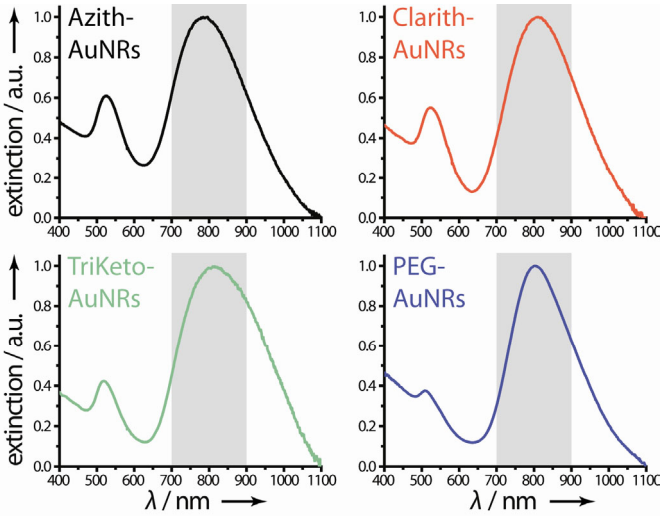

Figure 5.12. Extinction spectra of the purified macrolide-gold nanorod conjugates. The near-infrared (NIR) tissue penetration window is highlighted in gray reference. Adapted from Dreaden et al. [*37*].

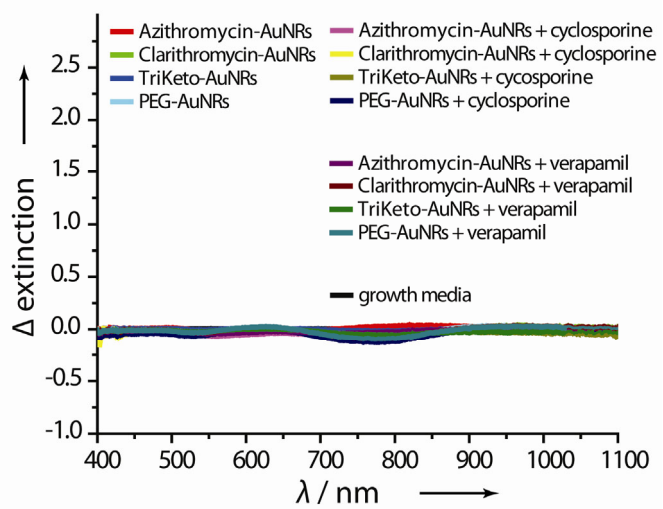

Figure 5.13. Spectral stability of macrolide-gold nanorod conjugates dispersed in complete cell growth media (24 h, Dulbecco's modified eagle's medium supplanted with 10% v/v fetal bovine serum, 20 I.U./mL penicillin, 100 ug/mL streptomycin, and 250 ng/mL amphotericin B). Adapted from Dreaden et al. [*37*].

Cell Culture. RAW264.7 (ATCC) and J774.2 (Sigma) cells were subcultured in Dulbecco's modified eagle's medium supplanted with 10% v/v fetal bovine serum (FBS), 20 I.U./mL penicillin, 100 ug/mL streptomycin, and 250 ng/mL amphotericin B at 37 ºC in a 5% CO_2 humidified atmosphere. COLO 205 (ATCC) cells were subcultured in Roswell Park Memorial Institute-1640 medium with similar supplements and under similar conditions. Spectroscopic assays were performed in media lacking phenol red. All experiments were performed on cells passaged 12 h prior. P-gp inhibitors were co-incubated with nanoparticle-supplanted media for 24 h.

Nanoparticle Uptake and Localization. Nanoparticle accumulation was assessed using an inverted-objective dark-field scattering microscope (DFSM) and an inverted-objective laser-scanning confocal microscope. In dark-field imaging experiments, collagen-coated coverslips were prepared by incubating 0.04 mg/mL rat tail collagen/DPBS with glass coverslips (18 mm dia) for 6 h at 37 °C in a 5% CO_2 humidified atmosphere. The coated substrates were rinsed in DPBS and cells were passaged onto the coverslips. After 12 h, growth solutions were replaced with media containing 0.5

nM of the nanoconjugates and the cells were allowed to incubate for 24 h. Cell monolayers were then rinsed in DPBS and fixed in 4 % paraformaldehyde/DPBS for 15 min at 4 °C. The fixed coverslips were coated in glycerol, and mounted and sealed onto glass slides. Dark-field microscopy was performed using an inverted objective Olympus IX70 microscope fitted with a dark-field condenser (U-DCW), 100x/1.35 oil Iris objective (UPLANAPO), tungsten lamp, and a Nikon D200 digital SLR camera. In confocal fluorescence colocalization experiments, macrolide-AuNR conjugates were labeled with a carboxyfluorescein-terminal PEG-SH and cellular endosomes were labeled with a fluorescent dextran conjugate. Carboxyfluorescein-PEG-SH was obtained by reacting NH_2-PEG-SH (5 kDa, Laysan Bio) with 5-(and-6)-carboxyfluorescein succinimidyl ester (Molecular Probes) in a 10 mM HEPES buffered aqueous solution containing 30% v/v ethanol (pH 7.4) for 24 h at room temperature in dark. Fluorescently-labeled PEG-SH was dialyzed twice (500 MWCO, Spectra/Por), each time at a 10^3 volume excess for 24 h with three solvent exchanges. Purified gold nanorod concentrates were rapidly injected into aqueous solutions containing PEG-thiol and fluorescently-labeled PEG-SH or PEG-thiol, fluorescently-labeled PEG-SH, and macrolide ligands **9**, **11**, or **13** in dark, under sonication, at 30 °C for 12 h. Molar excesses of polymers and ligands were identical to those used to prepare unlabeled nanoconjugates, with 11 mol% of the polymer component substituted for fluorescently-labeled PEG-SH. Fluorescent macrolide-AuNRs were dialyzed for two days (12-14 kDa MWCO) in dark, then centrifuged twice at 4185 × g for 5 min and redispersed in deionized water. RAW264.7 cells were incubated in dark with 6 μM Alexa Fluor 647-dextran (10 kDa, Invitrogen) and 0.5 nM macrolide-AuNR conjugates for 24 h under growth conditions. The labeled cells were washed in PBS buffer and fixed in 4% paraformaldehyde/DPBS for 30 min at 4 °C and imaged using an inverted-objective laser-scanning confocal microscope (FluoView 1000; Olympus, 60x/1.42).

5.2.2 Evidence for the Susceptibility of Nanoscale Drug Carriers to Multiple Drug Resistance: Ligand-Dependent P-glycoprotein Efflux and Inhibition

Targeted cellular uptake of the model nanoscale drug carriers was assessed using a lung macrophage cell line, commonly employed in conjunction with studies involving macrolides due to their high in vivo accumulation in tumor-associated macrophages and in lung tissues.[*30,31*] **Figure 5.14A** shows that macrolide-AuNRs preferentially accumulate in macrophage cells relative to PEGylated control nanoparticles and do so in a dose-dependent manner (t=24 h). As expected, trends in accumulation observed here correlate directly with reported trends in efficacy for these drugs in treating MDR cell lines.[*55*] Confocal imaging of fluorescently-labeled nanoparticles (**Figure 5.14B**) further show that uptake and intracellular colocalization of the nanoparticles occurs in a manner consistent with that previously reported for macrolide accumulation in phagocytic cells.[*65*] Dark-field scattering microscopy (DFSM) also found that uptake of the nanoconjugates occurred in a macrolide-competitive manner (**Figure 5.15**). Together, these data support that intracellular transport of the nanocarriers is directed by their macrolide substrate ligands and that endosomal uptake of the nanocarriers could potentially diminish their recognition and efflux by P-gp.

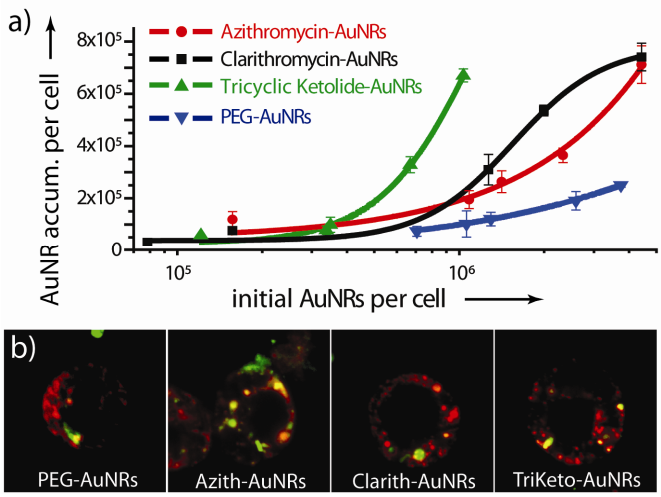

Figure 5.14. A) Targeted cellular delivery of macrolide-gold nanorods (AuNRs) to macrophage cells illustrating preferential accumulation relative to untargeted control nanoparticles (PEG-AuNRs). B) Confocal microscopy of fluorescently-labeled AuNRs (green) illustrating colocalization patterns (yellow) similar to that of free macrolides which localize within endocytic organelles (red). Error bars represent SD. Adapted from Dreaden et al. [*37*].

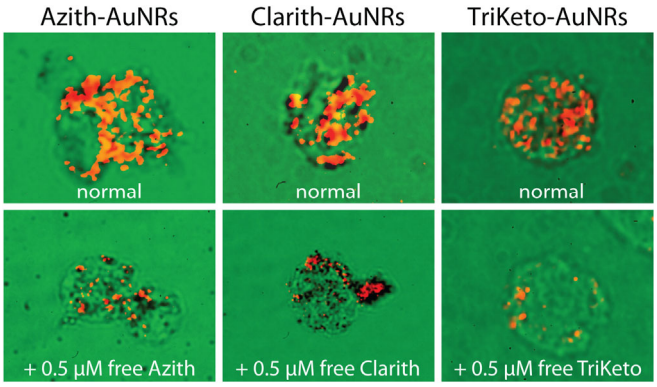

Figure 5.15. Dark-field scattering microscopy (DFSM) of lung macrophage cells illustrating ligand-competitive cellular accumulation of macrolide-AuNRs. RAW264.7 cells were incubated with 0.5 nM nanoparticle-supplanted media in the presence and absence of 0.5 μM of their corresponding free, non-thiol PEGylated macrolide compounds (24 h). Accumulation was significantly diminished in the presence of the free macrolides, corroborating previous finding of macrolide-dependent trafficking observed in spectrophotometric assay and intracellular co-localization studies. Adapted from Dreaden et al. [*37*].

Cellular accumulation of the macrolide-AuNRs was assessed in the presence and absence of specific inhibitors [*53*] for P-gp to determine the effect of P-gp-mediated efflux on retention of the nanoparticle constructs. No significant changes in cellular accumulation were observed with P-gp(-)

COLO 205 cells [*61*] in response to P-gp inhibition by either cyclosporine A or verapamil HCl (**Figure 5.16A**). Surprisingly, we observed significantly increased accumulation of Azith- and Clarith-AuNRs with P-gp(+) J774.2 cells [*53*] in response to both inhibitors, with no significant changes in TriKeto-AuNR accumulation (**Figure 5.16B**). These findings agree well with previous reports indicating i) macrolide-competitive P-gp binding by verapamil and cyclosporine,[*66,67*] ii) diminished recognition of TriKeto (TE-802) by P-gp,[*58*] iii) enhanced activity by third-generation tricyclic ketolides towards MDR cell lines,[*56,57*] and iv) P-gp-dependent accumulation/cytotoxicity by the free macrolide ligands (**Figure 5.17**). These data show that P-gp-mediated drug efflux can play a significant role in the cellular trafficking and retention of nanoscale drug carriers to which P-gp substrates (e.g. chemotherapeutics, imaging agents, etc.) are appended. Concurrent DFSM of nanoparticle- and P-gp inhibitor-treated cells (**Figure 5.18**) further corroborate the findings in **Figure 5.16**, showing augmented cellular accumulation of Azith- and Clarith-AuNRs in the presence of both P-gp inhibitors and no significant change in the accumulation of TriKeto-AuNRs.

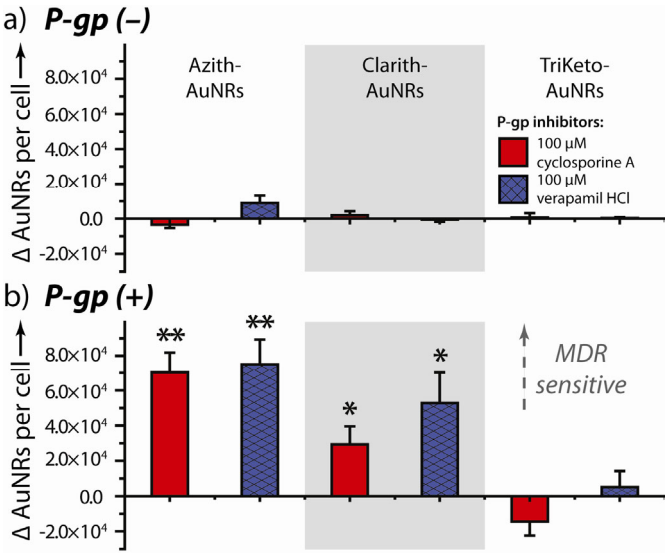

Figure 5.16. Changes in the cellular accumulation of macrolide-gold nanorods in response to competitive inhibition of P-glycoprotein (P-gp) in (A) P-gp null COLO 205 cells and (B) P-gp-expressing J774.2 cells. P-gp(-) cells exhibit nanoparticle accumulation independent of P-gp inhibition by both verapamil and cyclosporine, while P-gp(+) cells exhibit augmented accumulation of nanoparticles covalently conjugated with the highly-susceptible P-gp substrates azithromycin (Azith-) and clarithromycin (Clarith-). Error bars represent SD. P≤ *0.05, **0.01, ***0.001. Adapted from Dreaden et al. [*37*].

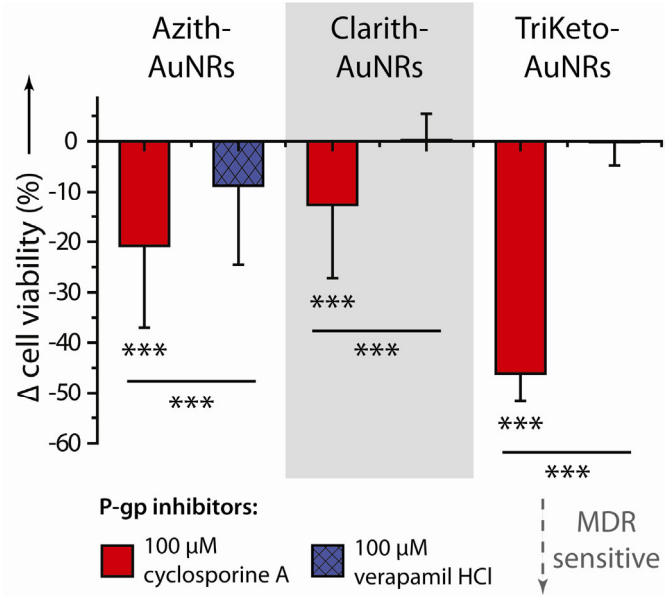

Figure 5.17. Enhanced cytotoxicity of the macrolide ligands (0.5 μM, 24 h) towards P-gp(+) J774.2 cells in response to competitive P-gp inhibition by cyclosporine A and verapamil HCl. Although the macrolide ligands were not toxic up to 10 μM (24 h), cell viability was significantly decreased relative to inhibitor-treated control cells following P-gp inhibition and associated [*53*] increases in intracellular macrolide accumulation. Cell viability was assessed by tetrazolium assay (Sigma, XTT). Error bars represent SD. P≤ *0.05, **0.01, ***0.001. Adapted from Dreaden et al. [*37*].

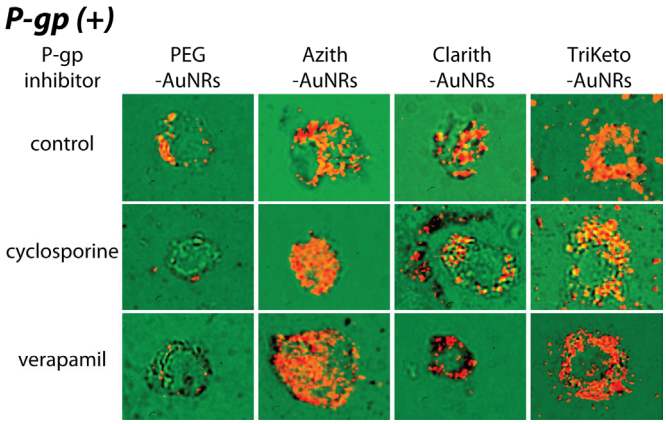

Figure 5.18. Dark-field scattering microscopy (DFSM) showing augmented cellular accumulation of Azith- and Clarith-AuNRs in the presence of both P-gp inhibitors and no significant change in the accumulation of TriKeto-AuNRs (24 h). P-gp(+) RAW264.7 cells were incubated with 0.5 nM nanoparticle-supplanted media for 24 h in the presence of ligand-competitive inhibitors for the drug efflux pump P-gp. Images are false color with scattering (orange) overlaid with bright-field micrographs (green) for contrast. Adapted from Dreaden et al. [*37*].

5.2.3 Outlook and Conclusions

In summary, we have demonstrated that the transmembrane drug efflux pump MDR1 P-glycoprotein (P-gp) can significantly decrease the accumulation of nanoscale drug carriers bearing ligands recognized by multiple drug resistance (MDR) protein 1. Specifically, we found that the cellular accumulation of gold nanorods conjugated with MDR-evasive substrate ligands was unaffected by competitive inhibitors for P-gp, while the accumulation of those conjugated with MDR-susceptible substrates was significantly enhanced. Although the exocytosis of gold nanoparticles [*68*] and other nanoscale drug carriers is commonly observed, we believe this to be the first report of P-gp-mediated drug efflux of a biomedical nanoparticle and suggests that these constructs, as a whole, are susceptible to both acquired and intrinsic multiple drug resistance. Because P-gp-mediated efflux was found to be ligand-dependent, the use of non-substrate ligands, semi-labile or cleavable anchoring groups, or the co-administration of blocking antibodies for P-gp [*61*] may serve to increase the efficacy of these and other therapeutic nanotechnologies in the future. While

detailed studies are currently underway to determine the precise mechanism(s) by which P-gp facilitates nanocarrier efflux, recent crystallographic studies by Higgins [*69*] and Chang [*44*] indicate that P-gp's binding sites are accessible via both the cytoplasm and the inner membrane leaflet, suggesting that protection of nanocarriers by the endosomal bilayer may be less effective in MDR evasion than previously hypothesized. Further, because of the large size of these particles relative to the central pore diameter of P-gp (ca. 5 nm), these findings suggest that the so-called "pore model" is less dominant here and that efflux likely proceeds via partitioning of the macrolide ligands into the inner membrane leaflet, followed by lateral diffusion and recognition/efflux. P-gp recognizes approximately 50% of all chemotherapeutics (e.g. doxorubicin, vinblastine, taxol, etoposide, topotecan) and a variety of other compounds (0.3-4 kDa) which bind at multiple and partially overlapping sites with a high degree of structural diversity and stereoselectivity.[*44,70*] Nanoscale drug carriers that incorporate P-gp substrate compounds may benefit from minimizing surface presentation of efflux-susceptible ligands.

5.3 References

1. Jokerst, J. V., Miao, Z., Zavaleta, C., Cheng, Z., & Gambhir, S. S. Affibody-Functionalized Gold–Silica Nanoparticles for Raman Molecular Imaging of the Epidermal Growth Factor Receptor. *Small* **7**, 625-633 (2011).

2. Zavaleta, C. L., Hartman, K. B., Miao, Z., James, M. L., Kempen, P., Thakor, A. S., Nielsen, C. H., Sinclair, R., Cheng, Z., & Gambhir, S. S. Preclinical Evaluation of Raman Nanoparticle Biodistribution for their Potential Use in Clinical Endoscopy Imaging. *Small* **7**, 2232-2240 (2011).

3. Cheng, Y., C. Samia, A., Meyers, J. D., Panagopoulos, I., Fei, B., & Burda, C. Highly Efficient Drug Delivery with Gold Nanoparticle Vectors for in Vivo Photodynamic Therapy of Cancer. *J. Am. Chem. Soc.* **130**, 10643-10647 (2008).

4. Cheng, Y., Meyers, J. D., Broome, A.-M., Kenney, M. E., Basilion, J. P., & Burda, C. Deep Penetration of a PDT Drug into Tumors by Noncovalent Drug-Gold Nanoparticle Conjugates. *J. Am. Chem. Soc.* **133**, 2583-2591 (2011).

5. Perrault, S. D., Walkey, C., Jennings, T., Fischer, H. C., & Chan, W. C. W. Mediating Tumor Targeting Efficiency of Nanoparticles Through Design. *Nano Lett.* **9**, 1909-1915 (2009).

6. Kim, B. Y. S., Rutka, J. T., & Chan, W. C. W. Nanomedicine. *New Engl. J. Med.* **363**, 2434-2443 (2010).

7. Libutti, S. K., Paciotti, G. F., Byrnes, A. A., Alexander, H. R., Gannon, W. E., Walker, M., Seidel, G. D., Yuldasheva, N., & Tamarkin, L. Phase I and Pharmacokinetic Studies of CYT-6091, a Novel PEGylated Colloidal Gold-rhTNF Nanomedicine. *Clin. Cancer Res.* **16**, 6139-6149 (2010).

8. Hirsch, L. R., Stafford, R. J., Bankson, J. A., Sershen, S. R., Rivera, B., Price, R. E., Hazle, J. D., Halas, N. J., & West, J. L. Nanoshell-mediated near-infrared thermal therapy of tumors under magnetic resonance guidance. *Proc. Natl. Acad. Sci. U.S.A.* **100**, 13549-13554 (2003).

9. Dickerson, E. B., Dreaden, E. C., Huang, X., El-Sayed, I. H., Chu, H., Pushpanketh, S., McDonald, J. F., & El-Sayed, M. A. Gold nanorod assisted near-infrared plasmonic photothermal therapy (PPTT) of squamous cell carcinoma in mice. *Cancer Lett.* **269**, 57-66 (2008).

10. Lu, W., Xiong, C., Zhang, G., Huang, Q., Zhang, R., Zhang, J. Z., & Li, C. Targeted Photothermal Ablation of Murine Melanomas with Melanocyte-Stimulating Hormone Analog–Conjugated Hollow Gold Nanospheres. *Clin. Cancer Res.* **15**, 876-886 (2009).

11. von Maltzahn, G., Park, J.-H., Agrawal, A., Bandaru, N. K., Das, S. K., Sailor, M. J., & Bhatia, S. N. Computationally Guided Photothermal Tumor Therapy Using Long-Circulating Gold Nanorod Antennas. *Cancer Res.* **69**, 3892-3900 (2009).

12. Chen, J., Glaus, C., Laforest, R., Zhang, Q., Yang, M., Gidding, M., Welch, M. J., & Xia, Y. Gold nanocages as photothermal transducers for cancer treatment. *Small* **6**, 811-817 (2010).

13. Bajaj, A., Miranda, O. R., Kim, I.-B., Phillips, R. L., Jerry, D. J., Bunz, U. H. F., & Rotello, V. M. Detection and differentiation of normal, cancerous, and metastatic cells using nanoparticle-polymer sensor arrays. *Proc. Natl. Acad. Sci. U.S.A.* **106**, 10912-10916 (2009).

14. Millstone, J. E., Park, S., Shuford, K. L., Qin, L., Schatz, G. C., & Mirkin, C. A. Observation of a Quadrupole Plasmon Mode for a Colloidal Solution of Gold Nanoprisms. *J. Am. Chem. Soc.* **127**, 5312-5313 (2005).

15. Giljohann, D. A., Seferos, D. S., Prigodich, A. E., Patel, P. C., & Mirkin, C. A. Gene regulation with polyvalent siRNA-nanoparticle conjugates. *J. Am. Chem. Soc.* **131**, 2072-2073 (2009).

16. Arvizo, R. R., Miranda, O. R., Moyano, D. F., Walden, C. A., Giri, K., Bhattacharya, R., Robertson, J. D., Rotello, V. M., Reid, J. M., & Mukherjee, P. Modulating

Pharmacokinetics, Tumor Uptake and Biodistribution by Engineered Nanoparticles. *PLoS ONE* **6**, e24374 (2011).

17. Hao, L., Patel, P. C., Alhasan, A. H., Giljohann, D. A., & Mirkin, C. A. Nucleic Acid–Gold Nanoparticle Conjugates as Mimics of microRNA. *Small* **7**, 3158-3162 (2011).

18. Hainfeld, J. F., Dilmanian, F. A., Zhong, Z., Slatkin, D. N., Kalef-Ezra, J. A., & Smilowitz, H. M. Gold nanoparticles enhance the radiation therapy of a murine squamous cell carcinoma. *Phys. Med. Biol.* **55**, 3045 (2010).

19. Formerly referred to as the reticuloendothelial system (RES).

20. Beatty, G. L., Chiorean, E. G., Fishman, M. P., Saboury, B., Teitelbaum, U. R., Sun, W., Huhn, R. D., Song, W., Li, D., Sharp, L. L., Torigian, D. A., O'Dwyer, P. J., & Vonderheide, R. H. CD40 Agonists Alter Tumor Stroma and Show Efficacy Against Pancreatic Carcinoma in Mice and Humans. *Science* **331**, 1612-1616 (2011).

21. Lewis, C., Leek, R., Harris, A., & McGee, J. Cytokine regulation of angiogenesis in breast cancer: the role of tumor-associated macrophages. *J. Leuk. Bio.* **57**, 747-751 (1995).

22. Alizadeh, D., Zhang, L., Hwang, J., Schluep, T., & Badie, B. Tumor-associated macrophages are predominant carriers of cyclodextrin-based nanoparticles into gliomas. *Nanomedicine* **6**, 382-390 (2010).

23. Djukic, M., Mildner, A., Schmidt, H., Czesnik, D., Brück, W., Priller, J., Nau, R., & Prinz, M. Circulating monocytes engraft in the brain, differentiate into microglia and contribute to the pathology following meningitis in mice. *Brain* **129**, 2394-2403 (2006).

24. Jackson, H., Muhammad, O., Daneshvar, H., Nelms, J., Popescu, A., Vogelbaum, M. A., Bruchez, M., & Toms, S. A. Quantum Dots Are Phagocytized By Macrophages and Colocalize With Experimental Gliomas. *Neurosurgery* **60**, 524-530 (2007).

25. Yu, W., Liu, C., Liu, Y., Zhang, N., & Xu, W. Mannan-Modified Solid Lipid Nanoparticles for Targeted Gene Delivery to Alveolar Macrophages. *Pharm. Res.* **27**, 1584-1596 (2010).

26. Daldrup-Link, H. E., Golovko, D., Ruffell, B., DeNardo, D. G., Castaneda, R., Ansari, C., Rao, J., Tikhomirov, G. A., Wendland, M. F., Corot, C., & Coussens, L. M. MRI of Tumor-Associated Macrophages with Clinically Applicable Iron Oxide Nanoparticles. *Clin. Cancer Res.* **17**, 5695-5704 (2011).

27. Castelli, D. D., Terreno, E., Cabella, C., Chaabane, L., Lanzardo, S., Tei, L., Visigalli, M., & Aime, S. Evidence for in vivo macrophage mediated tumor uptake of paramagnetic/fluorescent liposomes. *NMR in Biomedicine* **22**, 1084-1092 (2009).

28. Madsen, S. J., Baek, S. K., Makkouk, A. R., Krasieva, T., & Hirschberg, H. Macrophages as Cell-Based Delivery Systems for Nanoshells in Photothermal Therapy. *Ann. Biomed. Eng.*, 1-9 (2011).

29. Baek, S.-K., Makkouk, A., Krasieva, T., Sun, C.-H., Madsen, S., & Hirschberg, H. Photothermal treatment of glioma; an in vitro study of macrophage-mediated delivery of gold nanoshells. *J. Neurooncol.* **104**, 439-448 (2011).

30. Bryskier, A. J. *Macrolides: chemistry, pharmacology and clinical uses*. (Wiley-Blackwell, 1993).

31. Schönfeld, W., & Kirst, H. A. *Macrolide antibiotics*. (Birkhäuser Verlag, 2002).

32. Yen, H.-J., Hsu, S.-h., & Tsai, C.-L. Cytotoxicity and Immunological Response of Gold and Silver Nanoparticles of Different Sizes. *Small* **5**, 1553-1561 (2009).

33. Bastús, N. G., Sánchez-Tilló, E., Pujals, S., Farrera, C., López, C., Giralt, E., Celada, A., Lloberas, J., & Puntes, V. Homogeneous Conjugation of Peptides onto Gold Nanoparticles Enhances Macrophage Response. *ACS Nano* **3**, 1335-1344 (2009).

34. Bartneck, M., Keul, H. A., Singh, S., Czaja, K., Bornemann, J. r., Bockstaller, M., Moeller, M., Zwadlo-Klarwasser, G., & Groll, J. r. Rapid Uptake of Gold Nanorods by Primary Human Blood Phagocytes and Immunomodulatory Effects of Surface Chemistry. *ACS Nano* **4**, 3073-3086 (2010).

35. Nau, G. J., Richmond, J. F. L., Schlesinger, A., Jennings, E. G., Lander, E. S., & Young, R. A. Human macrophage activation programs induced by bacterial pathogens. *Proc. Natl. Acad. Sci. USA* **99**, 1503-1508 (2002).

36. Dreaden, E. C., Mwakwari, S. C., Austin, L. A., Kieffer, M. J., Oyelere, A. K., & El-Sayed, M. A. Small Molecule-Gold Nanorod Conjugates Selectively Target and Induce Macrophage Cytotoxicity Towards Breast Cancer Cells. *submitted to Small* (2012).

37. Dreaden, E. C., Mwakwari, S. C., Austin, L. A., Humphries IV, W. H., Oyelere, A. K., & El-Sayed, M. A. Evidence for the Susceptibility of Nanoscale Drug Carriers to Multiple Drug Resistance: Ligand-Dependent P-glycoprotein Efflux and Inhibition. *submitted to Angew. Chemie. Int. Ed.* (2012).

38. Dreaden, E. C., Mwakwari, S. C., Sodji, Q. H., Oyelere, A. K., & El-Sayed, M. A. Tamoxifen-Poly(ethylene glycol)-Thiol Gold Nanoparticle Conjugates: Enhanced Potency and Selective Delivery for Breast Cancer Treatment. *Bioconjugate Chem.* **20**, 2247-2253 (2009).

39. Orendorff, C. J., & Murphy, C. J. Quantitation of Metal Content in the Silver-Assisted Growth of Gold Nanorods. *J. Phys. Chem. B* **110**, 3990-3994 (2006).

40. Jain, R. K., & Stylianopoulos, T. Delivering nanomedicine to solid tumors. *Nat. Rev. Clin. Oncol.* **7**, 653-664 (2010).

41. Hsu, Y.-C., Acuña, M., Tahara, S. M., & Peng, C.-A. Reduced Phagocytosis of Colloidal Carriers Using Soluble CD47. *Pharm. Res.* **20**, 1539-1542 (2003).

42. Cho, W.-S., Cho, M., Jeong, J., Choi, M., Cho, H.-Y., Han, B. S., Kim, S. H., Kim, H. O., Lim, Y. T., Chung, B. H., & Jeong, J. Acute toxicity and pharmacokinetics of 13 nm-sized PEG-coated gold nanoparticles. *Toxicol. Appl. Pharmacol.* **236**, 16-24 (2009).

43. Higgins, C. F. Multiple molecular mechanisms for multidrug resistance transporters. *Nature* **446**, 749-757 (2007).

44. Aller, S. G., Yu, J., Ward, A., Weng, Y., Chittaboina, S., Zhuo, R., Harrell, P. M., Trinh, Y. T., Zhang, Q., Urbatsch, I. L., & Chang, G. Structure of P-Glycoprotein Reveals a Molecular Basis for Poly-Specific Drug Binding. *Science* **323**, 1718-1722 (2009).

45. Peer, D., Karp, J. M., Hong, S., Farokhzad, O. C., Margalit, R., & Langer, R. Nanocarriers as an emerging platform for cancer therapy. *Nat. Nanotechnol.* **2**, 751-760 (2007).

46. Heath, J. R., & Davis, M. E. Nanotechnology and Cancer. *Annu. Rev. Med.* **59**, 251-265 (2008).

47. Schluep, T., Hwang, J., Hildebrandt, I. J., Czernin, J., Choi, C. H. J., Alabi, C. A., Mack, B. C., & Davis, M. E. Pharmacokinetics and tumor dynamics of the nanoparticle IT-101 from PET imaging and tumor histological measurements. *Proc. Nat. Acad. Sci. U.S.A.* **106**, 11394-11399 (2009).

48. Davis, M. E., Chen, Z., & Shin, D. M. Nanoparticle therapeutics: an emerging treatment modality for cancer. *Nat. Rev. Drug Discov.* **7**, 771-782 (2008).

49. Dong, X., Mattingly, C. A., Tseng, M. T., Cho, M. J., Liu, Y., Adams, V. R., & Mumper, R. J. Doxorubicin and Paclitaxel-Loaded Lipid-Based Nanoparticles Overcome Multidrug Resistance by Inhibiting P-Glycoprotein and Depleting ATP. *Cancer Res.* **69**, 3918-3926 (2009).

50. Pang, K. S., Liu, L., & Sun, H. in *Role of Lipid Excipients in Modifying Oral and Parenteral Drug Delivery* (ed Kishor M. Wasan) 1-31 (John Wiley & Sons, Inc., 2006).

51. van Helvoort, A., Smith, A. J., Sprong, H., Fritzsche, I., Schinkel, A. H., Borst, P., & van Meer, G. MDR1 P-Glycoprotein Is a Lipid Translocase of Broad Specificity, While MDR3 P-Glycoprotein Specifically Translocates Phosphatidylcholine. *Cell* **87**, 507-517 (1996).

52. US National Institutes of Health. *Pilot Study of AuroLase(tm) Therapy in Refractory and/or Recurrent Tumors of the Head and Neck*, <http://clinicaltrials.gov/ct2/show/NCT00848042> (2009).

53. Seral, C., Michot, J.-M., Chanteux, H., Mingeot-Leclercq, M.-P., Tulkens, P. M., & Van Bambeke, F. Influence of P-Glycoprotein Inhibitors on Accumulation of Macrolides in J774 Murine Macrophages. *Antimicrob. Agents Chemother.* **47**, 1047-1051 (2003).

54. Bosnar, M., Kelneric, Z., Munic, V., Erakovic, V., & Parnham, M. J. Cellular Uptake and Efflux of Azithromycin, Erythromycin, Clarithromycin, Telithromycin, and Cethromycin. *Antimicrob. Agents Chemother.* **49**, 2372-2377 (2005).

55. Ma, Z., & Memoto, P. K. Discovery and Development of Ketolides as a New Generation of Macrolide Antimicrobial Agents. *Curr. Med. Chem. Anti-Infective Agents* **1**, 15-34 (2002).

56. Kashimura, M., Asaka, T., Misawa, Y., Matsumoto, K., & Morimoto, S. Synthesis and antibacterial activity of the tricyclic ketolides TE-802 and its analogs. *J. Antibiot.* **54**, 664-678 (2001).

57. Ono, T., Kashimura, M., Suzuki, K., Oyauchi, R., Miyachi, J., Ikuta, H., Kawauchi, H., Akashi, T., Asaka, T., & Morimoto, S. In vitro and in vivo antibacterial activities of the tricyclic ketolide TE-802 and its analogs. *J. Antibiot.* **57**, 518-527 (2004).

58. Raub, T. J. P-Glycoprotein Recognition of Substrates and Circumvention through Rational Drug Design. *Mol. Pharmaceutics* **3**, 3-25 (2005).

59. Constantinides, P. P., & Wasan, K. M. Lipid formulation strategies for enhancing intestinal transport and absorption of P-glycoprotein (P-gp) substrate drugs: In vitro/In vivo case studies. *J. Pharm. Sci.* **96**, 235-248 (2007).

60. Cho, E. C., Zhang, Q., & Xia, Y. The effect of sedimentation and diffusion on cellular uptake of gold nanoparticles. *Nat. Nanotechnol.* **6**, 385-391 (2011).

61. Iwahashi, T., Okochi, E., Ariyoshi, K., Watabe, H., Amann, E., Mori, S., Tsuruo, T., & Ono, K. Specific Targeting and Killing Activities of Anti-P-Glycoprotein Monoclonal Antibody MRK16 Directed against Intrinsically Multidrug-resistant Human Colorectal Carcinoma Cell Lines in the Nude Mouse Model. *Cancer Res.* **53**, 5475-5482 (1993).

62. Oyelere, A. K., Chen, P. C., Guerrant, W., Mwakwari, S. C., Hood, R., Zhang, Y., & Fan, Y. Non-Peptide Macrocyclic Histone Deacetylase Inhibitors. *J. Med. Chem.* **52**, 456–468 (2009).

63. Mwakwari, S. C., Guerrant, W., Patil, V., Khan, S. I., Tekwani, B. L., Gurard-Levin, Z. A., Mrksich, M., & Oyelere, A. K. Non-Peptide Macrocyclic Histone Deacetylase Inhibitors Derived from Tricyclic Ketolide Skeleton. *J. Med. Chem.* (2010).

64. Bouzide, A., & Sauvé, G. Silver(I) Oxide Mediated Highly Selective Monotosylation of Symmetrical Diols. Application to the Synthesis of Polysubstituted Cyclic Ethers. *Org. Lett.* **4**, 2329 - 2332 (2002).

65. Carlier, M. B., Zenebergh, A., & Tulkens, P. M. Cellular uptake and subcellular distribution of roxithromycin and erythromycin in phagocytic cells. *J. Antimicrob. Chemother.* **20**, 47-56 (1987).

66. Rao, U. S., & Scarborough, G. A. Direct demonstration of high affinity interactions of immunosuppressant drugs with the drug binding site of the human P-glycoprotein. *Mol. Pharmacol.* **45**, 773-776 (1994).

67. Vazifeh, D., Preira, A., Bryskier, A., & Labro, M. T. Interactions between HMR 3647, a New Ketolide, and Human Polymorphonuclear Neutrophils. *Antimicrob. Agents Chemother.* **42**, 1944-1951 (1998).

68. Chithrani, B. D., & Chan, W. C. W. Elucidating the Mechanism of Cellular Uptake and Removal of Protein-Coated Gold Nanoparticles of Different Sizes and Shapes. *Nano Lett.* **7**, 1542-1550 (2007).

69. Rosenberg, M. F., Callaghan, R., Ford, R. C., & Higgins, C. F. Structure of the Multidrug Resistance P-glycoprotein to 2.5 nm Resolution Determined by Electron Microscopy and Image Analysis. *J. Biol. Chem.* **272**, 10685-10694 (1997).

70. Ambudkar, S. V., Kimchi-Sarfaty, C., Sauna, Z. E., & Gottesman, M. M. P-glycoprotein: from genomics to mechanism. *Oncogene* **22**, 7468-7485 (2003).

CHAPTER 6

CHARGE CARRIER DYNAMICS IN SEMICONDUCTOR-GOLD CORE-SHELL NANOROD ARRAYS

6.1 Plasmon-Enhanced Optical and Electronic Processes in Molecules and Materials

The resonant interaction of electromagnetic waves with electron oscillations at the surfaces of nanoscale metals is known as localized surface plasmon resonance (LSPR). LSPR is determined by the nanoparticle's material, as well as its size, shape, and dielectric environment and results in intense absorption/scattering and the generation of highly polarized near-fields which dephase on the femtosecond time scale.[*1-4*] Absorbed energy can be dissipated through electron collisions,[*5*] lattice vibrations,[*2,6*] or resonant coupling to neighboring electronic systems. LSPR coupling interactions have been shown to enhance the absorption cross sections of molecules[*7*] and semiconductor nanoparticles[*8*] in their vicinity, as well as to enhance the optical activity of surface adsorbates.[*9*] Their interactions with radiative electronic systems have been shown to enhance molecular fluorescence intensity,[*10*] Raman scattering,[*11-13*] second- and third- harmonic generation (SHG and THG),[*14,15*] hyper-Rayleigh scattering,[*16*] and hyper-Raman scattering.[*17*] The rational design of photovoltaic and photodiode devices incorporating plasmonic elements has also resulted in improved performance[*18,19*] and recently allowed for ultrafast electron spin manipulation in colloidal core-shell nanoparticles.[*20*]

LSPR coupling with excitonic systems exhibiting well-defined band structure involves increasingly complex and varied interactions and has been shown to enhance Förster Resonance Energy Transfer (FRET) efficiency between semiconductor quantum dots (QDs),[*21*] as well as

resonant energy transfer between metallic and semiconducting nanoparticles.[*22,23*] In general, plasmon-exciton interactions in solid-state excitonic systems are characterized by i) enhanced quantum efficiency,[*8,24,25*] ii) exciton energy shift,[*26,27*] iii) increased radiative decay rate,[*26,28,29*] and iv) emission polarized parallel with resonantly coupled LSPR modes.[*24,30*] These phenomena require that the exciton energy overlap with that of the LSPR,[*25,31*] and that the transition dipole moment of the exciton lie collinear with the dipole moment of the LSPR.[*24,32*]

Although numerous reports have individually studied the aforementioned phenomena, few have performed systematic studies of distance-, energy-, and polarization- dependence. Kotov and coworkers have studied CdTe nanowire/Au nanoparticle assemblies in solution and shown a 5-fold enhancement in luminescence intensity and a ca. 1/3 reduction in photoluminescence (PL) lifetime.[*29*] Later, using a chemically-responsive molecular linker, they showed that a model based on the Förster relation can be used to describe the observed changes in exciton lifetime and emission energy due to distance-dependent effects of the LSPR on exciton mobility.[*27*] In a more recent report, Ginger and coworkers performed systematic studies of close-packed monolayers of CdSe quantum dots (QDs) upon which Ag nanoprisms with varying LSPRs were deposited.[*31*] They observed maximum enhancement of QD emission intensity, radiative decay rate, and non-radiative decay rate when the LSPR wavelength of the prisms coincided with the bandgap energy of the QDs. Atwater and Polman have fabricated horizontally aligned arrays of Ag nanorods on substrates containing immobilized Si QDs which photoluminesce over the wavelength range of the transverse and longitudinal LSPR modes of the nanorods.[*24*] They observed QD emission enhancement at each of the two orthogonally-polarized LSPR wavelengths which polarized parallel to the dipole moment of their resonantly coupled plasmon mode.

While radiative effects associated with plasmon-exciton coupling in the solid-state is actively studied, non-radiative effects[*26,33*] are less well characterized. In prior publications, we have studied plasmon-exciton coupling and non-radiative exciton relaxation in vertically aligned CdTe-Au core-shell nanorod arrays and found that Au shells supporting LSPRs resonant with the bandgap energy of the CdTe core resulted in increased non-radiative exciton relaxation rates which were highly sensitive to the incident polarization and the orientation of the longitudinal axis of the rod.[*34-36*] In low aspect ratio nanorod cores, we also observed that by increasing the thickness of the Au shell to maximize LSPR extinction, non-radiative excitonic relaxation was enhanced, but no longer exhibited tilt-anisotropy. Here, we analyze spectroscopic, computational, and theoretical results obtained from extinction-optimized, high aspect ratio nanorod arrays in the context of prior studies and present our overall conclusions of how plasmon-exciton coupling in this novel system results in differing mechanisms of enhanced non-radiative relaxation.

6.2 Design, Fabrication, and Modeling of a Nanoscale Electronic System to Study Polarization-, Wavelength-, and Field-Dependent Plasmon-Exciton Coupling

CdTe-Au core-shell nanorod arrays were fabricated as previously described.[*34,37,38*] Briefly, a layer of Bi_2Te_3 was deposited onto a polyvinyl alcohol surface-corrupted (0001) sapphire substrate by pulsed laser deposition (PLD, $\lambda_{excimer}$ = 248 nm). Heating of the Bi_2Te_3 layer to 370 °C caused the film to dewet and coalesce into isolated seeds which served as nucleation sites for the subsequent vapor-liquid-solid (VLS) growth of the CdTe nanorods. Varying thicknesses of Au were then sputtered onto half of each substrate at room temperature. CdTe core and Au shell dimensions were experimentally determined by scanning electron microscopy (SEM) and tapping-mode atomic force microscopy (AFM), respectively.

The experimental configuration of the ultrafast pump-probe measurements has also been described in detail elsewhere.[*34*] Briefly, the core-shell nanorod arrays were optically pumped (λ_{pump} = 400 nm) by a Ti-sapphire laser (Clark MXR) and absorption at the CdTe bandedge energy (λ_{probe} = 770 nm) was subsequently probed as a function of time delay. All experiments were performed at low pump fluence to exclude contributions from multiple carrier generation. Transient bleach intensity ($\Delta T_{(t)}/T_{(\infty)}$) was recorded for each array as a function of tilt angle and shell thickness where $\Delta T_{(t)}/T_{(\infty)} = |T_{(\infty)} - T_{(t)}|/T_{(\infty)}$ and $T_{(t)}$ and $T_{(\infty)}$ are transient and steady-state transmission, respectively. The array samples were rotated in the $\overrightarrow{kE}$-plane of the linear-polarized pump and probe beams such that θ = 0° corresponds to polarization along the transverse axes of the nanorods and θ = 90° corresponds to polarization along the longitudinal axes of the nanorods for propagation vector $\vec{k}$ and electric field polarization $\vec{E}$.

Optical spectra, electric field distribution, and particle polarization were calculated by Discrete Dipole Approximation (DDA). The method approximates a particle as an array of polarizable points in a cubic lattice which acquire dipole moments in response to an incident electromagnetic field. Each of these dipoles is assigned a position in the array, a relative volume, and a complex dielectric function for the particle and its surrounding environment. The method has been successfully employed to model the optical properties of plasmonic nanoparticles of complex geometry and their arrays for more than 15 years.[*3,39,40*]

Optical extinction, absorption, and scattering spectra were calculated using DDSCAT 6.1.[*41*] Electric field and polarization plots were calculated using modified Fortran codes of the program kindly provided by G.C. Schatz (Northwestern University). Calculations were performed using linearly polarized incident excitation for 184 x 74 nm and 283 x 72 nm hemispherically-capped, cylindrical wurtzite CdTe cores with homogenous Au shells of varying thickness covering all

sides but the flat base (~10^5 total dipoles per particle). Experimentally determined complex refractive indices for Au[*42*] and CdTe[*43*] were applied *in vacuo*. Briefly, the polarization *P* of each point in the (*i = 1,…,N)* dipole array is described in terms of its polarizability α_i and response to the local electromagnetic field E_{loc} at position r_i

$$P_i = \alpha_i \bullet E_{loc}(r_i), \tag{1}$$

where E_{loc} represents the sum of the incident electromagnetic field E_{inc} and those radiating from *N-1* surrounding dipoles

$$E_{loc}(r_i) = E_{loc,i} = E_{inc,i} + E_{dipole,i} = E_0 \exp(ik \bullet r_i) - \sum_{j \neq 1}^{N} A_{ij} \bullet P_j \tag{2}$$

for amplitude E_0 and wavevector $k=\omega/c$ of the incident electromagnetic field. The collective interactions of dipoles in the array are described by matrix A_{ij} for $j \neq i$

$$A_{ij} \bullet P_j = \frac{\exp(ikr_{ij})}{r_{ij}^3}\left\{k^2 r_{ij} \times (r_{ij} \times P_j) + \frac{(1-ikr_{ij})}{r_{ij}^2} \times [r_{ij}^2 P_j - 3r_{ij}(r_{ij} \bullet P_j)]\right\}. \tag{3}$$

Substitution and rearrangement of Equations (2) and (3) into Equation (1) gives

$$A' \bullet P = E, \tag{4}$$

where *A'* is a *3N*×*3N* interaction matrix for the system and *E* and *P* are *3N*-dimensional vectors. Solution of these *3N* complex linear equations yields wavelength-dependent polarization vectors for each dipole, from which electric field intensities, as well as extinction, absorption and scattering cross sections can be readily obtained[*44,45*]

$$C_{ext} = \frac{4\pi k}{|E_0|^2} \sum_{j=1}^{N} \{\mathrm{Im}\}(E_{inc,j}^{*} \bullet P_j) \tag{5}$$

$$C_{abs} = \frac{4\pi k}{|E_0|^2} \sum_{j=1}^{N} \left\{\{\mathrm{Im}\}[P_j(\alpha_j^{-1}) * P_j^{*}] - \frac{2}{3}k^3 |P_j|^2\right\} \tag{6}$$

for $C_{ext} = C_{abs} + C_{sca}$.

6.3 Plasmon-Enhanced Nonradiative Charge Carrier Relaxation in Nanoscale Semiconductor Photovoltaic Materials

Figures 6.1A,B show the SEM images of the of the fabricated low and high aspect ratio CdTe-Au core-shell nanorod arrays, respectively. As shown previously,[*38*] these nanorods appear structurally isolated from one another and exhibit a high degree of size and shape uniformity. Because the low and high aspect ratio nanorod arrays were grown from the same diameter seeds, their widths are likewise similar. X-ray diffraction indicates the CdTe cores to be wurtzite single crystal with alternating Cd^{2+} and Te^{2-} layers stacked along the growth direction of the rod (i.e. the c-axis). *Note that the ground-state absorption transition moment* $\vec{\mu}_{Eg}$ *of the nanorod therefore lies parallel to its longitudinal axis.* Following previous reports,[*24,32,35*] plasmon-exciton coupling is expected to be strongest when the surface plasmon field $\vec{E}_{SPR}$ is oriented parallel to the ground-state absorption moment $\vec{\mu}_{Eg}$. Quantum confinement effects are not expected here (r_{Bohr} = 7.5 nm). **Figure 6.1C** shows a schematic of the experimental configuration used for the ultrafast transient absorption measurements. Nanorod arrays were tilted from θ = 0 - 75 °, in the $\overrightarrow{kE}$-plane where θ is the angle between the longitudinal axis of the nanorod and the incident field propagation vector $\vec{k}$ with linear polarization $\vec{E}$ of the laser. The arrays are optically pumped at 400 nm by a Ti-sapphire laser and absorption (770 nm) is probed at varying delay times. The pump wavelength was chosen to coincide with the absorption bandedge of the CdTe core.

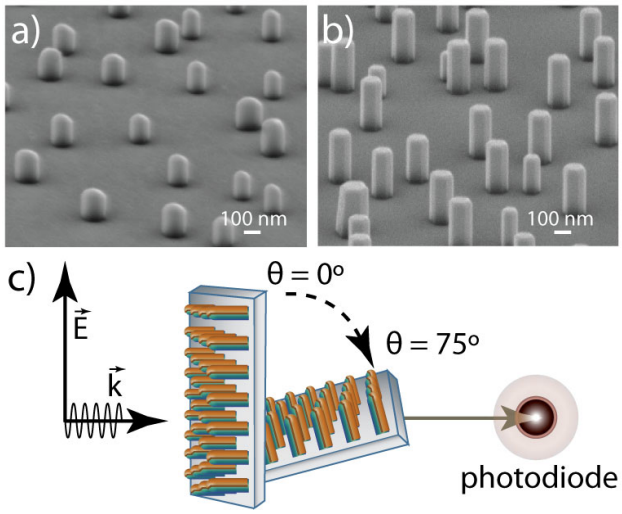

Figure 6.1. SEM images of (A) low and (B) high aspect ratio CdTe-Au core-shell nanorod arrays and (C) a schematic of the experimental configuration used for transient absorption measurements. The arrays were tilted from θ = 0 - 75 ° in the $\overrightarrow{kE}$ -plane, where θ is the angle between the longitudinal axis of the nanorod and the incident field propagation vector $\vec{k}$ with linear polarization $\vec{E}$. The arrays are optically pumped at 400 nm by a Ti-sapphire laser and absorption (770 nm) is probed at a varying time delay. Low and high aspect CdTe nanorod cores are ca. 74 nm in width with 184 nm and 285 nm length, respectively. Adapted from Dreaden et al. [*46*].

In order to maximize plasmonic field effects of the Au nanoshell on the CdTe nanorod cores, optical response at the ground-state absorption bandedge energy (770 nm) of the core was modeled as a function of Au shell thickness. **Figure 6.2A,B** show the calculated angle- and wavelength-dependent extinction cross sections of low and high aspect ratio CdTe cores, respectively, with thin, 15 nm Au shells. As depicted in the inset of **Figure 6.2A**, transverse and longitudinal pump laser polarizations are denoted 0° and 90°, respectively. **Figures 6.2C,D** illustrate similar plots for Au shell thicknesses theoretically predicted to maximize relative plasmon extinction anisotropy at the 770 nm probe wavelength. In both the low and high aspect ratio CdTe cores, thickening of the Au shell was found to result in a spectral blue-shift of the longitudinal (θ = 90°) plasmon resonance, thereby increasing its overlap with the 770 nm CdTe ground-state absorption wavelength. These spectral shifts are consistent with experimentally observed thickness-dependent optical responses from

spherical core-shell nanoparticles.[*4,20,47*] We observed 4.3- and 2.6- fold LSPR extinction anisotropy in low and high aspect ratio core-shell nanorods, respectively, with 15 nm Au shells, while 9.4- and 4.3- fold anisotropy was observed with optimized shell thicknesses.

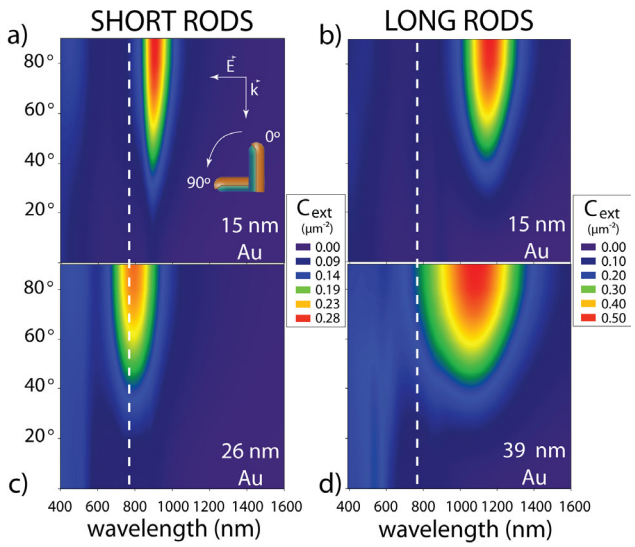

Figure 6.2. Calculated wavelength- and angle- dependent LSPR extinction cross section for CdTe-Au core-shell nanorods with varying shell thicknesses. Low aspect ratio nanostructures were approximated as 184 x 74 nm hemispherically-capped, cylindrical wurtzite CdTe cores with homogeneous (A) 15 nm and (C) 26 nm outer Au shells covering all sides but the rod base. High aspect ratio (283 x 72 nm) CdTe cores with (B) 15 nm and (D) 39 nm outer Au shells were similarly calculated in vacuo. The 770 nm CdTe absorption bandedge (probe wavelength) is denoted by dashed white lines. Adapted from Dreaden et al. [*46*].

Carrier dynamics in the nanorod cores were monitored at the CdTe bandgap energy so that the observed decay kinetics excluded contributions from rapid intraband relaxation.[*48*] **Figure 6.3** illustrates tilt-dependent transient absorption kinetics of the probe excitation (770 nm) in low and high aspect ratio CdTe-Au core-shell nanorod arrays with thin (15 nm) and thick (extinction-optimized) shell thicknesses. In all cases, enhanced relaxation rates were observed relative to bare CdTe nanorod arrays (4.5 ps). Both low and high aspect ratio CdTe nanorod cores with 15 nm outer Au shells exhibited enhanced non-radiative relaxation with increasing tilt angle, showing 60% and

50% reductions in decay lifetime, respectively. In contrast, both CdTe nanorod cores with outer Au shell thicknesses optimized for tilt-dependent LSPR extinction anisotropy exhibited orientationally isotropic decay kinetics. We note here dramatic differences in the order of the observed decay rate kinetics, indicating mechanisms with different dependencies on carrier concentration. Transient absorption kinetics of both CdTe nanorod cores with thin Au shells (*at low angle*) and those from the cores with thicker Au shells (*at all angles*) exhibit (semi-linear) second-order decay kinetics which we attribute to Auger recombination.[*49*] In contrast, decay kinetics of both CdTe nanorod cores with thin Au shells (*at high angle*) displayed increasingly rapid first-order (exponential) decay kinetics expected in the case of excited-state absorption. Contributions from electron-phonon coupling in the gold shell are not anticipated here due to the fact that such decay rates are insensitive to both size and shape and are much slower than those observed here.[*2,50*] Further, the decrease in decay lifetime relative to bare CdTe nanorod cores (4.5 ps) observed for all in the transverse configuration is believed to be associated charge-transfer interactions between the CdTe conduction band and the gold Fermi band.[*34*] We should also note that our analyses here are concerned with mechanisms of non-radiative relaxation in the absence of surface and/or defect contributions. In cases where surface and/or trap recombination become increasingly significant (i.e. higher surface:volume, lower aspect ratio nanorods), deviations from purely first- or second- order kinetics can be expected.

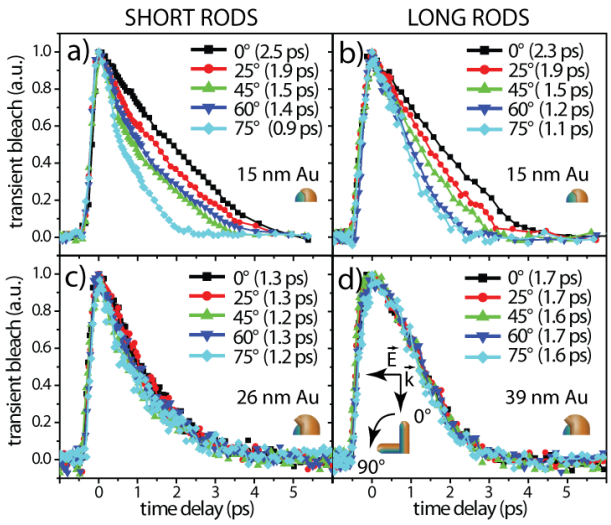

Figure 6.3. Transient bleach of CdTe absorption (770 nm) as a function of tilt angle (°) for vertically aligned arrays of low and high aspect ratio CdTe-Au core-shell nanorods with optimal and sub-optimal Au shell thicknesses. CdTe nanorod cores of aspect ratio (A) ca. 2 and (B) 3 coated with 15 nm outer Au shells exhibit tilt-dependent non-radiative relaxation of the probe excitation while CdTe nanorod cores of aspect ratio (C) ca. 2 and (D) 3 coated with Au shell thicknesses optimized for tilt-dependent LSPR extinction anisotropy exhibit orientationally isotropic non-radiative carrier relaxation. CdTe aspect ratio, Au shell thickness, incident field polarization, and decay lifetimes are as indicated. λ_{pump} = 400 nm, λ_{probe} = 770 nm. Adapted from Dreaden et al. [*46*].

Increased non-radiative exciton relaxation rates in the CdTe-Au nanorods are proposed to result from enhanced ground- and/or excited-state absorption processes.[*36*] Recall that the c-axis of the single crystal, wurtzite CdTe nanorod core lies along its longitudinal axis. Absorption from its ground electronic state therefore occurs with a transition moment $\vec{\mu}_{Eg}$ parallel to the long axis of the nanorod core, with enhanced rates observed for perturbations (e.g. surface plasmon fields) having significant dipolar contribution parallel to this moment. This ground-state absorption process, depicted in **Figure 6.4A**, increases exciton density and Coulomb coupling between charge carriers, in turn resulting in energy transfer from one exciton to another. This transfer (Auger recombination) occurs on the sub-nanosecond scale, competing with radiative relaxation and resulting in a net ionization of the nanorod core and second-order (semi-linear) relaxation kinetics.[*51*] Because the decay of excited-state electrons is equal to the decay rate of excited-state electrons times the

concentration of excited-state electrons, one can see that rearrangement and integration of the rate expression will yield an exponential decay function. In contrast, absorption from the excited-state (**Figure 6.4B**) may result in intraband electronic transitions into the CdTe conduction band, into the Au shell, or stimulated emission. Here, the excited-state decay rate is equal to the Auger recombination rate times the concentration of excitons squared, yielding a decay with linear dependency after integration. Because the decay rate involving excited-state absorption is first-order with respect to exciton concentration and Auger recombination (ground-state absorption) is second-order, we expect to observe exponential decay kinetics when excited-state absorption dominates and less rapid semi-linear decay kinetics when ground-state absorption (Auger recombination) dominates.[*36*]

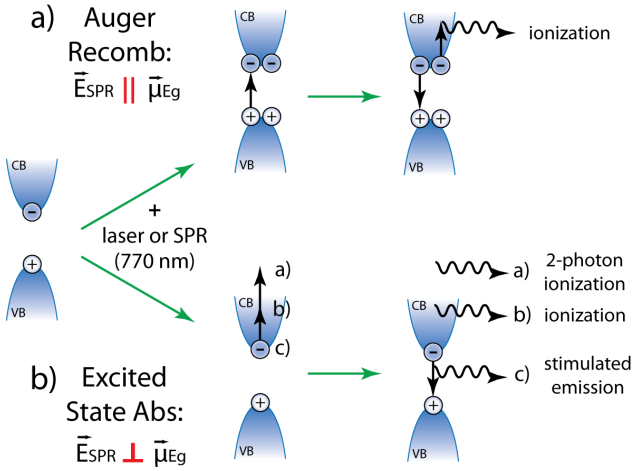

Figure 6.4. Proposed plasmon-enhanced exciton interactions in CdTe-Au core shell nanorod arrays. A) Enhanced ground-state absorption by resonantly-coupled plasmon fields E_{SPR} parallel to the bandgap absorption transition moment $\vec{\mu}_{Eg}$ results in increased carrier density and less rapid Auger recombination. B) Enhanced excited-state absorption by resonantly-coupled plasmon fields $\vec{E}_{SPR}$ non-parallel to the bandgap absorption transition moment $\vec{\mu}_{Eg}$ results in increasingly rapid ionization processes. The decay rate in (A) is second-order whereas in (B) it is first-order with respect to exciton concentration.[*36*] Semi-linear and semi-exponential decay kinetics are therefore expected when (A) and (B) dominate plasmon-enhanced relaxation, respectively. Adapted from Dreaden et al. [*46*].

Computational modeling of the plasmon field strength and induced polarization in the nanorod arrays further corroborates LSPR effects on ground- and excited-state absorption and subsequent tilt-dependent non-radiative decay kinetics. **Figure 6.5** illustrates the calculated electric field enhancement distribution (at λ = 770 nm) for CdTe-Au core-shell nanorods of varying aspect ratio, shell thickness, and tilt angle. The *distribution* of polarization induced parallel to the CdTe ground-state absorption transition moment $\vec{\mu}_{Eg}$ is also shown for these configurations. Significant plasmonic field enhancement was observed in all cases with apparent dipolar character for all in the transverse (0°) configuration, regardless of aspect ratio or shell thickness. Because this transverse dipolar plasmon field shows significant contributions for $\vec{E}_{SPR} \parallel \vec{\mu}_{Eg}$, it is thus expected to enhance ground-state absorption of the probe excitation and lead to second-order decay kinetics in all cases.

As in **Figure 6.4A**, the predominant contributor to second-order non-radiative decay kinetics observed for all in the transverse configuration is attributed to enhanced ground-state absorption and Auger recombination. In the longitudinal (90°) configuration, both nanorod cores with thin Au shells exhibit plasmon fields with diminished dipolar contributions along the ground-state absorption transition moment $\vec{\mu}_{Eg}$ of the core (**Figures 6.5A,B**). In this orientation, we expect, and indeed observe, increasingly rapid first-order non-radiative relaxation kinetics which we attribute to predominant excited-state absorption (**Figure 6.4B**). In contrast, when coated with LSPR extinction-optimized Au shell thicknesses, the longitudinal plasmon modes appear dipolar with respect to $\vec{\mu}_{Eg}$ (**Figuress 6.5C,D**) and we expect probe absorption decay similar to the second-order kinetics observed in the transverse configuration. Here, experimentally observed decay kinetics agree well with the excited-state absorption model and remain second-order regardless of orientation.

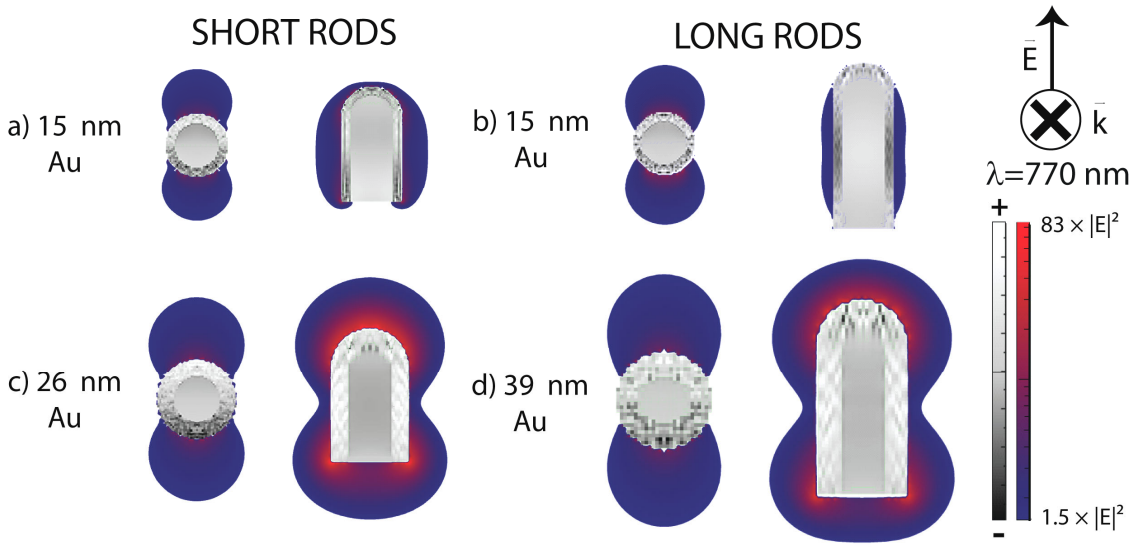

Figure 6.5. Calculated plasmonic field enhancement (color) and normalized polarization distribution induced parallel to the CdTe ground-state absorption transition moment $\vec{\mu}_{Eg}$ (grayscale) for 770 nm probe excitation in CdTe-Au core-shell nanorods of varying aspect ratio, shell thicknesses, and orientation. Transverse and longitudinal excitation of structures with 15 nm Au shells is shown for (A) low and (B) high aspect ratio CdTe nanorod cores. Transverse and longitudinal excitation of structures with extinction optimized Au shells is shown for (C) low and (D) high aspect ratio CdTe nanorod cores. Adapted from Dreaden et al. [*46*].

6.4 Outlook and Conclusions

In conclusion, plasmonic field enhancement of non-radiative exciton relaxation rates was investigated in vertically-aligned arrays of high aspect ratio CdTe-Au core-shell nanorods. Increasing shell thickness in the high aspect ratio nanorods was found to result in dramatic differences in the polarization-dependent non-radiative relaxation kinetics of charge carriers in the CdTe cores. Based on computational modeling and kinetics analyses, we attribute these differences to varying mechanisms of plasmonic field enhancement which result in either predominant ground- or excited-state absorption processes. Our results were compared with previous investigations of low aspect ratio CdTe-Au core-shell nanorods to provide overall conclusions regarding plasmonic field effects on non-radiative exciton relaxation rates in this system. We propose that when the dipolar component of the

resonantly-coupled plasmon field of the shell is polarized parallel to the ground-state absorption transition moment of the CdTe core that exciton-exciton annihilation (Auger recombination) dominates carrier relaxation kinetics and slower second-order decay rates are observed. When contributions of the resonantly-coupled plasmon field are non-dipolar or orthogonal to the ground-state absorption transition moment of the CdTe core, excited state absorption processes are believed to dominate and increasingly rapid first-order decay kinetics are observed. These processes were found to vary greatly depending on the thickness of the Au shell and the orientation of the array, but were insensitive to aspect ratio of the nanorods. These findings have significant implications in the optimal design of photovoltaic and optoelectronic devices incorporating anisotropic active layers and/or plasmonic elements.

6.5 References

1. Ritchie, R. H. Plasma Losses by Fast Electrons in Thin Films. *Phys. Rev.* **106**, 874 (1957).

2. Link, S., & El-Sayed, M. A. Shape and size dependence of radiative, non-radiative and photothermal properties of gold nanocrystals. *Int. Rev. Phys. Chem.* **19**, 409-453 (2000).

3. Kelly, K. L., Coronado, E., Zhao, L. L., & Schatz, G. C. The optical properties of metal nanoparticles: The influence of size, shape, and dielectric environment. *J. Phys. Chem. B* **107**, 668-677 (2003).

4. Wang, H., Brandl, D. W., Nordlander, P., & Halas, N. J. Plasmonic Nanostructures: Artificial Molecules. *Acc. Chem. Res.* **40**, 53-62 (2007).

5. Hu, M., Novo, C., Funston, A., Wang, H., Staleva, H., Zou, S., Mulvaney, P., Xia, Y., & Hartland, G. V. Dark-field microscopy studies of single metal nanoparticles: understanding the factors that influence the linewidth of the localized surface plasmon resonance. *J. Mater. Chem.* **18**, 1949-1960 (2008).

6. Hodak, J. H., Henglein, A., & Hartland, G. V. Electron-phonon coupling dynamics in very small (between 2 and 8 nm diameter) Au nanoparticles. *J. Chem. Phys.* **112**, 5942-5947 (2000).

7. Sipe, J. E. Surface plasmon-enhanced absorption of light by adsorbed molecules. *Solid State Commun.* **33**, 7-9 (1980).

8. Biteen, J. S., Pacifici, D., Lewis, N. S., & Atwater, H. A. Enhanced Radiative Emission Rate and Quantum Efficiency in Coupled Silicon Nanocrystal-Nanostructured Gold Emitters. *Nano Lett.* **5**, 1768-1773 (2005).

9. Lieberman, I., Shemer, G., Fried, T., Kosower, E., & Markovich, G. Plasmon-Resonance-Enhanced Absorption and Circular Dichroism. *Angew. Chem., Int. Ed.* **47**, 4855-4857 (2008).

10. Lakowicz, J. R. Radiative Decay Engineering: Biophysical and Biomedical Applications. *Anal. Biochem.* **298**, 1-24 (2001).

11. Fleischmann, M., Hendra, P. J., & McQuillan, A. J. Raman spectra of pyridine adsorbed at a silver electrode. *Chem. Phys. Lett.* **26**, 163-166 (1974).

12. Jeanmaire, D. L., & Van Duyne, R. P. Surface raman spectroelectrochemistry: Part I. Heterocyclic, aromatic, and aliphatic amines adsorbed on the anodized silver electrode. *J. Electroanal. Chem.* **84**, 1-20 (1977).

13. Albrecht, M. G., & Creighton, J. A. Anomalously intense Raman spectra of pyridine at a silver electrode. *J. Am. Chem. Soc.* **99**, 5215-5217 (1977).

14. Chen, C. K., de Castro, A. R. B., & Shen, Y. R. Surface-Enhanced Second-Harmonic Generation. *Phys. Rev. Lett.* **46**, 145 (1981).

15. Karatzas, N. E., & Georges, A. T. Model for ultrafast harmonic generation from a gold surface: extraction of dephasing times for continuum-continuum transitions. *J. Opt. Soc. Am. B* **26**, 2218-2227 (2009).

16. Johnson, R. C., Li, J., Hupp, J. T., & Schatz, G. C. Hyper-Rayleigh scattering studies of silver, copper, and platinum nanoparticle suspensions. *Chem. Phys. Lett.* **356**, 534-540 (2002).

17. Yang, W.-H., & Schatz, G. C. Ab initio and semiempirical molecular orbital studies of surface enhanced and bulk hyper-Raman scattering from pyridine. *J. Chem. Phys.* **97**, 3831-3845 (1992).

18. Sundararajan, S. P., Grady, N. K., Mirin, N., & Halas, N. J. Nanoparticle-Induced Enhancement and Suppression of Photocurrent in a Silicon Photodiode. *Nano Lett.* **8**, 624-630 (2008).

19. Nakayama, K., Tanabe, K., & Atwater, H. A. Plasmonic nanoparticle enhanced light absorption in GaAs solar cells. *Appl. Phys. Lett.* **93**, 121904 (2008).

20. Zhang, J., Tang, Y., Lee, K., & Ouyang, M. Tailoring light-matter-spin interactions in colloidal hetero-nanostructures. *Nature* **466**, 91-95 (2010).

21. Su, X.-R., Zhang, W., Zhou, L., Peng, X.-N., & Wang, Q.-Q. Plasmon-enhanced Förster energy transfer between semiconductor quantum dots: multipole effects. *Opt. Express* **18**, 6516-6521 (2010).

22. Nikoobakht, B., Burda, C., Braun, M., Hun, M., & El-Sayed, M. A. The Quenching of CdSe Quantum Dots Photoluminescence by Gold Nanoparticles in Solution¶. *Photochem. Photobiol.* **75**, 591-597 (2002).

23. Gómez, D. E., Vernon, K. C., Mulvaney, P., & Davis, T. J. Surface Plasmon Mediated Strong Exciton-Photon Coupling in Semiconductor Nanocrystals. *Nano Lett.* **10**, 274-278 (2009).

24. Mertens, H., Biteen, J. S., Atwater, H. A., & Polman, A. Polarization-Selective Plasmon-Enhanced Silicon Quantum-Dot Luminescence. *Nano Lett.* **6**, 2622-2625 (2006).

25. Chen, Y., Munechika, K., Plante, I. J.-L., Munro, A. M., Skrabalak, S. E., Xia, Y., & Ginger, D. S. Excitation enhancement of CdSe quantum dots by single metal nanoparticles. *Appl. Phys. Lett.* **93**, 053106-053103 (2008).

26. Shimizu, K. T., Woo, W. K., Fisher, B. R., Eisler, H. J., & Bawendi, M. G. Surface-Enhanced Emission from Single Semiconductor Nanocrystals. *Phys. Rev. Lett.* **89**, 117401 (2002).

27. Lee, J., Hernandez, P., Lee, J., Govorov, A. O., & Kotov, N. A. Exciton-plasmon interactions in molecular spring assemblies of nanowires and wavelength-based protein detection. *Nat. Mater.* **6**, 291-295 (2007).

28. Ray, K., Badugu, R., & Lakowicz, J. R. Metal-Enhanced Fluorescence from CdTe Nanocrystals: A Single-Molecule Fluorescence Study. *J. Am. Chem. Soc.* **128**, 8998-8999 (2006).

29. Lee, J., Govorov, A. O., Dulka, J., & Kotov, N. A. Bioconjugates of CdTe Nanowires and Au Nanoparticles: Plasmon-Exciton Interactions, Luminescence Enhancement, and Collective Effects. *Nano Lett.* **4**, 2323-2330 (2004).

30. Curto, A. G., Volpe, G., Taminiau, T. H., Kreuzer, M. P., Quidant, R., & van Hulst, N. F. Unidirectional Emission of a Quantum Dot Coupled to a Nanoantenna. *Science* **329**, 930-933 (2010).

31. Munechika, K., Chen, Y., Tillack, A. F., Kulkarni, A. P., Plante, I. J.-L., Munro, A. M., & Ginger, D. S. Spectral Control of Plasmonic Emission Enhancement from Quantum Dots near Single Silver Nanoprisms. *Nano Lett.* (2010).

32. Vasa, P., Pomraenke, R., Schwieger, S., Mazur, Y. I., Kunets, V., Srinivasan, P., Johnson, E., Kihm, J. E., Kim, D. S., Runge, E., Salamo, G., & Lienau, C. Coherent Exciton-Surface-Plasmon-Polariton Interaction in Hybrid Metal-Semiconductor Nanostructures. *Phys. Rev. Lett.* **101**, 116801 (2008).

33. Waldeck, D. H., Alivisatos, A. P., & Harris, C. B. Nonradiative damping of molecular electronic excited states by metal surfaces. *Surf. Sci.* **158**, 103-125 (1985).

34. Neretina, S., Qian, W., Dreaden, E., El-Sayed, M. A., Hughes, R. A., Preston, J. S., & Mascher, P. Plasmon Field Effects on the Nonradiative Relaxation of Hot Electrons in an Electronically Quantized System: CdTe-Au Core-Shell Nanowires. *Nano Lett.* **8**, 2410-2418 (2008).

35. Neretina, S., Qian, W., Dreaden, E. C., El-Sayed, M. A., Hughes, R. A., Preston, J. S., & Mascher, P. Exciton Lifetime Tuning by Changing the Plasmon Field Orientation with Respect to the Exciton Transition Moment Direction: CdTe-Au Core-Shell Nanorods. *Nano Lett.* **9**, 1242-1248 (2009).

36. Neretina, S., Dreaden, E. C., Qian, W., El-Sayed, M. A., Hughes, R. A., Preston, J. S., & Mascher, P. The Dependence of the Plasmon Field Induced Nonradiative Electronic Relaxation Mechanisms on the Gold Shell Thickness in Vertically Aligned CdTe-Au Core-Shell Nanorods. *Nano Lett.* **9**, 3772-3779 (2009).

37. Neretina, S., & et al. Vertically aligned wurtzite CdTe nanowires derived from a catalytically driven growth mode. *Nanotechnol.* **18**, 275301 (2007).

38. Neretina, S., & et al. The role of substrate surface alteration in the fabrication of vertically aligned CdTe nanowires. *Nanotechnol.* **19**, 185601 (2008).

39. Yang, W. H., Schatz, G. C., & Vanduyne, R. P. Discrete Dipole Approximation for Calculating Extinction and Raman Intensities for Small Particles with Arbitrary Shapes. *J. Chem. Phys.* **103**, 869-875 (1995).

40. Portales, H., Pinna, N., & Pileni, M.-P. Optical Response of Ultrafine Spherical Silver Nanoparticles Arranged in Hexagonal Planar Arrays Studied by the DDA Method. *J. Phys. Chem. A* **113**, 4094-4099 (2009).

41. DDSCAT 6.1 (Scripps Institute of Oceanography, University of California, San Diego, CA, 2005).

42. Johnson, P. B., & Christy, R. W. Optical Constants of the Noble Metals. *Phys. Rev. B: Condens. Matter* **6**, 4370 (1972).

43. Palik, E. D. Vol. 1 (Academic Press, New York, 1998).

44. Bohren, C. F., & Huffman, D. R. *Absorption and Scattering of Light by Small Particles*. (Wiley–Interscience, 1983).

45. Draine, B. T. The Discrete-Dipole Approximation and Its Application to Interstellar Graphite Grains. *Astrophys. J.* **333**, 848-872 (1988).

46. Dreaden, E. C., Neretina, S., Qian, W., El-Sayed, M. A., Hughes, R. A., Preston, J. S., & Mascher, P. Plasmonic Enhancement of Nonradiative Charge Carrier Relaxation and

Proposed Effects from Enhanced Radiative Electronic Processes in Semiconductor–Gold Core–Shell Nanorod Arrays. *J. Phys. Chem. C* **115**, 5578-5583 (2011).

47. Oldenburg, S. J., Averitt, R. D., Westcott, S. L., & Halas, N. J. Nanoengineering of optical resonances. *Chem. Phys. Lett.* **288**, 243-247 (1998).

48. Klimov, V. I., & McBranch, D. W. Femtosecond 1P-to- 1S Electron Relaxation in Strongly Confined Semiconductor Nanocrystals. *Phys. Rev. Lett.* **80**, 4028 (1998).

49. Klimov, V. I., Mikhailovsky, A. A., McBranch, D. W., Leatherdale, C. A., & Bawendi, M. G. Quantization of multiparticle Auger rates in semiconductor quantum dots. *Science* **287**, 1011-1013 (2000).

50. Link, S., Burda, C., Mohamed, M. B., Nikoobakht, B., & El-Sayed, M. A. Femtosecond transient-absorption dynamics of colloidal gold nanorods: Shape independence of the electron-phonon relaxation time. *Phys. Rev. B: Condens. Matter* **61**, 6086-6090 (2000).

51. Klimov, V. I., Mikhailovsky, A. A., Xu, S., Malko, A., Hollingsworth, J. A., Leatherdale, C. A., Eisler, H. J., & Bawendi, M. G. Optical Gain and Stimulated Emission in Nanocrystal Quantum Dots. *Science* **290**, 314-317 (2000).

52. Neretina, S., Qian, W., Dreaden, E. C., El-Sayed, M. A., Hughes, R. A., Preston, J. S., & Mascher, P. Plasmon Field Effects on the Nonradiative Relaxation of Hot Electrons in an Electronically Quantized System: CdTe-Au Core-Shell Nanowires. *Nano Lett.* **8**, 2410-2418 (2008).

CHAPTER 7

PLASMON HYBRIDIZATION IN SURFACE ENHANCED RAMAN SCATTERING

7.1 Raman Spectroscopy and Electromagnetic Contributions to Surface Enhanced Raman Scattering

Since its first observation in the mid-1970's,[*1-3*] significant progress in the fundamental understanding of processes associated with surface-enhanced Raman scattering (SERS) – namely, electromagnetic[*3-8*] (EM) and chemical[*2,9-12*] enhancement – has been achieved. Although only one in 10^6 photons incident upon a sample typically are Raman scattered,[*13*] proximity to a nanostructured metal surface has been shown increase Raman signal intensity by factors as much as 10^6 to 10^{14}.[*14-19*] EM enhancements arise in nanostructured metals, noble metals in particular, due to their large surface-to-volume ratio. While noble metals support bulk plasmons which oscillate at mid- to far- UV wavelengths, their surface plasmons do so at near-UV, visible, and near-IR wavelengths, resonantly coupling with light in the energetic range of commonly used laser excitation sources and their Raman scattered photons. Resonant excitation of surface plasmons (absorption) serves to focus and confine photons at sub-diffraction limited volumes, resulting in highly intense local electric fields which amplify both the incident and Raman-scattered photons (i.e. $|E|^2 \times |E|^2$). Electric field enhancements ($|E|^4$) can be as high as 10^5 at the surfaces of single nanoparticles[*20*] and as high as 10^{10} to 10^{14} in nanoparticle dimers,[*21*] arrays,[*22*] and aggregates.[*23*] EM enhancement by such multiparticle systems has allowed for the sensitive detection of SERS from single-molecules.[*15,17,24-27*] Surface plasmon resonance has also been shown to enhance

spectroscopically relevant non-linear optical processes such as second-harmonic generation,[*28-30*] hyper-Rayleigh scattering,[*31-34*] and hyper-Raman scattering.[*35*]

7.2 Hot Spots, Plasmon Resonance, and Symmetry

Coupled nanoparticles (e.g. dimers, arrays, and aggregates) supporting optical surface plasmons have been shown to generate highly intense local electric fields at their junctions – so called "hot spots"[*15,17,25,26*] – which allow the small fraction of molecules therein to contribute to the majority of the observed SERS signal.[*23*] Recently, plasmonic nanoparticles of triangular geometry[*36-38*] have been shown to generate large EM fields due to their sharp surface features and associated "lightning rod" effect.[*39,40*] Accordingly, coupled triangular nanoprisms,[*41,42*] or bowtie antennas,[*43-46*] have been shown by Van Duyne and Moerner to generate tremendous EM enhancement at their junctions due to near-field coupling between surface plasmon modes of the same parity (i.e. mode, order, symmetry, angular momentum, ℓ) on adjacent nanoprisms.

Studies of EM SERS enhancement, in particular, have spurred great interest in the plasmonic properties of nanoscale materials and the coupling interactions of their near-fields. Advances in lithographic,[*36,44,46,47*] spectroscopic,[*48-51*] computational,[*21,38,52-54*] and synthetic[*55-57*] methods have improved our fundamental understanding of how near-fields of surface plasmon modes can couple and enhance one another with decreasing distance. Schatz, Halas, and Nordlander have contributed greatly to our understanding of these processes, illustrating the complex, distance-dependent relationships between surface plasmon resonance mode, frequency, coupling strength, and field localization/intensity.[*21,50,52*] More recently, "forbidden" ($\Delta\ell>0$) coupling between surface plasmon modes of dissimilar order has been shown theoretically and experimentally to increase at small interparticle distances due to reduced symmetry.[*50,52,53,58-60*] This broken symmetry allows so-called "dark" plasmons – modes which lack a net moment in the

isolated (primitive) particle – to become optically excitable. More importantly, symmetry reduction also creates admixtures of these primitive plasmon modes, rendering them dipole-active. Because EM SERS enhancements are most often greatest at short interparticle distances, multimodal plasmon coupling interactions become increasingly important in interpreting observed Raman enhancements from multiparticle assemblies, particularly at the single-molecule level.

7.3 Design and Fabrication of Nanoparticle Arrays to Study Distance-Dependent Multipolar Plasmon Coupling

The work herein investigates the effect of reduced symmetry and multimodal plasmon coupling on SERS enhancements from Au nanoprism pair arrays separated at varying distances. We show that at short interparticle distances, intraparticle coupling of the primitive dipole plasmon modes with primitive higher order plasmon modes can increase SERS intensity by imparting dipolar character to the latter. Gold nanoprism pair arrays were fabricated by electron-beam lithography and distance-dependent SERS enhancement of substrate phonon vibrations excited in the vicinity of the prism pair's primitive quadrupolar surface plasmon resonance was investigated. In contrast to that expected for single-mode coupling interactions alone, we found that SERS intensity increased significantly when the particles approached one another. Theoretical modeling found this effect to result from a further reduction in symmetry and increased dipolar character of the plasmon resonance at the Raman excitation/scattering wavelength. These results reiterate the importance of considering changes in both plasmon field intensity *and* mode in the interpretation of Raman enhancement from multiparticle assemblies and roughened surfaces, particularly at the single-molecule level.

Au nanoprism arrays were fabricated using a JEOL JBX-9300FS 100 kV electron beam lithography (EBL) system. Silicon nitride substrates were pre-fabricated as described elsewhere.[*61*] Briefly, a layer of Si_3N_4 was deposited onto a prime grade double-side polished silicon wafer, followed

by selective etching of the Si wafer to produce an array of freely supported silicon nitride membrane windows ca. 150 x 150 μm^2 in area. Each window was covered in its entirety by a single 200 x 200 μm^2 design pattern comprising several thousand particle pairs spaced >800 nm from one another to reduce far-field coupling. Tip-to-tip separation of the nanoprism pairs was varied from 9-220 nm. The Si_3N_4 membrane was spin-coated with an 80 nm poly methyl methacrylate (PMMA) resist and patterned with electron beam doses 2500-3500 $\mu C/cm^2$ with a 2 nA beam current. Following exposure, the wafer was developed in a solution of isopropyl alcohol and methyl isobutyl ketone (3:1, IPA:MIBK) for 10 sec, rinsed in IPA for >60 sec, and dried in N_2. A CVC electron beam evaporator was then used to deposit a 0.5 nm Cr adhesion layer (0.1 Å/sec), followed by 19 nm of Au (0.5 Å/sec). After deposition, the remaining PMMA was removed by imersion in 1165 remover (MicroChem), leaving the gold nanoprism arrays. Samples were imaged by scanning electron microscopy (SEM, Zeiss Ultra 60 FE-SEM) at 10 kV accelerating voltage using a secondary electron detector. Topographical analyses of the deposits were performed using a Dimension 3000 (Digital Instruments) atomic force microscope in tapping mode. All nanoprism arrays were deposited on the same Si_3N_4 membrane array.

Electric field distribution, particle polarization, and optical spectra were calculated by the Discrete Dipole Approximation (DDA), a finite-element computational method used to model the electromagnetic properties of sub-wavelength particles. DDA approximates a nanoparticle as a 3-dimensional array of points in a cubic lattice which acquire dipole moments upon excitation by an incident electromagnetic field. Each dipole possesses a unique position in the array, a volume, and a complex dielectric function for the material and its surroundings. DDA has been used to model the electromagnetic responses of plamonic nanoparticles with high precision for more than a decade.[*38,54,62-66*]

Optical spectra (extinction, absorption, and scattering) were calculated using DDSCAT 6.1.[*67-71*] Electric field enhancement and particle polarization plots were calculated using Fortran codes of the program modified by G.C. Schatz (Northwestern University). All calculations were performed for triangular plates 18 nm in height with 59 nm base length and 70 nm bisector length (ca. 3.7×10^4 dipoles per particle) for incident field polarization parallel with the prism's bisector. Particle pairs were coupled coplanar with tip-to-tip orientation. Electric field and polarization plots were taken in the plane of the particle's center of mass. Complex dielectric functions for Au [*72*] and the Si_3N_4 [*73*] support were applied using effective medium theory.[*47,74-76*] Note that herein we model the optical response of nanoparticle pairs down to 9 nm edge-to-edge separation and therefore neglect quantum mechanical contributions which impart a spatially non-local dielectric function at gaps ca. 2 nm and below.[*77-79*]

Dipole-dipole coupling of prism pairs was approximated using a derivation[*49*] of the quasistatic interaction of coupled dipoles model by Kreibig and Volmer [*80,81*] where Claussius-Missoti dipole polarizabilities, near-linearity of the Au dielectric function over the wavelength shift region, effective medium,[*47,74-76*] and "head-to-tail" orientation of dipoles is assumed. The function was solved by deriving the prism shape factor (γ) which is equal to the negative of the ratio of the metal:medium dielectric functions at the dipolar surface plasmon resonance wavelength. Volume polarizability (Λ=6) was adjusted until reasonable fit was observed. In agreement with previous reports of shape factors derived for colloidal Ag prismsatic plates,[*82*] the shape factor (γ) for this prism was found to be 12.5 (or L=0.0739). The sensitivity factor (S), which describes the change in a particle's surface plasmon resonance wavelength as a function of its medium's refractive index ($\partial\lambda/\partial$RIU), was found to be 209 nm/RIU, remarkably, within 2% of that experimentally determined by Mirkin, Schatz, and Van Duyne (205 nm/RIU, **Figure 7.1**).[*83*]

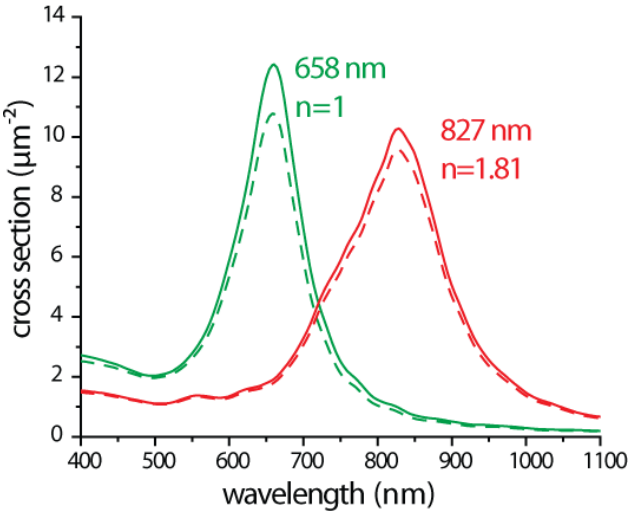

Figure 7.1. Calculated change in Au nanoparism extinction (solid) and absorption (dashed) cross section in varying medium refractive index. Adapted from Dreaden et al. [*84*].

Steady-state optical extinction spectra were obtained using a SEE110 microspectrometer fitted with a pinhole aperture, fiber optic-coupled CCD array detector, 20× objective (ca. 64 μm^2 detection area), and tungsten lamp. Spectra were averaged over 500 scans to minimize noise. The incident beam propagated perpendicular to the plane of the nanoparism array was polarized parallel to their interparticle axis.

Raman spectroscopy was performed using a JOBIN YVON Ramanor HG2S spectrometer equipped with a μ-Raman attachment and argon ion laser excitation (514.5 nm, 390 s int, 10 accum, 14 mW input). Stokes-shifted spectra were collected in a backscattering configuration. The incident beam propagated perpendicular to the plane of the nanoprism array and was polarized parallel to the interparticle axis.

7.4 Contributions from Plasmon Hybridization to Off-Resonance SERS in Nanoparticle Assemblies

Figure 7.2A,B illustrate SEM images of the fabricated Au nanoprism pair arrays showing well-defined shape and homogenous separation. The nanoprisms were found by scanning electron

microscopy (SEM) and atomic force microscopy (AFM) to be 19±1 nm in height with a 59±4 nm base length and 70±5 nm bisector length. Optical extinction spectra of the arrays (**Figure 7.2C**) exhibit spectral red-shift in surface plasmon resonance when polarized along the interparticle axis of the prisms, a characteristic indicative of near-field plasmon coupling.[*21,42 ,50-53,85*] Computational electromagnetics calculations (**Figure 7.2D**) show excellent agreement with experimental results (**Figure 7.3**).

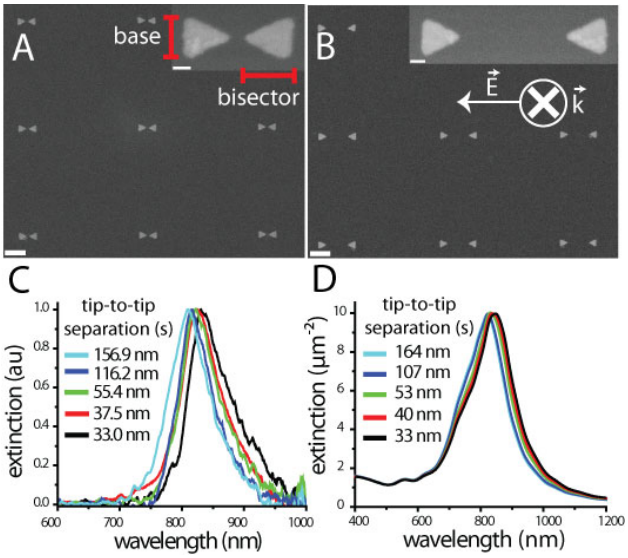

Figure 7.2. SEM images of Au nanoprism pair arrays fabricated by electron beam lithography (EBL) with (A) 28.9 nm and (B) 219.6 nm tip-to-tip separation. C) Selected experimental and (D) calculated polarized optical extinction spectra of Au nanoprism pairs illustrating spectral red-shift from distance-dependent plasmon coupling. Scale bars in (A,B) and their insets represent 200 nm and 30 nm, respectively. The incident field in (C) and (D) propagate into the plane of the prism pairs and is polarized along their interparticle axis. Adapted from Dreaden et al. [*84*].

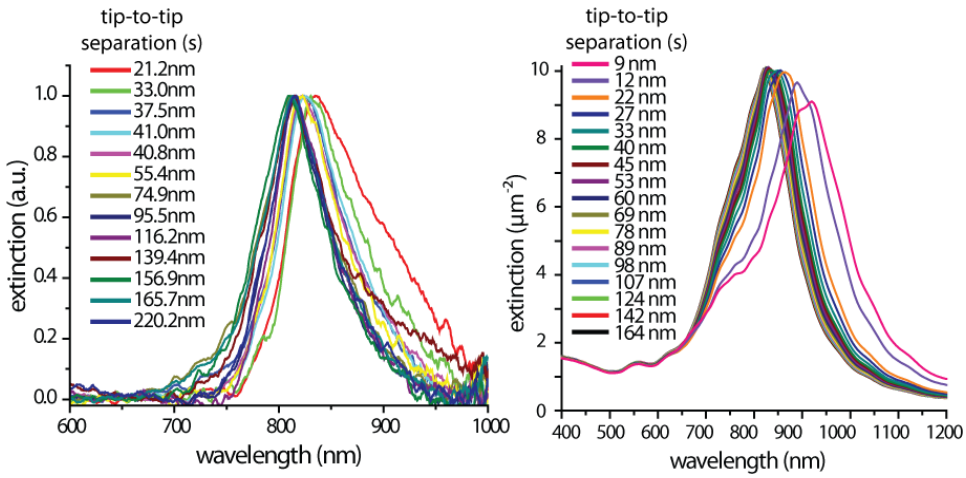

Figure 7.3. Normalized observed (left) and calculated (right) extinction spectra of Au nanoprism pairs oriented tip-to-tip at and polarized along the interparticle axis at varying separation distances. Experimental spectra required normalization due to signal intensity fluctuations. Observed prisms are 19±1 nm in height with 59±4 nm base length and 70±5 nm bisector length. Calculations were performed for prisms 18 nm in height with 59 nm base length and 70 nm in bisector length. Adapted from Dreaden et al. [*84*].

Calculations of the electric field distribution, induced polarization, and near-field coupling were performed to correlate the SERS responses from the Au nanoprism pair arrays with changes in their respective plasmon modes and field enhancements as a function of distance. **Figure 7.4** illustrates wavelength-dependent electric field intensity distributions (top panel) and induced particle polarizations (bottom panel) for a single (i.e. unpaired) Au nanoprism polarized along its bisector (see **Figure 7.2A inset**). The strong extinction band observed at 827 nm in **Figure 7.2C,D and Figure 7.3** is attributed to the dipolar surface plasmon resonance (**Figure 7.4**). Consistent with reports by Schatz and coworkers,[*21,38*] this resonant mode exhibits maximum field intensity at the prism tips with opposing poles observed along the bisector at the particle-medium interface. The weak, blue-shifted band at 558 nm is assigned to the quadrupolar surface plasmon mode of the prism. In contrast to the dipolar mode, this resonance exhibits maximum field intensity along its sides with like poles observed both along the bisector and its orthogonal axis (**Figure 7.4**).[*21,38*] The peak shoulders at 623 and 514.5 nm exhibit mixed modes of surface plasmon resonance with field

intensity and polarization distributions characteristic of admixtures of dipolar and quadrupolar modes. In both cases, field intensity is neither fully localized at the prism tips, nor its sides. Particle polarization at both wavelengths (623 and 514.5 nm) appears as the superposition of those observed in the dipolar and quadrupolar modes with the shoulder at 623 nm exhibiting a stronger dipolar contribution (**Figure 7.5**). Note that the aforementioned conclusions are true only for incident polarization along the prism bisectior; orthogonal polarization has been discussed in detail elsewhere.[*86*]

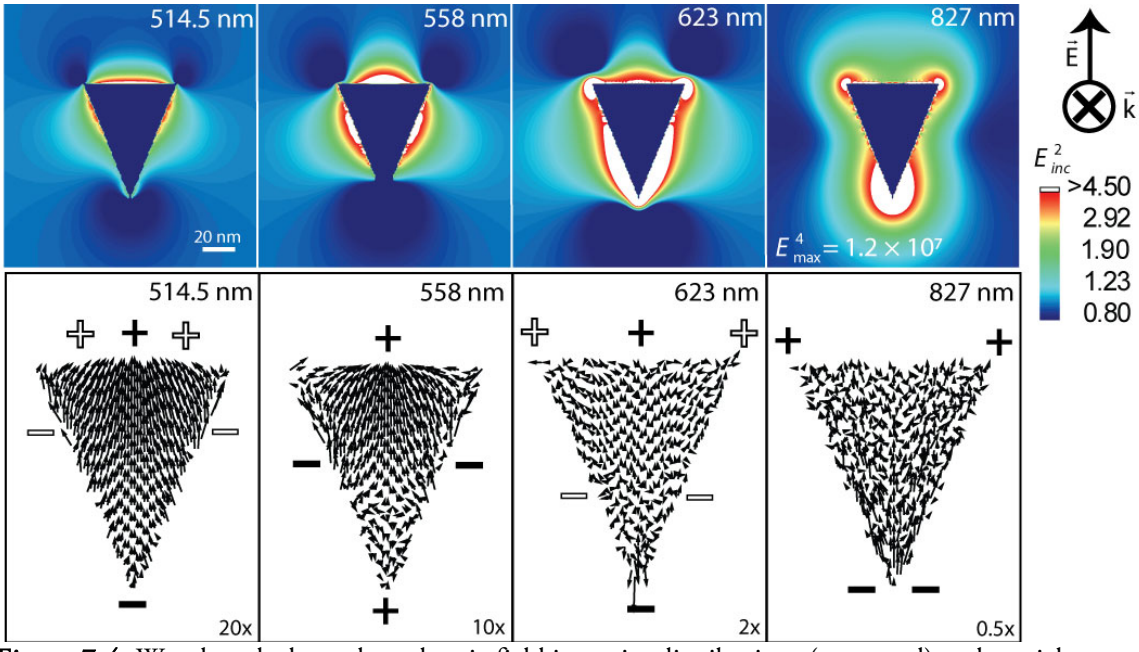

Figure 7.4. Wavelength-dependent electric field intensity distributions (top panel) and particle polarization plots (bottom panel) for a single, unpaired, Au nanoprism. Dipolar and quadrupolar surface plasmon modes correspond to 827 and 558 nm, respectively, with mixed modes at 623 and 514.5 nm. Wavelengths, incident field polarization, and color intensity scale are as indicated. Solid and open poles indicate strong and weak directionality, respectively, and have been qualitatively added to facilitate interpretation. Maximum color intensity of the 827 nm dipole resonance is scaled to 10% and magnitudes of the displacement vectors are scaled as indicated to aid in comparison. Asymmetry in some particle polarization plots is due to a random 75% reduction in illustrated dipole density. Adapted from Dreaden et al. [*84*].

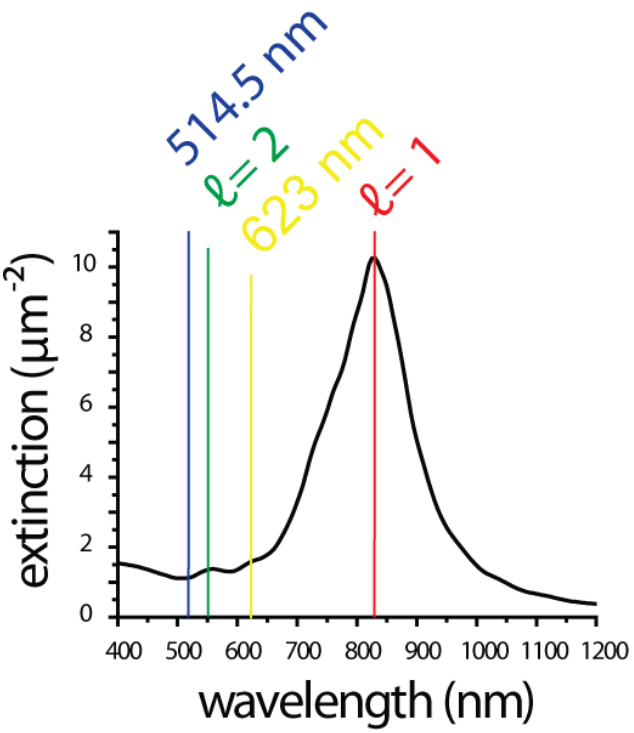

Figure 7.5. Calculated extinction spectrum of a single Au nanoprism with peak assignments and wavelengths of interest noted. The dipolar surface plasmon resonance (red, ℓ=1), quadrupolar surface plasmon resonance (green, ℓ=2), 623 nm shoulder resonance (yellow), and shoulder resonance at the 514.4 nm SERS excitation wavelength (blue) are illustrated for a prism 18 nm in height with 59 nm base length and 70 nm bisector length. Adapted from Dreaden et al. [*84*].

Having determined the surface plasmon contributions at our Raman excitation wavelength (514.5 nm) for single Au nanoprism particles, we now consider distance-dependent electromagnetic properties of pairs coupled tip-to-tip. As can be seen in **Figure 7.2C,D and Figure 7.3**, the polarized dipolar surface plasmon resonance of individual Au nanoprisms (ca. 827 nm) red-shifts considerably as their near-fields couple with decreasing distance. Fractional wavelength shifts observed from this mode (**Figure 7.6**), show excellent agreement with both computational and classical electromagnetic calculations for dipole-dipole coupling (i.e. 1/distance^3 dependence as $1/d^{\ell+\ell'+1}$ for ℓ=1 for dipoles and ℓ=2 for quadrupoles, etc.). Moreover, we note a significant increase in peak broadening and asymmetry, as well as a decrease peak intensity, of the coupled dipolar mode as the prisms approach (**Figure 7.3**). These effects indicate redistribution of the primitive dipolar

plasmon's oscillator strength by coupling to higher order plasmon modes on the adjacent prism as symmetry is reduced with distance.[*87*] In agreement with the plasmon hybridization model, a small increase in oscillator strength of the quadrupolar surface plasmon resonance at 558 nm is indeed observed (**Figure 7.7**).

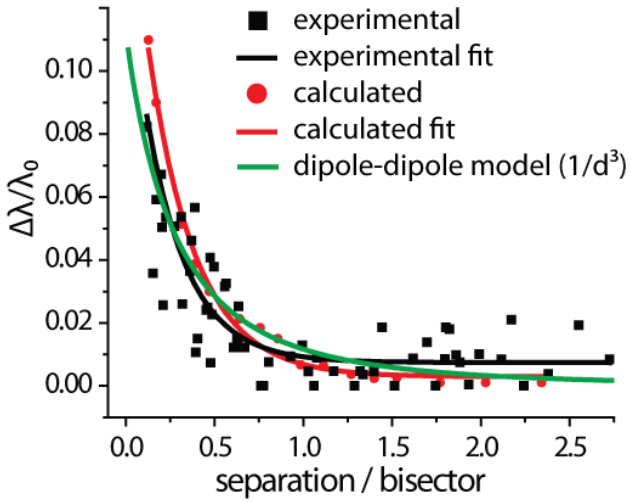

Figure 7.6. Experimental and calculated fractional wavelength shift of the dipolar surface plasmon resonance mode of Au nanoprism pairs oriented tip-to-tip as a function of separation:bisector ratio indicating strong near-field coupling characteristic of dipole-dipole interactions. Au nanoprism pairs are polarized along their interparticle axis. Adapted from Dreaden et al. [*84*].

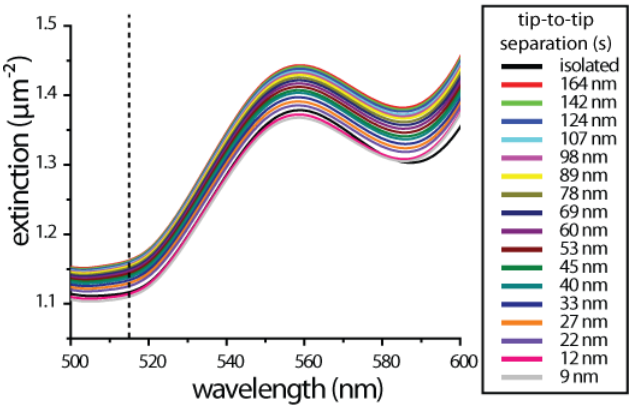

Figure 7.7. Calculated extinction spectrum of Au nanoprism pairs oriented tip-to-tip at varying separation distances in the region of 514.5 nm SERS excitation (dotted black line). Each prism is 18 nm in height with 59 nm base length and 70 nm in bisector length. Adapted from Dreaden et al. [*84*].

As discussed previously,[*50,52,53,58-60*] coupling interactions between surface plasmon modes of unequal parity become allowed at short distances due to reduced symmetry, increasing the relative dipolar character of higher order plasmon modes. Calculations presented in **Figure 7.8** further support this behavior in the Au nanoprism pairs. Change (%) in field intensity distribution at the Raman excitation wavelength was plotted for a fixed Au nanoprism as another prism interacts with it from 164 nm to 9 nm tip-to-tip separation. Redistribution of the electric field intensity clearly shows increased dipolar character and further indicates mixing of the adjacent particle's primitive dipolar plasmon mode with that of the resonance at 514.5 nm. This mixing reflects a further reduction in symmetry of the charge distribution about the prism due to field perturbation by adjacent particle. Because of this, the plasmon mode at the Raman scattering wavelength becomes increasingly dipole-active as the prisms approach, increasing their ability to enhance the incident and Raman scattered photons.

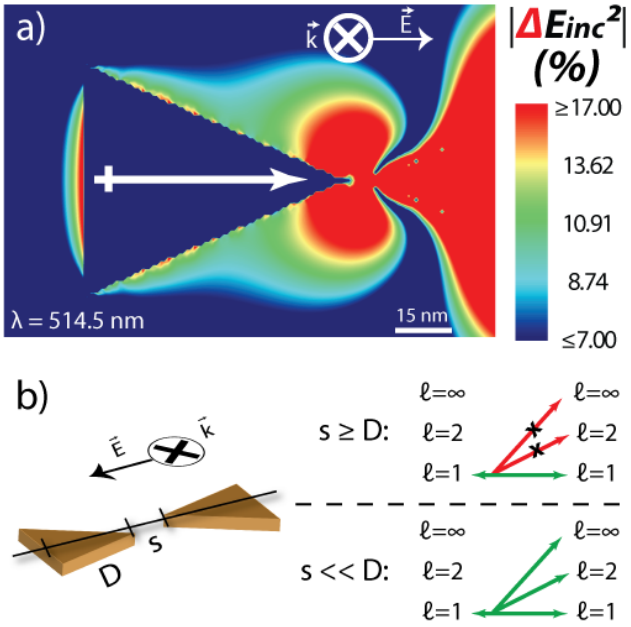

Figure 7.8. A) Calculated percent change in electric field intensity distribution for a fixed Au nanoprism (λ=514.5 nm) as another approaches from 164 to 9 nm tip-to-tip separation. B) Increased dipolar (ℓ =1) character at small distances indicates mixing of the prism's 514.5 nm mode with the primitive dipolar surface plasmon mode of the adjacent particle due to reduced symmetry and allows for increased coupling to the incident and Raman scattered photons. Wavelength, incident field polarization, and color intensity scale are as indicated. Adapted from Dreaden et al. [*84*].

Distance-dependent EM enhancement was further examined and is shown in **Figure 7.9,10**. Maximum and integrated SERS enhancement $|E|^4$ was calculated for Au nanoprism pairs at the 514.5 nm Raman scattering wavelength and at their coupled dipolar surface plasmon mode as a function of distance (**Figure 7.10**). It assumed here that field enhancement at the incident and Stokes-shifted wavelengths are effectively equivalent. Almost no change in the maximum and integrated $|E|^4$ is observed at our Raman scattering wavelength, while that of the coupled dipolar mode noticeably increases with decreasing distance.[*46*] This data indicates that distance-dependent EM SERS enhancement can occur only as a result of dipolar redistribution of plasmon field intensity.

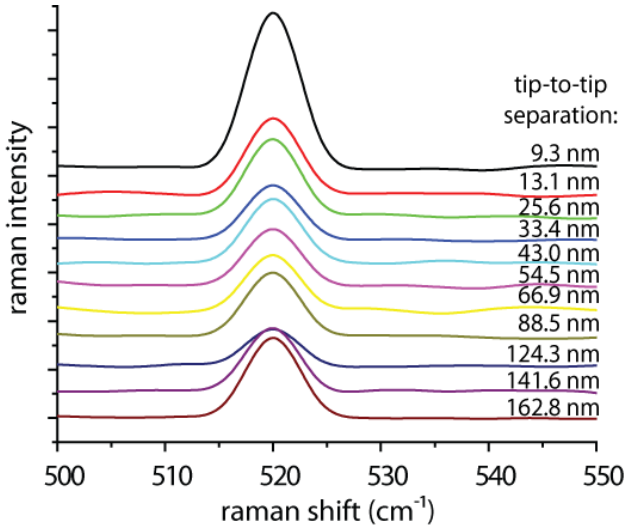

Figure 7.9. Raman spectrum of the first-order optical phonon resonance of silicon (520 cm^{-1}) at varying Au nanoprism pair separations. The incident field (λ_{ex}=514.5 nm) was polarized along the interparticle axis. Adapted from Dreaden et al. [*84*].

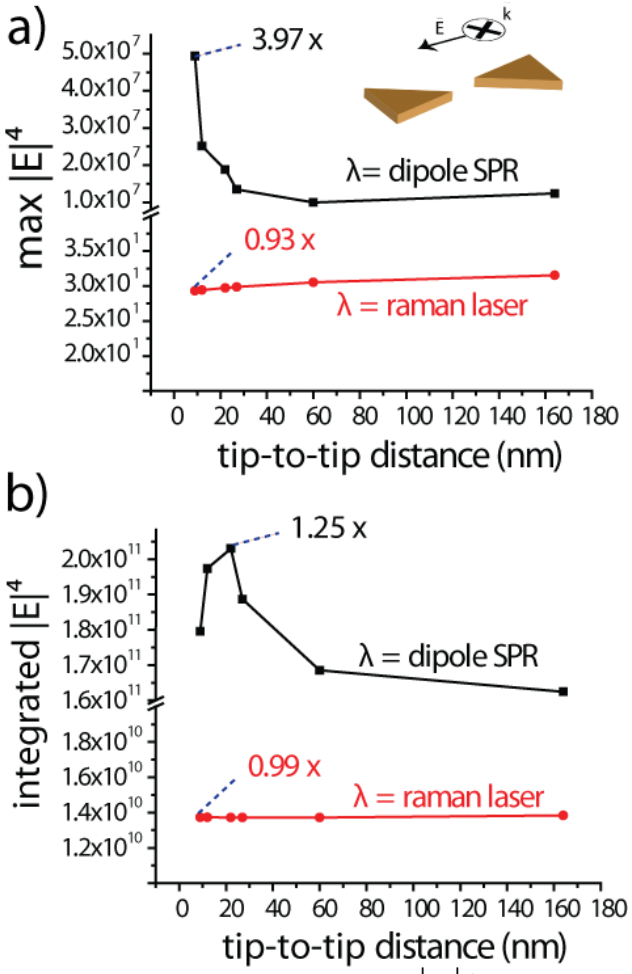

Figure 7.10. A) Calculated maximum SERS enhancement $|E|^4$ and (B) integrated $|E|^4$ of the dipolar surface plasmon modes and that at the 514.5 nm Raman laser wavelength as a function of Au nanoprism separation for interparticle coupling interactions alone. Note the sensitivity to distance by the dipolar mode and lack thereof by the mode at the 514.5 nm Raman scattering wavelength. Maximum $|E|^4$ was observed at the central plane bisecting the Au nanoprism pairs and integrated $|E|^4$ was taken across a 0.12 $\mu m^2 \times 0.001$ μm plane bisecting the prism pair. Adapted from Dreaden et al. [*84*].

Results from finite-element calculations can be summarized as such: i) distance-dependent redistribution of the primitive dipole plasmon's oscillator strength to higher order plasmon modes (specifically to that at the Raman excitation wavelength) was observed; ii) net electric field intensity at the Raman excitation wavelength was found to be insensitive to interparticle distance; iii) dipolar redistribution of the electric field intensity at the Raman excitation wavelength was found at short

interparticle distances. Based on these results, we expect distance-dependent optical coupling and polarized SERS enhancement to occur only at short interparticle distances.

Raman spectroscopy is often used in microelectronics processing to characterize semiconductor materials and their associated electronics states, phonon interactions, charge carriers, purity, crystal structure, etc.[*88-91*] The first order (q=0) optical phonon resonance of silicon[*92*] (520 cm^{-1}) is particularly useful and can be used to probe stress/strain,[*89,93,94*] temperature,[*95,96*] crystallinity,[*90*] and charge carrier concentrations,[*97*] in silicon chip devices. Enhancement of the first-order optical phonon resonance of silicon (520 cm^{-1}), commonly observed in Si_3N_4 thin films,[*98-100*] was probed by polarized Raman spectroscopy (λ_{ex}=514.5 nm). **Figure 7.11** compares observed and calculated enhancement of integrated Raman intensity at decreasing Au nanoprism distances. Although EM calculations predict negligible distance-dependent changes in $|E|^4$, SERS enhancement is indeed observed as Au nanoprism pairs approach. Moreover, the observed enhancement is found to occur with a distance-dependence similar with that predicted for dipole-dipole interactions. Note that these factors do not reflect so called "SERS enhancement factors" as considerable signal amplification can be expected from unpaired Au nanoprisms as well.

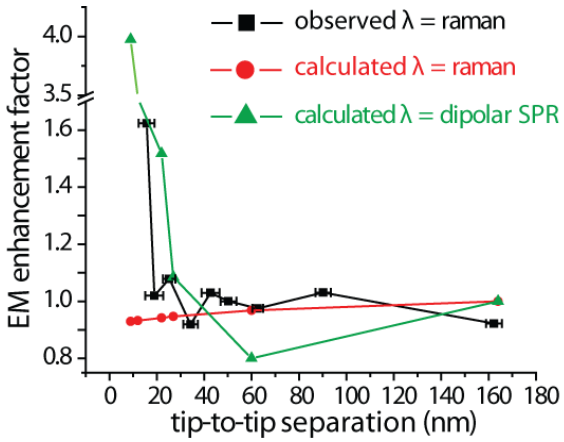

Figure 7.11. Observed distance-dependent enhancement of polarized Raman scattering intensity (520 cm^{-1}) for the Au nanoprism array (black squares) and that calculated based on maximum field intensity alone (red circles). Distance-dependent enhancement calculated for dipole-dipole coupling between Au nanoprism pairs is shown for reference. Calculated enhancement is reported as fractional $|E|^4$ relative to 164 nm separation, as shown in Figure 4, left panel. Error bars represent standard deviation. Adapted from Dreaden et al. [*84*].

7.5 Outlook and Conclusions

In conclusion, we have studied distance-dependent SERS enhancement from electron-beam fabricated Au nanoprism pair arrays in the vicinity of their quadrupolar surface plasmon resonance. In agreement with the results of Halas and Nordlander, we find that at short interparticle distances, reduced symmetry and associated mixed-mode plasmon coupling results in increased dipolar character of the plasmon mode resonant with our Raman excitation. Theoretical modeling finds that this increased dipolar character does not result in increased field intensity, but instead, dipolar spatial redistribution of the field. As a result, we observed enhanced optical coupling and SERS with decreasing distance. These findings show that multimodal surface plasmon interactions can significantly contribute to SERS enhancement from coupled nanoparticle systems and that changes in both field intensity *and* mode should be thoughtfully considered when interpreting contributions to Raman scattering from such systems.

7.6 References

1. Fleischmann, M., Hendra, P. J., & McQuillan, A. J. Raman spectra of pyridine adsorbed at a silver electrode. *Chem. Phys. Lett.* **26**, 163-166 (1974).

2. Albrecht, M. G., & Creighton, J. A. Anomalously intense Raman spectra of pyridine at a silver electrode. *J. Am. Chem. Soc.* **99**, 5215-5217 (1977).

3. Jeanmaire, D. L., & Van Duyne, R. P. Surface raman spectroelectrochemistry: Part I. Heterocyclic, aromatic, and aliphatic amines adsorbed on the anodized silver electrode. *J. Electroanal. Chem.* **84**, 1-20 (1977).

4. Metiu, H., & Das, P. The Electromagnetic Theory of Surface Enhanced Spectroscopy. *Annu. Rev. Phys. Chem.* **35**, 507-536 (1984).

5. Schatz, G. C. Theoretical studies of surface enhanced Raman scattering. *Acc. Chem. Res.* **17**, 370-376 (1984).

6. Kerker, M. Electromagnetic model for surface-enhanced Raman scattering (SERS) on metal colloids. *Acc. Chem. Res.* **17**, 271-277 (1984).

7. Moskovits, M. Surface-enhanced spectroscopy. *Rev. Mod. Phys.* **57**, 783 (1985).

8. Xu, H., Aizpurua, J., Käll, M., & Apell, P. Electromagnetic contributions to single-molecule sensitivity in surface-enhanced Raman scattering. *Phys. Rev. E* **62**, 4318 (2000).

9. Hildebrandt, P., & Stockburger, M. Surface-enhanced resonance Raman spectroscopy of Rhodamine 6G adsorbed on colloidal silver. *J. Phys. Chem.* **88**, 5935-5944 (1984).

10. Zeman, E. J., Carron, K. T., Schatz, G. C., & Van Duyne, R. P. A surface enhanced resonance Raman study of cobalt phthalocyanine on rough Ag films: Theory and experiment. *J. Chem. Phys.* **87**, 4189-4200 (1987).

11. Hill, W., & Wehling, B. Potential- and pH-dependent surface-enhanced Raman scattering of p-mercapto aniline on silver and gold substrates. *J. Phys. Chem.* **97**, 9451-9455 (1993).

12. Osawa, M., Matsuda, N., Yoshii, K., & Uchida, I. Charge transfer resonance Raman process in surface-enhanced Raman scattering from p-aminothiophenol adsorbed on silver: Herzberg-Teller contribution. *J. Phys. Chem.* **98**, 12702-12707 (1994).

13. Harris, D. C., & Bertolucci, M. D. *Symmetry and Spectroscopy*. (Dover, 1978).

14. Caldwell, W. B., Chen, K., Herr, B. R., Mirkin, C. A., Hulteen, J. C., & Van Duyne, R. P. Self-Assembled Monolayers of Ferrocenylazobenzenes on Au(111)/Mica Films: Surface-Enhanced Raman Scattering Response vs Surface Morphology. *Langmuir* **10**, 4109-4115 (1994).

15. Nie, S., & Emory, S. R. Probing Single Molecules and Single Nanoparticles by Surface-Enhanced Raman Scattering. *Science* **275**, 1102-1106 (1997).

16. Campion, A., & Kambhampati, P. Surface-enhanced Raman scattering. *Chem. Soc. Rev.* **27** (1998).

17. Michaels, A. M., Nirmal, M., & Brus, L. E. Surface Enhanced Raman Spectroscopy of Individual Rhodamine 6G Molecules on Large Ag Nanocrystals. *J. Am. Chem. Soc.* **121**, 9932-9939 (1999).

18. Kneipp, K., Moskovits, M., & Kneipp, H. *Surface-Enhanced Raman Scattering: Physics and Applications*. (Springer-Verlang Berlin Heidelberg, 2006).

19. Lombardi, J. R., & Birke, R. L. A Unified View of Surface-Enhanced Raman Scattering. *Acc. Chem. Res.* **42**, 734-742 (2009).

20. Grady, N. K., Halas, N. J., & Nordlander, P. Influence of dielectric function properties on the optical response of plasmon resonant metallic nanoparticles. *Chem. Phys. Lett.* **399**, 167-171 (2004).

21. Hao, E., & Schatz, G. C. Electromagnetic fields around silver nanoparticles and dimers. *J. Chem. Phys.* **120**, 357-366 (2004).

22. Zou, S., & Schatz, G. C. Silver nanoparticle array structures that produce giant enhancements in electromagnetic fields. *Chem. Phys. Lett.* **403**, 62-67 (2005).

23. McMahon, J., Henry, A.-I., Wustholz, K., Natan, M., Freeman, R., Van Duyne, R., & Schatz, G. Gold nanoparticle dimer plasmonics: finite element method calculations of the electromagnetic enhancement to surface-enhanced Raman spectroscopy. *Anal. Bioanal. Chem.* **394**, 1819-1825 (2009).

24. Kneipp, K., Wang, Y., Kneipp, H., Perelman, L. T., Itzkan, I., Dasari, R. R., & Feld, M. S. Single Molecule Detection Using Surface-Enhanced Raman Scattering (SERS). *Phys. Rev. Lett.* **78**, 1667 (1997).

25. Xu, H., Bjerneld, E. J., Käll, M., & Börjesson, L. Spectroscopy of Single Hemoglobin Molecules by Surface Enhanced Raman Scattering. *Phys. Rev. Lett.* **83**, 4357 (1999).

26. Michaels, A. M., Jiang, J., & Brus, L. Ag Nanocrystal Junctions as the Site for Surface-Enhanced Raman Scattering of Single Rhodamine 6G Molecules. *J. Phys. Chem. B* **104**, 11965-11971 (2000).

27. Jiang, J., Bosnick, K., Maillard, M., & Brus, L. Single Molecule Raman Spectroscopy at the Junctions of Large Ag Nanocrystals. *J. Phys. Chem. B* **107**, 9964-9972 (2003).

28. Chen, C. K., de Castro, A. R. B., & Shen, Y. R. Surface-Enhanced Second-Harmonic Generation. *Phys. Rev. Lett.* **46**, 145 (1981).

29. Boyd, G. T., Rasing, T., Leite, J. R. R., & Shen, Y. R. Local-field enhancement on rough surfaces of metals, semimetals, and semiconductors with the use of optical second-harmonic generation. *Phys. Rev. B* **30**, 519 (1984).

30. Antoine, R., Pellarin, M., Palpant, B., Broyer, M., Prevel, B., Galletto, P., Brevet, P. F., & Girault, H. H. Surface plasmon enhanced second harmonic response from gold clusters embedded in an alumina matrix. *J. Appl. Phys.* **84**, 4532-4536 (1998).

31. Galletto, P., Brevet, P. F., Girault, H. H., Antoine, R., & Broyer, M. Enhancement of the Second Harmonic Response by Adsorbates on Gold Colloids: The Effect of Aggregation. *J. Phys. Chem. B* **103**, 8706-8710 (1999).

32. Kim, Y., Johnson, R. C., Li, J., Hupp, J. T., & Schatz, G. C. Synthesis, linear extinction, and preliminary resonant hyper-Rayleigh scattering studies of gold-core/silver-shell nanoparticles: comparisons of theory and experiment. *Chem. Phys. Lett.* **352**, 421-428 (2002).

33. Johnson, R. C., Li, J., Hupp, J. T., & Schatz, G. C. Hyper-Rayleigh scattering studies of silver, copper, and platinum nanoparticle suspensions. *Chem. Phys. Lett.* **356**, 534-540 (2002).

34. Hao, E. C., Schatz, G. C., Johnson, R. C., & Hupp, J. T. Hyper-Rayleigh scattering from silver nanoparticles. *J. Chem. Phys.* **117**, 5963-5966 (2002).

35. Yang, W.-H., & Schatz, G. C. Ab initio and semiempirical molecular orbital studies of surface enhanced and bulk hyper-Raman scattering from pyridine. *J. Chem. Phys.* **97**, 3831-3845 (1992).

36. Haes, A. J., & Van Duyne, R. P. A nanoscale optical blosensor: Sensitivity and selectivity of an approach based on the localized surface plasmon resonance spectroscopy of triangular silver nanoparticles. *J. Am. Chem. Soc.* **124**, 10596-10604 (2002).

37. Jin, R. C., Cao, Y. W., Mirkin, C. A., Kelly, K. L., Schatz, G. C., & Zheng, J. G. Photoinduced conversion of silver nanospheres to nanoprisms. *Science* **294**, 1901-1903 (2001).

38. Kelly, K. L., Coronado, E., Zhao, L. L., & Schatz, G. C. The optical properties of metal nanoparticles: The influence of size, shape, and dielectric environment. *J. Phys. Chem. B* **107**, 668-677 (2003).

39. Mohamed, M. B., Volkov, V., Link, S., & El-Sayed, M. A. The 'lightning' gold nanorods: fluorescence enhancement of over a million compared to the gold metal. *Chem. Phys. Lett.* **317**, 517-523 (2000).

40. Liao, P. F., & Wokaun, A. Lightning Rod Effect in Surface Enhanced Raman-Scattering. *J. Chem. Phys.* **76**, 751-752 (1982).

41. Haynes, C. L., & Van Duyne, R. P. Nanosphere lithography: A versatile nanofabrication tool for studies of size-dependent nanoparticle optics. *J. Phys. Chem. B* **105**, 5599-5611 (2001).

42. Haynes, C. L., McFarland, A. D., Zhao, L. L., Van Duyne, R. P., Schatz, G. C., Gunnarsson, L., Prikulis, J., Kasemo, B., & Kall, M. Nanoparticle optics: The importance of radiative dipole coupling in two-dimensional nanoparticle arrays. *J. Phys. Chem. B* **107**, 7337-7342 (2003).

43. Grober, R. D., Schoelkopf, R. J., & Prober, D. E. Optical antenna: Towards a unity efficiency near-field optical probe. *Appl. Phys. Lett.* **70**, 1354-1356 (1997).

44. Fromm, D. P., Sundaramurthy, A., Schuck, P. J., Kino, G., & Moerner, W. E. Gap-Dependent Optical Coupling of Single Bowtie Nanoantennas Resonant in the Visible. *Nano Lett.* **4**, 957-961 (2004).

45. Fromm, D. P., Sundaramurthy, A., Kinkhabwala, A., Schuck, P. J., Kino, G. S., & Moerner, W. E. Exploring the chemical enhancement for surface-enhanced Raman scattering with Au bowtie nanoantennas. *J. Chem. Phys.* **124**, 061101-061104 (2006).

46. Schuck, P. J., Fromm, D. P., Sundaramurthy, A., Kino, G. S., & Moerner, W. E. Improving the Mismatch between Light and Nanoscale Objects with Gold Bowtie Nanoantennas. *Phys. Rev. Lett.* **94**, 017402 (2005).

47. Duval Malinsky, M., Kelly, K. L., Schatz, G. C., & Van Duyne, R. P. Nanosphere Lithography: Effect of Substrate on the Localized Surface Plasmon Resonance Spectrum of Silver Nanoparticles. *J. Phys. Chem. B* **105**, 2343-2350 (2001).

48. Talley, C. E., Jackson, J. B., Oubre, C., Grady, N. K., Hollars, C. W., Lane, S. M., Huser, T. R., Nordlander, P., & Halas, N. J. Surface-Enhanced Raman Scattering from Individual Au Nanoparticles and Nanoparticle Dimer Substrates. *Nano Lett.* **5**, 1569-1574 (2005).

49. Jain, P. K., Huang, W., & El-Sayed, M. A. On the Universal Scaling Behavior of the Distance Decay of Plasmon Coupling in Metal Nanoparticle Pairs: A Plasmon Ruler Equation. *Nano Lett.* **7**, 2080-2088 (2007).

50. Lassiter, J. B., Aizpurua, J., Hernandez, L. I., Brandl, D. W., Romero, I., Lal, S., Hafner, J. H., Nordlander, P., & Halas, N. J. Close Encounters between Two Nanoshells. *Nano Lett.* **8**, 1212-1218 (2008).

51. Jain, P. K., & El-Sayed, M. A. Plasmonic coupling in noble metal nanostructures. *Chem. Phys. Lett.* **487**, 153-164 (2010).

52. Nordlander, P., Oubre, C., Prodan, E., Li, K., & Stockman, M. I. Plasmon Hybridization in Nanoparticle Dimers. *Nano Lett.* **4**, 899-903 (2004).

53. Wang, H., Brandl, D. W., Nordlander, P., & Halas, N. J. Plasmonic nanostructures: Artificial molecules. *Acc. Chem. Res.* **40**, 53-62 (2007).

54. Zhao, J., Pinchuk, A. O., McMahon, J. M., Li, S., Ausman, L. K., Atkinson, A. L., & Schatz, G. C. Methods for Describing the Electromagnetic Properties of Silver and Gold Nanoparticles. *Acc. Chem. Res.* **41**, 1710-1720 (2008).

55. Reinhard, B. r. M., Sheikholeslami, S., Mastroianni, A., Alivisatos, A. P., & Liphardt, J. Use of plasmon coupling to reveal the dynamics of DNA bending and cleavage by single EcoRV restriction enzymes. *Proc. Natl. Acad. Sci. U. S. A* **104**, 2667-2672 (2007).

56. Sonnichsen, C., Reinhard, B. M., Liphardt, J., & Alivisatos, A. P. A molecular ruler based on plasmon coupling of single gold and silver nanoparticles. *Nat. Biotechnol.* **23**, 741-745 (2005).

57. Liu, G. L., Yin, Y., Kunchakarra, S., Mukherjee, B., Gerion, D., Jett, S. D., Bear, D. G., Gray, J. W., Alivisatos, A. P., Lee, L. P., & Chen, F. F. A nanoplasmonic molecular ruler for measuring nuclease activity and DNA footprinting. *Nat Nano* **1**, 47-52 (2006).

58. Wang, H., Wu, Y., Lassiter, B., Nehl, C. L., Hafner, J. H., Nordlander, P., & Halas, N. J. Symmetry breaking in individual plasmonic nanoparticles. *Proc. Natl. Acad. Sci. U. S. A* **103**, 10856-10860 (2006).

59. Wu, Y., & Nordlander, P. Plasmon hybridization in nanoshells with a nonconcentric core. *J. Chem. Phys.* **125**, 124708-124710 (2006).

60. Hao, F., Larsson, E. M., Ali, T. A., Sutherland, D. S., & Nordlander, P. Shedding light on dark plasmons in gold nanorings. *Chem. Phys. Lett.* **458**, 262-266 (2008).

61. Cheng-Tsung, L., Mingxing, W., Nathan, D. J., Kenneth, E. G., Jeanette, M. R., Wang, Y., & Clifford, L. H. (ed Lin Qinghuang) 65191E (SPIE).

62. Yang, W. H., Schatz, G. C., & Vanduyne, R. P. Discrete Dipole Approximation for Calculating Extinction and Raman Intensities for Small Particles with Arbitrary Shapes. *J. Chem. Phys.* **103**, 869-875 (1995).

63. Lee, K.-S., & El-Sayed, M. A. Gold and Silver Nanoparticles in Sensing and Imaging: Sensitivity of Plasmon Response to Size, Shape, and Metal Composition. *J. Phys. Chem. B* **110**, 19220-19225 (2006).

64. Jain, P. K., Lee, K. S., El-Sayed, I. H., & El-Sayed, M. A. Calculated Absorption and Scattering Properties of Gold Nanoparticles of Different Size, Shape, and Composition:â€‰ Applications in Biological Imaging and Biomedicine. *J. Phys. Chem. B* **110**, 7238-7248 (2006).

65. Noguez, C. Surface plasmons on metal nanoparticles: The influence of shape and physical environment. *J. Phys. Chem. C* **111**, 3806-3819 (2007).

66. Portales, H., Pinna, N., & Pileni, M.-P. Optical Response of Ultrafine Spherical Silver Nanoparticles Arranged in Hexagonal Planar Arrays Studied by the DDA Method. *J. Phys. Chem. A* **113**, 4094-4099 (2009).

67. Purcell, E. M., & Pennypacker, C. R. Scattering and Absorption of Light by Nonspherical Dielectric Grains. *Astrophys. J.* **186**, 705-714 (1973).

68. Draine, B. T. The Discrete-Dipole Approximation and Its Application to Interstellar Graphite Grains. *Astrophys. J.* **333**, 848-872 (1988).

69. Draine, B. T., & Goodman, J. Beyond Clausius-Mossotti - Wave-Propagation on a Polarizable Point Lattice and the Discrete Dipole Approximation. *Astrophys. J.* **405**, 685-697 (1993).

70. Draine, B. T., & Flatau, P. J. Discrete-Dipole Approximation for Scattering Calculations. *J. Opt. Soc. Am. A-Opt. Image Sci. Vis.* **11**, 1491-1499 (1994).

71. DDSCAT 6.1 (Scripps Institute of Oceanography, University of California, San Diego, CA, 2005).

72. Johnson, P. B., & Christy, R. W. Optical Constants of the Noble Metals. *Phys. Rev. B* **6**, 4370 (1972).

73. Palik, E. D. *Handbook of optical constants of solids*. Vol. 1 (Academic Press, 1998).

74. Haes, A. J., Zou, S., Schatz, G. C., & Van Duyne, R. P. Nanoscale Optical Biosensor: Short Range Distance Dependence of the Localized Surface Plasmon Resonance of Noble Metal Nanoparticles. *J. Phys. Chem. B* **108**, 6961-6968 (2004).

75. Chan, G. H., Zhao, J., Hicks, E. M., Schatz, G. C., & Van Duyne, R. P. Plasmonic Properties of Copper Nanoparticles Fabricated by Nanosphere Lithography. *Nano Lett.* **7**, 1947-1952 (2007).

76. Chan, G. H., Zhao, J., Schatz, G. C., & Duyne, R. P. V. Localized Surface Plasmon Resonance Spectroscopy of Triangular Aluminum Nanoparticles. *J. Phys. Chem. C* **112**, 13958-13963 (2008).

77. García de Abajo, F. J. Nonlocal Effects in the Plasmons of Strongly Interacting Nanoparticles, Dimers, and Waveguides. *J. Phys. Chem. C* **112**, 17983-17987 (2008).

78. McMahon, J. M., Gray, S. K., & Schatz, G. C. Nonlocal Optical Response of Metal Nanostructures with Arbitrary Shape. *Phys. Rev. Lett.* **103**, 097403 (2009).

79. McMahon, J. M., Gray, S. K., & Schatz, G. C. Optical Properties of Nanowire Dimers with a Spatially Nonlocal Dielectric Function. *Nano Letters*, ASAP (2010).

80. Kreibig, U., & Vollmer, M. *Optical Properties of Metal Clusters*. Vol. 25 (Springer-Verlag, 1995).

81. Gluodenis, M., & Foss, C. A. The Effect of Mutual Orientation on the Spectra of Metal Nanoparticle Rod–Rod and Rod–Sphere Pairs. *J. Phys. Chem. B* **106**, 9484-9489 (2002).

82. Charles, D. E., Aherne, D., Gara, M., Ledwith, D. M., Gun'ko, Y. K., Kelly, J. M., Blau, W. J., & Brennan-Fournet, M. E. Versatile Solution Phase Triangular Silver Nanoplates for Highly Sensitive Plasmon Resonance Sensing. *ACS Nano* **4**, 55-64 (2009).

83. Sherry, L. J., Jin, R. C., Mirkin, C. A., Schatz, G. C., & Van Duyne, R. P. Localized surface plasmon resonance spectroscopy of single silver triangular nanoprisms. *Nano Lett.* **6**, 2060-2065 (2006).

84. Dreaden, E. C., Near, R. D., Abdallah, T., Talaat, M. H., & El-Sayed, M. A. Multimodal plasmon coupling in low symmetry gold nanoparticle pairs detected in surface-enhanced Raman scattering. *Appl. Phys. Lett.* **98**, 183115-183113 (2011).

85. Tabor, C., Murali, R., Mahmoud, M., & El-Sayed, M. A. On the Use of Plasmonic Nanoparticle Pairs As a Plasmon Ruler: The Dependence of the Near-Field Dipole Plasmon Coupling on Nanoparticle Size and Shape. *J. Phys. Chem. A* **113**, 1946-1953 (2009).

86. Shuford, K. L., Ratner, M. A., & Schatz, G. C. Multipolar excitation in triangular nanoprisms. *J. Chem. Phys.* **123**, 114713-114719 (2005).

87. Marhaba, S., Bachelier, G., Bonnet, C., Broyer, M., Cottancin, E., Grillet, N., Lermeì , J., Vialle, J.-L., & Pellarin, M. Surface Plasmon Resonance of Single Gold Nanodimers near the Conductive Contact Limit. *J. Phys. Chem. C* **113**, 4349-4356 (2009).

88. Smith, J. E., Brodsky, M. H., Crowder, B. L., Nathan, M. I., & Pinczuk, A. Raman spectra of amorphous si and related tetrahedrally bonded semiconductors. *Phys. Rev. Lett.* **26**, 642-& (1971).

89. Cerdeira, F., Buchenau, C. J., Cardona, M., & Pollak, F. H. Stress-Induced Shifts of First-Order Raman Frequencies of Diamond- and Zinc-Blende-Type Semiconductors. *Phys. Rev. B* **5**, 580-& (1972).

90. Campbell, I. H., & Fauchet, P. M. The effects of microcrystal size and shape on the one phonon Raman spectra of crystalline semiconductors. *Solid State Commun.* **58**, 739-741 (1986).

91. De Wolf, I., Jian, C., & van Spengen, W. M. The investigation of microsystems using Raman spectroscopy. *Opt. Laser Eng.* **36**, 213-223 (2001).

92. Richter, H., Wang, Z. P., & Ley, L. The one phonon Raman spectrum in microcrystalline silicon. *Solid State Commun.* **39**, 625-629 (1981).

93. Ingrid De, W. Stress measurements in Si microelectronics devices using Raman spectroscopy. *J. Raman Spectrosc.* **30**, 877-883 (1999).

94. Dombrowski, K. F., De Wolf, I., & Dietrich, B. Stress measurements using ultraviolet micro-Raman spectroscopy. *Appl. Phys. Lett.* **75**, 2450-2451 (1999).

95. Menendez, J., & Cardona, M. Temperature dependence of the first-order Raman scattering by phonons in Si, Ge, and α-Sn: Anharmonic effects. *Phys. Rev. B* **29**, 2051-2059 (1984).

96. Hart, T. R., Aggarwal, R. L., & Lax, B. Temperature dependence of Raman scattering in silicon. *Phys. Rev. B* **1**, 638-& (1970).

97. Abstreiter, G., Cardona, M., & Pinczuk, A. Light scattering by free carrier excitations in semiconductors. *Top. Appl. Phys.* **54**, 5-150 (1984).

VITA

ERIK C. DREADEN

ERIK C. DREADEN was born May 12, 1984 in Atlanta, Georgia. He completed his secondary education at Eagles Landing High School in 2002 and received a B.S. in Chemistry (BSCHEM) from the University of Georgia in 2006, studying under Prof. John L. Stickney. He is currently a Ph. D. candidate in the School of Chemistry and Biochemistry at Georgia Institute of Technology, studying under Prof. Mostafa A. El-Sayed at the Institute's Laser Dynamics Laboratory. His current research interests include the design, synthesis, properties, and applications of colloidal bio-nanotechnologies, fundamental and applied plasmonics, photovoltaic devices, and spectroscopy. In the Spring of 2012, Erik will begin research in the labs of Prof. Paula T. Hammond at MIT, developing platforms for targeted RNA interference therapy for cancer.